



HAL
open science

Finite elements transfer functions accuracy related to human perception

Giorgio Pulvirenti

► **To cite this version:**

Giorgio Pulvirenti. Finite elements transfer functions accuracy related to human perception. Acoustics [physics.class-ph]. Université de Lyon, 2021. English. NNT : 2021LYSEI059 . tel-03625309

HAL Id: tel-03625309

<https://theses.hal.science/tel-03625309v1>

Submitted on 30 Mar 2022

HAL is a multi-disciplinary open access archive for the deposit and dissemination of scientific research documents, whether they are published or not. The documents may come from teaching and research institutions in France or abroad, or from public or private research centers.

L'archive ouverte pluridisciplinaire **HAL**, est destinée au dépôt et à la diffusion de documents scientifiques de niveau recherche, publiés ou non, émanant des établissements d'enseignement et de recherche français ou étrangers, des laboratoires publics ou privés.



INSA

N°d'ordre NNT : 2021LYSEI059

THESE de DOCTORAT DE L'UNIVERSITE DE LYON
opérée au sein de
I'INSA Lyon

École Doctorale ED 162
MEGA (Mécanique, Energétique, Génie Civil, Acoustique)

Spécialité/ discipline de doctorat : Acoustique

Soutenue publiquement le 19/10/2021, par :
PULVIRENTI Giorgio

Finite elements transfer functions accuracy related to human perception

Devant le jury composé de :

Deckers, Elke, professeure, KUL

Présidente, rapporteure

Kropp, Wolfgang, professeur, Chalmers University
García, Jouan J., docteur, Applus+ IDIADA

Rapporteur
Examineur

Parizet, Etienne, professeur, INSA-LYON
Totaro, Nicolas, professeur, INSA-LYON

Directeur de thèse
Co-directeur de thèse

Département FEDORA – INSA Lyon - Ecoles Doctorales – Quinquennal 2016-2020

SIGLE	ECOLE DOCTORALE	NOM ET COORDONNEES DU RESPONSABLE
CHIMIE	CHIMIE DE LYON http://www.edchimie-lyon.fr Sec : Renée EL MELHEM Bat Blaise Pascal 3 ^e étage secretariat@edchimie-lyon.fr Insa : R. GOURDON	M. Stéphane DANIELE Institut de Recherches sur la Catalyse et l'Environnement de Lyon IRCELYON-UMR 5256 Équipe CDFA 2 avenue Albert Einstein 69626 Villeurbanne cedex directeur@edchimie-lyon.fr
E.E.A.	ELECTRONIQUE, ELECTROTECHNIQUE, AUTOMATIQUE http://edeea.ec-lyon.fr Sec : M.C. HAVGOUDOUKIAN Ecole-Doctorale.eea@ec-lyon.fr	M. Gérard SCORLETTI Ecole Centrale de Lyon 36 avenue Guy de Collongue 69134 ECULLY Tél : 04.72.18 60.97 Fax : 04 78 43 37 17 Gerard.scorletti@ec-lyon.fr
E2M2	EVOLUTION, ECOSYSTEME, MICROBIOLOGIE, MODELISATION http://e2m2.universite-lyon.fr Sec : Safia AIT CHALAL Bat Darwin - UCB Lyon 1 04.72.43.28.91 Insa : H. CHARLES Safia.ait-chalal@univ-lyon1.fr	Mme Gudrun BORNETTE CNRS UMR 5023 LEHNA Université Claude Bernard Lyon 1 Bât Forel 43 bd du 11 novembre 1918 69622 VILLEURBANNE Cédex Tél : 06.07.53.89.13 e2m2@univ-lyon1.fr
EDISS	INTERDISCIPLINAIRE SCIENCES-SANTE http://www.ediss-lyon.fr Sec : Safia AIT CHALAL Hôpital Louis Pradel - Bron 04 72 68 49 09 Insa : M. LAGARDE Safia.ait-chalal@univ-lyon1.fr	Mme Emmanuelle CANET-SOULAS INSERM U1060, CarMeN lab, Univ. Lyon 1 Bâtiment IMBL 11 avenue Jean Capelle INSA de Lyon 696621 Villeurbanne Tél : 04.72.68.49.09 Fax :04 72 68 49 16 Emmanuelle.canet@univ-lyon1.fr
INFOMATHS	INFORMATIQUE ET MATHEMATIQUES http://infomaths.univ-lyon1.fr Sec : Renée EL MELHEM Bat Blaise Pascal 3 ^e étage infomaths@univ-lyon1.fr	Mme Sylvie CALABRETTO LIRIS – INSA de Lyon Bat Blaise Pascal 7 avenue Jean Capelle 69622 VILLEURBANNE Cedex Tél : 04.72. 43. 80. 46 Fax 04 72 43 16 87 Sylvie.calabretto@insa-lyon.fr
Matériaux	MATERIAUX DE LYON http://ed34.universite-lyon.fr Sec : M. LABOUNE PM : 71.70 –Fax : 87.12 Bat. Saint Exupéry Ed.materiaux@insa-lyon.fr	M. Jean-Yves BUFFIERE INSA de Lyon MATEIS Bâtiment Saint Exupéry 7 avenue Jean Capelle 69621 VILLEURBANNE Cedex Tél : 04.72.43 71.70 Fax 04 72 43 85 28 Ed.materiaux@insa-lyon.fr
MEGA	MECANIQUE, ENERGETIQUE, GENIE CIVIL, ACOUSTIQUE http://mega.universite-lyon.fr Sec : M. LABOUNE PM : 71.70 –Fax : 87.12 Bat. Saint Exupéry mega@insa-lyon.fr	M. Philippe BOISSE INSA de Lyon Laboratoire LAMCOS Bâtiment Jacquard 25 bis avenue Jean Capelle 69621 VILLEURBANNE Cedex Tél : 04.72 .43.71.70 Fax : 04 72 43 72 37 Philippe.boisse@insa-lyon.fr
ScSo	ScSo* http://recherche.univ-lyon2.fr/scso/ Sec : Viviane POLSINELLI Brigitte DUBOIS Insa : J.Y. TOUSSAINT viviane.polsinelli@univ-lyon2.fr	Mme Isabelle VON BUELTZINGLOEWEN Université Lyon 2 86 rue Pasteur 69365 LYON Cedex 07 Tél : 04.78.77.23.86 Fax : 04.37.28.04.48

*ScSo : Histoire, Géographie, Aménagement, Urbanisme, Archéologie, Science politique, Sociologie, Anthropologie

Acknowledgments

The authors gratefully acknowledge the European Commission for its support of the Marie Skłodowska Curie program through the ETN PBNv2 project (GA 721615). This work was performed within the framework of the LABEX CeLyA (ANR-10-LABX-0060) of Université de Lyon, within the program «Investissementsd’Avenir» (ANR-16-IDEX-0005) operated by the French National Research Agency (ANR).

Dedication

To my family.

Résumé

Dans le domaine de la qualité du son, les techniques d'auralisation exploitent les méthodes de simulations numériques pour reproduire les sons même en l'absence de prototype physique, ce qui accélère le processus de conception. Cependant, les simulations nécessitent des temps de calcul importants : comment les réduire ?

Cette thèse évalue l'influence des erreurs des simulations par éléments finis (FEM) sur les sons perçus après synthèse sonore. Si ces erreurs influent peu sur la perception humaine, alors les ingénieurs en acoustique pourraient en tirer parti en utilisant des modèles numériques moins précis mais perçus de manière équivalente à des modèles plus coûteux en ressources numériques. Après un état de l'art, la théorie des éléments finis est ici décrite et les erreurs numériques sont analysées. Des expériences numériques montrent comment cette théorie s'adapte à la réalité des simulations pour cas simples. Ensuite, un prototype de quart de véhicule est construit, simulé et testé ; le cas étudié représente la transmission du son entre le point de contact pneu-chaussée et un piéton à quelques mètres du véhicule. Un modèle de référence est construit et validé à partir des mesures. Quinze autres modèles sont obtenus en dégradant progressivement les paramètres initiaux. Les fonctions de transfert obtenues sont utilisées pour obtenir des signaux acoustiques par convolution avec l'enregistrement temporel d'un pneu. L'analyse de différentes métriques des sons suggère que les différences dues aux erreurs numériques ne sont pas significatives, ce que l'expérience perceptive confirme : les participants ont trouvé les tests difficiles, et seuls certains sons ont été perçus comme "différents" des sons de référence. Toutefois, certains paramètres des éléments finis ont été identifiés comme des paramètres clés de la qualité de la restitution sonore et sont analysés. La thèse se termine par un résumé et des propositions de perspectives pour les recherches futures.

Mots clés : Éléments finis, auralisation, fonctions de transfert acoustique, qualité du son.

Abstract

In the field of sound quality, auralization techniques exploit numerical simulation methods to reproduce sounds even in the absence of a physical prototype, which accelerates the design process. However, simulations require significant computational time: how to reduce them?

This thesis evaluates the influence of the errors of finite element simulations (FEM) on the sounds perceived after sound synthesis. If these errors have little influence on human perception, then acoustical engineers could benefit from using less accurate but equally perceived numerical models to more numerically expensive ones. After a state of the art, finite element theory is described here and numerical errors are analyzed. Numerical experiments show how this theory adapts to the reality of simulations for simple cases. Then, a prototype of a quarter vehicle is built, simulated and tested; the case studied represents the transmission of sound between the tire-road contact point and a pedestrian a few meters away from the vehicle. A reference model is built and validated from the measurements. Fifteen other models are obtained by progressively degrading the initial parameters. The obtained transfer functions are used to obtain acoustic signals by convolution with the temporal recording of a tire. Analysis of different sound metrics suggests that differences due to numerical errors are not significant, which is confirmed by perceptual experience: participants found the tests difficult, and only some sounds were perceived as "different" from reference sounds. However, some finite element parameters were identified as key parameters of sound reproduction quality and are analyzed. The thesis concludes with a summary and proposed perspectives for future research.

Keywords: Finite elements, auralization, acoustic transfer functions, sound quality.

Résumé étendu

De nos jours, les ingénieurs travaillant dans le domaine des transports, et notamment les acousticiens, sont confrontés à trois défis essentiels :

- (1) D'une part, ils doivent répondre aux demandes de clients de plus en plus exigeants en termes de qualité des produits. En particulier, dans le domaine acoustique, on parle de qualité de la perception du son.
- (2) Ils doivent respecter des réglementations de plus en plus strictes.
- (3) Enfin, ils doivent être capables de concevoir et de produire de nouveaux produits en fonction des délais de plus en plus courts du marché.

Les deux premiers problèmes constituent un défi car ils entraînent un certain nombre de compromis qui compliquent énormément le problème d'ingénierie. Le troisième problème impose la rapidité dans la résolution de ce défi. L'évolution technologique a permis de développer des outils de simulations numériques pour aider les ingénieurs dans ce processus. Dans le cas de la qualité du son, par exemple, des signaux numériques simulés peuvent être utilisés pour créer un environnement sonore permettant une immersion de l'ingénieur ou du client et donnant ainsi une idée de la qualité sonore du produit, même en l'absence de prototypes physiques.

Toutefois, ces outils sont loin d'être parfaits : ils fournissent une solution approchée du problème (dépendant des paramètres du modèle) et sont parfois limités par des temps de calculs trop importants. Ces deux points sont extrêmement liés : pour diminuer l'erreur d'approximation des modèles, la solution la plus simple est d'affiner le modèle ce qui mène directement à une augmentation des temps de calculs.

Une approche souvent utilisée par les chercheurs consiste à développer des techniques mathématiques capables de réduire considérablement le temps de calcul tout en n'altérant que très peu la précision du résultat. Les techniques de réduction d'ordre des modèles et le développement de solveurs efficaces en sont des exemples. Nombre de ces techniques sont déjà mûres et utilisées de manière systématique dans l'industrie.

Mais une autre approche est sans doute possible. Le système auditif humain n'est pas capable de distinguer parfaitement des sons extrêmement similaires les uns aux autres. En outre, même si deux sons sont distingués, ceci n'implique pas forcément qu'ils soient jugés très différents du point de vue de la qualité sonore. Cette thèse vise à exploiter ces caractéristiques afin de comprendre dans quelle mesure il est possible de détériorer la qualité des simulations sans modifier substantiellement la qualité du son perçue.

Cette thèse porte sur la simulation des fonctions de transfert (TF, de l'anglais "transfer functions") à l'aide de la méthode des éléments finis (FEM, de l'anglais "finite element method"). Cette méthode de simulation est extrêmement répandue, tant au niveau industriel qu'universitaire. Son succès est essentiellement dû à sa polyvalence : dans le domaine de la vibroacoustique, elle permet de traiter des problèmes d'acoustique interne et externe, mais également des problèmes couplés (interactions fluide-structure). La raison pour laquelle nous nous concentrons exclusivement sur la simulation des fonctions de transfert est double. D'une part, la flexibilité de cette approche a des applications pratiques significatives d'un grand intérêt scientifique et industriel ; par exemple, le levier d'action le plus couramment utilisé par l'ingénieur porte sur l'optimisation des transferts entre la source (qu'il ne contrôle généralement pas) et l'auditeur. D'autre part, elle permet de se concentrer sur un seul aspect du problème, en s'assurant que les résultats obtenus dépendent exclusivement des erreurs numériques de la TF.

Le travail de cette thèse est divisé en trois chapitres principaux. Le premier concerne une analyse de la méthode des éléments finis et des erreurs inhérentes à cette méthode. En particulier, quatre points sont analysés en détails.

Tout d’abord, l’acoustique linéaire et ses propriétés mathématiques sont présentés. En particulier, l’équation de Helmholtz et les principales propriétés des systèmes linéaires invariants dans le temps sont brièvement décrits. Le problème de Helmholtz est ensuite réécrit dans une formulation faible, au moyen de dérivées distributionnelles, afin de rendre sa solution mathématique applicable dans tout domaine géométrique tridimensionnel. A ce stade, tous les éléments nécessaires pour décrire les fonctions de transfert associées à un chemin acoustique donné sont définis.

Ensuite, la méthode des éléments finis est présentée comme un cas particulier des méthodes de Galerkin (d’autres façons d’introduire la méthode des éléments finis sont mentionnées dans les annexes). À ce stade, un accent particulier est mis sur la structure matricielle des équations FEM et les fonctions mathématiques (fonctions de forme polynomiale) qui sous-tendent le modèle d’éléments finis sont introduites. Une analyse des erreurs FEM les plus typiques, telles que les erreurs de pollution et d’approximation, est ensuite effectuée. En particulier, l’erreur de pollution provient d’un comportement dispersif des éléments finis (le nombre d’ondes simulé n’est pas constant lorsque la fréquence varie). Une série d’exemples montre les effets de cette erreur dans les réponses en fréquence dans le cas d’une source monopolaire placée dans un espace tri-dimensionnel. Dès ce stade de la discussion, il apparaît que les paramètres les plus pertinents du modèle d’éléments finis sont l’ordre des fonctions de forme \mathfrak{p}_{FE} et la taille moyenne \mathfrak{h} des éléments finis. Un autre résultat important de cette section est le lien entre le comportement dispersif des éléments finis (qui dépend des paramètres \mathfrak{p}_{FE} et \mathfrak{h}) et l’énergie du spectre de la fonction de transfert correspondante.

Ensuite, les principales techniques permettant d’assurer la condition de rayonnement de Sommerfeld sont ensuite analysées, avec un accent particulier sur la méthode des couches absorbantes parfaitement adaptées (en anglais “perfectly matched layer”, PML), utilisée dans la phase suivante de la thèse. Dans ce cas, un paramètre crucial est l’épaisseur de la PML. En particulier, une épaisseur réduite de la PML conduit, selon la formulation mathématique, à une augmentation de l’énergie du spectre de la fonction de transfert et, par conséquent, à une augmentation de l’énergie du spectre.

Enfin, des simulations simples sont effectuées à l’aide du logiciel Actran pour vérifier les conclusions de l’analyse théorique sur les résultats numériques réels. Ces simulations sont extrêmement simples et traitent d’une source monopolaire en champ libre. En plus des résultats précédents, il est mis en évidence comment la PML interagit avec certains paramètres des éléments finis (en particulier avec l’ordre des fonctions de forme). Par conséquent, une épaisseur plus faible n’est pas toujours associée à une réduction de l’énergie du spectre. De plus, il est montré que lorsque la précision de la simulation diminue, dans le cas d’éléments linéaires ($\mathfrak{p}_{FE} = 1$), l’énergie du spectre tend à diminuer ; la tendance est inverse dans le cas d’éléments quadratiques.

Le chapitre se termine par une introduction à certaines métriques acoustiques couramment utilisées par les ingénieurs dans l’analyse de la qualité sonore, en expliquant comment les erreurs numériques étudiées précédemment peuvent affecter ces métriques. En particulier, l’énergie du spectre sonore aural est liée à trois mesures fondamentales en ingénierie acoustique : le niveau de pression acoustique pondéré A (SPL(A), de l’anglais “sound pressure level A-weighted”), la sonie N et l’acuité S . Puisque le spectre du son auditif dépend au moins en partie de la fonction de transfert, les changements du spectre mentionnés précédemment acquièrent une importance considérable. Cependant, à ce stade, il n’est pas encore possible de comprendre s’il est possible d’étendre, au moins partiellement, ces résultats à des applications pratiques.

Par conséquent, une application pratique est conçue pour tester les résultats précédents. Le troisième chapitre est consacré à la description de cette application et aux principaux résultats concernant les simulations et les métriques acoustiques associées.

L’application présentée est un quart de modèle d’un véhicule acoustique simplifié. Le prototype comprend un cadre en bois, une roue et un pneu. Le modèle a été testé dans une

salle anéchoïque pour mesurer les fonctions de transfert liées au trajet du son entre le pneu et un piéton. En particulier, 16 fonctions de transfert ont été enregistrées à l'aide d'une source monopolaire et de microphones. Ensuite, un modèle éléments finis précis a été créé et les fonctions de transfert simulées ont été comparées qualitativement à celles testées afin d'assurer d'un réalisme suffisant des simulations. Le modèle numérique est basé sur des éléments quadratiques et fait appel à un algorithme adaptatif (le maillage change en fonction de la fréquence du calcul). Ainsi, des bandes de fréquences ont été définies et des maillages ont été construits pour chacune d'entre elles. Chaque maillage comporte des éléments de tailles moyennes h différentes (la taille est fixée en fonction de la bande de fréquence associée au maillage).

Le modèle le plus précis possible sera ici utilisé comme référence. Ensuite, ce maillage de référence a été dégradé afin d'obtenir des maillages de moins bonne qualité. En particulier, les facteurs suivants ont été modifiés :

- (1) \mathfrak{N} , nombre de nœuds par longueur d'onde,
- (2) p_{FE} ; ordre d'interpolation des éléments finis,
- (3) t_{FE} , épaisseur de la coque convexe de l'élément fini (utilisée pour créer le maillage),
- (4) t_{PML} , épaisseur de la PML.

Pour chacun des 4 facteurs, deux niveaux ont été utilisés, pour un total de $4^2 = 16$ combinaisons. Le maillage de référence est défini de telle manière que tous ses facteurs sont au niveau 2, le plus précis. Ces nouvelles simulations ont été utilisées pour simuler les mêmes chemins acoustiques. Ensuite, une série d'analyses a été effectuée.

Le "poids" de chacun des modèles a été estimé à partir du nombre de degrés de liberté des maillages. L'adaptativité des maillages ayant été utilisée, le poids estimé correspond à la somme des degrés de liberté de maillages mise en place pour les différentes bandes de fréquence. Bien que cette méthode ne soit pas exacte dans l'estimation du poids de calcul, elle fournit une estimation suffisante pour hiérarchiser les modèles entre eux.

Ensuite, la métrique "response vector assurance criterion" (RVAC) a été exploitée pour estimer les différences globales entre chaque modèle et la référence. Ensuite, les décalages de fréquence, principalement dus aux erreurs de pollution, ont été estimés. Puisque les décalages ont tendance à s'aggraver de la même manière que le RVAC, il a été décidé d'utiliser uniquement le RVAC tout au long de la thèse pour représenter ces différences globales.

Ensuite, une erreur a été calculée entre chaque TF et la TF relative calculée via le modèle de référence ; l'erreur quadratique a été moyennée sur toute les bandes de fréquence : cette métrique, appelée \mathfrak{E} , représente l'erreur locale des fonctions de transfert.

A ce stade, les signaux acoustiques sont générés par convolution des fonctions de transfert avec un signal source. Le signal source utilisé est une portion d'un enregistrement du bruit émis par un pneu lors d'un test sur banc à rouleaux. La source étant toujours la même, toute différence dans les signaux audio est attribuée aux TF et, par conséquent, aux paramètres des simulations. Les métriques acoustiques SPL(A), sonie N et acuité S sont calculées pour chaque signal audio et comparées. Il est démontré que les métriques acoustiques varient peu d'un signal à l'autre. En particulier, la variation de l'intensité sonore est, pour de nombreux signaux audio, nettement inférieure à la différence juste perceptible. Les phénomènes décrits dans le chapitre précédent sont vérifiés et analysés plus en détails.

L'analyse du chapitre 3 est limitée aux paramètres acoustiques choisis. Afin d'avoir une vision globale de la manière dont les erreurs numériques influencent la perception, il est nécessaire de réaliser des tests de perceptifs. Nous avons choisi de réaliser des tests pour analyser les similitudes entre les sons. Ces tests nous permettent de comprendre dans quelle mesure des sons objectivement différents sont perçus comme tels par les humains. Lors de la conception de ces tests, un certain nombre de facteurs doivent être pris en compte. Tout d'abord, les facteurs

techniques tels que l’environnement, le support d’écoute et la manière d’interagir avec les participants. À cette fin, une salle acoustiquement isolée a été choisie, des écouteurs professionnels ont été utilisés et une interface graphique a été construite afin que les participants puissent gérer l’écoute des signaux audio de manière autonome. Le facteur le plus critique concerne le choix des sons à écouter. En fait, un total de 256 sons ont été synthétisés : seize pour chacun des seize chemins de transfert acoustiques étudiés. Pour éviter un état d’inconfort qui influencerait sans aucun doute les résultats du test lui-même, seuls cinq fonctions de transfert ont été sélectionnées. 18 participants ont pris part aux tests.

Les résultats des tests ont d’abord été analysés en vérifiant la répétabilité de chaque candidat, puis la corrélation. Enfin l’absence d’éventuels groupements est également contrôlée ; en fait, la présence de groupes de personnes ayant des perceptions similaires au sein du groupe, mais différentes des autres groupes, peut nécessiter des techniques statistiques différentes de celles utilisées ici. Un participant a été rejeté car il contrastait fortement avec les autres selon les matrices de corrélation. Une série d’indications statistiques, ainsi que les réactions rapportées par les participants, ont permis de conclure que les tests étaient difficiles : cette conclusion signifie que des simulations potentiellement imprécises conduisent à des résultats comparables en termes de perception.

Par la suite, une analyse de la variance (ANOVA) a été effectuée, montrant que les facteurs qui affectent le plus la perception sont \mathfrak{N} , \mathfrak{p}_{FE} , et partiellement aussi t_{PML} . De plus, bien que les résultats soient généraux, le chemin sonore semble influencer les différences perçues ; en particulier, les sons associés à certains chemins sonores ont un degré de similarité différent des autres. Enfin, il semble que le t_{FE} n’ait pas d’importance.

Par la suite, une analyse plus approfondie montre que seuls certains modèles s’avèrent être perçus différemment de la référence. De tels modèles ont les paramètres suivants :

- (1) $L[N]=1$;
- (2) $L[\mathfrak{p}_{FE}]=2$ et $L[t_{PML}]=1$, ou $L[\mathfrak{p}_{FE}]=1$.

où $L[\cdot]$ représente le niveau du facteur. En outre, il est vérifié que les modèles dont le RVAC est inférieur à une certaine valeur produisent des sons différents, tandis que ceux dont le RVAC est supérieure à cette valeur ne peuvent être distingués les uns des autres. Ainsi, une différence entre ces deux valeurs pourrait potentiellement être une différence juste perceptible.

Il est également testé que \mathfrak{E} n’est pas un bon prédicteur de la diversité sonore. D’autres métriques locales sont testées, mais aucune ne prédit la qualité du son mieux que le RVAC. Par conséquent, il semble que la métrique globale soit suffisante pour prédire la qualité des sons audibles. Étant donné que les mesures globales dépendent fortement des paramètres numériques du modèle, il s’ensuit que les ingénieurs peuvent se concentrer sur ces derniers au lieu d’essayer de comprendre comment les éléments locaux peuvent affecter la qualité du son.

En outre, la relation entre les métriques acoustiques et les résultats des tests perceptifs est analysée. Cette analyse montre que N et S sont de bons descripteurs des critères de perception des auditeurs.

Enfin, une analyse de la sonie spécifique montre comment les variations par bande de fréquence affectent les résultats des tests perceptifs, confirmant les résultats mentionnés dans les deuxième et troisième chapitres.

À ce stade, les résultats sont clairs et la thèse se termine par un compte rendu de ce qui a été trouvé et des orientations pour les recherches futures.

Plus précisément, nous expliquons comment les erreurs numériques se reflètent dans les spectres des fonctions de transfert simulées, essentiellement de deux manières :

- (1) Par des variations d’amplitude par rapport au spectre théorique
- (2) Par un décalage de fréquence par rapport au spectre théorique.

Les changements dans (1) sont essentiellement dus aux erreurs de pollution et d'approximation (dus aux paramètres des éléments finis, en particulier \mathbf{p}_{FE} et \mathbf{h}), aux erreurs de réflexion parasite (causées par la PML, et significatives lorsque l'épaisseur de t_{PML} est trop faible), et aux interactions entre la PML et les éléments finis. Les maillages caractérisés par des paramètres numériques égaux mais géométriquement différents (par exemple, en raison d'une épaisseur de volume d'élément fini différente t_{FE}) produisent également des spectres différents, mais l'erreur de discrétisation introduite de cette manière semble être moins influente que les autres, et certainement moins prévisible.

Les changements dans (2) sont essentiellement dus à l'erreur de pollution, sont plus présents aux hautes fréquences, et sont principalement influencés par l'ordre d'interpolation des fonctions de forme \mathbf{p}_{FE} .

Ces modifications produisent des changements à la fois dans le niveau d'énergie du spectre simulé et dans la distribution de l'énergie en fonction de la fréquence. Par conséquent, ils affectent à la fois N et S . Ces deux paramètres semblent suffisants pour rendre compte des principales différences perçues par les participants au test.

Un autre facteur extrêmement important concerne les difficultés rencontrées par les participants au test perceptif. Ces difficultés signifient que les sons ne sont pas trop différents en termes de perception, de sorte que, au moins pour certaines applications, des simulations avec un niveau de précision relativement faible peuvent être utilisées.

En ce qui concerne les orientations futures possibles de la recherche, les domaines suivants ont été identifiés :

- (1) Généralisation des résultats.
- (2) Applications pratiques.
- (3) Autres techniques.

Concernant le point (1), tout d'abord, il serait intéressant d'étudier l'effet du signal source ; qu'est-ce qui change lorsque le signal source a un spectre différent ? En particulier, l'effet des sources à haute énergie à haute fréquence ou avec de fortes composantes tonales est potentiellement très intéressant. En outre, un effort considérable pourrait être consacré à l'étude séparée des problèmes acoustiques internes, afin d'isoler les paramètres des éléments finis sans l'interaction et les effets des techniques pour assurer la condition de rayonnement de Sommerfeld. En ce qui concerne les problèmes acoustiques externes, d'autres méthodes pour assurer la condition de rayonnement de Sommerfeld pourraient être étudiées.

En ce qui concerne le point (2), deux applications pratiques ont été identifiées et pourraient être étudiées. Tout d'abord, les applications dans lesquelles les classements des préférences jouent un rôle clé ; ces applications ont déjà été étudiées dans la littérature, et il a été démontré que des erreurs importantes n'affectent pas les classements finaux. Cela pourrait signifier que, dans ces applications, une très faible précision des modèles numériques pourrait être suffisante. Une autre application pratique concerne les modèles prédictifs capables de prévoir les différences de perception des résultats, ou du moins de fixer des orientations pour différentes applications.

En ce qui concerne le point (3), il suffirait de répéter ce qui a été testé dans cette thèse avec différentes techniques, telles que méthode des éléments finis de frontière, à la méthode de tirs de rayon ou aux méthodes dites "moyennes et hautes fréquences" qui ont une description énergétique des voies de transfert.

Mots clés : Éléments finis, auralisation, fonctions de transfert acoustique, qualité du son.

Acronyms	29
Symbols	33
1 Introduction	37
1.1 Specific context of automotive industry	38
1.2 Sound quality and simulations	39
1.3 The toolbox of acoustic engineers	41
1.4 Problem statement	43
1.4.1 State of the art	43
1.4.2 Gap in knowledge	44
1.4.3 Research questions	44
1.5 The structure of the approach	46
2 Errors introduced by Finite Elements solving for unbounded acoustic problems	49
2.1 Linear-time-harmonic acoustics	49
2.2 Basic concepts of the Finite Element Method	51
2.2.1 The Galerkin method	51
2.2.2 The Finite Element Method equation	52
2.2.3 Solvers	53
2.3 Errors and adaptivity	55
2.3.1 Numerical dispersion	55
2.3.2 Interpolation and pollution errors	56
2.3.3 Adaptive meshes	59
2.4 Ensuring the Sommerfeld radiation condition	61
2.4.1 Perfectly Matched Layers	62
2.5 Numerical examples	64
2.5.1 PML and FE performance	66
2.5.2 PML thickness	68
2.5.3 Shape of the FE volume	68
2.5.4 Performance of the FW-H algorithm	69
2.6 Linking FE theory to sound perception	72
2.6.1 An introduction to acoustic metrics	72
2.6.2 How do the errors affect the metrics?	73

3	Experimental characterization and numerical modeling of the considered scenario for sound perception	77
3.1	Definition of the scenario	77
3.1.1	The mock-up	77
3.1.2	Sources and receivers positioning	78
3.1.3	Experimental measurements of transfer functions	81
3.2	The Reference Numerical Model	82
3.3	Design of Experiments	86
3.4	Models Analysis	88
3.4.1	Computational size of numerical models	90
3.4.2	Calculation of numerical errors	92
3.5	Acoustic metrics	99
4	Jury Tests	105
4.1	Design of the Tests	105
4.2	Data processing	109
4.3	Acoustic analysis	111
4.3.1	Univariate ANOVA	111
4.3.2	Post-hoc analysis and grouping	117
4.4	Linking perception and simulation	119
4.4.1	Perception vs. numerical errors	119
4.4.2	Criteria used by participants to distinguish noise samples	121
4.4.3	Specific loudness and timber features	123
4.4.4	From numerical errors to perception: a summary	127
5	General Conclusions and Perspectives	129
5.1	From numerical errors to human perception - overview of the process	129
5.2	Main results for the tire example	131
5.3	Future Research	132
5.3.1	Generalization of the results	132
5.3.2	Practical applications	133
5.3.3	Other techniques	133
	Bibliography	135
A	Basis of Functional Analysis	147
A.1	Norms and semi-norms	147
A.2	Banach and Hilbert spaces	147
A.3	L^p -spaces	148
A.4	Functionals and duality	148
A.5	Distributions	148
A.6	Distributional Derivatives and H^1 Sobolev spaces	149
B	Insights into the FEM	151
C	Details on the source	153
C.1	Response vector assurance criterion: matrices	153
C.2	Response vector assurance criterion: vectors	157
D	PML vs. IEM	165
D.1	The infinite element method	165
D.2	Infinite element performances	167

E	Detailed effect of PML thickness on the acoustic samples	169
F	Jury tests data	173
F.1	Correlation tables	173
F.2	Jury test score vs. quadratic error	174
F.3	Jury test score vs. \overline{RVAC}	175

List of Figures

1.1	Sound quality via simulation	40
1.2	Map of simulation techniques	42
1.3	Source - Transfer Path - Receiver	45
2.1	The FEM for Helmholtz problems	54
2.2	Exact vs. approximated wavenumber	57
2.3	Pollution of reflected waves: setup	57
2.4	Pollution of reflected waves: spectrum	58
2.5	Pollution effect with adaptive meshes	60
2.6	PML in Cartesian coordinates	63
2.7	Monopolar source geometries	65
2.8	Linear FE and PML performances	66
2.9	Linear vs. quadratic elements at high nodal resolution	67
2.10	Linear vs. quadratic elements at low nodal resolution	68
2.11	Influence of PML thickness	69
2.12	FEM solution - cubic vs. spherical volumes	69
2.13	Monopolar source's cuboid geometry	70
2.14	Cuboid geometry - spectra's amplitude	70
2.15	Cuboid geometry - spectra's phase	71
2.16	FE volume's thickness vs. wavelength	71
3.1	Mock-up projections	79
3.2	Monopole and receiver positions	80
3.3	The microflown source	82
3.4	FE surface mesh of the mock-up	83
3.5	Gradient factor effects	84
3.6	Test vs. simulated TFs	85
3.7	Monopole vs. mock-up	86
3.8	Convex hulls comparison	87
3.9	Source spectrum	88
3.10	TFs comparison	89
3.11	RVAC matrix	93
3.12	<i>RVAC</i> and Δf	94
3.13	Simulated vs. shifted TFs	94
3.14	Reference vs. Simulated vs. shifted TFs	95
3.15	\overline{RVAC} vs. $\overline{\Delta f}$	96

3.16	Examples of $RVAC$	97
3.17	DoF and \overline{RVAC}	97
3.18	DoF and \overline{RVAC}_{band-i}	98
3.19	$\overline{\mathcal{E}}$ vs. \overline{RVAC}	99
3.20	Simulated TFs and auralized sounds spectra	100
3.21	$\Delta SPL(A)$ vs. $\overline{\mathcal{E}}$	101
3.22	ΔN vs. $\overline{\mathcal{E}}$	101
3.23	ΔS vs. $\overline{\mathcal{E}}$	102
4.1	SQ target development process	106
4.2	Listening room	107
4.3	ΔN of the jury test TPs	108
4.4	Jury test GI	108
4.5	Repeatability analysis	109
4.6	Jury test scores box plots	110
4.7	Correlation matrix: TPs G-11 and S+20	111
4.8	Reduced datas box plot	112
4.9	ANOVA - main effects	114
4.10	ANOVA - two-factor interactions	115
4.11	ANOVA - three-factor interactions	116
4.12	Jury test scores - TPs: G-11, S-21, G+10, and S+20	118
4.13	Jury test scores - TP S+11	119
4.14	Jury test score vs. $\overline{\mathcal{E}}$ - TP S+20	120
4.15	Jury test score vs. $\overline{\mathcal{E}}$ - TP S+11	120
4.16	Jury test score vs. \overline{RVAC} - TP S+11	121
4.17	Jury test scores vs. predictive model	123
4.18	Specific loudness and TF spectra - TP G-11, high PML thickness and quadratic FE	125
4.19	Specific loudness and TF spectra - TP G-11, low PML thickness and quadratic FE	126
4.20	Specific loudness - TP G-11, linear FE	127
5.1	From numerical errors to sound perception	129
C.1	RVAC matrix: other models (1)	153
C.2	RVAC matrix: other models (2)	153
C.3	RVAC matrix: other models (3)	154
C.4	RVAC matrix: other models (4)	154
C.5	RVAC matrix: other models (5)	154
C.6	RVAC matrix: other models (6)	154
C.7	RVAC matrix: other models (7)	155
C.8	RVAC matrix: other models (8)	155
C.9	RVAC matrix: other models (9)	155
C.10	RVAC matrix: other models (10)	155
C.11	RVAC matrix: other models (11)	156
C.12	RVAC matrix: other models (12)	156
C.13	RVAC matrix: other models (13)	156
C.14	RVAC matrix: other models (14)	156
C.15	$RVAC$ and Δf : other models (1)	157
C.16	$RVAC$ and Δf : other models (2)	157
C.17	$RVAC$ and Δf : other models (3)	158
C.18	$RVAC$ and Δf : other models (4)	158
C.19	$RVAC$ and Δf : other models (4)	159

C.20	<i>RVAC</i> and Δf : other models (6)	159
C.21	<i>RVAC</i> and Δf : other models (7)	160
C.22	<i>RVAC</i> and Δf : other models (8)	160
C.23	<i>RVAC</i> and Δf : other models (9)	161
C.24	<i>RVAC</i> and Δf : other models (10)	161
C.25	<i>RVAC</i> and Δf : other models (11)	162
C.26	<i>RVAC</i> and Δf : other models (12)	162
C.27	<i>RVAC</i> and Δf : other models (13)	163
C.28	<i>RVAC</i> and Δf : other models (14)	163
D.1	The FE/IE model	166
D.2	The IE geometry	166
D.3	IEM - linear FE, high vs. low nodal resolution	168
D.4	IEM - linear vs. quadratic FE	168
F.1	Correlation matrix - TP S-21	173
F.2	Correlation matrix - TP G+10	173
F.3	Correlation matrix - TP S+11	174
F.4	Jury test score vs. $\bar{\mathcal{E}}$ - TP S-21	174
F.5	Jury test score vs. $\bar{\mathcal{E}}$ - TP G+10	175
F.6	Jury test score vs. $\bar{\mathcal{E}}$ - G-11	175
F.7	Jury test score vs. \overline{RVAC} - TP S-21	176
F.8	Jury test score vs. \overline{RVAC} - TP G+10	176
F.9	Jury test score vs. \overline{RVAC} - TP G-11	177
F.10	Jury test score vs. \overline{RVAC} - TP S+20	177

List of Tables

2.1	Critical-band rate	72
3.1	Mono-poles location coordinates	81
3.2	Receivers position coordinates	81
3.3	Adaptive frequency bands	84
3.4	Factors and their levels	88
3.5	Computational size of numerical models	91
4.1	Jury test participants	106
4.2	ANOVA - main effects	113
4.3	ANOVA - two-factor interactions	113
4.4	Models producing sounds different from the reference ones	119
E.1	SPL(A) increases due to PML thickness	170
E.2	N increases due to PML thickness	170
E.3	S increases due to PML thickness	171

Acronyms

ABC	Absorbing boundary conditions
ANOVA	Analysis of Variance
BEM	Boundary Element Method
CMS	Component Mode Synthesis
CAD	Computer aided design
CAE	Computer aided engineering
DOE	Design of Experiment
dof	degrees of freedom
<i>DtN</i>	Dirichlet to Neumann
EV	Electric Vehicle
FE	Finite Element
FEM	Finite Element Method
FW-H	Ffwoocs Williams and Hawkings
GF	Gradient factor
HEV	Hybrid-Electric Vehicles
HEV	Heating, ventilation, and air conditioning
ICE	Internal Combustion Engine
IC	Infinite element
IEM	Infinite element method
IRF	Impulse Response Function
MUMPS	Massively parallel sparse direct solver
NVH	Noise, vibration and harshness

PBN Pass By Noise
PCA Principal Component Analysis
PDE Partial Differential Equation
PML Perfectly matched layer
PTF Patch Transfer Function
RVAC Response vector assurance criterion
SEA Statistical Energy Analysis
TF Transfer Function
TP Transfer Path
TPA Transfer Path Analysis
TPS Transfer Path Synthesis

Symbols

c Speed of sound

f Frequency

h FE size

i Imaginary unit

k Wave number

$L[factor]$ Level of a *factor*

N Loudness

\mathfrak{N} Nodal resolution

p Acoustic pressure

p_{FE} Order of interpolation of polynomial FE shape functions

$\Re\{a\}$ Real part of a

\mathbb{R} Set of real numbers

S Sharpness

SPL(A) A-weighted sound pressure level

t Time

t_{FE} FE volume thickness

t_{PML} PML thickness

u Particles velocity

Y Admittance

Z Impedance

λ Wavelength

ρ Density

σ Standard deviation

ω Angular velocity

Δ Laplacian operator

∇ Gradient operator

NOWADAYS, for a noise vibration and harshness (NVH) engineer, pressure from the market requires increasingly shorter development cycles and a continuous reduction of design costs. Engineers also have to face increased expectations of customers who demand high-quality products and tightened norms about social, environmental and health issues expected by regulators. Even if researchers regularly produce promising results which drastically improves performances of available tools, reaching and merging all these sometimes antagonist constraints is a challenging task.

The consequences are clear: engineers must take correct design decisions early in the design process which is, usually, an arduous task. In this context, the use of virtual prototyping represents a keystone. Such approaches, based on performing simulation models, allow multi-attribute optimization schemes. In other words, they bring decision-making to be a computer-aided job, possible even in the absence of physical prototypes.

In the NVH context, the main keyword is sound quality, which Blauert and Jekosch defined in the context of industrial products as [1]:

Product sound quality is a descriptor of the adequacy of the sound attached to a product. It results from judgements upon the totality of auditory characteristics of the said sound - the judgements being performed with reference to the sets of those desired features of the product which are apparent to the users in their actual cognitive, actional and emotional situation.

In this definition, the term sound refers to the percepts of hearing rather than the acoustic waves. To make sound quality design decisions, engineers create sound files from simulated, measured, or synthesized data for listening purpose. This process is called auralization [2]. In the early stage of development and in case of auralization aim, the use of simulated sounds is critical. The first strategy is to set the best possible model, accounting for all the phenomena involved in the acoustic transfer path (TP), from the source to the listener. Even if modern simulations tools are incredibly powerful, they still face some limitations. The bitter endpoint of their capabilities is the requirement of high computational power to produce finely tuned models. Researchers proposed many different techniques to tackle this issue (see, for example, [3, 4]). Many of these methodologies are strictly mathematical, meaning that the use of a particular algorithm allows to reduce the calculation time by reducing the size of data-sets, by increasing the efficiency of the calculation process, or by rewriting the original problem in a simplified manner, for instance. A second possible approach, addressed in the present work, is to take benefit of the purpose of simulated sound: the auralization and sound perception. Following this strategy, the objective is not to carry out the best simulations but the sufficient ones. Human hearing system presents some filtering effects that might be useful to decrease the computational need.

Instead of developing further mathematical tools to improve simulation performances, the focus switches to the production of "fine enough" models which are expected to be much coarser than the ones needed following the first strategy. The outcomes will be faster computations and same perception evaluation of sounds. Obviously, the resulting auralized sounds need at any rate to keep essential aims-dependant psychoacoustic properties. The following aims at answering the question: "How much can a model be degraded, in comparison to a very accurate one, to reach a significant advantage in terms of computation, but without losing perceptual significance?"

1.1 Specific context of automotive industry

Automotive industry is submitted to many standards among them standards on pollutant emission and standards on acoustic emission. The most straightforward way to decrease pollutant emission is to decrease the overall mass of the car. Unfortunately, this often results in a degradation of acoustic efficiency of both exterior and interior noise emission. However, respecting both standards is mandatory. Indeed, it is well known pollutants and noise have dramatic effects on public health. In 2011, World Health Organization estimated an interval between 1 and 1.6 million disability-adjusted life-years due to noise pollution in the western Europe area alone [5]. As a consequence, European Pass By Noise (PBN, [6]) regulations have become continually more rigorous, requiring lower levels of maximum acceptable radiated sound pressure. Alongside, norms on atmospheric pollution are becoming so stringent that they have forced a radical change in the industry: the switch from internal combustion engine (ICE) to hybrid-electric and electric vehicles (HEV and EV, respectively). Since these types of machines have a completely different acoustic signature, they are strongly affecting the work of NVH engineers. As they are almost silent, HEV and EV bring new challenges, completely different from those historically tackled by NVH engineers. For example, as quieter cars have proven to be more likely to be involved in incidents, especially with visually impaired pedestrians [7, 8], PBN regulations started requiring a minimum level of produced noise. A possible approach is the generation of auditory warning sounds via loudspeakers. A currently ongoing field of research is the design of such sounds (see, for instance, [9]).

Road vehicles are complicated ensembles of several systems and subsystems interacting with each other. From an acoustic perspective, this results in two sets of difficulties: knowing the sources and evaluating the acoustic transfer path. Many physical phenomena can act as acoustic sources and consequently require a specific mathematical description; summaries of them are available in literature [10–12]. As far as they are concerned, the transfer paths from sources to receivers can be very complicated in terms of geometry, materials (frequency, temperature and humidity dependant materials for example) and environment (road surface, atmospheric effects on acoustic radiation, etc...). Switching to HEV and EV comes with modifications of sources and transfer paths. Indeed, while ICEs mask noises coming from a wide variety of sources and phenomena, HEV and EV, reveal them since their engines are significantly quieter and have different architectures. Consequently, many additional sounds become audible, changing the acoustic signature of vehicles. In addition, while ICEs noise provides the driver with feedback about vehicle speed and acceleration, this is not true in the case of HEV and EV. Companies can address both these issues, for instance, by injecting sound in the vehicle cabin by means of loudspeakers or other active devices [10]. As can be seen, NVH engineers have a lot of various constraints to deal with. This comes together with further limits due to trade-off with other design aspects, such as durability, dynamics and comfort [13, 14]. Put in a nutshell, sound engineers in the automotive industry have few possibilities and few time to improve the design from a sound quality perspective without violating some other constraints. Therefore, NVH engineers have to continuously settle a trade-off to respect all these quickly changing standards and to deal with concomitant old (ICE) and new (HEV and EV) paradigms. To this aim and to avoid

expensive trial and error processes, they largely use numerical simulations. Unfortunately, even if the use of numerical simulations to predict the acoustic response is common and sometimes obligated [2], they still face some huge problems as well for the computation time as for the representativeness of the reality.

Despite these difficulties, setting realistic psychoacoustic targets to ensure commercial appeal has become a priority for automotive companies. By tightly integrating sound quality with vehicle development in its early stages, engineers are nowadays able to design noise attributes that express a very strong brand identity [15]. Attention goes to any detail that can affect customer choices, including those that may appear unnoticeable at first sight, like door closing sounds [16].

1.2 Sound quality and simulations

During the development phase of the product, it is likely that engineers want to assess the sound quality of several alternative configurations. With sound samples available thanks to simulation, this is a doable task, but not straightforward. Indeed, how is it possible to evaluate the luxurious and the sportive character of a sound for high-end cars? What about robustness and reliability, which are undoubtedly characteristics desired for any vehicle? These tasks are hard at least for two reasons:

- (1) humans perception is a complicated phenomenon;
- (2) there are no universal quality indicators available in scientific literature.

Concerning point (1), the complexity of our hearing system has been subject to several researches and many publications discussing the subject are available [17, 18]. Without touching all aspects, it is worth mentioning that the hearing system weights the input signal in some regions of the frequency spectrum differently than others. For this reason, researches have developed weighting functions such as the A-weight. Another important aspect is the masking effect: given two sounds, one may become inaudible under certain circumstances; for instance, a noise can mask others if their loudness is lower enough. Lastly, in the automotive industry, also the ability of our hearing system to separate different sources, called stream segregation, is of particular importance [19].

As to point (2), it is relatively known how we react to specific characteristics of sounds, such as loudness and sharpness, for which metrics are available in literature [17, 18]. Individuals can evaluate sounds using words such as ‘high quality’, ‘clear and precise’, ‘pleasant’ [16], for which metrics usually do not exist^a. However, given two (or more) spectra, a single metric (or a combination of metrics) able to find the spectrum with the best quality does not exist for general cases. To overcome this issue, subjective tests that respect simple guidelines [21] are a powerful tool, allowing engineers to have a satisfactory and realistic evaluation of sound quality. It is also possible to correlate the sound quality evaluation with objective metrics, such as the loudness and sharpness mentioned above, or others. Techniques such as regression (linear, multi-linear, non-linear) or neural networks can fulfil this purpose. A reliable and exhaustive correlation allows engineers to avoid subjective tests in future development.

The introduction of simulation techniques into this process usually brings two problems inherent in computer-aided techniques: limitations in computational efficiency and loss of information due to approximation. The first one is a mathematical issue that researchers tackle by trying to reduce the number of operations required to calculate the solution of a simulation. Theoretically, this action should go together with a minimal loss of information about the physical

^aMetrics exist for complicated characteristics of sounds; see for instance [18] for roughness and fluctuation strength, and [20] for sportyness, powerfulness and luxury.

problem. The second issue is significant only when simulations induce errors higher than the desired accuracy and precision.

In reality, computation inefficiency and approximation related inaccuracies often go together, and smart approaches usually sacrifice numerical performances by neglecting physical information in a way that final results are in any case satisfactory for the user. Achieving such a balance requires proper management of the mathematical parameters involved. On the one hand, the criteria of approximation of reality, which depend on the choices of the user, are dependent on the physics of the problem and cannot be treated in general terms. On the other hand, the numerical formulation itself affects the final result depending on mathematical parameters. Therefore, the user himself needs to know these factors and their impact in the calculation process, at least in broad terms, to be able to take his decisions appropriately.

The scheme in Figure 1.1 represents this intricate set of relations. Sharp edge boxes represent the user's actions, while round edge ones represent any entity (physical or abstract) involved in the process. Single arrows represent the flow of the process; double arrows represent mutual interactions^b.

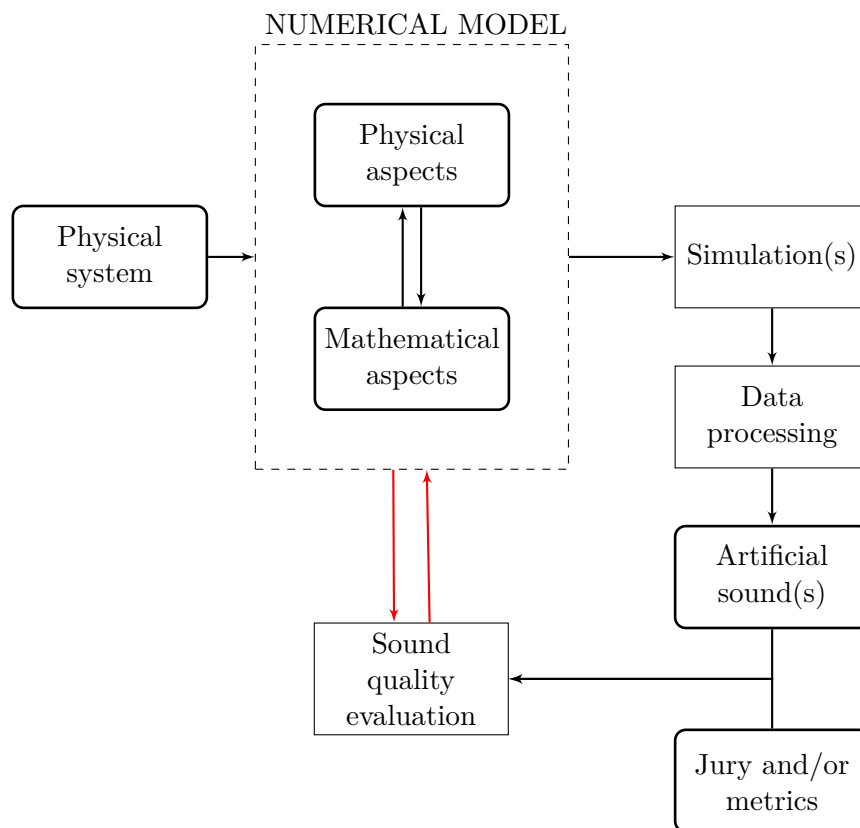


Figure 1.1: The figure is a scheme of the main process that leads to sound quality starting from simulation of a physical system. Sharp edges boxes represent the action of the user, while round edge ones are the main elements of the process. Double arrows represent mutual interactions, the red ones being the *simulation-perception relation*.

The user first chooses a technique to model the problem; clearly, the choice depends on the considered system and the frequency range of interest. To build the numerical model, the user has to make choices related to both the physics of the problem and the mathematical formulation. For a given technique, these two aspects are interdependent. Numerical limits affect the physical

^bInteractions can always be seen as mutual: the process is simplified to highlight just what is useful for the thesis.

representation by introducing an error, and on the other sense, physical traits put constraints on mathematical parameters. In certain circumstances, the user may even decide to neglect some phenomena. This mutual interaction makes this step, represented by the dashed box, crucial, since the performance of the entire process strongly depends on what decisions the user takes at this point. An inappropriate choice might radically vitiate the final result. Subsequently, the user calculates the solution of the problem through the simulation (whose running time depends on the decisions made at the previous step) and, in a second step, process the data to obtain the artificial sound. Processing can involve, for instance, inverse Fourier transform to calculate the IRF and convolution, which is the only choice if the source is not in steady-state. A jury lastly evaluates the sound quality properties of the latter. Alternatively, the user himself gives his conclusions based on acoustic metrics such as loudness, sharpness and others, after an opportune analysis which may or not involve correlation models.

In this framework and with the objective being sound quality evaluation, the simulation should need to produce sounds that are finely represented from a perceptive point of view, and not from a physical one. Perception accuracy, in turn, depends heavily on the performed analysis of sound quality. Studies about intensity, acuity, acoustic annoyance/comfort could require different levels of detail at the simulation level. Comparative analysis only requires that acoustic samples maintain their perceptual rankings relatively to each other. Hence, assuming a negligible impact of data processing into the artificial sound, the interaction between numerical model characteristics and human perception is mutual in this sense. The red double arrow in Figure 1.1 represents such interaction, which will be called from now on called here *simulation-perception relation*.

1.3 The toolbox of acoustic engineers

The acoustic problem in the automotive industry is intricate and in conflict with other design aspects. It is helpful in this sense to make a distinction between source, transfer path (TP) and receiver. Thanks to this approach, engineers keep a holistic view of the global system, while profoundly understanding the interaction between subsystems.

One of the advantages of such *modus operandi* is the possibility for engineers of troubleshooting the dominant TPs or the sources without affecting other subsystems that may need to satisfy strict design requirements. In this context, the process of assembling data of TP elements is called transfer path synthesis (TPS, [22]). Test-based TPS constitutes the foundations of the test-based techniques called transfer path analysis (TPA, [23]), very widely used in industry [24]. HEAD acoustics GmbH developed a TPA dedicated to sound quality, the binaural transfer path analysis [25].

At an earlier stage of the process, without any prototype available, the only way to anticipate the system behaviour is by synthesizing both the TPs and the functions to emulate the action of the sources via modelling techniques. Companies have invested significantly in the development of a virtual environment to perform simulation for sound quality evaluation [26, 27]. In particular, when fairly complex problems are the objects of simulations, the use of numerical methods capable to accurately represent complicated geometrical domains and (or) elaborate sources becomes necessary.

In the frequency-domain, there is not a single simulation approach well-performing in the whole spectrum. In general, element-based techniques such as the finite element methods (FEM) and the boundary element methods (BEM) perform quite well at low frequencies [3, 4]. At high frequency, there is a need for very fine meshes, and the consequent computational cost makes these techniques prohibitive. However, it is possible to reduce the dimensionality of the original problem through the so-called model order reduction techniques [3, 28]. A particularly common one is the modal approximation, based on the projection of the system matrices onto the space spanned by a set of the first n eigenvalues, where n is a choice of the user. In the case of problems

comprising several distinctly separated geometrical areas, another approach is to sub-structure the original domain into sub-problems opportunely coupled. Examples of these techniques are the component mode synthesis (CMS, [29]) and the patch transfer function method (PTF, [30]). At higher frequency, the cost of these approaches become too expensive. Furthermore, mechanical systems start exhibiting a statistical behaviour as the modal density increase. For instance, Kompella showed that nominally identical vehicles have significantly different dynamic behaviour in the frequency range where the modal density increases [31]. In this area of the spectrum, statistical techniques such as statistical energy analysis (SEA, [32]) have proved to be quite effective. The scheme in Figure 1.2 summarizes these techniques. This list is not exhaustive (for example, see chapter 2 for a further discussion). There also exists a so-called “mid-frequency” area particularly hard to study. Here, deterministic techniques are too much time-demanding in terms of calculation, and the modal density is not sufficiently high to satisfy the strict hypothesis of statistical techniques. Hybrid methods such as statistical modal energy analysis [33] find a place between statistical techniques and low-frequency techniques; reviews of techniques to tackle the mid-frequency problem are available in the literature [4, 34].

Once TP and source models are available, their combination can reproduce the phenomenon at the receiver location. In some cases it is possible to substitute the source with adequately placed mono-poles [35], in which case it is convenient to reproduce the phenomena at the receivers through the following steps [2]:

- (1) simulation or other means provide the transfer function (TF) associated with the TP in the frequency-domain;
- (2) the inverse Fourier transform modifies the TF into the impulse response function (IRF) of the TP;
- (3) the convolution of this IRF with an adequate signal representing the source produces the desired outcome.

Although this approach assumes the system to be linear in time, it is flexible since it allows to simulate source(s) and TP(s) separately, with considerable advantages in terms of reduced computational time. Furthermore, a combination of test measurements and simulation is possible.

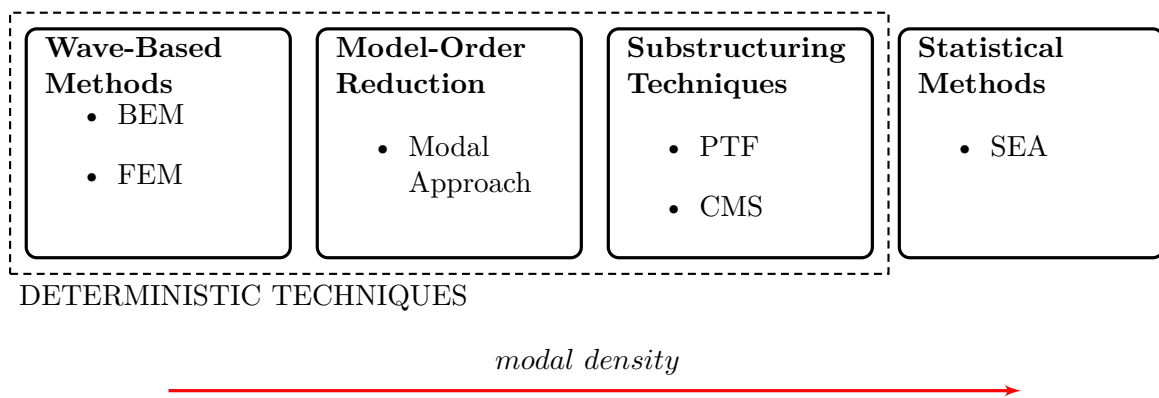


Figure 1.2: A map of simulation techniques in function of the modal density of the modelled system.

1.4 Problem statement

1.4.1 State of the art

Auralization is not a new field of research. Scientific papers related to this concept can be tracked at least to the beginning of this century, for instance in [27, 36]. The subsequent development of these early jobs leads to the already mentioned presence in the market of solutions and products. As to entirely modelling approaches, research is still ongoing, and it has been particularly productive in the last years. Several reasons might be concurrent to this vibrant activity.

Firstly, the inherent complexity of some physical mechanisms makes the simulation process arduous, even without considering sound perception. Some phenomena are so difficult to model that researchers developed ad-hoc techniques. Only most modern advancements allowed to discuss the use of simulation tools for sound quality applications in such complicated situation, at least in some cases, like for tire noise [13, 37].

Another reason is probably related to the computational cost associated with more standard techniques, such as the BEM or the FEM. Recent developments have at any rate permitted enhanced calculation rapidity: as a consequence, studies focusing on these methods have started appearing.

Researchers from Zhejiang University used an approach including finite elements for the structural problem and boundary elements for the acoustic one aiming at optimizing the sound quality of a diesel engine [38]. Xu et al. used a simulation method based, again, on the FEM for structures and the BEM for acoustics to optimize, through a genetic algorithm, the subjective annoyance of sounds perceived in the cabin of a car [39]. Hodor et al. were able to predict the less uncomfortable fan on a set of three thanks to a computational fluid dynamics approach with large eddy simulation [40]. Regarding the use of acoustic FEs, a group of researchers from Otto-von-Guericke-University Magdeburg studied both the thermal and the psychoacoustic behaviour of an encapsulation for a diesel engine. They carried out simulations in parallel with tests on an experimental set up that showed a good agreement. Although the tested encapsulation showed a decrease in terms of radiated sound power, simulations showed a margin for further improvements [41]. In another article, the group of researchers mentioned above proposed a predictive psychoacoustic model based on a virtual prototype representing, again, a diesel engine [42]. Through the simulations, they generated time signals, eight of which were selected to perform a jury test. The latter had the purpose of deriving a qualitative comparison between each sound. An analysis of results produced a quantitative characterization of each signal perceptive quality. Authors performed the process twice, to verify predictability of the model, with satisfactory results.

Those above studies proposed promising ways to exploit auralization techniques exclusively relying on simulations for sound quality prediction. Making such techniques robust, reliable and efficient requires a deep comprehension of the impact of simulation errors on acoustic perception and constitutes a necessary further step. Such knowledge can give indications on how to adequately set parameters of the mathematical models and, eventually, even to optimize them. For example, the following studies focused on this issue, contributing with essential results.

In 2011, Nykänen et al. [43] investigated the impact of frequency resolution and spectrum smoothing of binaural TFs into perception. The test case was the contribution of engine sounds to interior sounds of a truck. They performed tests to compare artificial head recordings to modified binaural TFs. Their findings showed that a resolution of 4 Hz or higher and a smoothing with maximum 1/96 octave moving average filters were comparable to artificial head recordings. Trollé et al. confirmed this frequency resolution value for vibroacoustic applications [44].

Nykänen, together with the same researchers of the previous work, continued their research by publishing further results [45] in 2013. This time the objective was to evaluate the maximum changes in frequency resolution and smoothing to preserve preference rating. They found that a

much higher degree of degradation for binaural TFs was possible. They found a value of 32 Hz for frequency resolution, and 1/24 octave bandwidth filters or 63 Hz absolute bandwidth filters for smoothing operations. Even though these values preserved preference ratings, the degradation comes together with a loss of consistency between participants of jury tests. Furthermore, results were not general since the modifications affected only TFs, and not the source. Final recommendations included the need for variance analysis when repeating a similar approach.

In 2018, Aujogue and Parizet further extended scientific knowledge about the accuracy of TFs for auralization purposes [46] in the case of TFs from input forces to acoustic pressure. Furthermore, the modifications were different for diverse area of the audible spectrum. At low frequency (i.e. low modal density), the study focused on displacements of eigenfrequencies. At mid and high frequencies, the main changes were smoothing techniques, consistently with previous studies. Results were similar to the ones of Nykänen et al. Besides, they found that at low frequency ranges, shift of the resonance frequency could easily be detected, in part due to the strong harmonic structure of the source.

1.4.2 Gap in knowledge

Results in literature are consistent and suggest not only that simulations might represent an efficient supporting tool for auralization, but also that users can be flexible in setting simulation parameters since the introduced modifications of TFs does not affect too much people's perception.

Contrary to the previously mentioned studies, which focused on modifications of experimental TFs, in this research, the focus is on the influence of simulation parameters in the perception of auralized sounds. The main reason to study in detail the TP modelling via simulation is the evident flexibility of this approach. As mentioned, it allows engineers to analyze different design configurations without the need for prototypes, taking into account only the TPs of interests. Evaluation of potential TP modifications would become simple even for complex geometries, thanks to simulation capabilities. Furthermore, assuming a description of the source being available as a set of monopoles (or other simple sources), either with a testing or a modelling approach, the coupling with the TPs would be possible relatively straightforwardly. All of this would already be possible in the early stages of development, with significant advantages for the process. The success of simulations in industrial applications is a proof of such strengths, and a crucial reason to bring improvements to the field.

Another decisive point is that even the studies that focused more deeply on the effect of errors in transfer functions introduced generic modifications. On the contrary, simulations present specific errors that might peculiarly affect perception. Understanding how people perceive and react to these errors is a crucial step towards the definition of thresholds between acceptable and unacceptable compromises in the use of these virtual methods.

1.4.3 Research questions

In this context, the *Simulation-Perception Relation* plays a critical role that is easy to comprehend. Its knowledge would allow engineers to set parameters of simulations correctly and to obtain the desired accuracy without excessively tuned models. However, the gap to be covered is vast, and it is not rational to tackle it at once, but some considerations are possible that allows to increase the knowledge in the field while providing some insight of immediate practical application.

First of all, there is a huge variety of transfer elements that characterize the typical automotive scenarios, both in the case of interior and exterior problems. Moreover, depending on how one is looking at the problem, an element can be a source, a receiver or even a TP. For instance, the vibrating panels inside the cabin of a car are a source of noise for the driver and the passengers, and are also receivers of the engine vibrations transmitted through the chassis. For

engineers, it is critical to understand what the objective is, how to tackle it and how to define the domain of intervention. With a focus on the acoustic part of the problem, receivers are humans interacting with the vehicle: driver, passengers, pedestrians, drivers and passengers of other vehicles. Section 1.1 already mentioned a review of some possible sources. Anything in between is a TP. A possible approach to simplify the TP is to consider only the geometry of the problem comprising the fluid. In this case, the vibrating parts of the boundary act as sources, while its geometry and the medium properties completely define the TP; this is the case of the acoustic domain in figure 1.3. The fluid medium is a constant of many (if not all) acoustic problems. Consequently, it is necessary to study in-depth the error related to it.

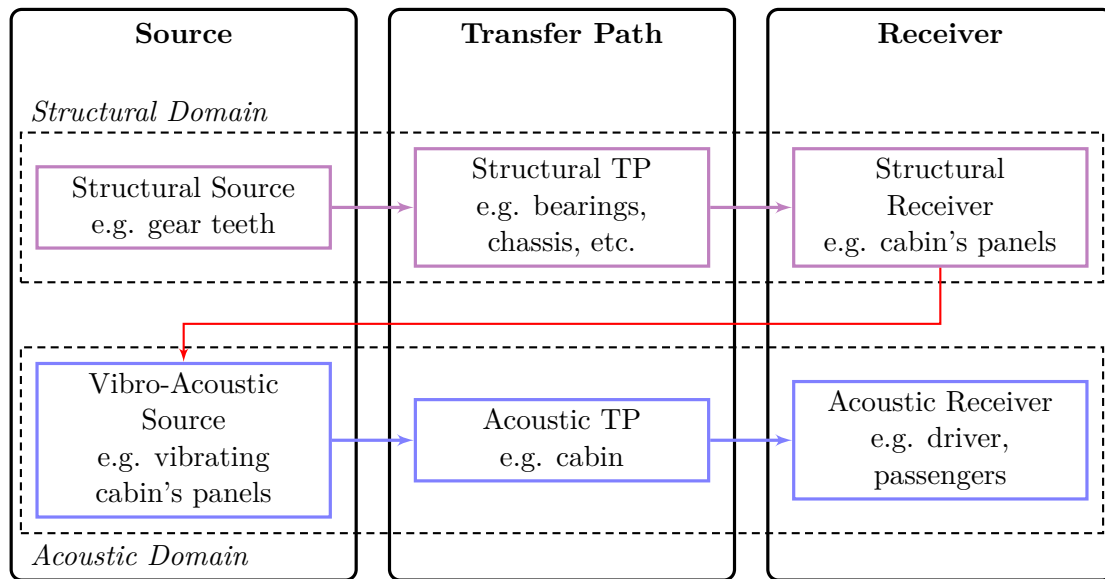


Figure 1.3: Source-Path-Receiver approach; most elements can be receivers, transfer elements or sources, depending on the sub-domain of interest. In this example, cabin's panels act as receivers of the structural domain, and as a source in the acoustic domain.

Another essential aspect to consider is related to the number of techniques currently available on the market, too ample to cover all of them. However, in the case of the FEM, scientists extensively studied numerical errors. A wide range of articles and books scrupulously describes their behaviour from a mathematical perspective and their implications in practical engineering problems. Moreover, the FEM is a conventional method in the industry. Therefore, it seems reasonable and useful to analyse the effect of FEs errors.

Lastly, as the use of synthesised TFs to describe TPs is so prevalent in the industry, it makes perfect sense to focus on this element of the source-path-receiver approach, since it is straightforward to calculate TFs with a geometry and a monopole source. On the contrary, source modelling represents an open challenge and, again, the field of application would restrict significantly.

With these facts in mind, a first approach to the use of the FEM to model TPs for auralization should focus on these issues:

1. do the various parameters of FE acoustic models introduce errors that humans perceive differently?
2. do common guidelines impose an accuracy that is adequate, insufficient or excessive for human perception?

1.5 The structure of the approach

In the scenario of this thesis, the numerical models serve to calculate TFs. The inverse Fourier transform modifies these TFs into their equivalent IRFs, thus removing the constraint of time-harmonicity. The convolutions of a source signal with these impulse response functions result in several sounds, which differ because of the different numerical errors of the original TFs. In this context, the easiest way to answer the research questions of subsection 1.4.3 is through a 2^n factorial experiment^c [47]. The process is the following:

- (1) select the n *factors* of the experiment, which are the numerical parameters supposed to affect the precision and accuracy of simulations;
- (2) fix two *levels* for each *factor*, namely two values different enough to introduce significant differences into the result of simulations;
- (3) build a *reference numerical model*, which should be realistic enough and whose *factors* are at the *level* corresponding to highest accuracy and precision;
- (4) build other $2^n - 1$ models, so to fulfill all the possible combinations of *levels* for the *factors*;
- (5) run the 2^n simulations and to analyze their results with objective metrics;
- (6) perform jury tests and to analyze their outcome.

Going through each step, the choice of *factors* and *levels* constitutes the first difficulty. First, the formulation of the FEM is rather complicated and has roots into deep mathematics (functional analysis, see app. A). Chapter 2 will discuss the theoretical reasons upon which the choices of these *factors*, and their *levels* are based. However, also practical considerations related to the meshing process affect these choices; for this reason, *factors* and *levels* are discussed later on, in Chapter 3.

The validation of the *reference numerical model* does not constitute a critical concern, since the objective is to have just a realistic model, and not a real one. A qualitative comparison between an actual mock-up and the outcome of a simulation of the *reference numerical model* is more than sufficient. Chapter 3, which focuses on the simulation side of this thesis, discusses the details.

Another issue related to simulations is the analysis of their results. In principle, the chosen path is to calculate some acoustic metrics and to perform a statistical analysis to understand if they vary depending on the *factors*. Sound pressure level A-weighted, Zwicker loudness and sharpness [18], which are common in literature, are the chosen metrics. The steps detailed in Chapter 3 provide a more in-depth understanding of the relation between numerical accuracy, acoustic metrics, and *factors*.

Lastly, Chapter 4 describes the jury tests, which are in charge to provide results about how much similarly people perceive the sounds. A careful analysis of repeatability and data distribution ensure that tests do not carry conceptual errors. Correlation analysis and clustering techniques allow to evaluate how many groups of people with similar perceptual score have raised during the tests. An analysis of variance (ANOVA) provides important conclusions about relations between *factors* and similarity scores. Correlation between the latter and some acoustic metrics, and an in-depth analysis of specific loudness give the final insights of this research.

^cUsually, the number of factors is indicated with the letter k , and the factorial experiment called 2^k ; here, the letter n is used instead, in order to avoid confusion with the wave-number.

Errors introduced by Finite Elements solving for unbounded acoustic problems

2.1 Linear-time-harmonic acoustics

TO understand the source of errors of a simulation method, its formulation needs to be understood, which in turn depends on the partial differential equations governing the physical phenomenon as well as on the boundary conditions. The purpose of this section is to detail the equations of linear-time-harmonic acoustics, which is the main subject of this research. Two considerations are necessary at this point.

First, although structural vibrations can be included in the field of acoustics [48], this is not the case in this dissertation. This choice has been made at purpose for sake of clarity of the study: fluid-structure interactions will not be considered in the following. Furthermore, the frequency range of interests is the audible one (here defined as the range between 20 and 20000 Hz, [18]), leaving out of the dissertation infra- and ultra-sounds.

Second, the acoustic motion derives from vibration energy propagating into an elastic medium in the form of compression-expansion pressure waves. However, any perturbing phenomenon strong enough to alter or to make the overall thermodynamic equilibrium unstable is not acoustical anymore [49]; this fact is fundamental to understand the logic process of this section.

Several references, available in literature, introduce the general equations of linear acoustics (see, for example, [50–52]). This section provides a summary of them. First of all, the variables of interest become small perturbations of ambient values. In the case of pressure and velocity, for instance, it results:

$$\tilde{p}(\mathbf{x}, t) = p_{tot}(\mathbf{x}, t) - p_{amb} \quad (2.1)$$

$$\tilde{u}(\mathbf{x}, t) = u_{tot}(\mathbf{x}, t) - u_{amb} \quad (2.2)$$

in which \mathbf{x} is the coordinate vector, t the time, subscripts *tot* and *amb* indicate respectively total and ambient values at the considered location, while \tilde{p} and \tilde{u} are the perturbations of pressure and velocity. The values of \tilde{p} and \tilde{u} generally need to be estimated in a geometric domain $\Omega \subseteq \mathbb{R}^d$, with d the number of spatial dimensions; Ω can be bounded or unbounded. The equation governing this class of problems is the inhomogeneous wave equation. It ensues, from mass conservation (both locally and globally), the Euler's equations of motion^a:

$$\frac{\partial^2 \tilde{p}(\mathbf{x}, t)}{\partial t^2} - c^2 \Delta \tilde{p}(\mathbf{x}, t) = 0, \quad (2.3)$$

^aThe following hypothesis hold: the fluid has zero heat conductivity, is inviscid, and the associated flow is adiabatic ([53], section 6.2).

where c is the (constant) speed of sound and Δ is the Laplacian operator. Assuming a time-harmonic dependence for the generic function $\tilde{f}(\mathbf{x}, t) = \Re\{f(\mathbf{x}, \omega)e^{-i\omega t}\}$, the homogeneous Helmholtz equation 2.4 is obtained by separation of variables:

$$\Delta p(\mathbf{x}, \omega) + k^2 p(\mathbf{x}, \omega) = 0, \quad (2.4)$$

where the wave-number^b k is given by $k = \omega/c$. A problem governed by the Helmholtz equation is Linear-Time-Harmonic. Despite the simplification introduced by the linear approximation and the time-harmonic assumption, this class of problems has a wide range of applications. Through a proper mathematical formulation of the problem, it is possible to calculate (or approximate, in the case of simulations) transfer functions between a monopole source and a point inside Ω . As mentioned in subsection 1.3, the so obtained TFs transmute into impulse response functions under the inverse Fourier transform. The convolution between IRFs and appropriate signals allows a move back towards the time-domain, removing the harmonicity constraint. This approach is per se of interests in many practical situations, and becomes even more useful when a superposition of linear pointwise sources can represent more complex radiating patterns. Indeed, in the latter case, the effect of complicated systems resolves into the sum of simple linear TFs or their time-domain equivalent via convolution of IRFs and source signals. Besides, these simplifications allow tackling issues related to steady-state systems without incurring in errors associated with incorrect formulations of time-dependencies.

Equation (2.4) is not sufficient to fully describe a linear time harmonic problem. The definition of proper conditions on the boundary $\Gamma \subseteq \mathbb{R}^{d-1}$ is necessary. The Robin boundary condition^c can be adapted to the linear-time-harmonic problem by including the Euler equation in frequency domain $u(\mathbf{x}, \omega) = \frac{1}{i\omega\rho_0} \frac{\partial p(\mathbf{x}, \omega)}{\partial n(\mathbf{x}, \omega)}$, with ρ_0 density of the medium at rest, into the admittance boundary condition:

$$u(\mathbf{x}, \omega) - u_s(\mathbf{x}, \omega) = Y(\mathbf{x}, \omega)p(\mathbf{x}, \omega). \quad (2.5)$$

in which Y is the admittance, n the outward normal to the boundary and u_s an assigned value. If $Y = 0$, Equation (2.5) degenerates into the Newman boundary condition and u_s becomes the velocity on Γ . Alternatively, it is possible to reformulate Equation (2.5) into the impedance boundary condition:

$$Z(\mathbf{x}, \omega)[u(\mathbf{x}, \omega) - u_s(\mathbf{x}, \omega)] = p(\mathbf{x}, \omega). \quad (2.6)$$

in which Z is the impedance. The latter condition degenerates to the Dirichlet boundary condition when $Z = 0$. In general, boundary conditions can be ‘mixed’: that is, different conditions apply to different subsets of Γ .

The solution of the described problem is given by outgoing (scattered by the geometry and radiated by sources) and incoming (originating at infinity) waves. However, in the case of unbounded problems, the incoming waves do not have any physical meaning: they need to be removed. The Sommerfeld radiation condition provides a simple mathematical statement that ensures only outgoing waves are present in the solution. [54]. It can be written as:

$$\lim_{\|\mathbf{x}\| \rightarrow +\infty} \|\mathbf{x}\|^{\frac{d-1}{2}} \left(\frac{\partial}{\partial \|\mathbf{x}\|} - ik \right) u(\mathbf{x}) \rightarrow 0 \quad (2.7)$$

in which the operator $\|\cdot\|$ is the Euclidean norm.

Mathematical description of boundary conditions becomes more complex in case of interactions between different types of phenomena. A typical example is the structural-acoustic strong

^bIn multidimensional spaces, the wavenumber has components related to the spatial dimensions of the solution: it is, therefore, a vector. Throughout this thesis, for the sake of simplicity, it is treated as a scalar, except where otherwise stated.

^cThis is a general boundary conditions taking the form $a(\mathbf{x})p(\mathbf{x}) + b(\mathbf{x})\frac{\partial p(\mathbf{x})}{\partial n(\mathbf{x})} = g(\mathbf{x})$.

coupling, in which a vibrating surface radiating power inside Ω is affected by the acoustic waves in Ω itself [52]. This thesis does not consider such types of coupling between boundaries and acoustic domain, since they are typical of only some applications in which a vibrating body is immersed in a heavy fluid (e.g., submarine industry). Furthermore, this assumption grants to focus on specific issues without introducing further errors.

From now on, variables dependence on \mathbf{x} and ω is assumed, and will be omitted except for underlining some essential aspects.

2.2 Basic concepts of the Finite Element Method

It may be hard to analytically handle the Helmholtz Equation (2.4) in some cases, for instance, when the geometry involves crooked boundaries [55]. In these situations, the use of numerical approximations, such as the finite element method (FEM) is more convenient. However, the formulation of the FEM is not straightforward and deserves some attention, especially to understand which parameters are mostly responsible for building errors with respect to the non-approximated solution of the Helmholtz problem.

The following introduction to the FEM comprises two parts. First, the Helmholtz problem is projected into a subspace through the Galerkin method, which, however, requires some basis functions not yet defined. Secondly, the geometric domain is discretized through finite elements to find the missing basis for the Galerkin method. There are actually other ways to formulate the FEM, for an insight see appendix B.

2.2.1 The Galerkin method

A first step for the FEM is to introduce the weak solution of the Helmholtz Equation (2.4). Initially, assuming that p is a function in the Sobolev space^d $H^1(\Omega)$, Equation (2.4) is multiplied by a generic test function $\chi \in W(\Omega) \subseteq H^1(\Omega)$, whose definition depends on the boundary conditions (for a full discussion, see [51, 56]). Then, its integral over Ω (including boundary conditions) is solved by part^e. Posing $s = i\rho_0 c$ and assuming a bounded geometrical domain, the governing equation becomes [50]:

$$\int_{\Omega} [\Delta p + k^2 p] \chi \, d\Omega = \int_{\Omega} (\nabla \chi \cdot \nabla p - \chi k^2 p) \, d\Omega - sk \int_{\Gamma} \chi (Yp + u_s) \, d\Gamma = 0, \quad \forall \chi \in W(\Omega). \quad (2.8)$$

The main obstacle to obtain an exact solution of Equation (2.8) is the infinite dimension of $H^1(\Omega)$. However, practical applications require a solution only within a certain precision and accuracy range: some approximations (for instance, the ones obtained via simulations such as BEM, SEA, and others) satisfy these criteria when the mathematical parameters are appropriately chosen: the FEM is part of this group of methodologies. The FEM is introduced here as a Galerkin method^f.

Firstly, the weak problem described by Equation (2.8) is projected on a ‘trial’ function space $V(\Omega) \subset H^1(\Omega)$ of finite dimension D spanned by a basis $\{\phi_n^{(p)}\}$. A trial solution is taken as:

$$p \approx \sum_{n=1}^{D(p)} p_n \phi_n^{(p)}, \quad (2.9)$$

^dSobolev spaces are discussed in Appendix A.

^eSee equation A.8.

^fSee Appendix B for more details about other ways to introduce the FEM

where p_n are the unknowns and $D^{(p)}$ are the degrees of freedom (DoF) associated to p_n (in terms of FE meshes, $D^{(p)}$ is equal to the number of nodes on which the pressure can have a value different from zero). Similar approximations hold for boundary velocity u_s and admittance Y : $u_s \approx \sum_{n=1}^{N^{(u_s)}} u_{sn} \phi_n^{(u_s)}$, $Y \approx \sum_{n=1}^{D^{(Y)}} Y_n \phi_n^{(Y)}$. The test functions are projected on a ‘test’ function space $W(\Omega) \subset H^1(\Omega)$ of finite dimension spanned by a basis $\{\varrho_n\}$; consequently it results $V = W$. Therefore, Equation (2.8) becomes:

$$\int_{\Omega} \left[\nabla \varrho_i \cdot \nabla \left(\sum_{n=1}^{D^{(p)}} p_n \phi_n^{(p)} \right) - \varrho_i k^2 \left(\sum_{n=1}^{D^{(p)}} p_n \phi_n^{(p)} \right) \right] d\Omega - sk \int_{\Gamma} \varrho_i \left[\left(\sum_{j=1}^{D^{(Y)}} Y_j \phi_j^{(Y)} \right) \left(\sum_{l=1}^{D^{(p)}} p_l \phi_l^{(p)} \right) + \sum_{m=1}^{D^{(u_s)}} u_{sm} \phi_m^{(u_s)} \right] d\Gamma = 0, \quad \forall \varrho_i \in \{\varrho_n\}. \quad (2.10)$$

By considering $\{\varrho_n\}$ a set of weighting functions, Equation (2.10) represents the well known weighted residual method [57]. The trial and test spaces, together with their basis, can be chosen according to several rules, see for instance [52]. The projection obtained by choosing $\{\varrho_n\} = \{\phi_n^{(p)}\}$ is called the Galerkin method (that is, trial and test functions are equal). The known terms in Equation (2.10) can be rearranged into three symmetric matrices and one vector, provided the boundary admittance is independent of the frequency [50]. The mass matrix \mathbf{M} has entries:

$$m_{jl} = \int_{\Omega} \phi_j^{(p)} \phi_l^{(p)} d\Omega. \quad (2.11)$$

The stiffness matrix \mathbf{K} has entries:

$$k_{jl} = \int_{\Omega} \nabla \phi_j^{(p)} \cdot \nabla \phi_l^{(p)} d\Omega. \quad (2.12)$$

The damping matrix \mathbf{C} has entries:

$$c_{jl} = \rho_0 c \int_{\Gamma} \phi_j^{(p)} \left[\{\phi^{(Y)}\}^T \{Y\} \right] \phi_l^{(p)} d\Gamma. \quad (2.13)$$

The boundary mass matrix Θ has entries:

$$\theta_{jl} = \int_{\Gamma} \phi_j^{(p)} \phi_l^{(u_s)} d\Gamma, \quad (2.14)$$

and it combines with the vector \mathbf{u}_s to build the boundary vector \mathbf{f} :

$$\mathbf{f} = sk[\Theta]\mathbf{u}_s. \quad (2.15)$$

The approximated governing equation is now:

$$[-k^2\mathbf{M} - ik\mathbf{C} + \mathbf{K}]\mathbf{p} = \mathbf{f}. \quad (2.16)$$

At this point, the set of functions $\{\phi_n^{(\cdot)}\}$ (the dot between parenthesis being p , Y or u_s) is not defined yet. It is here that the FEM comes to help.

2.2.2 The Finite Element Method equation

In the FEM, the basis functions $\{\phi_n^{(\cdot)}\}$ are piecewise polynomials defined over intervals called precisely finite elements. The process to define these functions is the following.

First, to discretize the geometrical domain Ω through FEs, several disjoint polytopes $\Omega_j \subset \Omega$

such that $\cup_{\Omega_j \in \Omega} \Omega_j = \Omega_{\mathcal{C}} \cong \Omega$, with $\Omega_{\mathcal{C}}$ the computational domain, and $\Omega_j \cap \Omega_l = \partial\Omega_j \cap \partial\Omega_l \quad \forall i \neq j$ ($\partial\Omega_j$ is the boundary of Ω_j) are identified in a mesh that is usually automatically built or manually created by the user in a virtual environment. The vertices of the polytopes are called nodes.

On each of the generated FEs, a space of polynomials is introduced with basis $\{F_l\}_i$ where $l = 1, 2, \dots, m$, m depends on the geometry and i is the considered element. Each F_l can be written as:

$$F_l(\xi) = \sum_{k=0}^{\mathfrak{p}_{FE}} a_k \xi^k, \quad (2.17)$$

where ξ_j is the local coordinate of the FE; the F_l are called shape functions. Several strategies can be used to determine the coefficients a_k in Equation (2.17); the Lagrangian polynomials are common, and even the Legendre polynomials can be found [58]. Equation (2.17) serves to interpolate the variable $p_{\mathcal{C}}$ inside each element, given the values at each node of the element itself; for these reasons, the order of the polynomial \mathfrak{p}_{FE} is here called order of interpolation of the shape functions. The latter parameter is chosen by the user, and it is usually the same across all the elements, but not always: see, for instance, [59].

The union of the $\{F_l\}_i$ is called here $\{F_l\}$ and is a polynomial basis for the entire geometrical domain $\Omega_{\mathcal{C}}$. Strictly speaking, in order to obtain $\{F_l\}$, some specific conditions must be ensured; since these conditions do not have implications in this thesis, they are not discussed here, but can be found in literature [52].

The finite element method consists in imposing $\{\phi_n^{(\cdot)}\} = \{F_l\}$ while enforcing continuity between elements. Thus, the entries of the matrices in Equation (2.16) are immediately defined; the process of assembling the matrices is widely discussed in literature [52, 60]. As a consequence of the aforementioned properties, Equation (2.16) is approximated by piecewise polynomial functions. The scheme in Figure 2.1 summarizes the steps necessary to reach the formulation (2.16) from the Helmholtz problem; the process in purple, representing the Galerkin method, and the blue process, representing the meshing process, are not parallel.

2.2.3 Solvers

At this stage, all the elements of the problem are defined, with the matrices of Equation (2.16) being sparse and banded. In details, higher orders of interpolation of shape functions \mathfrak{p}_{FE} are responsible for larger bands of the matrices. In turns, larger matrix bands make the equations of the linear system more complicated. This generates a trade-off with the better ability of higher-order FE to deal with high-frequency problems. Users should be aware that reaching a compromise between \mathfrak{h} and \mathfrak{p}_{FE} is the optimal path to achieve the desired accuracy in an acceptable amount of time.

Intuitively, large matrix systems to solve make computation more challenging because of more non-zero entries of the matrices. There are essentially two effects associated with many non-zero entries:

- (1) they correspond to a higher number of operations needed for factorization;
- (2) the memory to store the matrices increases as well with the number of non-zero entries.

Because of these reasons, the users should try to maintain a low amount of DoF, which can be done by increasing \mathfrak{h} or reducing \mathfrak{p}_{FE} .

Scientists developed special algorithms to tackle FE problems, starting from the frontal solver proposed by Irons [61] in 1970. The algorithm used in this thesis is a more modern one, known as multifrontal massively parallel sparse direct solver (MUMPS [62]).

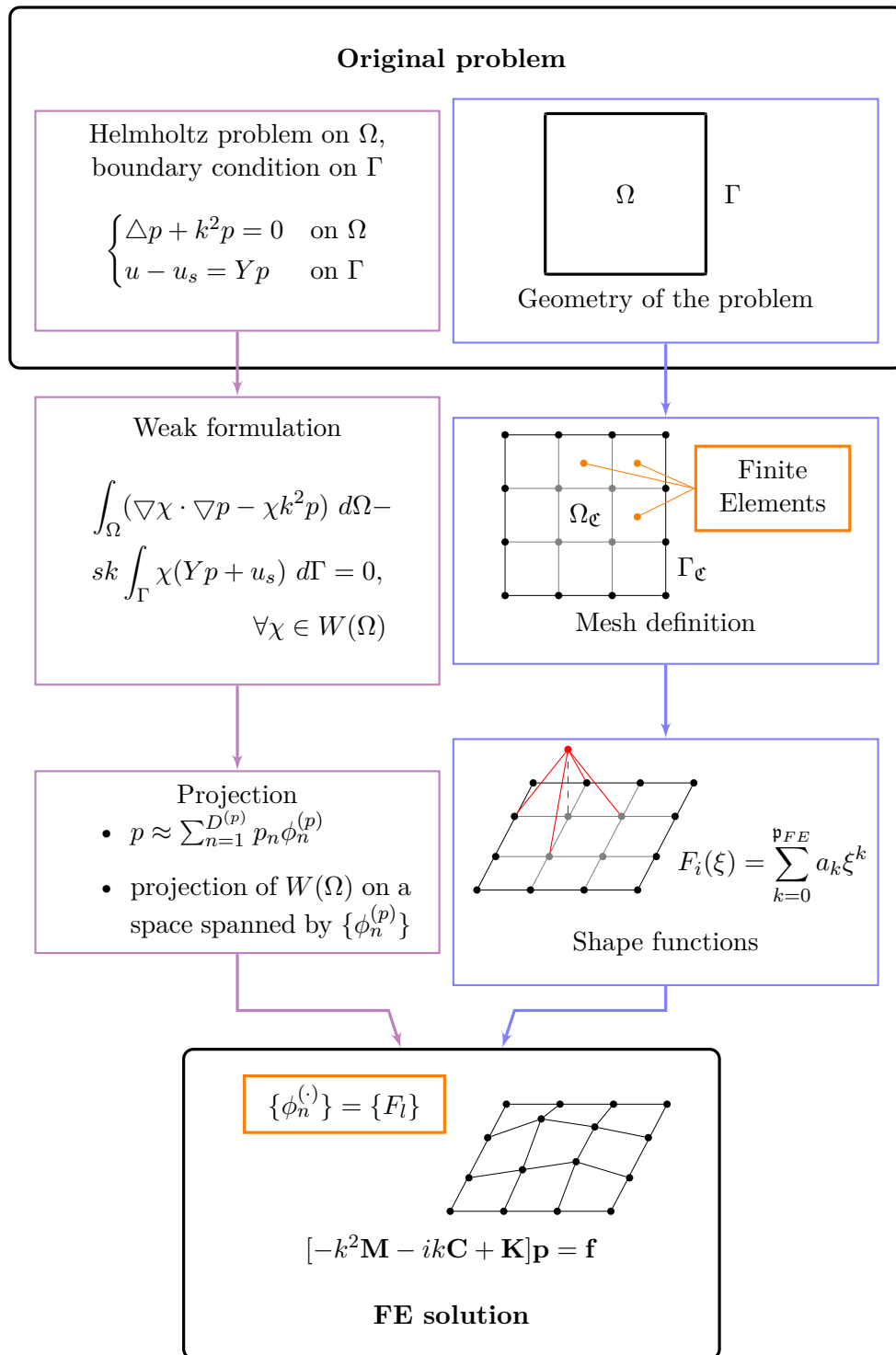


Figure 2.1: Steps of the FEM formulation for linear-time-harmonic acoustics. The process inside the magenta boxes is the Galerkin method, while the process in the blue boxes is the meshing procedure; these two processes are mathematically independent from each other.

2.3 Errors and adaptivity

2.3.1 Numerical dispersion

Given an acoustic wave propagating in a homogeneous and isotropic medium, the following linear dispersion relation holds [63]:

$$\frac{\omega}{k} = c, \quad (2.18)$$

with speed of sound c independent from frequency. When discretizing the propagative phenomenon via FEM, the linear dispersion relation does not hold anymore, leading to spurious dispersion^g. An introduction of this phenomenon is provided here for plane waves, based on [64]. An extension exists in the literature that leads to the same numerical dispersion relation for the cylindrical and the spherical cases [65]. In case of spherical waves, the dispersion relation (2.18) is true for $3r^2 \gg \mathfrak{h}^2$, with r distance from the disturbance and \mathfrak{h} size of the elements.

A representation of plane waves in one dimension is possible along their direction of propagation. In this case, the exact solution of the Helmholtz equation is:

$$p(x) = p_0 e^{ikx}, \quad (2.19)$$

in which x is the spatial coordinate; for simplicity, $p_0 = 1$ in the following. In dispersion analysis for FEM, a regular mesh (with n nodes located at positions $x_n = n\mathfrak{h}$ with $n \in \mathbb{Z}$) supports linear FEs that approximate the acoustic problem. $V_{\mathfrak{C}}$ indicates here the set of all the linear piecewise functions supported by the nodes x_n . The interpolant produced with polynomials in $V_{\mathfrak{C}}$ is characterized by having exact values at nodes:

$$p(x_n) = e^{ikn\mathfrak{h}}. \quad (2.20)$$

The latter equation is equal to Equation (2.19), but evaluated at the nodes.

The Galerkin FE solutions is^h:

$$p_{\mathfrak{C}}(x_n) = e^{ik_{\mathfrak{C}}n\mathfrak{h}}, \quad (2.21)$$

where $k_{\mathfrak{C}}$ is the wave-number resulting from the calculation.

The matrix of the FEM leads to a set of algebraic equations at each node that, substituted in Equation (2.21) provides the following dispersion relationⁱ:

$$k_{\mathfrak{C}}\mathfrak{h} = \arccos \left[\frac{1 - (k\mathfrak{h})^2/3}{1 - (k\mathfrak{h})^2/6} \right], \quad (2.22)$$

which is valid for $k\mathfrak{h} \leq \sqrt{12}$, since above this threshold the approximated waves become evanescent (see [66], section 3.2); $k\mathfrak{h} = \sqrt{12}$ is a resolution of about two nodes per wavelength. Next section will present some plots and results of the dispersion analysis.

^gA detailed description of the dispersion is available in [63], section 7.2; here a summary is given. In the case of linear differential equations, the four-dimensional solution is in the form

$$e^{i(\mathbf{k}\mathbf{r} - \omega t)},$$

in which the four dimensions are:

- (1) the three spacial ones of the vectors \mathbf{k} and \mathbf{r} ;
- (2) the time dimension of ω and t .

Alternative equivalent formulations are possible (e.g. in trigonometric form). The dispersion relation connects the space-related quantity \mathbf{k} and the time related one ω . More precisely, the quantity $\frac{\omega}{\mathbf{k}}$ is the phase velocity, while the quantity $\frac{d\omega}{d\mathbf{k}}$ is the group velocity. If the dispersion relation is linear, these two quantities are equal.

^hDifferent approaches are available in literature; see Ihlenburg and Babuška [66], section 3.2, or Anisworth, [67], section 2.1; Anisworth justified his approach with Bloch waves.

ⁱCalculations are available here [64, 67]

In higher dimensions, the situation is similar. Historically, analysis of the two dimensional Helmholtz equation [68, 69] showed that the results of the above simple cases well explain the error in most complicated cases. Thereafter, rigorous investigations of the two and three dimensional problems appeared [70, 71] and, finally, Ainsworth proposed a generalization in the multi-dimensional case [67]. The general behaviour in higher dimension does not change, but the FE solution exhibits a slight anisotropic behaviour. Furthermore, the pollution error becomes not avoidable, not even with the so-called stabilized method [72]. A clarifying introduction to the anisotropy issue is available in [64].

2.3.2 Interpolation and pollution errors

The finite element wavenumber produces a different phase velocity $\frac{\omega}{\mathbf{k}}$ for the Galerkin FE solution \mathcal{S}_{FE} with respect to the exact solution \mathcal{S}_E . A simple analytical experiment can simulate the FEM response^j. To better understand the mathematical behaviour of the FE solution, another function \mathcal{S}_I is introduced: it is the linear interpolant of the exact solution \mathcal{S}_E at the finite element nodes. The influence of the approximation of the wavenumber and so in turn of the wave propagation can be illustrated defining the following functions:

$$\begin{aligned}\mathcal{S}_E &= \Re(e^{ikx}) & \forall x \in \Omega, \\ \mathcal{S}_I &= \Re(e^{iknh}) & \forall nh \in \Omega_{\mathcal{E}}, \\ \mathcal{S}_{FE} &= \Re(e^{ik_{\mathcal{E}}nh}) & \forall nh \in \Omega_{\mathcal{E}},\end{aligned}$$

where $\Omega_{\mathcal{E}}$ represents the set of all the nodal coordinates of the FE mesh. The case of interest is a purely tonal planar wave; the spatial resolution is $kh \simeq 1.0472$, that is, six elements per wavelength. Equations of section 2.3.1 provide the means to calculate values for this simulation. Figure 2.2 shows the real part of \mathcal{S}_E (back, continuous line), \mathcal{S}_I (red, dashed line on dots) and \mathcal{S}_{FE} (blue, continuous line on dots). The spatial coordinate, normalized per the wavelength, is the abscissa. In this example, kh is independent of frequency f , and as a consequence $k_{\mathcal{E}}h$ too. Therefore, results in figure 2.2 would hold at any wavenumber, but the spatial coordinate would have a different value in absolute terms (six wavelengths at frequency $f_1 \gg f_2$ are shorter than six wavelengths at f_2).

Clearly, decreasing the product kh makes \mathcal{S}_{FE} closer to \mathcal{S}_I , and \mathcal{S}_I itself closer to \mathcal{S}_E . At this point, it is useful to introduce the H^1 -seminorm $\|\cdot\|_{H^1}^*$, defined as the norm of the first distributional derivative of its argument. The minimum error (in $\|\cdot\|_{H^1}^*$) between \mathcal{S}_E and any element $\mathcal{S}_{V_{\mathcal{E}}} \in V_{\mathcal{E}}$ is the one between \mathcal{S}_E and \mathcal{S}_I , which in literature is often called best approximation error [73]. On the other hand, the error between \mathcal{S}_{FE} and \mathcal{S}_I is due to the phase delay, and it builds up in space; this part of the error is usually called pollution error [64]. Ihlenburg and Babuška showed that there exists a supremum for the error of the Galerkin FE solution that comprises two parts: the best approximation error and another part related to the pollution error. They first find the supremum for the linear Galerkin FEM [66], and then extended the result to the Galerkin FEM with polynomial shape functions of generic order \mathbf{p}_{FE} [73]:

$$\|\mathbf{err}\|_{H^1}^* \leq C_1 \left(\frac{kh}{2\mathbf{p}_{FE}} \right)^{\mathbf{p}_{FE}} + C_2 Lk \left(\frac{kh}{2\mathbf{p}_{FE}} \right)^{2\mathbf{p}_{FE}} \quad (2.23)$$

where C_1 and C_2 are problem dependent constants, L is the characteristic length of the problem. It appears clear from this formula that \mathbf{p}_{FE} plays a significant role in controlling the pollution error at high wavenumbers. It comes with no surprise that several articles are present in literature that deal with high order schemes for FE acoustics [74, 75]

An interesting effect of the pollution error appears in case of reflected wave. In this case, a

^jThis is a simulation of a simulation (!).

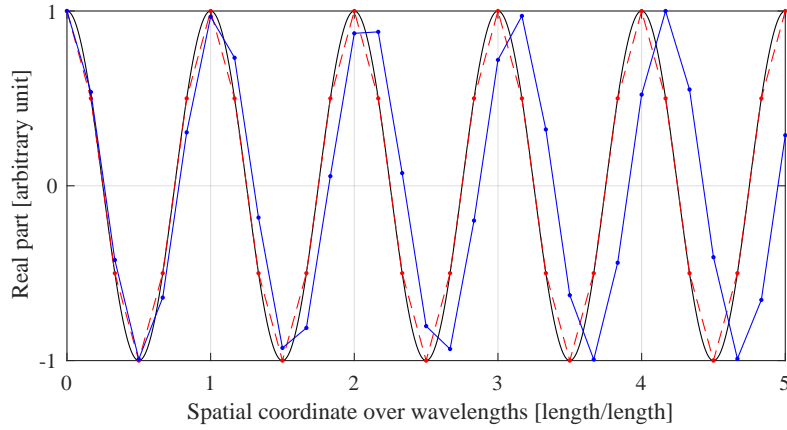


Figure 2.2: The exact solution of Helmholtz equation \mathcal{S}_E (black continuous line) and its interpolant with linear piecewise polynomials \mathcal{S}_I (red, dots on dashed line) propagate with the same wavenumber k , here in the one dimensional case. The Galerkin FE approximation \mathcal{S}_{FE} (blue, dots on continuous line) propagates with a different wavenumber $k_{\mathcal{E}}$.

train of stationary plane waves with the spectrum of a white noise propagates towards a rigid infinite plane with a direction inclined of 45° . A regular mesh of square elements discretizes the domain, and an ideal boundary condition on the truncated boundary absorbs all the reflected waves^k; therefore, the FE solution exists only inside the FE domain Ω_{FE} . Most points $P_{FE} \in \Omega_{FE}$ are reached by the train of planar waves and by its reflection on the rigid wall. For some points P_{FE}^* , the distance covered by the train that directly reaches a point is half of the one covered by the train that is reflected by the rigid wall. Figures 2.3 (a) and (b) show this scenario; point $P_{FE}^{(1)}$ is one of the points P_{FE}^* . Since the angle between the waves and the faces of the square FEs is 45° , the formula for $k_{\mathcal{E}}\mathfrak{h}$ is [64]:

$$k_{\mathcal{E}}\mathfrak{h} = \sqrt{2} \arccos \left[\frac{1 - (k\mathfrak{h})^2/6}{1 + (k\mathfrak{h})^2/12} \right]. \quad (2.24)$$

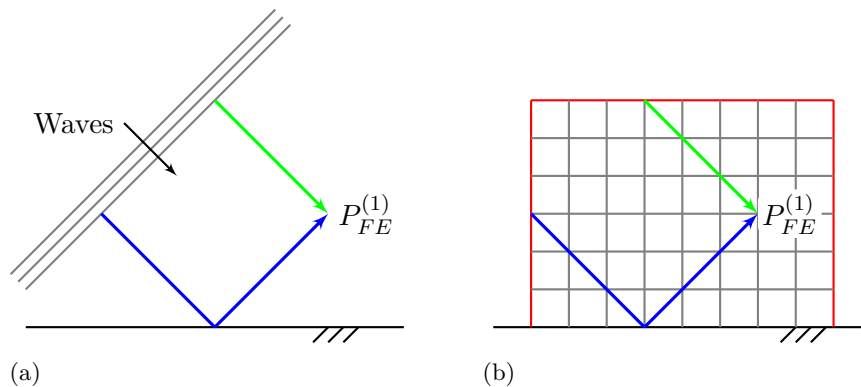
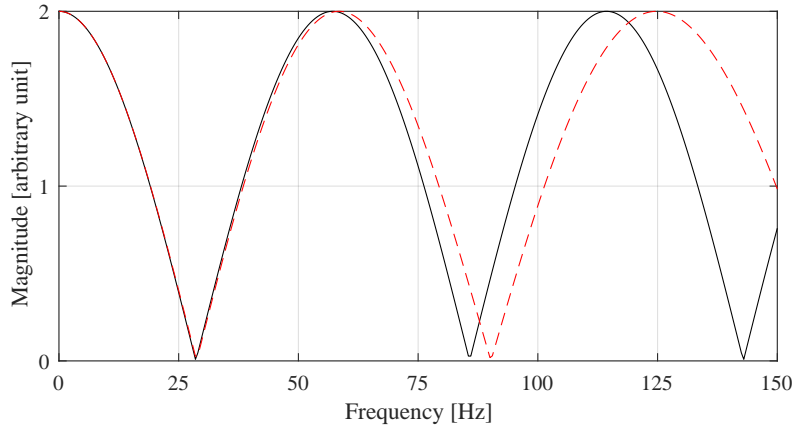


Figure 2.3: A train of planar waves incident on a rigid plane (a) is discretized with a regular FE mesh of square elements (b).

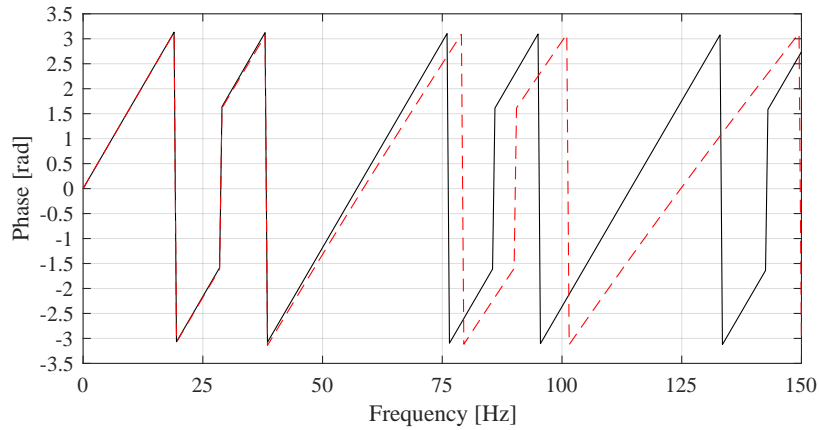
Figure 2.4 shows amplitude (a) and phase (b) of the spectra of the exact solution and of the

^kClearly, such boundary condition does not exist in reality: the scenario is ideal.

Galerkin FE solution at point $P_{FE}^{(1)}$. The effect of the pollution error is clear: in the spectrum, points of destructive interference shift towards higher frequencies. The higher the frequency, the more pollution error plays a role, as expected. The reason for this shift is simple: the two FE waves hit $P_{FE}^{(1)}$ with similar amplitudes, but with different phases in comparison with the exact solutions, causing this phenomenon. The phase presents the same frequency shift than the amplitude. From a psychoacoustic perspective, the evaluation of the integral of the curves in Figure 2.4 is interesting since it is related to some metrics, such as loudness and sharpness.



(a)



(b)

Figure 2.4: Pressure amplitude (a) and phase (b) at point $P_{FE}^{(1)}$ (fig.2.3) calculated assuming a white noise source: exact (black continuous line) and Galerkin FE (dashed red line) solutions.

The above examples discuss straightforward scenarios, with one source and zero or one reflecting surfaces. What happens in case of a more complex environment, with crooked geometrical boundaries and several reflecting surfaces? It is interesting to point out that, in simulations, the shape of the spectra can slightly change among simulations with different level of accuracy (see Section 3.4), but the frequency shift still plays a dominant role. The change in shape is likely to the fact that many acoustic “rays” hit a receiver points, each of them with a different phase delay, thus creating interference patterns significantly far from the theoretical ones.

2.3.3 Adaptive meshes

The error introduced by FE discretization is complicated to analyze. At low frequencies, it is relatively easy to control, since it is possible to decrease h without incurring in too high computational costs. At high frequencies, it deserves more attention. Ainsworth proposed the following practical formula to choose the two parameters h and p_{FE} [67]:

$$p_{FE} + \frac{1}{2} > \frac{kh}{2} + C(kh)^{1/3}, \quad (2.25)$$

where the constant C can be fixed to 1 for practical purposes. Importantly enough, if condition (2.25) is not satisfied, an increase of p_{FE} may lead to a deterioration of the FE result. The higher the wavenumber, the finer must be the mesh or the higher the order of the polynomial shape functions. In the case of a simulation of few frequencies close together in a restricted area of the spectrum, no problem arises. But in need to simulate in a broad bandwidth that covers several frequencies very far to each other, it makes sense to build different meshes for different frequency bands.

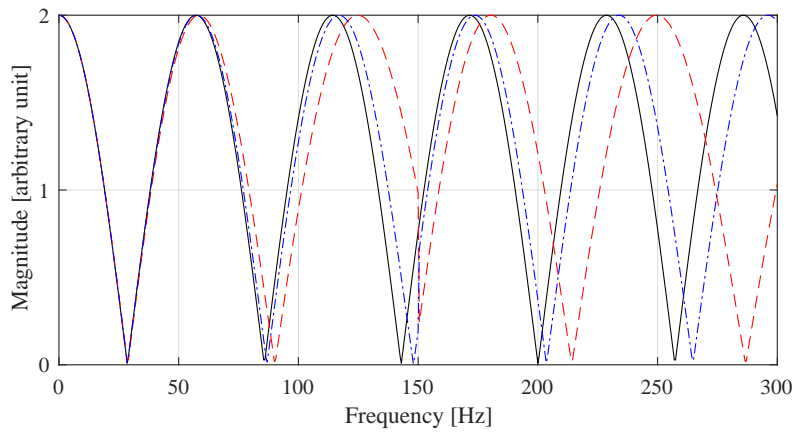
A mesh is said to be adaptive if the size h or the order p_{FE} of finite elements changes in function of frequency (at least, in the case of linear-time-harmonic acoustics). The first is called h -adaptation, the second p -adaptation¹. The process consists of creating a different mesh for each adaptive frequency band. Theoretically, since suprema of interpolation and pollution errors depend on the highest frequency of the simulation, an adaptive mesh allows similar levels of accuracy in the various bands, with a reduced calculation cost (indeed, h and p_{FE} result respectively bigger and smaller at lower frequencies). In practice, accuracy may vary across bands, especially in the case of relatively poor settings. However, with proper parameters, adaptive simulations proved to be effective in drastically reducing time while maintaining the same accuracy than more costly standard simulations. Indeed, several software companies have already implemented adaptive modules in their products (see, for instance, Siemens [59] and FFT [81]).

As an example, by referring to Figure 2.3, it is possible to calculate the spectra at point $P_{FE}^{(1)}$ with different analytical approaches. Figure 2.5 shows three spectra. In black (continuous line), the one calculated assuming a non-dispersive behaviour of the wave planes. The other two simulate adaptive numerical dispersion by using formula 2.24 and by fixing two frequency bands: 0-150 Hz and 150-300 Hz. At the maximum frequency band, the value of $k_h h$ are:

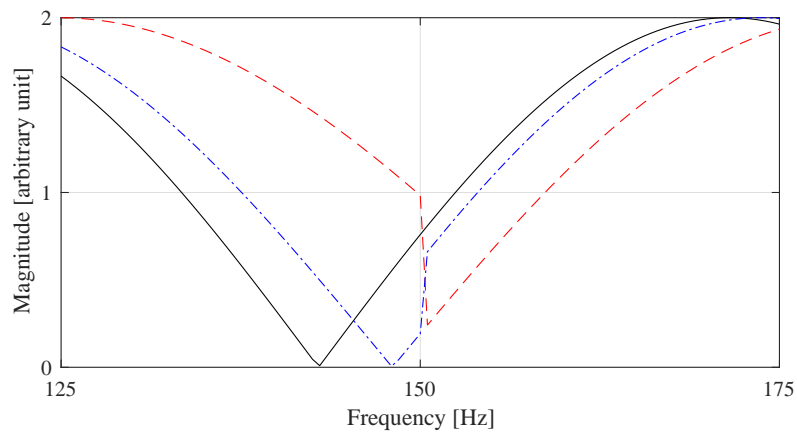
- (1) $k_{h,max,i} h = 1.3739$ for the blue dotted-dashed line;
- (2) $k_{h,max,i} h = 2.7477$ for the red dashed line;

where the subscripts max,i refer to the maximum (FE) wave number for each i adaptive frequency band. Figure 2.5 (b) zooms into the transition area, at 150 Hz. The jump is due to the abrupt change of $k_h h$. The error is higher at high frequency, and this should come with no surprise. Indeed, as per Equation (2.23), for a fixed value of $\left(\frac{k_{max,i} h}{k_{max,i} p_{FE}}\right)^{p_{FE}}$, the pollution error increases with frequency. If this is the case, where is the advantage of adaptive meshes? Assuming $\left(\frac{k_{max,i} h}{k_{max,i} p_{FE}}\right)^{p_{FE}}$ constant, the main advantage lays in the reduced computational cost necessary to solve the system at lower frequency. In fact, if the mesh is accurate enough at the maximum frequency, it will be at least as accurate at lower frequencies; at the same time, the FE matrices calculated at lower frequency bandwidths will be smaller (due to the reduced number of nodes), allowing for a reduced computational cost.

¹Other refinement criteria exist, for instance β -, τ - [76], h_p - [77], ξ -, $p\xi$ -, $h\xi$ -, $h_p\xi$ -, [78–80].



(a)



(b)

Figure 2.5: The spectrum at point $P_{FE}^{(1)}$ (fig.2.3) is calculated assuming that the source behaves as a white noise (a) and a zoom around 150 Hz (b): exact solution (black continuous line) Galerkin FE with $k_h h \simeq 1.4$ (dashed red line) solutions and Galerkin FE with $k_h h \simeq 2.7$ (dashed red line) solutions.

2.4 Ensuring the Sommerfeld radiation condition

Equation (2.16) has been derived without taking into account the Sommerfeld radiation condition, that is, for bounded acoustic problems. The introduction of condition (2.7) introduces non trivial complications. From a purely mathematical perspective, trial and test space are not anymore coincident (see [51], section 2.3.2). However, due to the nature of the FEM ^m, the computational domain needs to be truncated at an appropriate artificial boundary Γ_A properly introduced, which divides the original unbounded domain into two regions: a bounded computational domain Ω_{FE} discretized with FE and an infinite residual region $\mathcal{R} = \mathbb{R}^3 \setminus \Omega_{FE}$. Subsequently, some techniques acting on Γ_A that satisfy the Sommerfeld radiation condition are in charge of ensuring a solution to the problem. Intuitively, the most straightforward solution would be to use some boundary condition in the form of Equation (2.7), but this one produces spurious reflections that seriously affect the quality of results (see [55], section 3.3 and 10.3). Because of this reason, some alternative techniques that emulate the Sommerfeld radiation conditions without introducing spurious reflections are necessary.

Accurate reviews of the most common methodologies for modelling the infinite region exterior to the artificial boundary are available in literature [82, 83]. Here a summary is provided, in which these techniques belong to the following three categories:

- absorbing boundary conditions (ABC);
- infinite elements method (IEM);
- absorbing layers.

In ABC, the originally unbounded exterior problem is reduced to an equivalent one defined on the bounded domain in which Equation (2.7) is replaced by:

$$\frac{\partial u}{\partial n} = \mathcal{B}u \quad \text{on } \Gamma_A \quad (2.26)$$

where \mathcal{B} is a linear operator, called *DtN* (Dirichlet to Neumann) map, which approximates the Sommerfeld radiation condition at Γ_A .

In literature both local (based on differential operators) and non-local (based on integral operators) absorbing boundary conditions can be found. The first ones find their base on the Atkinson-Wilcox radial expansion (of the field u or p) in powers of $1/kr$ for a sphere [84, 85], defined for $r > r_0$ (the second being the radius of a spherical surface circumscribing the target). For $r > R$ (with R being the radius at Γ_A) the domain must be homogeneous and may not contain any obstacles. Some differential operators of different orders able to annihilate terms in the Atkinson-Wilcox expansion are available in the literature [86]. The expansion can use spheroidal or rectangular coordinates allowing the artificial boundary to obtain a tight fit around elongated objects. If not placed sufficiently far from the radiating/scattering object, low-order local approximate absorbing boundary conditions may produce significant spurious reflections which can pollute the entire numerical solution. Usually, it is more efficient to use high-order accurate absorbing conditions which enable smaller computational domains. The development of high-order local boundary conditions for which the order can be easily increased to a desired level are usually based on using auxiliary variables to eliminate higher-order derivatives [87]. While generally derived for the time-dependent case, time-harmonic counterparts are readily implemented with time derivatives replaced by $i\omega = kc$. The main disadvantage of these techniques is that for spheroidal, and other convex shapes, the conditions tend to lose accuracy for higher wavenumbers [88].

^mIn the FEM, the discretization is on the volume; hence, an unbounded geometrical domain requires an infinite number of elements, which is not a feasible solution for numerical computation.

An alternative to high-order local absorbing conditions are non-local DtN non-reflecting boundary conditions. The conceptual foundation and experimental validation for the DtN FEM have been developed for both acoustic radiation and scattering. The DtN map on a sphere of radius R can be constructed directly and implemented in the standard Galerkin FEM by expanding the outgoing acoustic field in a spherical harmonic series [89]. Numerical studies [90] show that due to the particular structure, and ability to tightly fit around scattering objects with minimal spurious reflection, the non-local DtN condition can be implemented with significant overall cost savings compared to the local operators of first and second order. Furthermore, non-local conditions are very accurate, yet couple all solution unknowns on Γ_A , thus potentially rendering a full dense matrix with associated solution cost and memory requirements. However, if separable boundaries are utilized such as spheres or spheroids, a special structure in the resulting data structures may be exploited to avoid storage of a full dense matrix.

The infinite elements method (IEM) [91] replaces the non-reflecting boundary condition on Γ_A with a single layer of elements with endless extent. An IE is constructed by replacing the classic linear or polynomial shape function with radial wave functions which automatically satisfy the Sommerfeld condition at infinity. The final result is an element with infinite extension. The residual region \mathcal{R} results discretized into a set of IEs that decompose the field at the surface via a multi-pole expansion. The first n components of the expansion propagates towards infinity. The Atkinson-Wilcox theorem [92] ensures that the multipole expansion is absolutely and uniformly convergent provided that a sphere encloses all the radiating and scattering elements of the problem, except for baffled planes. This result has been extended for prolate ellipsoid FE volumes [93]. Curvilinear coordinate allows to use any shape for the FE volume Ω_{FE} , as long as Ω_{FE} itself encloses the prolate ellipsoid that encompasses all the sources and radiating surfaces [81]. The main drawback of the IEM is the decrease of performance at larger wavenumbers and highly elongated artificial interfaces.

A multitude of techniques belongs to category (3), most noticeably the perfectly matched layers (PML, [94]). In principle, an extra layer of damping elements is added above Γ_A that is in charge to absorb all the acoustic energy. Next section provides an overview of the PML.

If the used technique does not appropriately propagate the acoustic field towards infinity (as this is the case, for instance, of PML), an integral formulation can fulfil this aim. Several formulations, usually based on free field Green's functions, are available [95]: Lighthill's acoustic analogy [96], the Curle's formulation [97], the Ffwocs Williams and Hawkings formulation (FW-H, [98]) and Kirchhoff methods [99]. The FW-H formulation is the most widely used among these since it can take into account for noise generation effects due to moving surfaces immersed in a turbulent flow. An important feature of the FW-H technique is that it allows to place the truncated boundary relatively close to the sources [100]. As a consequence, the FE volume can be rather small, especially at high frequencies. Techniques based on the FW-H formulation that does not need to satisfy any condition about the FE volume have therefore an intrinsic advantage in comparison with techniques based on multi-pole expansion at high frequencies. Indeed, in this part of the spectrum, the extension of the spherical/ellipsoidal volume may require a high number of finite elements, thus increasing the computational cost.

2.4.1 Perfectly Matched Layers

An option for absorbing the acoustic energy for exterior problems is the PML. Berenger originally introduced this concept [101, 102] for electromagnetic waves (that satisfy as well the Helmholtz equation). The idea is to add an exterior layer of finite thickness at an artificial interface such that outgoing plane waves are absorbed before reaching the outer layer truncation boundary. The mathematical formulation of the PML is such that the following properties hold [83]:

- (1) no reflection occurs at Γ_A ;

(2) the decay of the solution inside the layer is exponential.

The splitting of the scalar field into nonphysical components satisfying equations which describe decaying waves, and a proper selection of PML coefficients, theoretically eliminate plane-wave reflection for an arbitrary angle of incidence [82], that is, property (1). Property (2) comes from a proper tuning of some damping functions.

By referring to figure 2.6, the original formulation of the PML method in two dimensions and Cartesian coordinates starts from the wave equation rewritten as the following system [94]:

$$\begin{cases} \frac{\partial p}{\partial t} + \rho_0 c^2 \left(\sum_{i=1}^j \frac{\partial u_i}{\partial x_i} \right) = 0 \\ \rho_0 \frac{\partial \mathbf{u}}{\partial t} + \left(\sum_{i=1}^n \frac{\partial p}{\partial x_i} \mathbf{n}_i \right) = 0 \end{cases} \quad j = 2, \quad (2.27)$$

by imposing $p = p_1 + p_2$ without physical meaning such that:

$$\begin{cases} \frac{\partial p_i}{\partial t} + \rho_0 c^2 \frac{\partial u_i}{\partial x_i} = 0 \\ \rho_0 \frac{\partial u_i}{\partial t} + \frac{\partial p}{\partial x_i} = 0 \\ p_1 + p_2 = p \end{cases} \quad i = 1, 2. \quad (2.28)$$

At this point dissipative terms are added to equations (2.28) as:

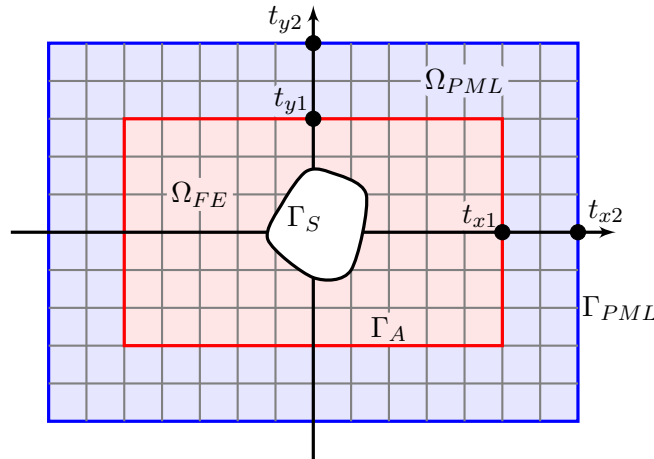


Figure 2.6: PML in Cartesian coordinates: FEs are red, the PML is blue; the points t_{jk} , with $j = x, y$ and $k = 1, 2$, identify the layer thickness.

$$\begin{cases} \frac{\partial p_i}{\partial t} + \varsigma_i p_i \rho_0 c^2 \frac{\partial u_i}{\partial x_i} = 0 \\ \left(\rho_0 \frac{\partial u_i}{\partial t} \varsigma_i u_i \right) + \frac{\partial p}{\partial x_i} = 0 \\ p_1 + p_2 = p \end{cases} \quad i = 1, 2. \quad (2.29)$$

Where ς denotes a damping function. The derivation of time-harmonic equations is now straight-

forward and results in:

$$\begin{cases} p_j = -\frac{\rho_0 c^2}{\varsigma_j - i\omega} \frac{\partial u_j}{\partial x_j} \\ u_j = -\frac{1}{\rho_0(\varsigma_j - i\omega)} \frac{\partial p}{\partial x_j} \\ p_1 + p_2 = p \end{cases} \quad j = 1, 2. \quad (2.30)$$

Introducing the following function:

$$\gamma_j(x_j) := \begin{cases} 1, & \text{if } |x_j| < t_j \\ 1 + \frac{i}{\omega} \varsigma_j(|x_j|) & \text{if } t_j \leq |x_j| < t_j^* \end{cases} \quad j = 1, 2. \quad (2.31)$$

it is possible to rewrite equations (2.30) asⁿ:

$$-\rho_0 \omega^2 \gamma_1 \gamma_2 p - \rho_0 c \left[\frac{\partial}{\partial x_1} \left(\frac{\gamma_2}{\gamma_1} \frac{\partial p}{\partial x_1} \right) + \frac{\partial}{\partial x_2} \left(\frac{\gamma_1}{\gamma_2} \frac{\partial p}{\partial x_2} \right) \right] = 0. \quad (2.32)$$

The above equations define the so-called split formulation in cartesian coordinate. An unsplit formulation exists too [103]. The interface in rectilinear Cartesian coordinates allows a tight fit around elongated objects, but can also be reformulated in spherical and other general curvilinear coordinates (see, for instance, [81]). As mentioned, the damping functions ς_j are in charge of ensuring an exponential decay inside the layer.

The PML converges to perfect wave absorption as the thickness of the layer is increased [104]. However, a compromise between a thin layer which requires a rapid variation of the absorption parameters and a thick layer which requires more elements is required [105]. In general, this implementation allows using any convex shape wrapped tightly around a limited conventional FEM domain [82].

Due to the dissipative nature of the PML, the role of the engineer is to choose an appropriate thickness that allows to dissipate enough energy so that the reflection error does not affect excessively the solution inside the FE volume. Therefore, the only two requirements for an effective PML are:

- (1) truncated FE boundary Γ_{FE} located far enough from the sources, to reproduce a realistic field on Γ_{FE} itself;
- (2) thickness of the PML enough to ensure a sufficient dissipation of energy, so to avoid excessive reflection error.

Under these conditions, PML offers some advantages in comparison with other techniques. First of all, it allows to treat properly non-homogeneous exterior domain, which is not the case, for instance, of IEM. Secondly, no requirements on the shape of Γ_{FE} are present, allowing the use of small computational volumes at high frequencies.

2.5 Numerical examples

How do FE and PML behave in simulations? Some numerical experiments can provide the answer. Specifically, some numerical experiments are designed to illustrate and try to answer the following questions:

- (1) How does the FE accuracy affect the quality of a simulation (in the case of unbounded problems)?

ⁿFor the algebra see [94]

- (2) Does the thickness of the PML increase the amplitude of the spectrum computed at a geometrical point?
- (3) Does the shape of the FE volume affect the spectrum computed at a geometrical point?
- (4) Is there any difference between the spectrum computed via FE and the spectrum computed via FW-H algorithm?
- (5) Does the FW-H algorithm propagate the FE error?

To answer these questions, results from different sets of simulations involving a monopolar source in a space are exploited; all simulations are performed in Actran [81]. The monopole generates an omnidirectional sound field in which the pressure follows the law:

$$p(r, \omega, t) = \left[P \frac{e^{-ikr}}{r} \right] e^{i\omega t}, \quad (2.33)$$

with r the distance from the monopole and P the acoustic pressure amplitude at unitary r . P is associated to the monopole and linked to its mass flow rate Q through the relation:

$$P = i \frac{Qck\rho}{4\pi}, \quad (2.34)$$

with ρ the fluid density. The associated linear time-invariant system is comprehensively described in frequency domain, so that dependence on time can be neglected. Equation (2.33) can be rewritten as:

$$p(r, \omega) = P \frac{e^{-ikr}}{r}. \quad (2.35)$$

Equation (2.35) is independent of direction, depending only on the spectrum of P (or Q) and on r . Given a receiver at 0.5 m from the source, and fixing $P = 1$, the spectrum of acoustic pressure at the receiver is a constant of amplitude $p(f) = 2$. Figure 2.7 shows two possible approaches to study this scenario with FE and PML:

- (1) a sphere of radius $r_s = 0.3$ m, figure 2.7 (a);
- (2) a cube of side $l_c = 0.612$ m, figure 2.7 (b).

In both cases, the monopole is located at the barycenter of the finite element volumes. In addition, the volumes of the sphere and the cube are identical and the distance between the receiver and the monopole is set at $r = 0.5$ m in both cases.

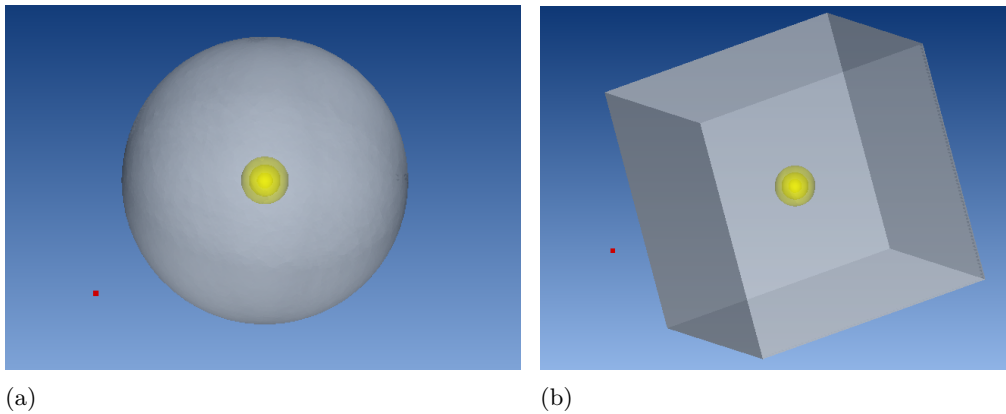


Figure 2.7: (a) Spherical and (b) cubic FE models of a monopolar source in the free space and a receiver at a distance $r = 0.5$ m.

2.5.1 PML and FE performance

The first set of simulations has the purpose of evaluating the performance of PML with respect to frequency. It involves the geometry in Figure 2.7 (a) meshed with tetrahedral linear finite elements. Three different spheres were constructed using tetrahedral linear finite elements with increasing average size of elements ($h = 0.009$ m , $h = 0.018$ m and $h = 0.037$ m). In all these cases, the frequency resolution is 25 Hz and the Sommerfeld radiation condition is ensured with adaptive PML in the following frequency bands:

- (1) 1000-1500 Hz;
- (2) 1525-2000 Hz;
- (3) 2025-2500 Hz;
- (4) 2525-3000 Hz.

The software is asked to use six elements per minimum wavelength in each adaptive frequency band. However, at the interface between FE and PML the finite element mesh dictates the spatial resolution; to overcome this inconvenience, a gradient factor is fixed to a value 2. The latter parameter imposes that any element can not be more than twice its adjacent elements in terms of size. Therefore, the average size of PML elements smoothly varies from the one at the FE/PML interface to the one set in the software. The thickness of the PML t_{PML} is defined per each frequency band via the ratio $\frac{t_{PML}}{\lambda_{max}}$, where λ_{max} is the longest wavelength per adaptive band, which is associated to the lowest frequency. The ratio $\frac{t_{PML}}{\lambda_{max}}$ is fixed equal to one; this approach ensures that at of each adaptive band the thickness will be equal to or bigger than the wavelength at any frequency.

Figure 2.8 shows the theoretical spectrum in black, and the spectra calculated with the spherical geometries: $h = 0.009$ m in blue plus signs, $h = 0.018$ m in red asterisks and $h = 0.037$ m in green crosses. An effect of adaptivity similar to the one shown in figure 2.5 is present. In fact, PML are known for their dispersive behaviour that is similar to the one of standard FEM [106]. Furthermore, the spectra are characterized by:

- (1) a wave-like shape;
- (2) a decay of the amplitude when the FE nodal resolution (number of nodes per wavelength) decreases.

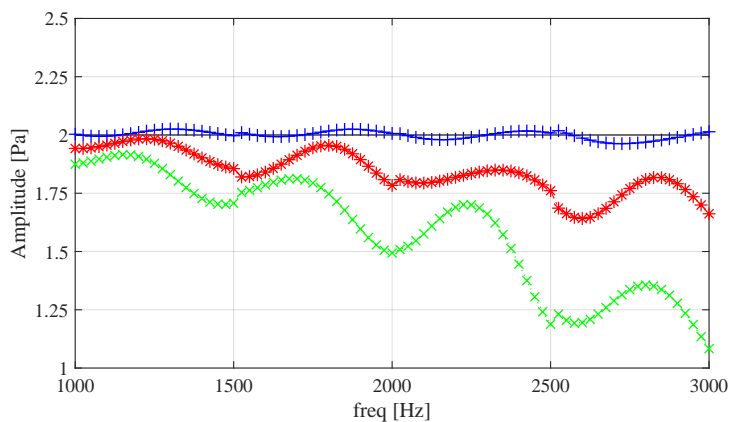


Figure 2.8: Spectra of the receiver in Figure 2.7 (a) calculated via FEM with average size of elements h equal to 0.009 m (blue plus signs), 0.018 m (red asterisks) and 0.037 m (green crosses); the theoretical spectrum is in black.

A comparison with the infinite element method (see appendix D) shows that the wave-like shape is more emphasized in the PML case than in the IEM one, while the amplitude decays more or less at the same rate with both techniques.

Performances of the simulation changes also as a function of the polynomial order of shape functions. Figure 2.9 shows the spectra of the receiver presented in Figure 2.7 (a) calculated via FEM with average size of linear elements h equal to 0.009 m (blue plus signs), and of quadratic elements 0.018 m (magenta asterisks); as usual, the theoretical spectrum is in black. These two configurations have the same number of nodes per wavelength \mathfrak{N} in the FE volume, and as such should have a very similar degree of accuracy (except for the pollution error). However, the spectrum obtained with the quadratic model has a slightly higher amplitude and a different shape (crests and troughs of the “waves” are not at the same frequency of the other spectrum). Looking at this picture, it seems that linear elements, when combined with PML, perform fairly better. In reality, this is not always true; for example, Figure 2.10 shows the same spectra calculated via FEM with average size of linear elements h equal to 0.018 m (red plus signs), and of quadratic elements 0.037 m (light blue asterisks). Even in this case, the number of nodes per wavelength \mathfrak{N} is constant, but in this case the quadratic model perform better. The reasons behind these contradictory results lies in a strong interaction between the PML and the FE. In fact, Appendix D shows the result of the same scenario, with the same meshes, using infinite elements instead of PML. Contrary to many practical applications, the proposed case is particularly favorable to the IE, so better results are expected. However, in the case of infinite elements, quadratic FEs perform always better, confirming that:

- (1) without *external factors* affecting the simulation, quadratic elements perform better;
- (2) the PML strongly interact with the FE parameters, introducing thus an *external factor* that affects the results.

For the purposes of this thesis, it is crucial to consider this interaction between PML and FE, and to analyze how it affects the results in a case of practical interest. This interaction is likely related to the way the software produces the meshes. Indeed, the used software allows only to impose the number of elements per wavelength, and not the number of nodes; furthermore, this number of elements per wavelength is the same for the FE volume and the PML. Consequently, in the case of the quadratic FE (whose size is twice the one of linear FE, once \mathfrak{N} is fixed), the PML mesh results slightly coarser. This may explain the increased energy in the quadratic models previously discussed.

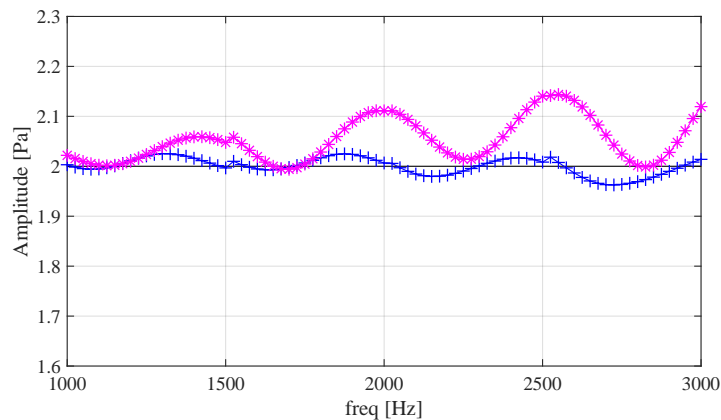


Figure 2.9: Spectra of the receiver in fig. 2.7 (a) calculated via FEM with average size of linear elements h equal to 0.009 m (blue plus signs), and of quadratic elements 0.018 m (magenta asterisks); the theoretical spectrum is in black.

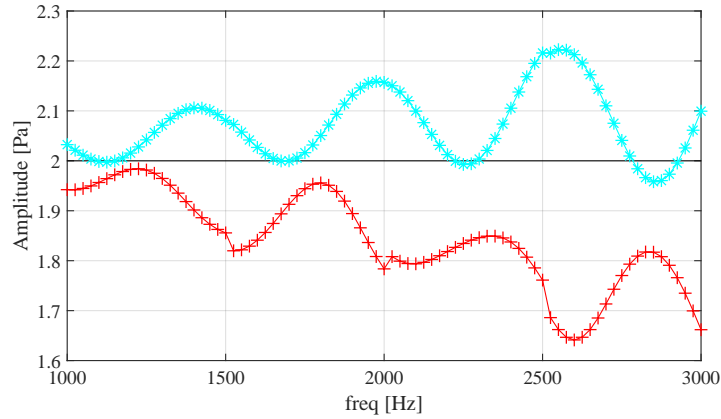


Figure 2.10: Spectra of the receiver in Figure 2.7 (a) calculated via FEM with average size of linear elements $h = 0.018$ m (red plus signs), and of quadratic elements $h = 0.037$ m (light blue asterisks); the theoretical spectrum is in black.

2.5.2 PML thickness

The second set of simulations aims at producing results to evaluate the influence of the PML thickness. For this second set, the average size of the elements is set to $h = 0.009$ m for which good results were observed in the whole frequency range in previous section. Simulations are defined in the same way, but this time two different values for the ratio $\frac{t_{PML}}{\lambda_{max}}$ (number of wavelengths with respect to the thickness of the layer) have been used:

- (1) $\frac{t_{PML}}{\lambda_{max}} = 1$;
- (2) $\frac{t_{PML}}{\lambda_{max}} = 0.2$.

Figure 2.11 shows the spectra obtained using $\frac{t_{PML}}{\lambda_{max}} = 1$ (blue crosses) and $\frac{t_{PML}}{\lambda_{max}} = 0.2$ (red asterisks); the theoretical solution is shown for comparison (black continuous line). The increase of amplitude in the case of lower thickness is evident, although the behaviour of the spectra becomes strongly irregular. The increased energy of the low thickness case confirms what was explained in Section 2.4.1. Indeed, if the PML is not thick enough to absorb the energy radiated by the sources, such energy will be reflected inside the FE volume, thus increasing the energy of the acoustic field at the interface FE/PML. The latter is then propagated via FW-H, giving raise to higher amplitude at points outside the FE domain (obviously a similar effect takes place at any point inside the FE volume). The irregular behaviour is another confirmation that using an excessively low thickness produces results too far from the theory.

2.5.3 Shape of the FE volume

Another set of simulations is defined to compare the influence of the shape of the FE volume. In this case both the sphere and the cube of Figure 2.7 are used. The cube was meshed by means of cubic linear finite elements of size $h = 0.009$ m, while the sphere is the same of the latter simulation set (that is, averaged $h = 0.009$ m). All the other parameters are unchanged. Figure 2.12 compares the spectra computed with the spherical mesh, in blue plus signs, and the regular cubic mesh, in magenta circles. A difference is visible, in certain cases up to 5% of the amplitude, showing that the shape of the FE volume has a certain impact on the solution.

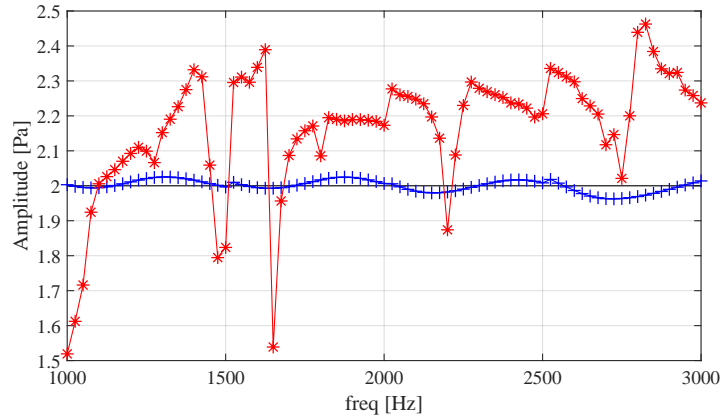


Figure 2.11: Amplitude of the receiver in fig. 2.7 calculated with $\frac{t_{PML}}{\lambda_{max}} = 1$ (blue crosses) and $\frac{t_{PML}}{\lambda_{max}} = 0.2$ (red asterisks) compared with the theoretical solution (black continuous line).

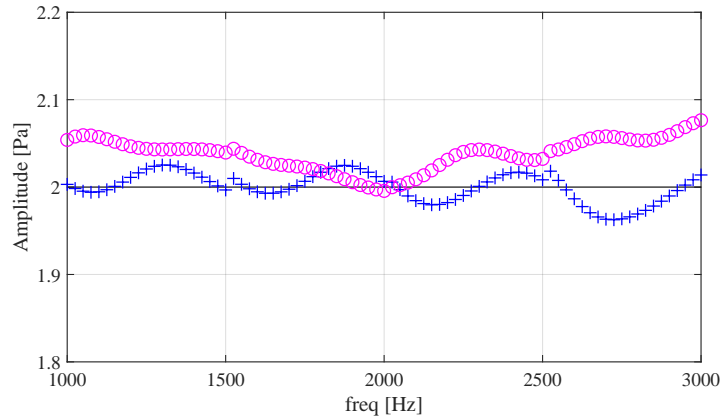


Figure 2.12: Spectra of the receiver in Figure 2.7 calculated via FEM with spherical (blue plus signs) and with regular cubic (magenta circles) meshes compared with the theoretical solution (black continuous line).

2.5.4 Performance of the FW-H algorithm

The last set of simulations has the purpose of showing the performances of the FW-H formulation; Figure 2.13 shows the geometry used for this purpose. A monopolar source is located at the origin of a cartesian reference system; two receivers are located along the y axis at distances of 0.5 ($P_{y0.5}$) and 1 m (P_{y1}), and other two along the x axis at the same distances ($P_{x0.5}$ and P_{x1}). The solutions at points equally distant from the source should be equal according to the theory. The FE volume is a cuboid with a square face of side $l_c = 0.612$ m perpendicular to the y axis. The FE volume is built so that $P_{x0.5}$ is outside the FE volume, while $P_{y0.5}$ is inside. Therefore, any difference in these two points' spectra is imputable to the mesh and associated numerical errors. Similarly, P_{x1} is at a distance of 0.694 m from the mesh, while $P_{y0.5}$ is at 0.388 m; again, any difference between the spectra of these two points is due numerical errors. It is worth noting that all the spectra are calculated via FW-H, except for the one of point $P_{y0.5}$ which is the only one to be included in the FE volume.

Figure 2.14 shows the spectra obtained with a regular cubic mesh with $h = 0.009$ m:

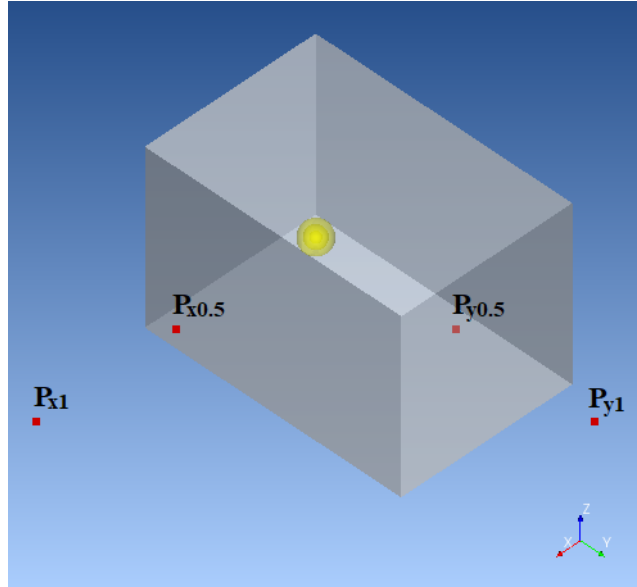


Figure 2.13: A cuboid geometry with a monopole source on the origin (yellow), two receivers on the y -axis and two receivers on the x axis; distance between receivers and source is either 0.5 or 1 m.

- (a) $P_{y0.5}$ (blue plus signs), $P_{x0.5}$ (red asterisks) and theoretical solution (black continuous line);
- (b) P_{y1} (blue plus signs), P_{x1} (red asterisks) and theoretical solution (black continuous line).

There are some differences, implying that the thickness of the FE layer between the source and the receiver has an impact on the results. It is worth noting that all the spectra are calculated via FW-H, except for the one of point $P_{y0.5}$ (blue plus signs in Figure 2.14 (a)).

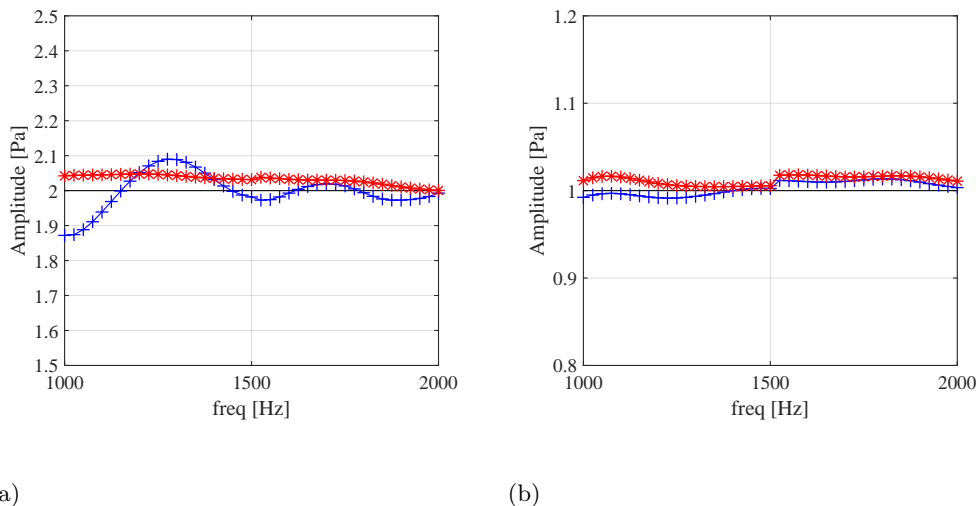


Figure 2.14: Amplitude of the receivers' spectra on the y -axis (blue) and on the x -axis (red) at a distance of 0.5 (a) and 1 m (b); the theoretical amplitude is in black.

Figure 2.15 shows the phase of the spectra computed at points P_{y1} (blue plus signs) and P_{x1} (red asterisks); the theoretical phase is add for comparison purposes (black continuous line). A

slight frequency shift is present in both cases but it is more marked for the spectrum at point P_{y1} . Similar results hold for the points $P_{y0.5}$ and $P_{x0.5}$.

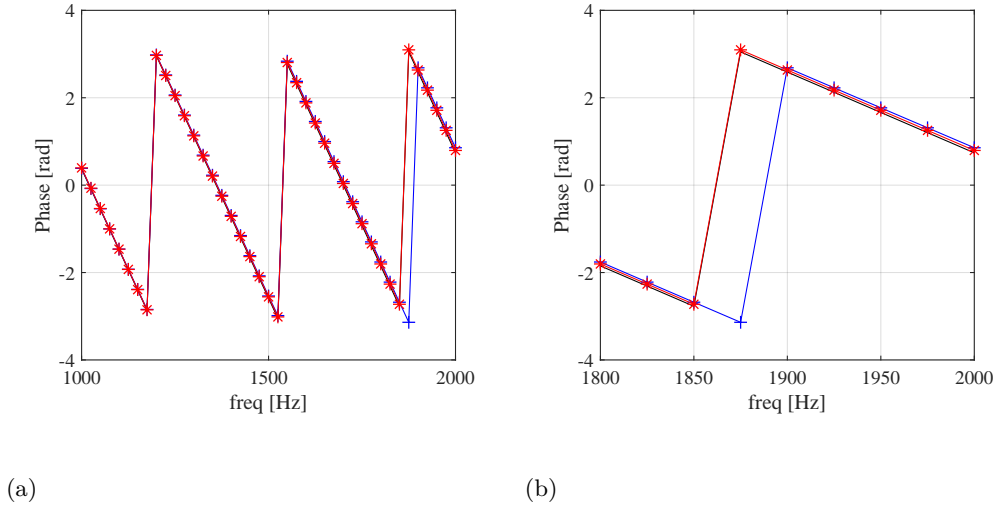


Figure 2.15: Phase of the receivers' spectra on the y -axis (blue) and on the x -axis (red) at a distance of 1 m (a) and a zoom in the 1800-2000 Hz frequency band (b); the theoretical phase is in black.

Overall, computations seem to be less accurate in y axis which corresponds to the length of the FE volume. These results suggest that the FW-H algorithm is more efficient than the FE one and that a small FE volume is therefore desirable. Obviously, some limits exist that cannot be surpassed, since the FE volume cannot simply disappear.

However, a quick check can reveal some hidden clues. Figure 2.16 shows the ratio between the thickness of the FE volume t_{FE} and the wavelength λ as a function of frequency along the x -axis (red) and the y -axis (blue). The thickness, in this case, is defined as the distance between the source and the boundaries of the FE volume (0.612 m and 0.306 m, respectively, along y and x directions). Since spectra of receivers on the x axis are reasonably good, one can conclude that a ratio $\frac{t_{FE}}{\lambda} = 1$ is acceptable: this value is considered the reference in this research.

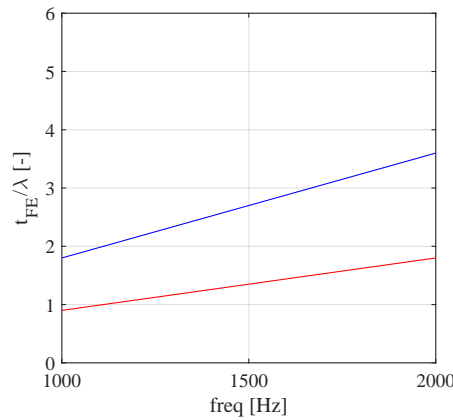


Figure 2.16: Ratio between the thickness of the FE volume t_{FE} and the wavelength λ in the x -axis (red) and in y -axis (blue) as a function of frequency.

2.6 Linking FE theory to sound perception

Despite the errors, the FEM is still a powerful tool to simulate TFs for auralization. Therefore, it becomes important to understand how these errors affect human perception, since they propagate into auralized sounds because of the convolution process. This section showed how numerical errors essentially affect the shape of TF spectra and cause a frequency shift of amplitude and phase. Psycho-acoustic theory helps to understand how these factors can influence human perception.

2.6.1 An introduction to acoustic metrics

In a first instance, it is worth noting that the human hearing system has different sensitivities at different frequencies. Its sensitivity is low at frequencies between 20 and 500 Hz, reaches the maximum around 3000 Hz, and decays at higher frequencies. In 1933, Fletcher published an article where he built curves taking into account this behaviour [107], which nowadays are known as “Equal-Loudness Contour” [17, 18] and are the basis for the well known A-weighting, used to calculate the A-weighted sound pressure level (SPL(A)). The high sensitivity in the frequency range above 500 Hz should already sounds like a warning for the pollution error, which is dominant at high frequencies (high, in this case, is related to the FEM capabilities).

The SPL(A) is a powerful metric, but does not take into account the masking effect. The masking effect is a fundamental phenomenon characterizing the human hearing system investigated since 1940 by Fletcher. During his experiment, he masked a sinusoidal signal with bandpass noise maskers with different bandwidth [108]; thus, the power of the masker increased together with the bandwidth. The aim of the study was to measure the threshold of the sinusoidal signal as a function of the bandwidth itself. This experiment, repeated several times (see [17], pag. 66) shows that the threshold increases only up to a certain point, then it remains constant. To account for these results, Fletcher proposed that the human auditory system comprises some filters. If the sinusoidal signal belongs to a certain filter, any bandwidth increase of the masker within the same filter will cause an increase of the threshold; an increase outside the filter does not have any effect. The critical-band (CB) is the frequency band of the auditory filter outside which the threshold of the signal does not increase. 25 CBs can be built as a function of frequency, meaning that each CB starts at the same frequency f_t where the previous CB ends (except for the first CB, which starts at 0 Hz). This approach result in the scale of critical-band rate z , which results to be a function of frequency. Table 2.1 summarizes the relation between z and frequency.

z [Bark]	f_l [Hz]						
1	100	7	770	13	2000	19	5300
2	200	8	920	14	2320	20	6400
3	300	9	1080	15	2700	21	7700
4	400	10	1270	16	3150	22	9500
5	510	11	1480	17	3700	23	12000
6	630	12	1720	18	4400	24	15000

Table 2.1: Relation between critical-band rate z and the lower frequency of critical-bands f_l ; more details in [18].

In the case of broadband noises, masking effect becomes more complicated; for the purpose of this thesis, it is useful to know that spectral masking can cause a decrease in the perceived loudness of an acoustic stimulus (for instance, see [18], Section 8.4), and therefore it makes sense to take this effect into account. A metric able to do so is the loudness N computed according

to Zwicker [18]:

$$N = \int_0^{24[\text{Bark}]} N' dz, \quad (2.36)$$

where N' is the specific loudness and the integral is computed across the 25 critical bands (measured in Bark). The specific loudness is a function of frequency that combines the spectral distribution of an acoustic input with the auditory filters of the human hearing system (for details, see [17, 18]). The unit of measure of N' is sonie/bark.

SPL(A) and N take into account significant aspects related to the power of a sound and how humans perceive it. However, these metrics take into account energy distribution across the spectrum only as a function of sensitivity, but do not say anything about pleasantness. A metric that take into account energy distribution and has good correlation with pleasantness^o is the sharpness S (in this thesis, calculated according to Zwicker [18]):

$$S = 0.11 \frac{\int_0^{24[\text{Bark}]} N' g(z) z dz}{\int_0^{24[\text{Bark}]} N' dz}, \quad (2.37)$$

where $g(z)$ is a weighting factor which is constant up to 16 Bark and then increases; the unit of measure is acum. In this metric, z and $g(z)$ being under the integral, higher frequencies play a more important role.

SPL(A), N and S are not able to exhaustively describe human perception, but they allow to identify first issues:

- (1) energy distribution across the spectrum;
- (2) masking effect;
- (3) importance of high frequency for pleasantness.

These factors are related to the area under the spectrum and to its shape. In the case of this thesis, the spectrum of the sound comes from the convolution between a source and a simulated TF, the latter being heavily affected by FE errors.

2.6.2 How do the errors affect the metrics?

Given the way humans perceive sounds, an immediate question arises: is it possible to predict how the FE errors modify the spectra? Unfortunately, the answer to this question is negative.

For instance, in Figure 2.4, it is possible to calculate the integral of the two spectra over the bandwidth 0-150 Hz^p. The integral of the FE spectrum (red dashed line) is 8.6% greater than the theoretical one (black continuous line). However, in Figure 2.5, the opposite happens: the integral of the FE spectra is smaller than the theoretical one by 1.2% (dashed red line) and 0.4% (dash-dot blue line); in particular, the more inaccurate the solution, the lower the integral of the spectrum is. In the first case, lower accuracy leads to higher energy, in the second to a lower one. These changes in the spectral areas happen because several factors interact together. The most important of these factors are:

- (1) the shift in frequency;
- (2) the shape of the spectrum in each spectral window of interest (which can be the entire spectrum or, if adaptivity is used, any of the adaptive frequency bands).

^oPleasantness is a complicated feeling that depends as well on sensations such as roughness, tonalness, and so on [18]

^pThe integral is particularly significant: the area under the spectrum is related to the energy of the sound, and, consequently, to the loudness N and the sharpness S .

The shift in frequency is not known a priori, nor the shape of the spectrum in each adaptive band. These two issues make the evaluation of the spectral area changes (with respect to the theoretical one) impractical (perhaps impossible). Furthermore, the aforementioned examples are based on simple scenarios in which only a monopolar source is present with only one reflective surface; only two acoustic rays hit the point $P_{FE}^{(1)}$ at which the spectrum is calculated (the blue and the green ones in Figure 2.3). In real applications many reflective surfaces can be present at the same time, forcing several acoustic rays to hit each point of the domain: in this case, the pollution error can cause not only a frequency shift, but also a change in the shape of the spectrum (see Section 3.4). To make things more complex, these examples take into account only best approximation and pollution errors.

The aforementioned differences between a theoretical and a real scenario make the use of FE simulations based on complex geometries a more pragmatic approach to answer the research questions of this thesis. However, in the case of realistic simulations, another question immediately arises: which numerical parameters must be considered? Section 2.5 provides some clues. First of all, this section shows that results can be very different depending on several factors. The theoretical formulation of the FEM and the PML helped identifying some fundamental parameters such as the order of polynomial interpolation \mathfrak{p}_{FE} , the average size of FE \mathfrak{h} and the thickness of the perfectly matched layers t_{PML} . Other factors play a significant role, but are usually not under control of the user (for instance, the ζ functions of the PML). Besides these factors related to the theory, the geometry of the FE volume plays a significant role, as shown in Section 2.5.4.

Next chapter describes a pragmatical way to evaluate how the FE error affects human perception. Based on a real scenario, it takes into account all the numerical parameters considered up to now.

Experimental characterization and numerical modeling of the considered scenario for sound perception

3.1 Definition of the scenario

THE definition of the scenario, that will be considered in the following jury tests, essentially consists in the choice of some sources, receivers and the related transfer paths. In principle, any scenario could be considered acceptable for the purpose of this research. However, as the PBNv2 project^a deals with pass-by-noise for future vehicle, a simplified application of automotive industry has been chosen, following the principles explained in this section.

In the case of road traffic noise, acoustic sources of vehicles can be grouped into three main categories [12]:

- propulsion noise sources (engine, power-train, exhaust system);
- airflow noise sources (incident airflow on the vehicle);
- rolling noise sources (tires, tire-road interaction).

Other sources (HVAC^b, ancillary systems, etc.) are often neglected. Airflow noise becomes significant at speed higher than pass-by-noise velocities [12], and propulsion noise plays a less significant role nowadays due to improvement in internal combustion engines and use of electric motors [13]. Therefore, the considered application will focus only on tire noise in pass-by-noise conditions.

For this kind of sources, essentially the driver, the passengers or the pedestrians are especially affected by vehicle noise. From a physical and geometrical point of view, the simplest transfer paths are between pedestrians and tires, since they go straight from the source to the receiver. In the chosen application, the complex physical aspects of the tire noise which are related to the mechanism of sound generation and are therefore part of the source, will not be considered. Therefore, the choice is to first focus on a tire-noise scenario, because of its geometrical simplicity combined with its major contributions in road traffic noise.

3.1.1 The mock-up

Once identified the category of TPs, the next step is to built and test a mock-up. But why testing a real system? The answer may look counter-intuitive. Indeed, the purpose of this research is to evaluate how numerical parameters affect human perception of synthesized sounds.

^aThis work was performed with the support of the European Commission's Marie Skłodowska Curie program through the ETN PBNv2 project (GA 721615).

^bHeating, ventilation, and air conditioning.

For this aim, a set of simulations might be sufficient. However, some crucial factors play against the intuitive choice of working without a real system. Indeed, all the errors introduced into the auralized sounds during the process must be under control, otherwise any psycho-acoustic analysis would reflect some hidden factors. Essentially, two most important factors have to be taken into account:

- (1) First, simulations in the previous chapter showed that simple changes in some aspects such as the FE volume shape could affect the spectrum. A methodology is required to ensure that this type of errors is not present or, at least, taken into account: the comparison between simulation results and data collected on a real system is a possible way.
- (2) Second, the human hearing system is known to react differently to diverse kind of stimuli (e.g. perception of pure tones is very different compared to perception of broadband noises, see [17]). Consequently, the shape of the spectra should not be qualitatively too far from the real one. Again, a check by comparison between simulation results and real data-sets can ensure this point.

There is also an inherent advantage in comparing simulations with test datasets: any simplification introduced in the virtual environment would be immediately tested and verified. The latter point is especially important for the boundary conditions, geometry, mechanical properties and all the other ingredients of the virtual models that represent an approximation of the reality.

Besides these considerations, which are fundamental for the achievement of the desired results, some practical implications must be considered. The mock-up geometry on computer aided design (CAD) software must be simple, in order to avoid excessive design time expenditure. The use of a real car as a mock-up results therefore impractical, because of all the details to model. The easy alternative is to build an ad-hoc geometrically simple structure that tries to maintain the main acoustic properties of a real vehicle. The choice was to assemble an acoustic quarter-model vehicle that comprises a wood body, a metal shaft and a real wheel.

The body is realised with wood tables jointed by bolted connections, and a circular wood panel cover the wheel's back. Two slim threaded bars blocked by bolts support the rear part. Figure 3.1 shows the assembled mock-up and the multi-view projections of the wood body.

3.1.2 Sources and receivers positioning

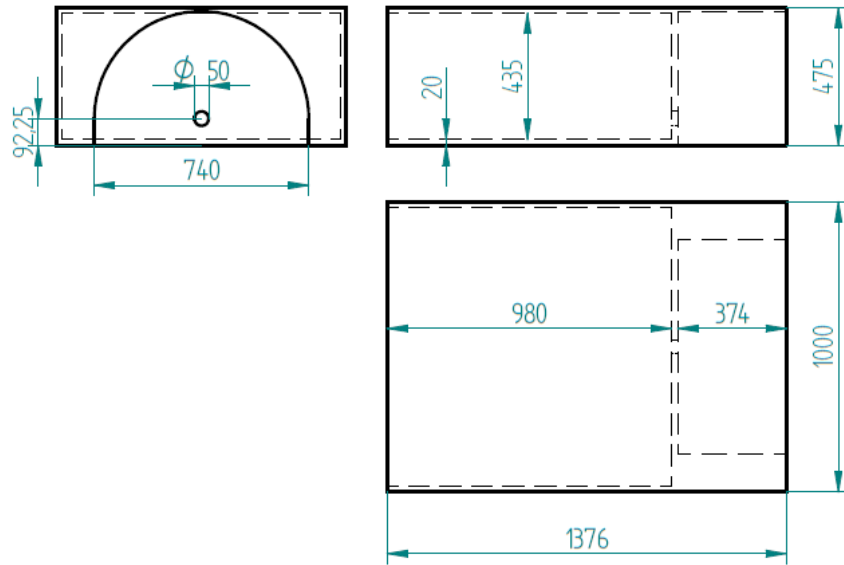
After the mock-up conception, acoustic properties of the environment needs to be defined. Pass-by-noise tests are performed in open-air on asphalt tracks. In laboratory controlled environment, a semi-anechoic chamber is the best choice to represents this situation. Obviously the two situations are not strictly comparable (e.g noise reflection differs from the one observed in real conditions of usage) but the semi-anechoic chamber presents some crucial advantages like repeatability of measurements, stable temperature or protection against weather conditions.

With regard to simulations, some differences exist between theoretical acoustic properties of the chamber and real ones:

- ground does not fully reflect noise;
- walls and ceiling do not fully absorb noise;
- acoustically speaking, the room is not perfectly symmetric.

Therefore, the chamber is tested to ensure that these factors do not affect the tests significantly.

The next step is to define transfer paths and the associated transfer functions. They have two main goals and a minor one. First, the TFs measured on the physical mock-up are used as guidelines to set-up a reference numerical model. Secondly, the simulated TFs will be used to create sounds for jury tests. The minor goal is to provide clues about eventual differences



(a)



(b)



(c)

Figure 3.1: Multi-view projections (a) and two views (b) (c) of the mock-up.

between real and theoretical test scenarios. All the TPs are identified by a monopolar source and a microphone (called here receiver). There are two main reasons to use this approach. Firstly, theoretical monopoles are used to numerically compute transfer functions, because this process is easy in the available computer aided engineering (CAE) environment (Actran [81]). Secondly, the use of monopole sound sources is advantageous for reciprocal measurements in tests [109], which is clearly an advantage.

A critical step is to define an appropriate number of TPs. A high amount of transfer paths would allow to better validate the virtual model, since it would be possible to evaluate its quality for more transfer paths. There is a trade-off between the number of TPs and the time spent for measurements and simulations. The choice is to have four sources and four receivers, for a total of sixteen TPs.

The spatial locations of sources and receivers are identified on a Cartesian reference system. Its origin is located in a position that exploits symmetry properties of the mock-up. This latter has only one symmetry plane, which is vertical and includes the axis of the wheel. The intersection of this plane with the ground and the plane comprising the front panel of the box is the origin O of the Cartesian coordinate system used hereby, as can be seen in Figure 3.2. The z -axis is vertical and positively oriented towards the top. The x -axis is parallel to the tire axis and is positive oriented towards the direction opposite to the mock-up itself. The y -axis is then immediately defined by the right-hand rule. Figure 3.2 schematically represents the mock-up in a virtual environment, showing the coordinate system at its origin.

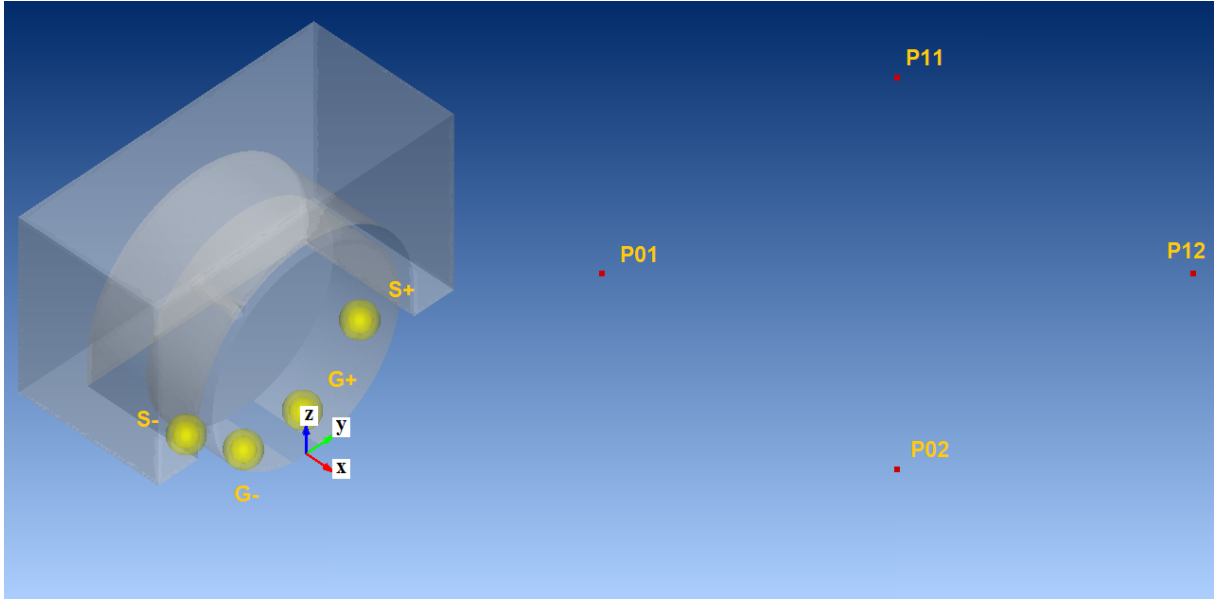


Figure 3.2: Monopole (yellow spheres) and receiver (red points) positions.

It is now possible to easily locate positions of monopoles and receivers. Ideally, the former ones should physically represent the field generated by rolling noise, to which many phenomena contribute [12]. A first one is the radiation from the vibrating tire. Structural vibrations are generated by tire-road interaction and are affected by several geometrical parameters (e.g. thread patterns, road roughness, etc.). Their role is significant below 1 kHz. Air pumping and horn effect are other essential phenomena generating noise. The degree of complexity caused by the involved phenomena and of their interactions is high. In order to recreate the tire acoustic fields through some monopoles, researchers have made significant efforts to identify their optimal locations (for instance in [35]). However such techniques are rather complex, requiring the implementation of optimization and regularization algorithms. In the end, in order to avoid excessive time expenses, the choice was to select the four source positions according to practical considerations. First, the chosen TPs must significantly affect the noise radiation. Second, the distribution is chosen symmetric, in order to gather data to evaluate environmental symmetry. Lastly, the placement of sensors at the correct locations should be realized without much effort. Figure 3.2 shows the selected locations with yellow spheres; in the scheme, the nomenclature of monopoles follows this logic:

- (1) “G” means “ground”, and is adopted for the two monopoles very close to the floor (and to the tire);
- (2) “S” means “suspended”, adopted for the two monopoles hanging in the space (close to the tire);
- (3) “+” is adopted for monopoles with positive y-coordinate;
- (4) “-” is adopted for monopoles with negative y-coordinate.

Table 3.1 summarizes the exact coordinates of the monopoles.

Receiver positions are mainly influenced by practical factors. Microphone positions in a pass-by-noise test are 7.5 m far from the road axis, but such a distance is impractical in the available room. A more convenient positioning for the receivers is closer to the mock-up, as schematically shown in Figure 3.2 by the red points; their coordinates are presented in Table 3.2.

From now on, the TPs will be indicated by the two letters associated to the monopole-microphone position followed by the two numbers associated to the receiver-source position, e.g.

Mono-pole	X [m]	Y [m]	Z [m]
S+	-0.204	0.29334	0.174
G+	-0.204	0.1	0.0065
G-	-0.204	-0.1	0.0065
S-	-0.204	-0.29334	0.174

Table 3.1: Mono-poles location coordinates.

Receiver	X [m]	Y [m]	Z [m]
P10	1	0	1.2
P20	2	0	1.2
P11	1	1	1.2
P21	2	1	1.2

Table 3.2: Receivers position coordinates.

TP S+12 is the transfer function between the mono-pole located at position S+ and receiver at position 12.

3.1.3 Experimental measurements of transfer functions

The first practical issue related to the tests is about the equipment to use; the choice is quite straightforward for microphones, but some considerations are useful for the source. Some sources are present in the market that satisfy these requirements for specific limited frequency bandwidths [109] called here *working bandwidths*. In such sources, an open-ended flexible tube connects a noise generator to a socket. The latter one has an aperture that generates an omnidirectional field thanks to diffraction. The acoustic center, representing a theoretical monopole, is located slightly above the socket aperture. In order to guarantee an omnidirectional behaviour of the radiated field, the waves inside the tube must be plane. This condition requires little diameters of the tube to produce high frequency spherical waves [109]. On the other hand, at low frequencies, a very high volume velocity is required to maintain an adequate sound pressure level.

The working bandwidth must be compatible with the simulation one. FEs work very well at low frequencies, and become impractical at higher frequency, due to the increased computational time required to solve the associated system of equations. The trade-off between all these advantages and disadvantages led to the choice of a MicroFlow source working (according to the constructor) in the frequency band between 200 Hz and 4000 Hz, with a tube diameter of 15 mm, shown in Figure 3.3 [109]^c.

With such a source, the scenario described in previous section is hard to realize. Indeed, the socket cannot fit between ground and tire in a position close to the symmetry axis. As a consequence, microphone and sources are interchanged, exploiting reciprocity. Therefore, microphones occupy monopole positions, and the Microflow source occupies receiver positions. Tests have been performed to ensure this exchange does not cause distortions in the results. In all tests, the signal used to produce the acoustic excitation was a white noise.

^cA source is available in the market able to reproduce a monopole at lower frequencies, but it comes with two downsides. First, it has a diameter of 15 cm and a $f_{max}=260$ Hz (too low for the purposes of this research). Secondly, it has a considerable size that makes its use impractical for the application of interest.

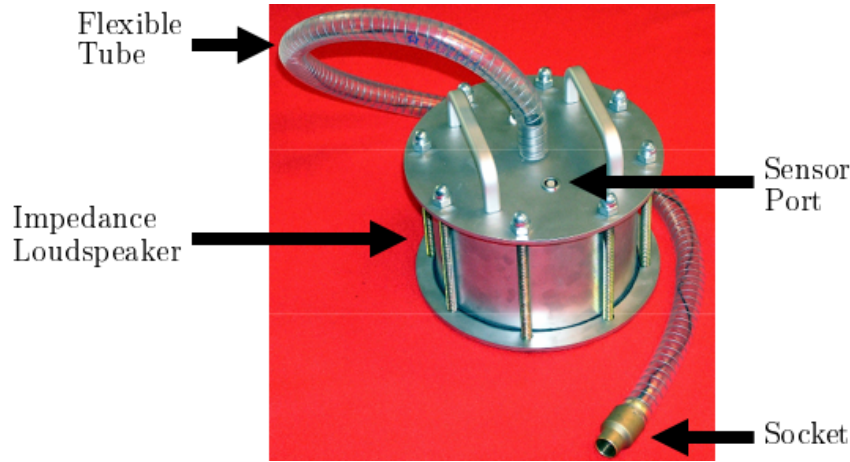


Figure 3.3: The microflow source.

3.2 The Reference Numerical Model

The next step is to build an accurate FE model that is simple in terms of numerical construction and realistic enough. Sounds auralized with this model will represent the reference in the psychoacoustic tests, and will be called reference sounds (associated to each TP); in other words:

- (1) the acoustic metrics of sounds auralized with other models will be compared to the ones associated to the reference sounds;
- (2) perceptual similarities will be evaluated between all the sounds and the reference sounds.

For this reasons, the FE model built now is called reference numerical model. Some practical considerations are useful before to discuss how the model is built.

To draw some conclusions about influences of FE parameters on noise perception, a reference numerical model has to be appropriately set to ensure the veracity of these conclusions^d. In this regard, a crucial aspect relates to the numerical parameters that one wants to consider in this analysis. Here, the main focus is to evaluate only the ones associated with the theoretical formulation described in chapter 2. Therefore, the numerical modelling will be limited to the purely acoustic radiation problem: structure-borne noise will not be considered. The structure of the mock-up is considered, in the simulation, as perfectly rigid.

Given these considerations, it is possible to properly model the mock-up described in section 3.1.1.

The geometry is meshed with Hypermesh [110] and modified in Actran, resulting in a surface mesh Ω_{start} . Quadratic serendipity elements (that is, without central node) are used. Serendipity elements have the advantage of reducing the computational cost of the simulation, but are very sensitive to distortions [111] ^e.

The FE volume is modeled through the Exterior Acoustic component of Actran, which permits to automatize the creation of an h -adaptive mesh. The surface mesh Ω_{start} is first extruded, and then a PML mesh can be obtained on top of the extrusion itself. In the case of three dimensional problems, the surface mesh Ω_{start} should cover any 3D mesh so to include all the surfaces, volumes and obstacles of the acoustic problems. All these meshes must be connected. Only some components of the problem, such as monopole sources, can be modeled in Actran as

^dBy way of completeness, the proper setting of a FE model relates to the convergence properties of the method; see Appendix B for details.

^eAlso, distortions may pose problems without proper settings for the numerical integration [112].

boundary conditions without the support of a mesh (and can be therefore outside the surface mesh Ω_{start}). In the case illustrated here, it was possible to use only the mesh Ω_{start} shown in Figure 3.4, since no 3D mesh was needed. Ω_{start} is rather fine, with an average size of finite elements $h \simeq 0.015$ m. The mesh has been conceived for simulations up to 3500 Hz.

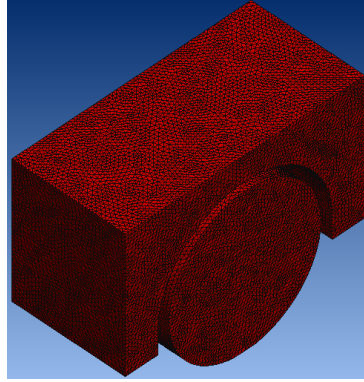


Figure 3.4: Surface mesh used as input for the Actran Exterior Acoustic Component.

Once Ω_{start} is defined, the user must choose the boundary method, since other settings depend on it. Afterwards, given the maximum and minimum wavelengths per adaptive frequency band λ_{max} and λ_{min} , the user must define (among others):

- (1) FE volume thickness (absolute or with respect to λ_{max});
- (2) minimum number of elements per λ_{min} ;
- (3) gradient factor.
- (4) PML thickness with respect to λ_{max} ;

Considerations about the minimum number of elements per wavelength and thickness of the FE volume and the PML come directly from the theoretical formulation discussed in chapter 2, but new practical aspects play a crucial role at this stage and deserve a further discussion. Firstly, regarding the FE volume thickness, it must be equal to at least two elements. If not, Actran automatically changes the size of the finite elements, leading to meshes with many more degrees of freedom than asked by the user. This is a lower limit for the FE volume thickness t_{FE} and for the elements size h , the upper one being dictated only by computational costs (a bigger volume lead to longer simulations).

The gradient factor (GF) represents the maximum change in size between two adjacent finite elements. To illustrate the effect of diverse values for this parameter, Figure 3.5 shows two different meshes. The red FE mesh Ω_{start} is regular with $h = 0.01$. The two PMLs, in grey, have an average size of elements $h_{PML} = 0.57$ and are both built with an APML component starting from Ω_{start} . Because $h_{PML} \gg h$, the PML mesh is more refined close to Ω_{start} : so the user needs to decide how “fast” the size of the elements must change from the interface with the FE volume towards the exterior. This task is performed by the GF.

The values for the GF are 1.2 (a) and 4 (b). The gradient factor 1.2 enforces adjacent elements to have a similar size, thus the mesh gradually evolves towards the exterior. Overall, the elements are well distributed in function of their size, with small elements closer to Ω_{start} ; also, the elements present a good aspect ratio (ratio of the shortest length of the element to the longest length of the element). Figure 3.5 (b), with GF=4, depicts a different situation. The elements change their size very fast, leading to the presence of several distorted elements (that is, with poor aspect ratio), especially close to Ω_{start} . Also, FEs of similar size are not well distributed: for instance, in the top right corner elements are fairly smaller than elements in the

Frequency bands [Hz]						
20-52	56-100	104-252	256-500	504-1000	1004-1500	1504-2000

Table 3.3: Boundaries of the adaptive frequency bands.

bottom right corner. As the figures show, a low value of the GF produces undoubtedly better meshes, but it may lead to excessively accurate meshes.

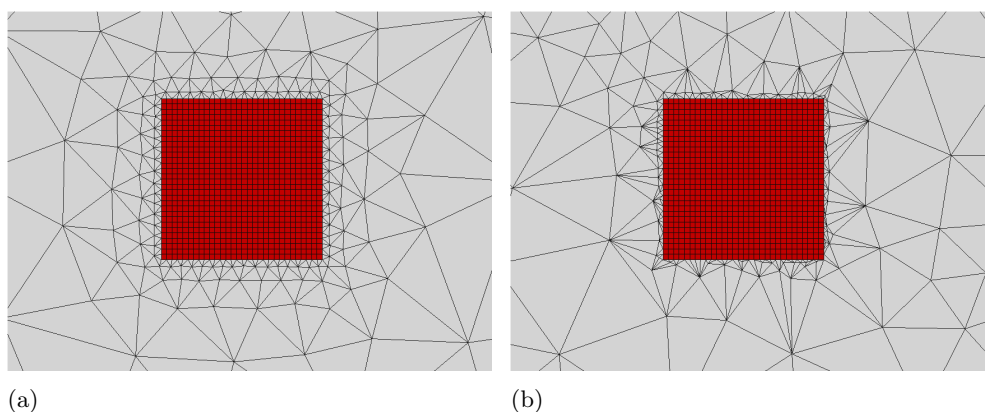


Figure 3.5: Given a regular mesh with $h = 0.01$, a PML with $h_{PML} = 0.57$ is constructed using gradient factors equal to 1.2 (a) and 4 (b).

For the reference numerical model, the chosen parameters per adaptive bandwidth are:

- (1) FE volume thickness t_{FE} equal to 1 (maximum) wavelength;
- (2) 6 quadratic elements per minimum wavelength^f;
- (3) gradient factor equal to 2;
- (4) PML thickness equal to 1 (maximum) wavelength.

Table 3.3 shows the adaptive frequency bands chosen for the simulations. The reader may notice that at low frequencies the bands are very narrow when compared with bands at higher frequencies. This is because the volume thickness is determined by λ_{max} , while the elements size by λ_{min} . The ratio between λ_{min} and λ_{max} must be kept high enough to avoid big volumes with small elements, which in turn would lead to high computational costs. This ratio changes faster at low frequencies than at high ones, explaining the higher density of adaptive frequency bands at low frequencies. For instance, $\lambda \simeq 17$ m at 20 Hz and $\lambda \simeq 7$ m at 52 Hz, resulting in a ratio between $\lambda_{min}/\lambda_{max}$ of about 0.41 over 32 Hz. A band between 20 Hz and 100 Hz would already lead to a ratio of about 0.2, and the resulting volume would require too many elements to be computed in an acceptable time. On the other hand, $\lambda \simeq 0.25$ m at 1500 Hz, and $\lambda \simeq 0.17$ m at 2000 Hz, with a ratio of about 0.68 spread over a band of 500 Hz, which is even higher than the one of the lowest frequency band.

At this point, the simulation is ready except for the environmental characteristics. So, speed of sound is calculated by linearly interpolating results of [113] with a relative humidity of 50%, a temperature of 25°C and an environmental pressure of 101325 Pa. Air density is calculated

^fNumerical experiments in the previous chapter show that spectra calculated via quadratic FE models with PML tend to have slightly more energy than the theoretical solution of a problem; however, the reference numerical model here discussed is pretty accurate, so this effect should be reduced. Furthermore, results of next chapters shows that there is no difference in perceptual terms between high accuracy linear and quadratic models.

according to the CIPM-2007 equation of state for moist air [114] with same setting used for speed of sound, and neglecting change of CO₂ concentration with respect to dry air. Simulations have been run in the frequency band between 20 Hz and 2000 Hz with a frequency step of 4 Hz. The latter one has been chosen in accordance with results found in literature. In particular, Nykänen *et al.* showed that binaural TFs with a resolution of 4 Hz are perceived as similar to artificial head recordings [43]. This result was later confirmed by Trollé *et al.* in the case of vibroacoustic applications [44].

First, a qualitative evaluation is done by comparing tested and simulated TFs. Figure 3.6 shows TP S+12: in blue, the tested TF, in red the simulated one. The trend is similar, both in amplitude (a) and phase (b), despite some differences in values. The proposed model is limited to a purely acoustic problem, not taking into account the air inside the tire, flexibility of the structure or surface details of the tire itself. Indeed, the introduction of tire details and properties would add other errors due to structure modelling and approximations. These errors need to be avoided so to restrict the focus on purely acoustic parameters for unbounded problems. On the other hand, a real representation of the mock-up is not necessary for the purpose of this research: it is only important to have realistic sounds. For these reasons, final results are considered acceptable.

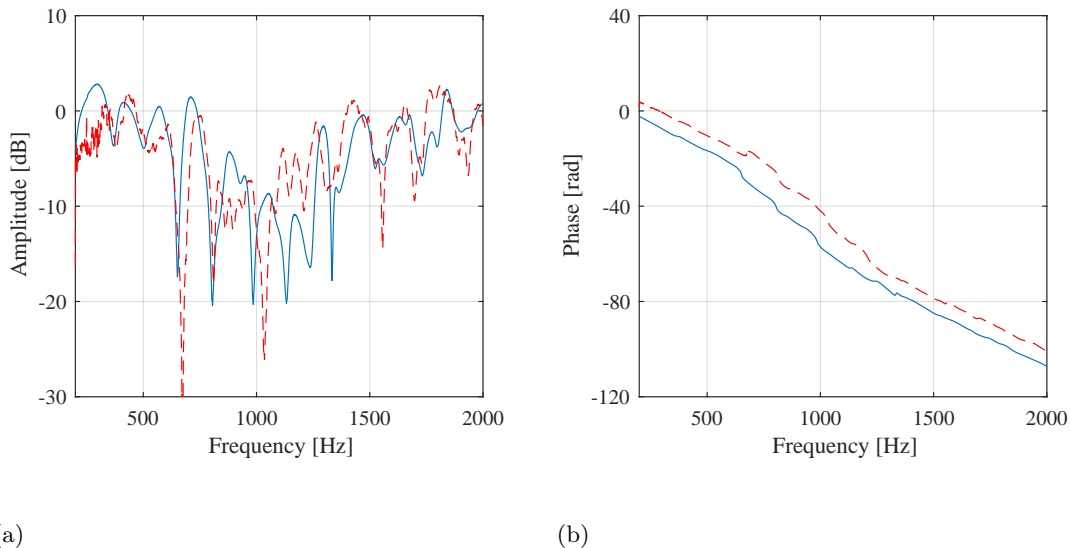


Figure 3.6: Simulated (blue continuous line) and tested (red dashed line) TFs S+02 comparison: amplitude (a) and phase (b).

Lastly, it appears critical to understand how much the computed transfer functions differ from theoretical scenarios like the ones discussed in Section 2.3.2. Indeed, with a small difference, the simple considerations of Section 2.3.2 would be sufficient to tackle this scientific challenge. For this purpose, the most similar theoretical scenario is represented by the monopole sources and the receivers over a horizontal rigid plane in the absence of the mock-up geometry. Figure 3.7 compare the amplitude (a) and the phase (b) of this theoretical scenario (red line) with the FE solution calculated with the reference numerical model (blue line) in the case of the TP S+11. The difference is significant, and shows that, in a complicated case like the one described, a theoretical approach is not possible.

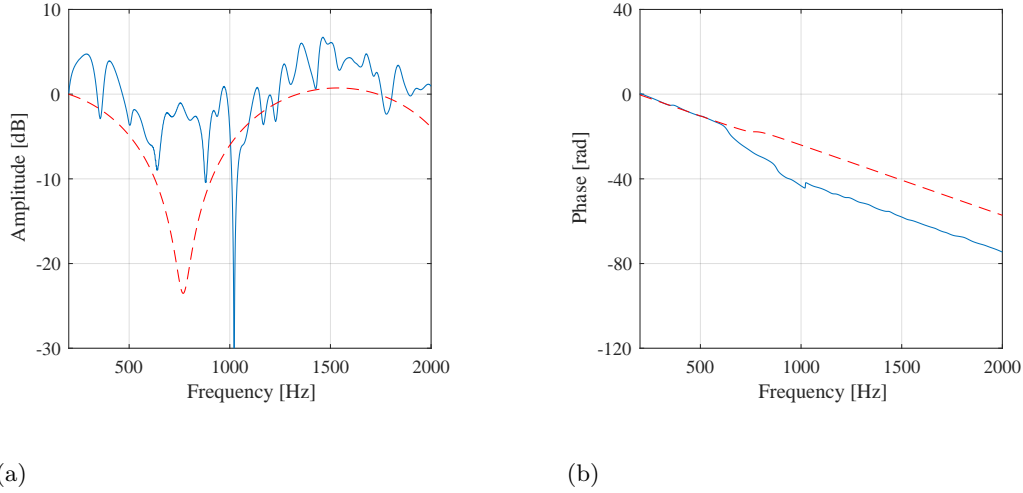


Figure 3.7: Simulated (blue continuous line) and theoretical (red dashed line) TFs S+02 comparison: amplitude (a) and phase (b); the theoretical TF is computed with the monopolar source, receiver and horizontal rigid plane of the simulated TF, but the mock-up geometry is absent.

3.3 Design of Experiments

Once the reference numerical model is ready and tested, the next step requires to properly prepare and produce the others simulations. Recalling that the main purpose is to evaluate the perception of the numerical errors, a strategy must be defined including the definitions of:

- (1) *factors*, namely those parameters that have a major influence on the accuracy of simulations;
- (2) *levels*, namely the values assumed for each *factor*;
- (3) *effects*, the qualitative or quantitative metrics used to derive conclusions.

Regarding *factors*, a summary of results from previous sections can provide a direction to the most appropriate choices. The order of polynomial shape functions \mathfrak{p}_{FE} and the average size of the finite elements \mathfrak{h} play a significant role in controlling approximation and pollution error. These two parameters are related together through the nodal resolution of the mesh $\mathfrak{N} = \frac{\lambda_{min}}{\mathfrak{h}\mathfrak{p}_{FE}}$ (where λ_{min} is relative to the maximum frequency), which depends on both of them. Two other key *factors* are the thickness and the nodal resolution of the PML (Actran does not allow to change the order of polynomial shape functions, which must be equal to the one of the FEs). Lastly, the two parameters that may affect the geometry of the FE mesh are the gradient factor and the thickness of the FE volume t_{FE} . The former is responsible for how the size of the FEs varies inside the volume, while the latter is responsible not only for the size of the volume, but also for the shape. Indeed, the FE volume generated with the Acoustic Exterior Component of Actran is a convex hull, whose boundaries significantly change shape depending on the thickness chosen. For instance, figure 3.8 shows two convex hulls of a cube with 1 m sides; the convex hull in subfigure (a) is tighter than the one in subfigure (b), and the curved portion of the external surface is a smaller percentage. Numerical experiment in chapter 2 showed that both the shape and the positioning of receivers with respect to the FE volume can affect the simulated spectra, thus it is reasonable to assume that t_{FE} might be responsible for some changes.

Another crucial aspect regards the strategy to test the error introduced by these *factors*. Since there is a lack of results in this field, the most reasonable approach is a *full factorial experiment*. In the present case, it consists in choosing some *levels* for each *factor*, and to define

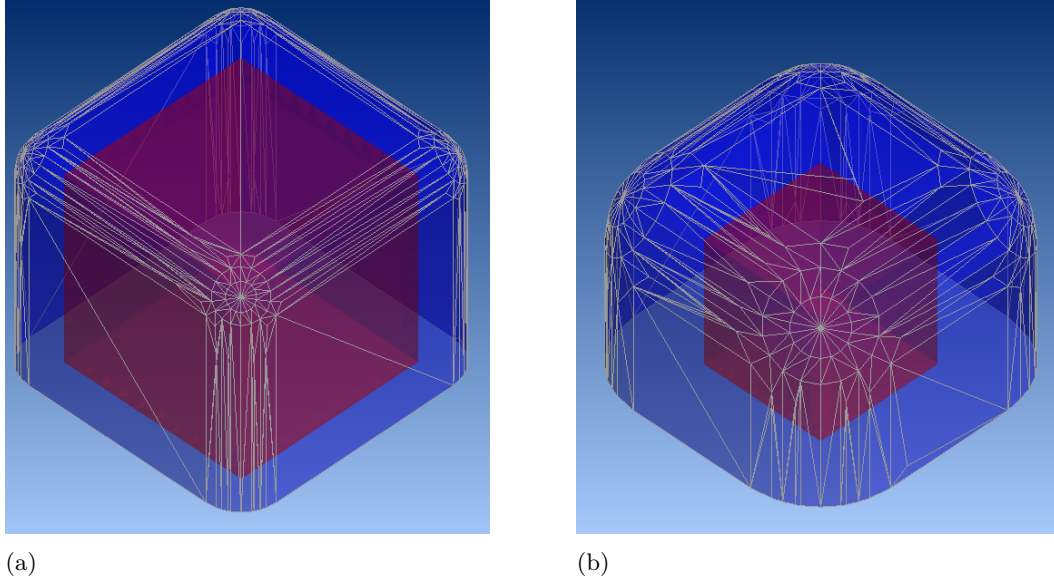


Figure 3.8: Examples of two convex hulls of the same cube (sides of 1 m); thickness is equal to 0.2 m in (a), 0.6 m in (b).

all the possible simulations with these sets of parameters. According to the theory previously discussed, the following *factors* are the most significant, and, consequently, are chosen:

- (1) numerical resolution \mathfrak{N} ;
- (2) order of polynomial shape function \mathfrak{p}_{FE} ;
- (3) thickness of PML $\frac{t_{PML}}{\lambda_{max}}$;
- (4) thickness of FE volume $\frac{t_{FE}}{\lambda_{max}}$.

Two *levels* for each factor are chosen, giving raise to a so-called 2^n factorial experiment^g. For each *factor*, *level 2* represents the most accurate solution, with *level 1* being a poorer choice. The reference numerical model described in section 3.2 has all the *factors* at *level 2*, thus being the most accurate simulation^h. On the other hand, *level 1* should be poor enough to introduce errors that make the simulated sounds perceptually different from the reference one. However, the difference should not be excessive; indeed, jury tests are conceived to analyse similarities, and the introduction of too different sounds might affect final results. Participants may use such extremely different sounds as the reference for the score "very different", consequently rating as "very similar" all the others (see chapters 4 for more details about the meaning of these scores). This fact would obviously be counterproductive.

In the end, $2^4 = 16$ models have been created; the factors chosen for creating the numerical models and their levels are summarized in table 3.4.

To create realistic sounds, each of the simulated TFs is convoluted with a tire noise signal of 3 seconds recorded in real conditions; in detail, the signal is obtained from a much longer laboratory time recording of a 195/65R15 tire rolling on a drum equipped with a rough surface. The test is a coast-down from 120 to 20 km/h (constant deceleration of 1 km/h/s) performed in a semi-anechoic environment. The part used for the convolution is between 51.5 and 48.5 km/h.

^gIt is recalled here that the notation 2^k , common in literature, is not utilized to avoid confusion with the wave-number k

^hIn the theory of Design Of Experiment (DOE), each experimental run is called 'test', see [47], page 1; here this nomenclature is not used, in order to avoid confusion.

Factor	L=1	L=2
$\mathfrak{N} = \frac{\lambda}{\mathfrak{h}\mathfrak{p}_{FE}}$	4	12
\mathfrak{p}_{FE}	1	2
$\frac{\mathfrak{t}_{FE}}{\lambda}$	0.4	1
$\frac{\mathfrak{t}_{PML}}{\lambda}$	0.6	1

Table 3.4: Factors and their levels L.

Figure 3.9 shows amplitude of the source’s power spectrum calculated with the Welch’s methodⁱ in Matlab [115].

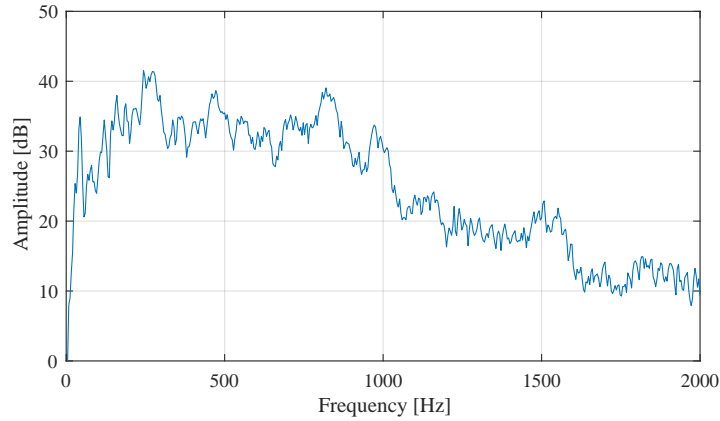


Figure 3.9: Spectrum of the source signal (only the amplitude is shown).

The sounds auralized with the reference numerical model are called reference sounds. At this point, it is possible to select appropriate *effects*:

- (1) acoustic metrics. The metrics analyzed are SPL(A), where the “A” indicates the A-weight, loudness N , and sharpness S . Loudness has been computed according to ISO 532B (1975) norms (Zwicker model), and sharpness according to Zwicker [18]. These metrics will be analyzed in the next section.
- (2) The perceived similarities assigned between the reference sounds and all the other sounds during jury tests. They are the subject of next chapter.

3.4 Models Analysis

Once that simulations are ready, is it possible to understand how the numerical parameters affect acoustic metrics of auralized sounds? First of all, to answer this question, it turns useful to recall that sounds are obtained via auralization. That is, numerical error has an influence directly on TFs, and consequently on auralized sounds. Therefore, it makes sense to split the analysis into two steps: first, focusing on TFs; second, taking into account the effect of the source. The purpose of this section is to focus on the first of these two steps. A simple qualitative comparison between TFs calculated with different parameters provides significant clues in this regard. Figure 3.10 shows two TFs, TP S+11 and TP G-02, computed using the

ⁱThe Welch’s method was set on Hanning windows lasting 0.25 s with 50% overlap; all the spectra of temporal signals in this thesis are calculated in the same way.

reference numerical model (red dashed lines) and using the model having the following levels L (blue continuous lines): $L[\mathbf{p}_{FE}] = 1$, $L[\mathfrak{N}] = 1$, $L\left[\frac{t_{FE}}{\lambda}\right] = 2$ and $L\left[\frac{t_{pml}}{\lambda}\right] = 2$. The figure shows a frequency shift towards higher frequencies compared to the reference computation as well as a slight change in shape. Even if these changes in shapes are clearly visible, the frequency shift is dominant. This effect will be crucial to take into account when comparing results of two different models.

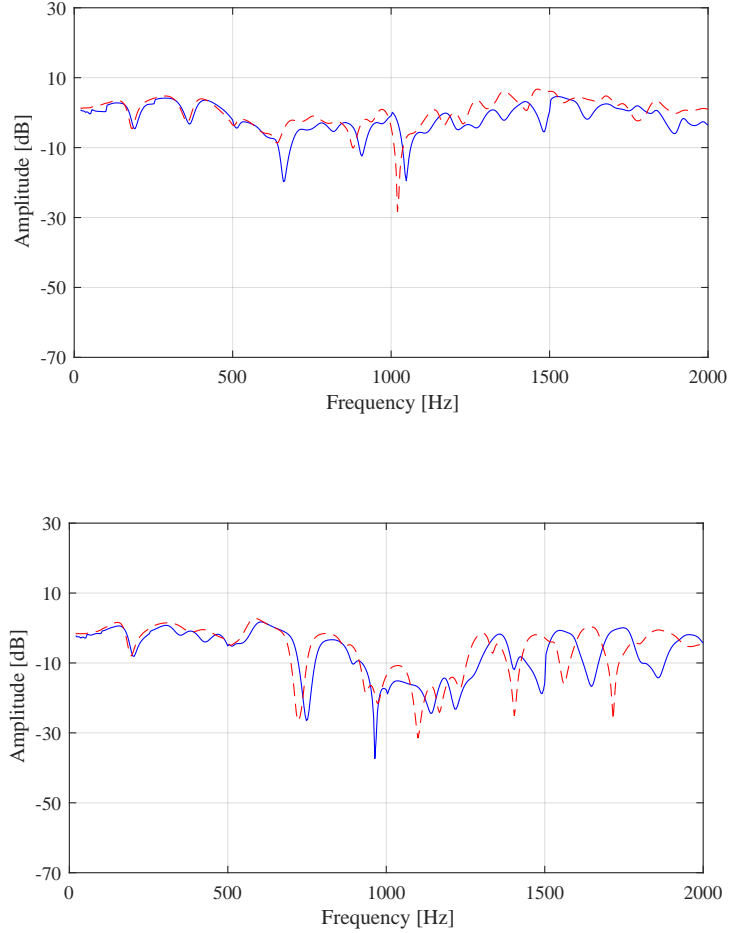


Figure 3.10: TFs associated to the TP S+11 (a) and G-02 (b) calculated with the reference numerical model (red dashed line) and the model having the following levels L (blue continuous line): $L[\mathbf{p}_{FE}] = 1$, $L[\mathfrak{N}] = 1$, $L\left[\frac{t_{FE}}{\lambda}\right] = 2$ and $L\left[\frac{t_{pml}}{\lambda}\right] = 2$.

In the following, objective metrics to evaluate the quality of the numerical models and simulated TFs will be introduced. In particular, when dealing with evaluating numerical errors, a key point is to use appropriate metrics able to take into account the most critical aspects:

- (1) computational complexity (related to the cost to solve each simulation);
- (2) numerical quality of each model, possibly making distinction between frequency shift and shape changes;
- (3) errors between each TFs and the reference ones.

The following subsections analyze in-depth these three elements.

3.4.1 Computational size of numerical models

As mentioned in section 2.2.3 a high number of degrees of freedom (DoF) is related to an increased computational cost to solve the simulation. Due to the importance of the computational aspects in practical applications, it makes sense to evaluate the size of the matrices. Because of adaptivity, each simulation comprises several meshes. Therefore, the computational size is calculated as the sum of DoF of all meshes of each model.

Table 3.5 shows these data. The models are ranked in Table 3.5 according to the sum of the numbers of degrees of freedom (last column). As a first guess, it is expected to have here a classification of the models, from the worst to the best according to the representativeness of the simulated sounds. The two metrics defined in the next section are introduced to check this first guess from an objective point of view. However, the ranking should not be taken as a strict metric of quality, but rather as an indicator. For instance, the reference numerical model is ranked 15th, while the biggest model has $L[\mathbf{p}_{FE}] = 1$. This situation is due to the lack of central nodes in the reference model, causing a smaller number of degrees of freedom in the reference model.

$L\left[\mathfrak{N} = \frac{\lambda}{6p_{FE}}\right]$	$L[p_{FE}]$	$L\left[\frac{t_{FE}}{\lambda}\right]$	$L\left[\frac{t_{PMLL}}{\lambda}\right]$	N° of DoF							SUM	RANK
				20-52 [Hz]	56-100 [Hz]	104-252 [Hz]	256-500 [Hz]	504-1000 [Hz]	1004-1500 [Hz]	1504-2000 [Hz]		
1	1	1	1	12519	9649	14308	14284	21101	22174	28371	122406	1
1	1	1	2	20446	12566	22711	20940	32254	32203	40121	181241	2
1	1	2	1	26430	14842	28763	25254	39610	37746	38417	211062	3
1	1	2	2	43887	21036	37351	45984	57666	51837	54018	311779	7
1	2	1	1	16954	14900	19104	20727	29105	45224	82546	228560	4
1	2	1	2	24193	17437	26840	26916	40311	55852	93470	285019	6
1	2	2	1	31177	19764	34065	30758	43588	42603	47755	249710	5
1	2	2	2	47762	25208	50704	42766	61574	56501	62487	347002	8
2	1	1	1	192469	129341	224815	220474	381209	409307	533798	2091413	9
2	1	1	2	388728	192597	437617	382936	666792	655101	803823	3527594	11
2	1	2	1	529224	242256	564260	469812	815906	783546	980170	4385174	13
2	1	2	2	959061	389966	993873	777182	1299749	1129174	1340451	6889456	16
2	2	1	1	267314	194524	314328	314471	483768	501960	490207	2566572	10
2	2	1	2	475746	270949	537566	491095	796917	648834	792928	4014035	12
2	2	2	1	620356	320268	681518	579963	825358	753569	850889	4631921	14
2	2	2	2	957017	485461	1018774	776522	1269320	1111976	1210569	6829639	15

Table 3.5: Number of degrees of freedom per adaptive frequency band for each model and size rank.

3.4.2 Calculation of numerical errors

A critical aspect of this research is to estimate the quality of numerical models. To this end, two approaches are possible: one can evaluate the quality of the model globally or locally. A global evaluation considers the simulated TFs calculated with a model altogether. On the other hand, a local approach takes into account each single TFs. Global and local approaches are usually complementary, but it is interesting in this thesis to check whether one approach proves to be sufficient to explicate differences in perception. Indeed, if the local approach does not correlate better with perception than the global one, scientists and engineers could simply refer to a qualitative estimation of the numerical model to assess how sounds will be perceived. On the contrary, if the local approach proves to be sufficient for sound quality purposes, some other strategies need to be used. Lastly, if both approaches prove to be necessary, the scientific challenge would be to appropriately combine them.

Global errors

The response vector assurance criterion^j (RVAC) is chosen to assess differences between numerical models globally. Given a reference vector $VTF_{ref}(f_{ref})$ and a vector to compare $VTF_i(f_i)$, both functions of frequency, this method consists in calculating the following correlation matrix **RVAC**:

$$\mathbf{RVAC}(f_i, f_{ref}) = \sqrt{\frac{|VTF_i(f_i)^H VTF_{ref}(f_{ref})|^2}{|VTF_i(f_i)^H VTF_i(f_i)| |VTF_{ref}(f_{ref})^H VTF_{ref}(f_{ref})|}} \quad (3.1)$$

where VTF_{ref} is the vector of TFs calculated with the reference numerical model, VTF_i is the vector of TFs computed with the model to compare. H denotes the Hermitian transpose. Each element of the **RVAC** matrix is associated with two frequencies: one of the reference model (f_{ref}), and the other with the compared model (f_i). The magnitude of the elements represents the correlation between the two models at the given frequencies: a value equal to 0 indicates that the two vectors are orthogonal, a value of 1 indicates that the vectors are identical. Figure 3.11 (a) shows this matrix between the reference numerical model and the model with levels: $L[\mathfrak{N}] = 1$, $L[\mathfrak{p}_{FE}] = 1$, $L\left[\frac{t_{FE}}{\lambda}\right] = 1$ and $L\left[\frac{t_{pml}}{\lambda}\right] = 1$. The darkest blue areas represent points of high correlation.

Given two equal models, the diagonal of the **RVAC** matrix would be unitary; this diagonal is the red line in Figure 3.11 (b). Because of differences introduced by numerical models, the points of highest correlation (not necessarily equal to 1) do not lie always on the diagonal. The white line in Figure 3.11 (b) represents the points of highest correlation between the two models. The more this line of maximal correlation is far from the diagonal, the higher the frequency shift between the two models. Since the reference numerical model used as a reference is very accurate, a low correlation can be considered here as an index of poor numerical quality. Appendix C shows **RVAC** matrices for the other fourteen models.

The vertical distance between the diagonal and the line of maximal correlation is:

$$\Delta f(f_{ref}) = f_{ref} - f_{i(max)}, \quad (3.2)$$

where the subscript $i(max)$ highlight that the point belongs to the maximal correlation line. Given two models with very similar TFs but shifted in frequency, $\Delta f(f_{ref})$ represents the frequency shift between these models.

For each frequency f_{ref} there is always a value of $f_{i(max)}$ at which $\max([\mathbf{RVAC}(f_{i(max)}, f_{ref})])$ occurs. The vector that comprises only these maximum values is called here *RVAC* and represents the correlation between two models adjusted by frequency shift. Figure 3.12 shows the

^jSometimes called frequency response assurance criterion, FRAC, see [116, 117].

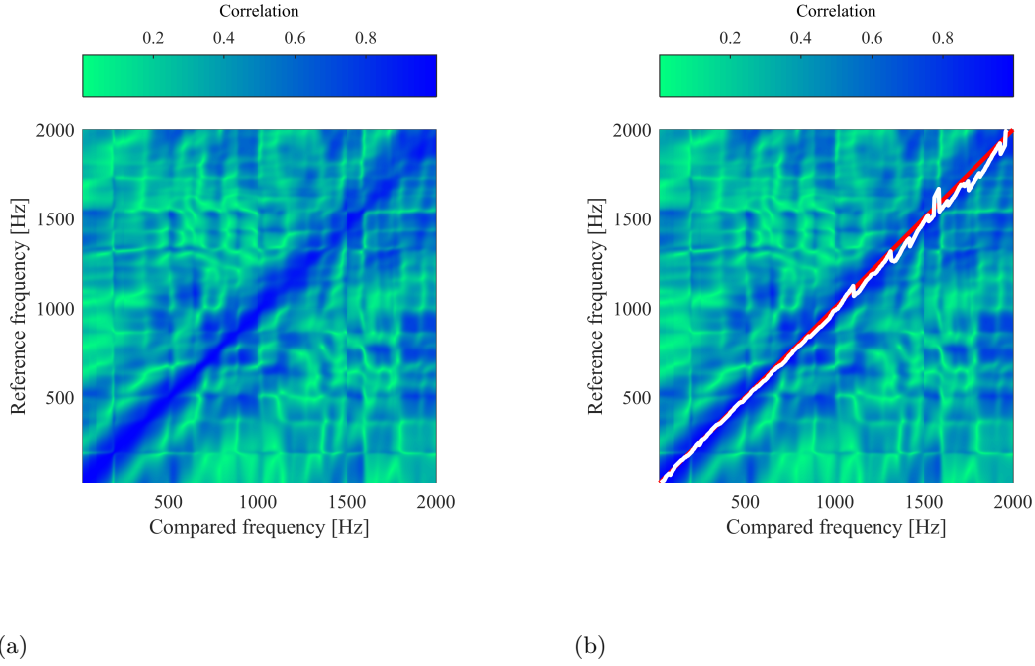


Figure 3.11: **RVAC** matrix of the model with levels: $L[\mathfrak{N}] = 1$, $L[\mathbf{p}_{FE}] = 1$, $L\left[\frac{t_{FE}}{\lambda}\right] = 1$ and $L\left[\frac{t_{pml}}{\lambda}\right] = 1$.

RVAC (black continuous line, left y-axis) and $\Delta f(f_{ref})$ (black dashed line, right y-axis) of the model with levels: $L[\mathfrak{N}] = 1$, $L[\mathbf{p}_{FE}] = 1$, $L\left[\frac{t_{FE}}{\lambda}\right] = 1$ and $L\left[\frac{t_{pml}}{\lambda}\right] = 1$. Appendix C includes similar graphs for the other fifteen models. A key insight coming from Figure 3.12 is that the values of the *RVAC* lower than 0.9 are consistently associated to an erratic behaviour of $\Delta f(f_{ref})$ characterized by high amplitude shifts. More precisely, the more erratic the behaviour of $\Delta f(f_{ref})$, the poorer is the *RVAC*.

Obviously, the meaning of the identified frequency shift is correlated to the comparability of the two models. When trying to force comparison (low *RVAC* value) the corresponding frequency shift is unrealistic and highly variable. However, both indicators are complementary and useful to identify when two models might be not comparable anymore. It is visible in Figure 3.12 that this happens at a frequency around 1000 Hz.

Taking with the needed caution the meaning of the frequency shift, it is possible to construct a "shifted Transfer Function" $TF_s(f)$:

$$TF_s(f) = TF_i(f + \Delta f(f)), \quad (3.3)$$

Recalling that, because of the dispersive behaviour of the FEM, the frequency shift of poor models is towards higher frequencies, one can expect TF_s to be adjusted towards lower frequencies: this is indeed what happens. Figure 3.13 shows two examples of this phenomenon for the TP G-02: the original TFs are in black, the shifted ones in red. The models used have the following factor levels: $L[\mathfrak{N}] = 1$, $L[\mathbf{p}_{FE}] = 1$, $L\left[\frac{t_{FE}}{\lambda}\right] = 1$ and $L\left[\frac{t_{pml}}{\lambda}\right] = 1$ (a), $L[\mathfrak{N}] = 1$, $L[\mathbf{p}_{FE}] = 2$, $L\left[\frac{t_{FE}}{\lambda}\right] = 1$ and $L\left[\frac{t_{pml}}{\lambda}\right] = 2$ (b); the model of Figure 3.13 (a) is the same than the one of Figure 3.12.

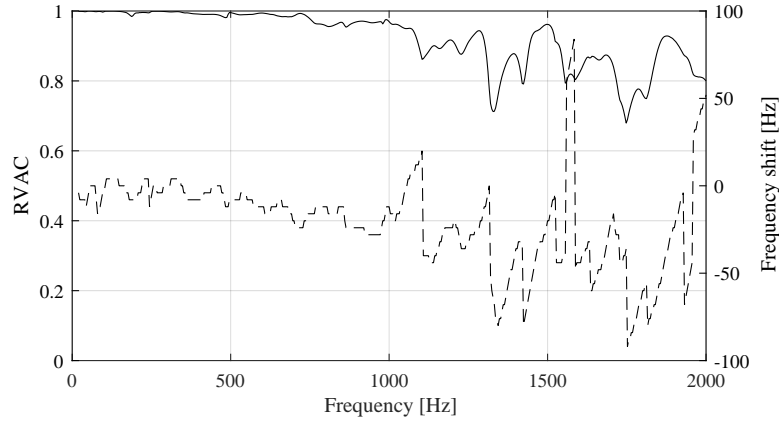
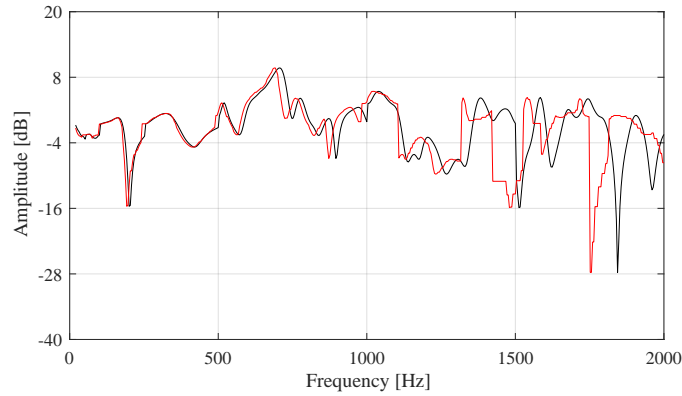
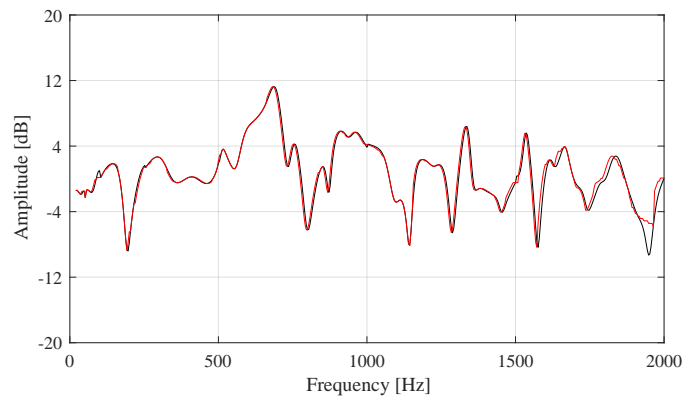


Figure 3.12: $RVAC$ (black continuous line, left y-axis) and Δf (black dashed line, right y-axis) of the model with levels: $L[\mathfrak{N}] = 1$, $L[\mathfrak{p}_{FE}] = 1$, $L\left[\frac{t_{FE}}{\lambda}\right] = 1$ and $L\left[\frac{t_{pml}}{\lambda}\right] = 1$.



(a)

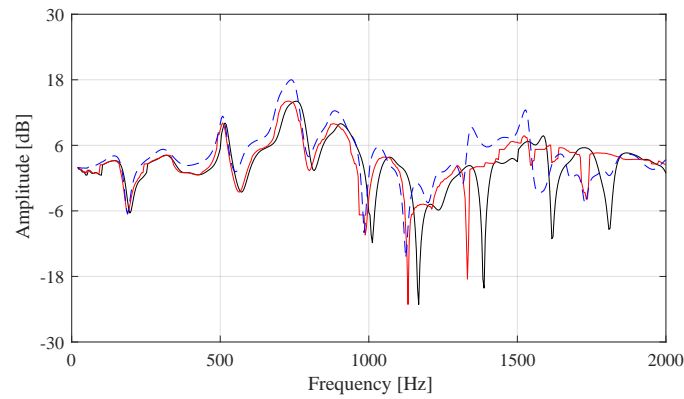


(b)

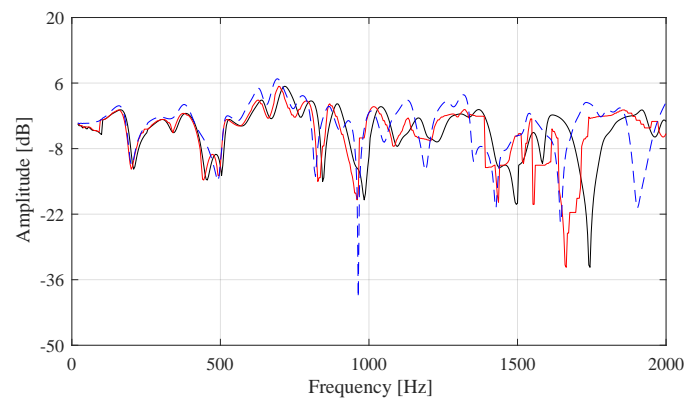
Figure 3.13: Simulated (black) and shifted (red) TFs for the TP G-02; model factor levels: $L[\mathfrak{N}] = 1$, $L[\mathfrak{p}_{FE}] = 1$, $L\left[\frac{t_{FE}}{\lambda}\right] = 1$ and $L\left[\frac{t_{pml}}{\lambda}\right] = 1$ (a), $L[\mathfrak{N}] = 1$, $L[\mathfrak{p}_{FE}] = 2$, $L\left[\frac{t_{FE}}{\lambda}\right] = 1$ and $L\left[\frac{t_{pml}}{\lambda}\right] = 2$ (b).

Δf is indeed towards lower frequencies, as expected, but the shifted TF in Figure 3.13 (a) becomes unsmooth and unnatural at high frequencies. On the other hand, the TF in Figure 3.13 (b) is shifted only of a few steps at high frequencies, maintaining a natural and smooth shape.

It is also helpful to understand how better the shifted TF_s compare with the reference. Figure 3.14 shows an example of the alignment between in the case of TPs G-10 (a) and G-21 (b); in black, the simulated TFs, in blue (dashed line) the reference TFs and in red the shifted TFs. The simulated TF is computed with levels: $L[\mathfrak{N}] = 1$, $L[\mathfrak{p}_{FE}] = 1$, $L\left[\frac{t_{FE}}{\lambda}\right] = 2$ and $L\left[\frac{t_{pmi}}{\lambda}\right] = 2$. Although these two examples have a poor *RVAC*, the shifted TFs are much closer to the reference than the original TFs in terms of frequency alignment and shape (in a lesser way). An essential fact emerges from this analysis. Despite the TPs being very different, the frequency shift is very similar between the two cases, except where the red transfer functions are very irregular (for frequencies roughly higher than 120 Hz): this is expected since, in these areas, the *RVAC* is very low. Therefore, as suggested in the previous chapter, the frequency shift can be considered as a global metric (that is, it depends only on the numerical accuracy but not on the TP).



(a)



(b)

Figure 3.14: Reference (blue dashed line), simulated (black line) and shifted (red line) TFs in the case of TPs G-10 (a) and G-21 (b); the compared TF is computed with levels: $L[\mathfrak{N}] = 1$, $L[\mathfrak{p}_{FE}] = 1$, $L\left[\frac{t_{FE}}{\lambda}\right] = 2$ and $L\left[\frac{t_{pmi}}{\lambda}\right] = 2$.

This can be highlighted by averaging both the *RVAC* and the absolute value of the frequency

shift $|\Delta f|$, giving rise to the new metrics \overline{RVAC} and $\overline{\Delta f}$. Figure 3.15 shows a scatter of these two variables^k: the link between them is evident, with significant $\overline{\Delta f}$ (>10 Hz) only for \overline{RVAC} lower than 0.925. Therefore, these two metrics provide an index of quality for the numerical models.

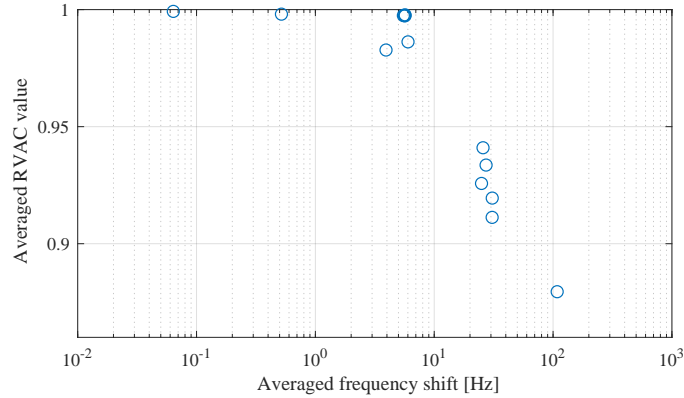


Figure 3.15: Scatter graph of \overline{RVAC} vs. $\overline{\Delta f}$.

A first useful way to exploit these metrics is to group the models according to their quality. It is possible to group the models into four different sets according to their performance as a function of frequency, revealing also some effects of adaptivity. The four sets are:

- (1) models with $L[\mathbf{p}_{FE}] = 1$ and $L[\mathfrak{N}] = 1$ with a $RVAC$ that decreases continuously, Figure 3.16 (a). This set comprises models ranked 1, 2, 3 and 7 according to Table 3.5;
- (2) models with $L[\mathbf{p}_{FE}] = 2$, $L[\mathfrak{N}] = 1$ and $L\left[\frac{t_{pml}}{\lambda_{max}}\right] = 1$, with a good $RVAC$ up to 1000 Hz, which is the maximum frequency of one of the adaptive bands, and a very poor one at higher frequencies, Figure 3.16 (b). This set comprises models ranked 4 and 5;
- (3) models with $L[\mathbf{p}_{FE}] = 2$, $L[\mathfrak{N}] = 1$ and $L\left[\frac{t_{pml}}{\lambda_{max}}\right] = 2$, and almost constantly good, Figure 3.16 (c). This set comprises models ranked 6 and 8;
- (4) models $L[\mathfrak{N}] = 2$ with constantly good $RVAC$, Figure 3.16 (d). This set comprises models ranked 9 to 16.

It is possible to summarize these results by plotting the \overline{RVAC} in function of the size ranks of Table 3.5, as in Figure 3.17.

^kTwo models have $\overline{\Delta f}=0$ and are not represented: the reference one, and the one with levels $L[\mathfrak{N}] = 2$, $L[\mathbf{p}_{FE}] = 2$, $L\left[\frac{t_{FE}}{\lambda}\right] = 1$ and $L\left[\frac{t_{pml}}{\lambda}\right] = 2$.

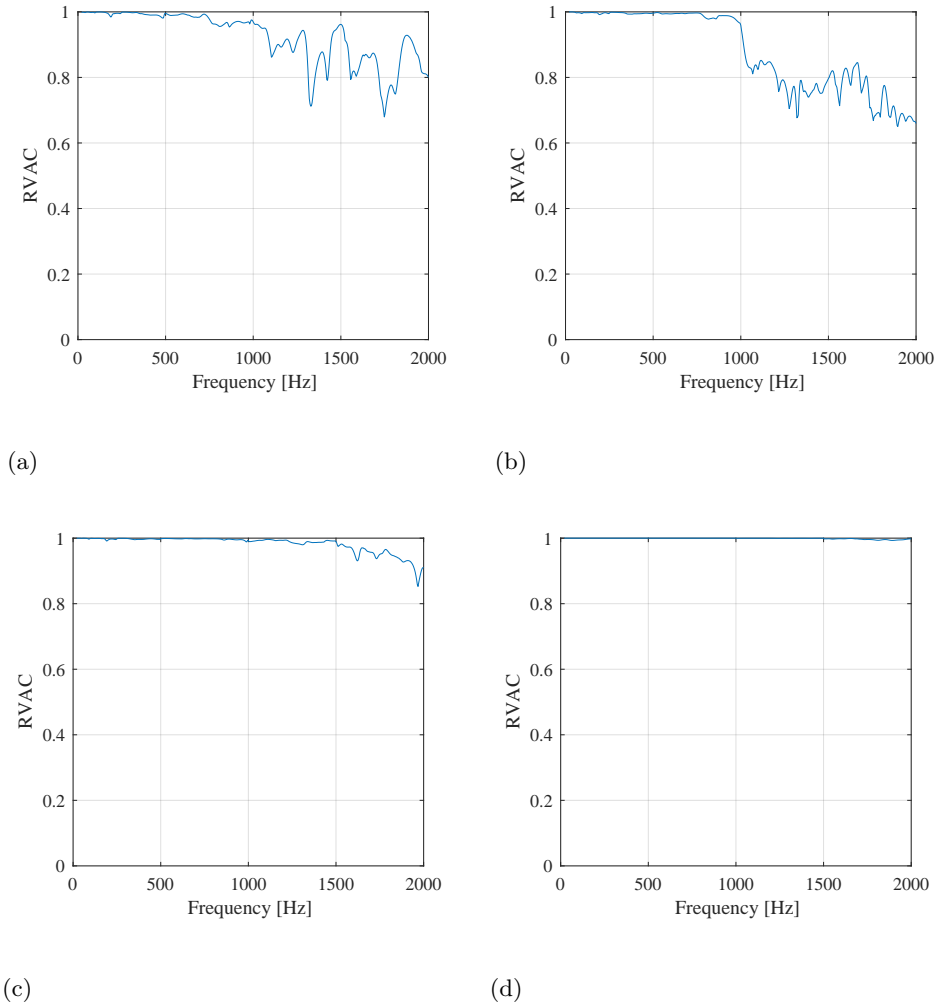


Figure 3.16: Examples of $RVAC$; model factor levels: $L[\mathfrak{N}] = 1$, $L[\mathfrak{p}_{FE}] = 1$, $L\left[\frac{t_{FE}}{\lambda}\right] = 1$ and $L\left[\frac{t_{pml}}{\lambda}\right] = 1$ (a), $L[\mathfrak{N}] = 1$, $L[\mathfrak{p}_{FE}] = 2$, $L\left[\frac{t_{FE}}{\lambda}\right] = 1$ and $L\left[\frac{t_{pml}}{\lambda}\right] = 1$ (b), $L[\mathfrak{N}] = 1$, $L[\mathfrak{p}_{FE}] = 2$, $L\left[\frac{t_{FE}}{\lambda}\right] = 1$ and $L\left[\frac{t_{pml}}{\lambda}\right] = 2$ (c), $L[\mathfrak{N}] = 2$, $L[\mathfrak{p}_{FE}] = 2$, $L\left[\frac{t_{FE}}{\lambda}\right] = 2$ and $L\left[\frac{t_{pml}}{\lambda}\right] = 1$ (d).

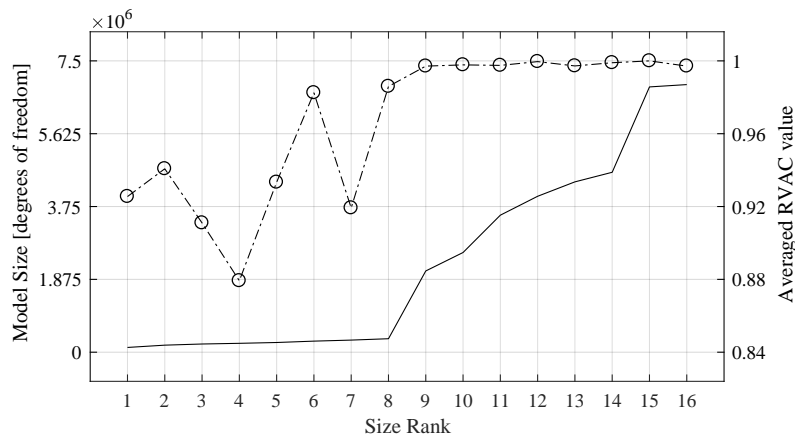


Figure 3.17: DoF (left axis) and \overline{RVAC} (right axis) in function of size rank in (a)

Figure 3.17 not only shows in a compact way the previous results, but also highlights a certain trend between the averaged \overline{RVAC} and model sizes. Not surprisingly, the eight biggest models are the ones with $L[\mathcal{N}] = 2$ and are the most accurate (\overline{RVAC} close to 1). However, Figure 3.17 is missing one key aspect: the $RVAC$ dependency on frequency as showed in Figure 3.16. To overcome this limit, Figure 3.18 shows four \overline{RVAC}_{band-i} calculated by averaging the vector $RVAC$ only in limited frequency bands i :

- 20-500 Hz, blue continuous line;
- 504-1000 Hz, blue dashed line;
- 1004-1500 Hz, red continuous line;
- 1504-2000 Hz, red dashed line.

Figure 3.17 shows how models with poor settings perform rather good at low frequencies, but their quality quickly decreases in higher area of the spectrum, despite the use of adaptation techniques.

A key takeaway is that all the discussed metrics¹ are coherent together, and therefore it makes sense to chose only one of them for further analysis. The choice is to make use of the \overline{RVAC} .

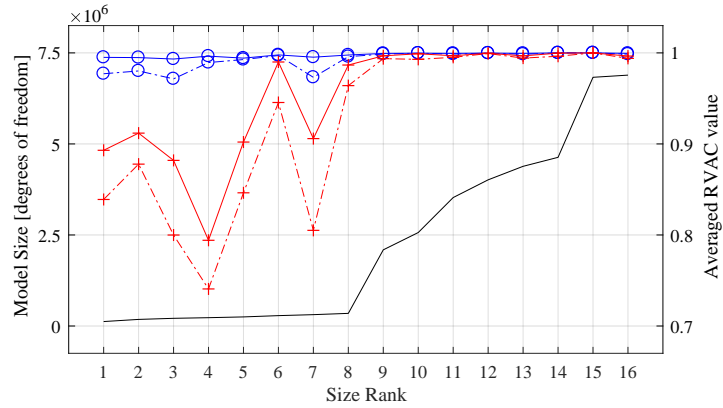


Figure 3.18: DoF (black continuous line, left axis) and \overline{RVAC}_{band-i} (right axis) averaged in four frequency bands (20-500 Hz: blue continuous line, circles; 504-1000 Hz: blue dashed line, circles; 1004-1500 Hz: red continuous line, crosses; 1504-2000 Hz: red dashed line, crosses) in function of size rank.

Local errors

The intrinsic advantage of the approach previously described lays in the ability to separate the part of the error coming from the frequency shift from the one associated to changes in shape of the spectrum. Furthermore, making use of global metrics, it gives useful insights about the behaviour of each model compared to the reference. However, that approach is independent of the levels of compared Transfer Functions. To account for these levels, an appropriate quadratic error between the amplitude of each TF and the reference TF is the best option. However, its computation is not straightforward. Indeed, at peaks and anti-peaks, a small frequency shift can lead to a very high error in absolute terms. A simple trick is to exploit the shifted transfer functions defined in Equation (3.3), recalled here for simplicity:

$$TF_s(f) = TF_i(f + \Delta f(f)).$$

¹That is, $RVAC$, \overline{RVAC} , \overline{RVAC}_{band-i} , Δf and $\overline{\Delta f}$.

The quadratic error on the amplitude is then calculated as:

$$\mathfrak{E}(f) = \frac{(|TF_i(f + \Delta f(f))| - |TF_{ref}(f)|)^2}{|TF_{ref}(f)|^2} = \frac{(|TF_s(f)| - |TF_{ref}(f)|)^2}{|TF_{ref}(f)|^2}. \quad (3.4)$$

As for the \overline{RVAC} , it is convenient to average the quadratic error in the full bandwidth for graphical representations. The new metric $\overline{\mathfrak{E}}$ is calculated as:

$$\overline{\mathfrak{E}} = \frac{\sum_{f=f_{min}}^{f_{max}} \mathfrak{E}(f)}{n_f}, \quad (3.5)$$

with f_{min} , f_{max} and n_f being, respectively, lowest frequency, highest frequency, and number of frequencies of each spectrum. For instance, Figure 3.19 shows the $\overline{\mathfrak{E}}$ as a function of \overline{RVAC} for four TPs: G-10 (blue), S-10 (red), G+20 (yellow) and S+20 (purple). This figure is interesting because it shows the relation between the two metrics. In particular, there is not a direct correspondence between the two; this fact shouldn't surprise, since the different purposes of the metrics (local vs. global). On the other hand, there is a certain trend for which poorer models produces less accurate TFs. This is a strong hint that both quadratic $\overline{\mathfrak{E}}$ and \overline{RVAC} are working properly. In the following, the two metrics will be considered (at a time, depending on the application) with the purpose to understand whether the local behaviour is predominant over the global one for perceptive objectives.

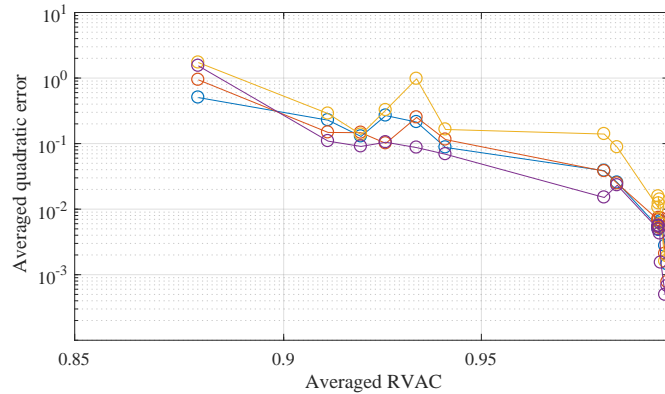


Figure 3.19: Averaged quadratic error $\overline{\mathfrak{E}}$ as a function of \overline{RVAC} for four TPs: G-10 (blue), S-10 (red), G+20 (yellow) and S+20 (purple).

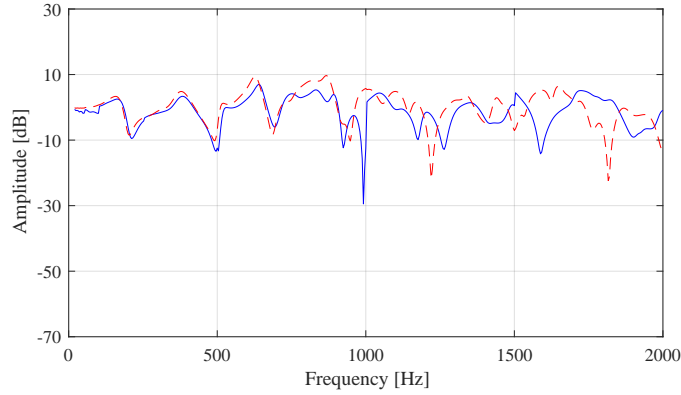
3.5 Acoustic metrics

The inaccuracies of TFs are only in part responsible for the errors of the auralized sound. The other, critical, component is the source signal, which is involved in the process via convolution. Figure 3.20 (a) shows two TFs associated to the TP G-11, the reference one (red dashed line) and the one calculated with the following levels (blue continuous line): $L[\mathfrak{N}] = 1$, $L[\mathfrak{p}_{FE}] = 1$, $L\left[\frac{t_{FE}}{\lambda}\right] = 2$ and $L\left[\frac{t_{pml}}{\lambda}\right] = 2$. Figure 3.20 (b) shows the spectra of the sound obtained via convolution with the source shown in Figure 3.9. These auralized sounds will be analyzed in the following using the acoustic metrics introduced in Section 3.3:

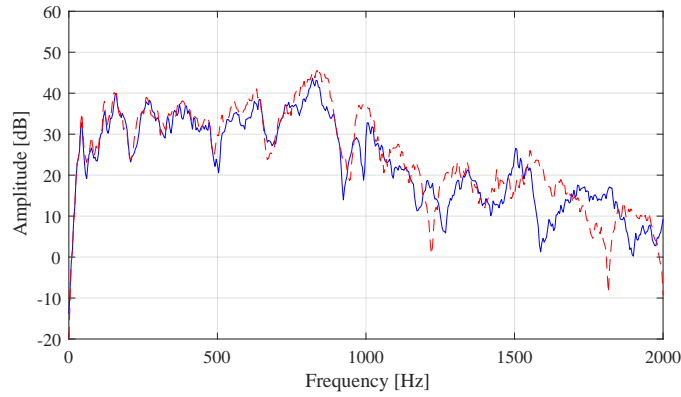
- (1) A-weighted sound pressure level SPL(A);
- (2) loudness N ;

(3) sharpness S .

Both N and S are calculated according to Zwicker [18].



(a)



(b)

Figure 3.20: Reference TF (red dashed line) and TF computed with levels (blue continuous blue line): $L[\mathfrak{N}] = 1$, $L[\mathfrak{p}_{FE}] = 1$, $L\left[\frac{t_{FE}}{\lambda}\right] = 2$ and $L\left[\frac{t_{pml}}{\lambda}\right] = 2$ in the case of TPs G-11 (a); spectra of the sounds auralized with these TFs in (b).

To understand the link between numerical accuracy and acoustic metrics, it is first fundamental to understand how much such metrics change with respect to the reference. The differences are estimated as:

- (1) ratios between each i -th model and the reference in the case of loudness and sharpness: $\Delta N_i = N_i/N_{ref}$, $\Delta S_i = S_i/S_{ref}$;
- (2) subtraction in the case of A-weighted sound pressure level: $\Delta \text{SPL}(A)_i = \text{SPL}(A)_i - \text{SPL}(A)_{ref}$.

Figure 3.21, Figure 3.22 and Figure 3.23 scatter, respectively, the so calculated $\Delta \text{SPL}(A)$, ΔN and ΔS as a function of the averaged quadratic error $\bar{\mathfrak{E}}$, in a semi-logarithmic scale. There are 240 points in each graph, one per every synthesized sound except for the reference. Colors and symbols refers to different levels of the factors:

- (1) circles, with $L[\mathfrak{N}] = 1$ and $L[\mathfrak{p}_{FE}] = 1$;

- (2) squares, with $L[\mathfrak{N}] = 1$ and $L[\mathfrak{p}_{FE}] = 2$;
- (3) hexagrams, with $L[\mathfrak{N}] = 2$ and $L[\mathfrak{p}_{FE}] = 1$;
- (4) diamonds, with $L[\mathfrak{N}] = 2$ and $L[\mathfrak{p}_{FE}] = 2$;
- (5) blue, with $L\left[\frac{t_{FE}}{\lambda}\right] = 1$ and $L\left[\frac{t_{PML}}{\lambda}\right] = 1$;
- (6) red, with $L\left[\frac{t_{FE}}{\lambda}\right] = 1$ and $L\left[\frac{t_{PML}}{\lambda}\right] = 2$;
- (7) green, with $L\left[\frac{t_{FE}}{\lambda}\right] = 2$ and $L\left[\frac{t_{PML}}{\lambda}\right] = 1$;
- (8) black, with $L\left[\frac{t_{FE}}{\lambda}\right] = 2$ and $L\left[\frac{t_{PML}}{\lambda}\right] = 2$.

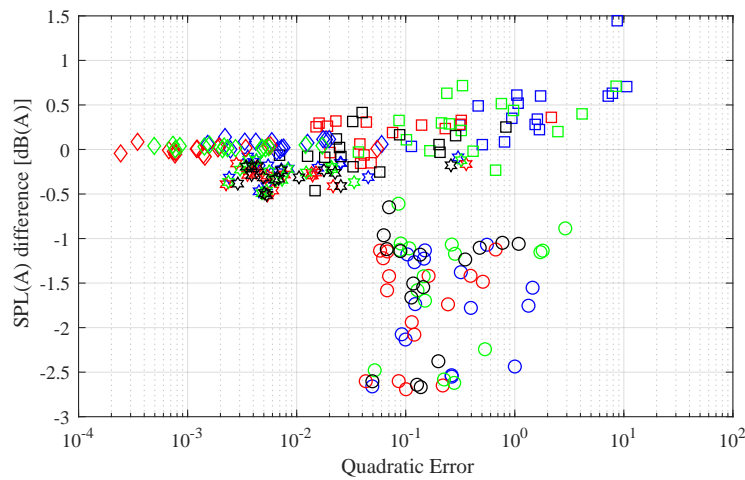


Figure 3.21: A-weighted sound pressure level difference $\Delta\text{SPL(A)}$ as a function of the averaged quadratic error $\overline{\mathfrak{E}}$, in a semi-logarithmic scale.

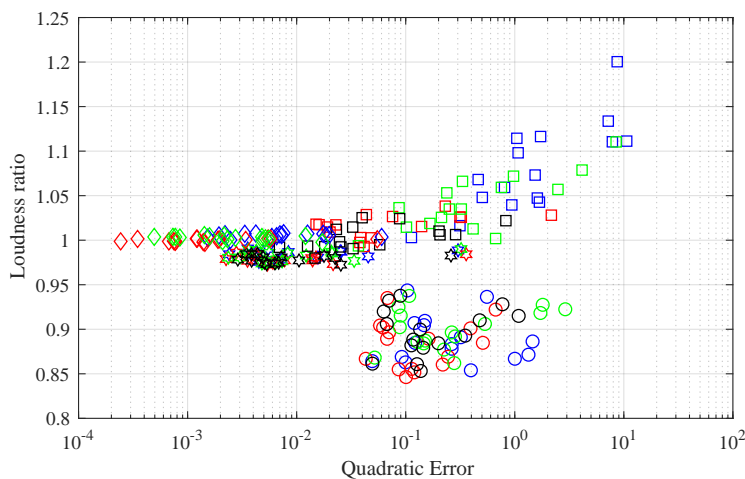


Figure 3.22: Loudness ratio ΔN as a function of the averaged quadratic error $\overline{\mathfrak{E}}$, in a semi-logarithmic scale.

Similar scatter graphs have been obtained by averaging the quadratic error in some selected reduced bandwidths (the same used in section 3.4.2 to calculate the different \overline{RVAC}), with

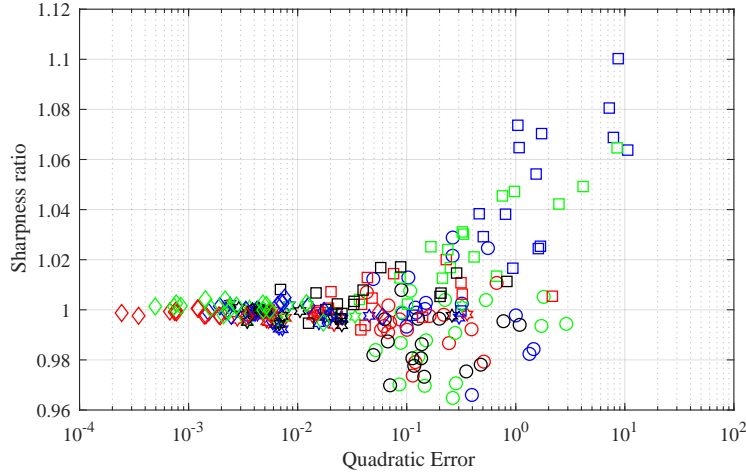


Figure 3.23: Sharpness ratio ΔS as a function of the averaged quadratic error $\bar{\mathcal{E}}$, in a semi-logarithmic scale.

comparable results. The figures show that high changes in acoustic metrics are linked to high quadratic errors. However, some sounds associated to high quadratic error may present a lower metric variation compared with other sounds associated to low quadratic error.

Shapes and colors provide other important clues. First of all, diamonds and hexagons ($L[\mathfrak{N}] = 2$) consistently constitute the group closest to the reference sounds. The ratios of these two groups are very low, as well as the error, except for some TPs. Models represented by circles ($L[\mathfrak{N}] = 1$, $L[\mathfrak{p}_{FE}] = 1$) perform worse than all other shapes in the case of SPL(A) and N . They also tend to have less energy than the reference sounds (they tend to have ratios lower than 1), on the contrary of squares ($L[\mathfrak{N}] = 1$, $L[\mathfrak{p}_{FE}] = 2$), which tend to have ratios higher than 1. Squares perform worst than all the other groups in the case of sharpness. In general, the energy of linear models is lower, as expected.

On the contrary, colors do not indicate strong patterns. Only blue and green ($L\left[\frac{t_{PML}}{\lambda}\right] = 0.6$) tend to locate at positions with higher errors and significant ratios in the case of $L[\mathfrak{p}_{FE}] = 2$, indicating a higher energy content of the sounds (for more details, see Appendix E). It is interesting that a lower PML thickness consistently increases the energy propagated via FW-H only for quadratic models. The interaction between PML and order of polynomial shape functions mentioned in the previous chapter is a possible explanation to this phenomenon (that adds to results of previous chapter). Lastly, no specific pattern related to the thickness of the FE volume could be identified.

Three critical points arise from to these scatter plots. First, high differences in metrics are strictly related to high $\bar{\mathcal{E}}$. Secondly, ratios and differences are relatively small; in the case of loudness, the difference between the reference and the sounds is often lower than the just noticeable difference, which is around 10% [18]. Lastly, several sounds have a relatively high error, but negligible psycho-acoustic metrics differences. Are the chosen acoustic metrics representing well enough the numerical error? Or are they missing something that human hearing system can actually perceive? A possible way to answer these questions is to perform jury tests, which are the topic of the next chapter.

The previous chapter showed how numerical parameters change the spectra of auralized sounds and, consequently, their acoustic metrics. However, acoustic metrics are only partially representative of sound perception, so that those results are not conclusive. In this context, jury tests provide a more exhaustive way to study sound perception. Jury test results can also be linked with acoustic metrics, bringing even more insights. Nonetheless, several procedures for jury tests exist, so the focus must be clear from the beginning.

In the present case, the main objective is to understand how humans perceive errors caused by FE simulations in auralized acoustic samples. Previous chapters already explained that the error is not quantifiable in absolute terms, which is why a reference numerical model has been used. Consequently, an efficient way to understand if and how much humans perceive these errors is by comparing each acoustic sample with the reference ones: in other words, by analysing perceptual similarities.

This chapter will first give an introduction to the jury test design, then will analyse the data gathered and, lastly, will provide in-depth statistical analysis to draw up insightful conclusions.

4.1 Design of the Tests

Commonly, industrial approaches for sound quality targets exploit jury tests to overcome the limits of acoustic metrics. In addition, the correlation between acoustic metrics and results of jury tests allows to find the dominant metrics and their threshold values for optimal engineering design, see Figure 4.1 [118].

A similar process can help understanding whether the local error $\bar{\epsilon}$ of Equation (3.5) is a better indicator than the \overline{RVAC} for sound quality purposes. Furthermore, it can estimate whether the metrics chosen in the previous chapter are significant. A lack of correlation would prove that $SPL(A)$, N and S are not the optimal choices, at least in some cases. Furthermore, a proper analysis of the jury tests' results can provide significant insights into the problem under observation.

A jury-test able to serve these purposes should respect some constraints with respect to the following points:

- (1) test preparation;
- (2) subjects;
- (3) listening environment and equipment;
- (4) test delivery;
- (5) sample selection.

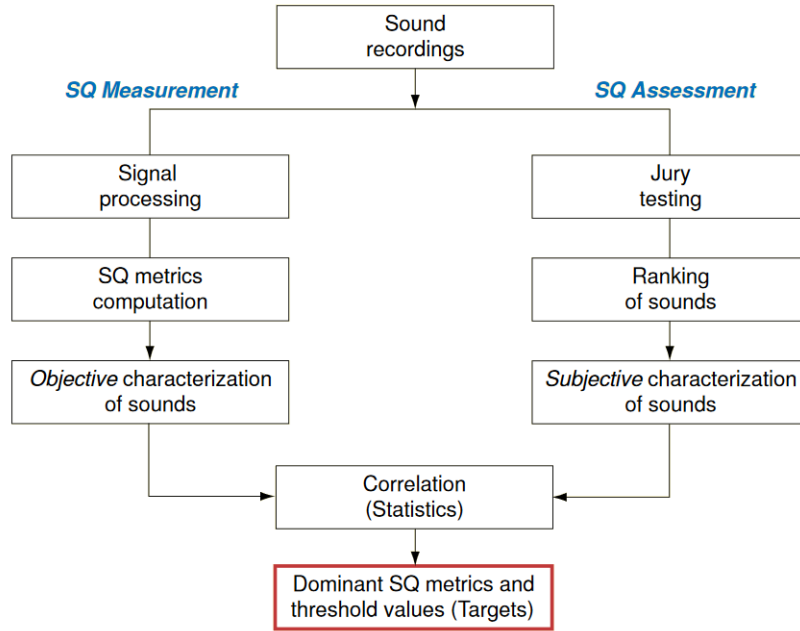


Figure 4.1: Sound quality (SQ) target development process [118].

Test preparation

Engineers used different kinds of procedure for sound quality evaluation, depending on their purposes; a review is available here [21]. Here, the natural choice is a paired comparison method since it permits the evaluation of similarities between sounds in a fast but efficient way. Specifically, given a TP, all the auralized sounds can be compared with the reference sound, which is auralized with the reference numerical model.

Subjects

This test does not require any peculiar skill. Also, the results of this research can be exploited virtually in any acoustic problem that involves simulation. Therefore, it is desirable to have untrained participants. In total, 18 people took part in this test, recruited among the university personnel. They included five females and thirteen males, ranging between 23 and 56 years, and represented six different nationalities: French, Italian, Chinese, Ghanaian, Chadian, Senegalese. Table 4.1 summarizes the data and shows each participant's IDs that will be used throughout this chapter.

ID	1	2	3	4	5	6	7	8	9	10	11	12	13	14	15	16	17	18
Gen. ¹	f	m	f	m	m	m	f	m	m	m	m	m	m	m	m	f	m	f
Age	30	27	27	28	23	26	23	34	56	23	37	32	26	26	26	25	29	25
Nat. ²	I	I	F	S	F	F	F	Gh	F	F	Ch	I	Ge	F	I	C	C	C

¹m=male, f=female.

²F=French, I=Italian, C=Chinese, Ch=Chadian, S=Senegalese, Gh=Ghanaian, Ge=German.

Table 4.1: Data of the participants: identification number (ID), gender (Gen.) age in years, and nationality (Nat.).

Listening environment and equipment

Sounds are presented over professional headphones for sound quality evaluation (Sennheiser HD 650). The listening environment was the sound-proof booth shown in Figure 4.2, which has a background noise of 25 dB(A). Participants can control the graphic interface (GI) of the test on a screen with a mouse.



Figure 4.2: Listening room where jury tests took place.

Sample selection

The sound samples are the ones described in the previous section. Each sound has a total duration of 3 seconds. To avoid excessive data-redundancy, only five transfer paths have been used for the jury tests. They have been selected to have a high variance of: metric and error variations, receivers, sources. To give an idea of the loudness and error variations, Figure 4.3 shows the loudness ratios calculated as in Section 3.5 for the chosen TPs:

- (1) G-11 (red circles);
- (2) G+10 (light blue asterisks);
- (3) S-21 (magenta plus signs);
- (4) S+11 (green crosses);
- (5) S+20 (blue diamonds).

In the abscissa, the averaged quadratic error $\bar{\mathcal{E}}$ of Equation (3.5).

Test delivery

Each participant was asked to compare, for each TP, the reference sounds with a set of sixteen sounds. The latter included all the auralized sounds for that TP, including the reference sound itself. Each sound was evaluated twice to collect data for repeatability analysis. Furthermore, the test comprised five different sections, between which the participant was allowed to take a break if needed; each session corresponded to the study of sounds associated with one TP.

The test was delivered to participants via the ad-hoc graphic interface in Figure 4.4. By clicking on the button “(re)écouter”, (french for re-listening), they could listen to a pair of sounds lasting 3 s and separated by a pause of 1 s. The pair consisted of the reference sound for the given TP and one of the other 32 sounds to evaluate. The participant could listen to a pair of sounds as many times as desired. The task was to move the horizontal scroll bar between

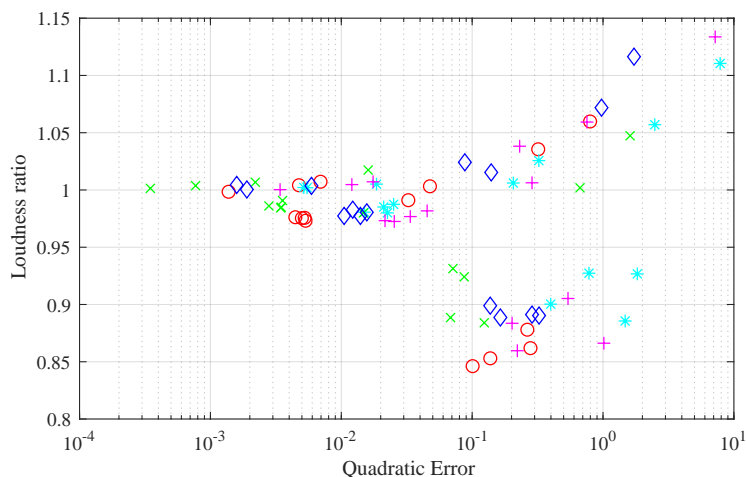


Figure 4.3: Loudness ratio ΔN of the TPs used for jury tests: G-11 (red circles), G+10 (light blue asterisks), S-21 (magenta plus signs), S+11 (green crosses), S+20 (blue diamonds); in the abscissa, the averaged quadratic error $\bar{\mathcal{E}}$ of Equation (3.5).

“très similaires” (very similar) and “très différents” (very different). The resulting score was converted into a real value between 0 (“très similaires”) and 10 (“très différents”). Thereafter, the participant could click on the button “suivant” (next).

The sounds were proposed in random order; this choice avoided that participants’ evaluations could be influenced by sounds gradually different from the reference.

This kind of tests often requires a training phase. Namely, participants are allowed to listen to very similar sounds and very different ones, with the purpose to get an idea of what to expect during the test [21]. However, in the proposed test, there are five different sessions, and each would require a training portion; the time consumption required for these training could alter the comfort of participants, affecting the results of the test. The solution was to launch the test without any training. The researcher responsible for the test informed the participants that there was the reference itself among the sounds to compare (thus, giving an idea of when using the “very similar” rating).

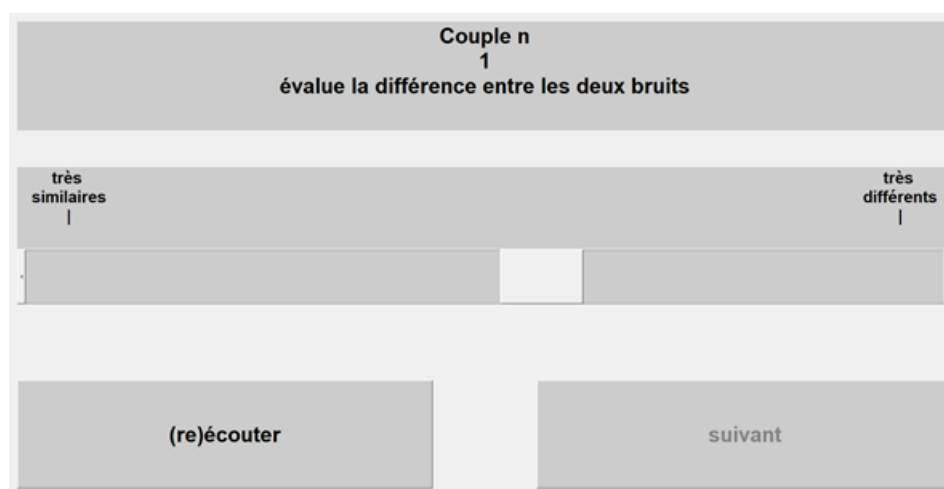


Figure 4.4: Graphic interface of the jury test.

4.2 Data processing

Data analysis for these kinds of tests is relatively standardized in terms of statistical tool to use. However, the case under study introduces a critical aspect. Since all the sounds come from the same TPs, and differences between TPs are not extreme, participants have to compare sounds that are, by nature, relatively similar. The difficulty of the test has been reported by all participants when asked to comment on the test itself.

A key aspect of analyzing is repeatability, which can be easily done since each sound has been scored twice. An l^1 norm perfectly serves this scope. Specifically, for each participant p , the following repeatability index \mathfrak{J}_p is defined:

$$\mathfrak{J}_p = \frac{1}{n} \sum_{i=1}^n |a_{1i,q} - a_{2i,q}| \quad (4.1)$$

in which $a_{1i,q}$ and $a_{2i,q}$ are the two similarity scores assigned to the i -th sample by the participant q , and $n = 16$ is the total number of different sounds used in each test. This index has values $0 < \mathfrak{J}_p < 10$, with 0 meaning that each sound has always obtained the same score, and 10 representing the maximum variation (each sound has been scored once 0 and once 10). The minimum \mathfrak{J}_p has been 0.0446, while the maximum 4.1853, with most values between 1 and 3. Figure 4.5 shows the repeatability index \mathfrak{J}_p for each participants and for each TPs; TP G-11 is in black circles, TP S-21 is in dark blue plus signes, TP G+10 is in red asterisks, TP S+11 is in magenta crosses and TP S+20 is in light blue squares. Usually, in jury test analysis, repeatability is considered satisfactory if it is lower than two (on a 0-10 scale [21]), but this value needs to take into account the complexity of the test. In the performed test case, many participants exceed the threshold of 2, indicating that they faced significant difficulties. Interestingly, participants 8 and 9 consistently outperformed all the others; however, the subsequent analysis will explain that these two participants are not more precise than the others: instead, they are more conservative.

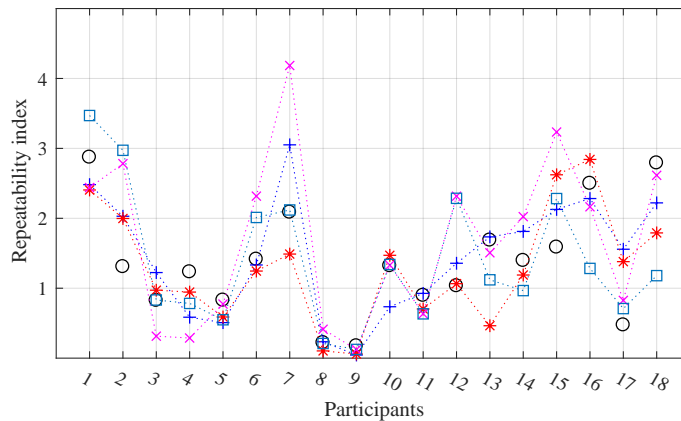


Figure 4.5: Repeatability of each participant; ; TP G-11 is in black circles, TP S-21 is in dark blue plus signes, TP G+10 is in red asterisks, TP S+11 is in magenta crosses and TP S+20 is in light blue squares.

Figure 4.6 (a) and (b) are two boxplots referring, respectively, to TPs G-11 and S+11, showing the entire range of similarity scores used by participants. On each box, the central red mark indicates the median, and the blue box contains all values between the 25th and 75th percentiles, respectively. The whiskers extend to the most extreme data points not considered outliers, the latter being plotted individually using the red plus symbols. It is clear from these data that participants used different scales to evaluate the similarities between sounds. Surprisingly, some

participants never used the minimum score, meaning that they did not recognize the equal sounds. This data reflects the difficulty of the test. It is worth noticing that participants 8 and 9 used a similar scale, much limited with respect to other people: this is the reason why their repeatability index \mathcal{J}_p is lower than the others in Figure 4.5.

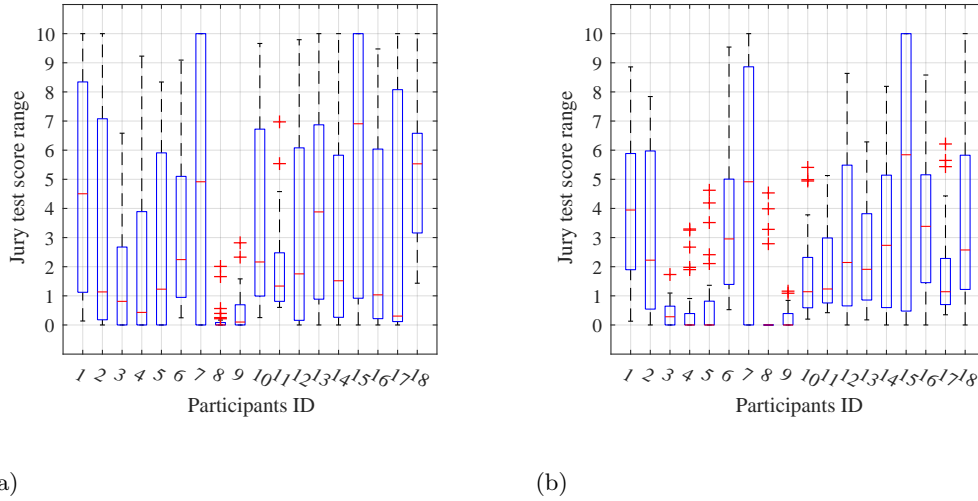


Figure 4.6: Box plots showing the entire range of jury test scores used by participants in the case of TPs G-11 (a) and S+11 (b).

At this point, each pair of similarity scores $a_{1i,q}$ and $a_{2i,q}$ was substituted by its average $a_{i,q} = (a_{1i,q} + a_{2i,q})/2$. Then, data are standardized^a according to the following transformation:

$$a_{i,q} = \frac{a_{i,q} - \bar{a}_q}{\sigma_q}, \quad (4.2)$$

where \bar{a}_q is the average of all the $a_{i,q}$ across the five TPs and σ_q is the associated standard deviation; the standardized data are from now on called center-reduced. Then, data consistency has been checked, exploiting the correlation matrices plotted in Figure 4.7. It is shown that participant 18 is always uncorrelated (or slightly negatively correlated) to the others, except in the case of TP G-11. Because of this reason, this participant has been removed from the following analysis (this subject may have misinterpreted the graphic interface of the test and assigned high scores to similar sounds). Besides participant 18, there is only one other case of negative correlation between participant 8 and 16 in the test on the G+10 TP: they have a correlation of -6.45%.

^aThis operation is the same to modify a *normal* distribution into a *standard normal* one.

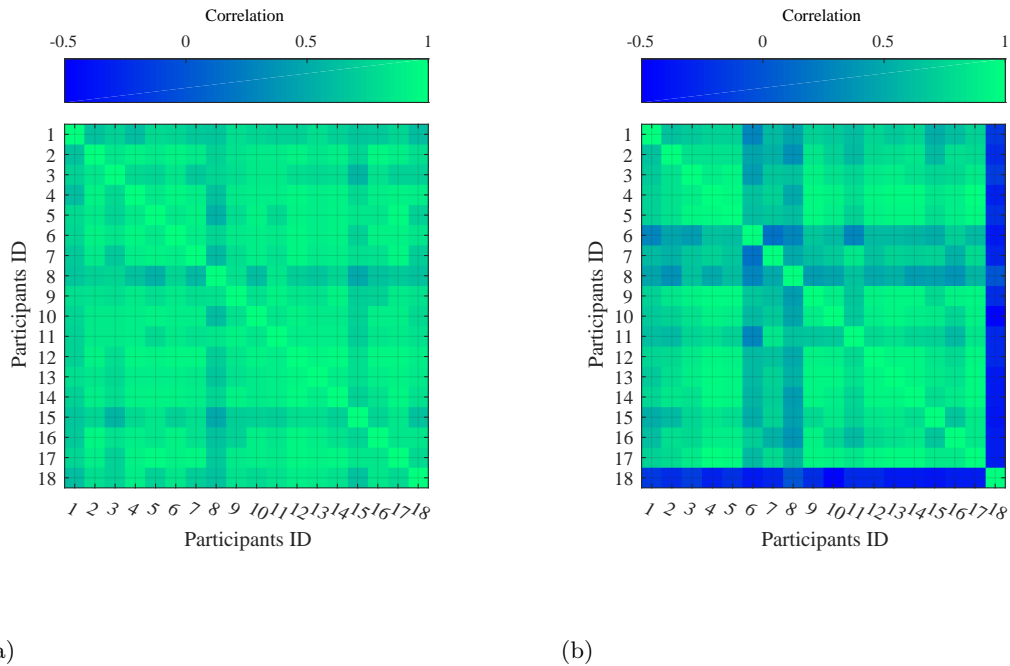


Figure 4.7: Correlation matrix in the case of TPs G-11 (a) and S+20 (b); participant 18 performed in all the other cases as in S+20.

Lastly, it is interesting to check whether a group of participants could be consistently clustered together across the different test; if yes, it would make sense to analyze it separately. Dendrograms have been computed to answer this question. Specifically, Ward algorithm [119] based on euclidean distances has been used to cluster participants. Interestingly, according to this criterion, the groups formed in the tests relative to the five TPs under analysis are always different; in other words, a specific group of participants did not appear, and data can be analyzed altogether.

4.3 Acoustic analysis

4.3.1 Univariate ANOVA

Given that no specific cluster could be identified, it is natural to analyze the aggregate data altogether. In the studied case, each transfer path represents a variable, each participant an observation. A comprehensive framework to serve these needs is the analysis of variance (ANOVA). The ANOVA requires stringent hypothesis [120]:

- (1) independence of observations;
- (2) normal distribution of observations on the dependent variable in each group;
- (3) homogeneity of variance (co-variance matrix), also called homoscedasticity.

However, the robustness of ANOVA to non-normality and heteroscedasticity (namely, inhomogeneous variance) has been subject of research for a long time. Recent results focused, among others, on skewness and kurtosis [121] to discuss normality, and on variance ratio (which is the ratio of the largest variance to the smallest of the groups, [122]) to discuss homoscedasticity. In general, limits for the variance ratio of 1.5, for the skewness of 2 and for the kurtosis of 6 are accepted [120]. There is not a uniform agreement on more extreme cases, but scientists

regularly use these tools anyway. If these hypotheses are not satisfied, other approaches coming from non-parametric statistics are preferable, such as the Kruskal-Wallis test [123]. However, non-parametric approaches have the limits of losing all the quantitative part of the information, being based only on ranks; for this reason, they are not considered in the following analysis.

Here, skewness and kurtosis reached levels higher than the recommended ones, depending on the considered subset. In details, if the data associated with a model and a TP had a critically high value of kurtosis (>6), the same was true for skewness (>2), and vice versa. Six datasets (each associated with a numerical model) reached such critical values: two models in the case of the TP G-11, one in the case of TP S-21, two in the case of TP G+10, zero in the case of TP S+11 and one in the case of TP S+20. Even variance ratio did not satisfy the previously mentioned limits, being higher than 1.5.

Therefore, only the independence of observations is considered satisfied (although biases could be present due to the limited number of participants). However, given the small amount of subsets that do not satisfy the above mentioned criteria, the total dataset is considered sufficiently close to a normal one to perform an univariate ANOVA with multiple factors is performed. Besides the four numerical parameters used in the last chapter (that is, \mathfrak{N} , \mathfrak{p}_{FE} , $\frac{t_{PML}}{\lambda}$, and $\frac{t_{FE}}{\lambda}$), also the TPs are considered as factors, bringing the total number to five. Two-factor interactions are considered as well. For each of the five factors and for each interaction, the H_1 hypothesis is that the factor or the interaction itself affects the perception of auralized sounds. Given the low number of participants, the H_0 hypothesis is rejected with a p -value of 1%

Before discussing the results, it is useful to have a reference in order to better understand the quantitative part of the analysis; therefore, the center-reduced data are box plotted in Figure 4.8. The dataset include all the five TPs, and shows that the reduced scale ranges between -1.7 and 3 except for six outliers (valued respectively 3.05, 4.94, 3.02, 6.47, 3.3, and 3.45). Lower values are always associated with acoustic samples similar to the reference.

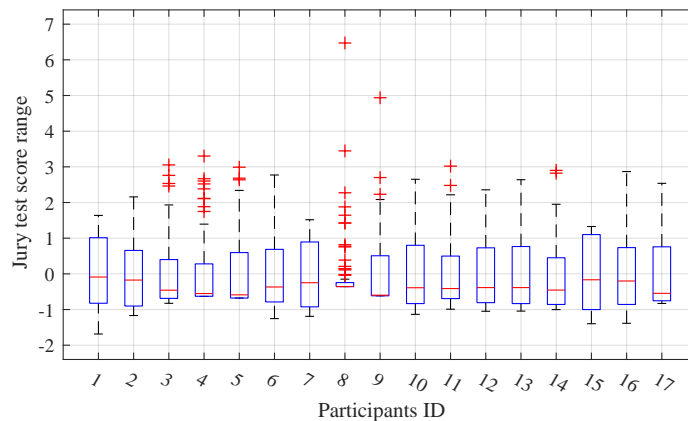


Figure 4.8: Box-plots of the reduced centered data.

The following subsection focuses on the first-order analysis (that is, the effects of each factor one by one), while the subsequent one analyses the cross-interactions.

Main effects

Table 4.2 shows the p -values associated to each factor. Interestingly, TPs play a critical role in this test. A quantitative analysis will provide more details later on. Regarding numerical parameters, they play a role in accordance with theory. The indices \mathfrak{N} , \mathfrak{p}_{FE} , and $\frac{t_{PML}}{\lambda}$ are

important contributing factor since the p -value is almost zero. On the other hand, $\frac{t_{FE}}{\lambda}$ seems not to play any role.

FACTOR	TP	$[\mathfrak{N} = \frac{\lambda}{\text{hp}_{FE}}]$	$[\mathfrak{p}_{FE}]$	$[\frac{t_{FE}}{\lambda}]$	$[\frac{t_{PML}}{\lambda}]$
p -value	0	0	0	0.017	0

Table 4.2: ANOVA test results for the five considered factors: p -values.

Figure 4.9 shows the effects of the four factors that proved to affect perception; the error-bars represent the standard error^b. The TPs, in Figure 4.9 (a), with lower values are associated with acoustic samples ranked more similarly to the reference. In other words, simulation of the TPs with lower values produced more similar sounds in terms of acoustic perception, even with poor meshes; these TPs are called here *low-score* TPs. On the other hand, *high-score* TPs produced sounds more different from the reference with poor meshes.

The parameter \mathfrak{N} , in Figure 4.9 (b), produced the biggest difference in terms of jury test score: it is by far the most critical parameter, at least in this frequency range. The other two parameters, \mathfrak{p}_{FE} and $\frac{t_{PML}}{\lambda}$, respectively Figure 4.9 (c) and (d), also impacted significantly the perception, but not quite as much as \mathfrak{N} . Given the frequency range tested and the levels used, these results confirm the theory discussed in Chapter 2.

Two-factor interactions

Table 4.3 shows p -values for cross-interactions.

INTERACTION	TP* $[\mathfrak{N}]$	TP* $[\mathfrak{p}_{FE}]$	TP* $[\frac{t_{FE}}{\lambda}]$	TP* $[\frac{t_{PML}}{\lambda}]$
p -value	0	0	0.560	0

INTERACTION	$[\mathfrak{N}]^*[\mathfrak{p}_{FE}]$	$[\mathfrak{N}]^*[\frac{t_{FE}}{\lambda}]$	$[\mathfrak{N}]^*[\frac{t_{PML}}{\lambda}]$
p -value	0	0.060	0

INTERACTION	$[\mathfrak{p}_{FE}]^*[\frac{t_{FE}}{\lambda}]$	$[\mathfrak{p}_{FE}]^*[\frac{t_{PML}}{\lambda}]$	$[\frac{t_{FE}}{\lambda}]^*[\frac{t_{PML}}{\lambda}]$
p -value	0.012	0	0.012

Table 4.3: ANOVA test results for the five considered factors: p -values.

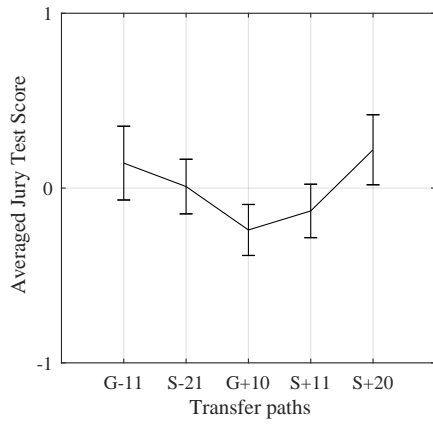
It resulted that TPs interacted strongly with all other meaningful factors. This fact does not surprise: in *low-score* TPs, level 1 of numerical factors did not affect perception as much as in *high-score* TPs. This is a further confirmation of what find in the previous subsection.

About numerical parameters, there have been strong interactions between all of them, with the exception of $\frac{t_{FE}}{\lambda}$. The pollution effect likely drives the cross-interaction between \mathfrak{N} and \mathfrak{p}_{FE} : with roughly the same number of degrees of freedom per wavelength, \mathfrak{p}_{FE} becomes the determinant factor for accuracy at higher frequency in low-accuracy models. Since the maximum frequency is only relatively high, it is also expected to notice this effect weakly. Figure 4.10 (a) graphically shows these effects: the continuous blue line corresponds to $L[\mathfrak{p}_{FE}] = 1$ (higher in

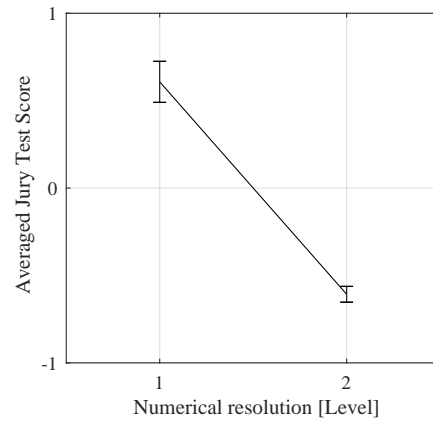
^bThe standard error has been calculated for a two-tailed distribution with 15 degrees of freedom and a p -value of 0.01 (thus $t_{0.995}(15) = 2.947$) as:

$$err = \frac{\sigma}{\sqrt{n-1}} t_{0.995}(15),$$

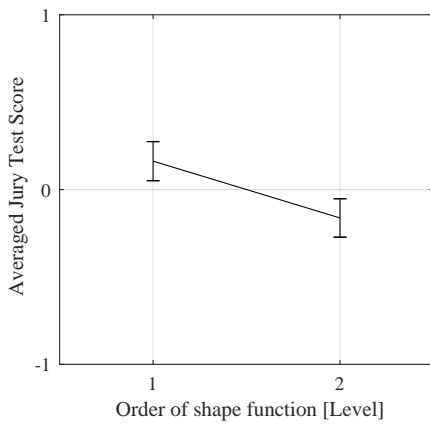
where n is the sample size and σ is the standard deviation.



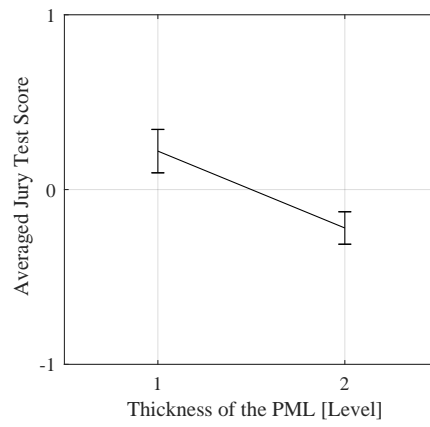
(a)



(b)



(c)



(d)

Figure 4.9: Effects of TPs (a), numerical resolution \mathfrak{N} (b), order of shape function \mathfrak{p}_{FE} (c) and PML thickness $\frac{t_{PML}}{\lambda}$ as a function of the level of the factors; the vertical bars represent standard errors.

terms of jury test score, that is, more different from the reference) and the red dashed line corresponds to $L[\mathfrak{p}_{FE}] = 2$. The figures clearly show that for high-accuracy models ($L[\mathfrak{N}]=2$) \mathfrak{p}_{FE} is less critical^c.

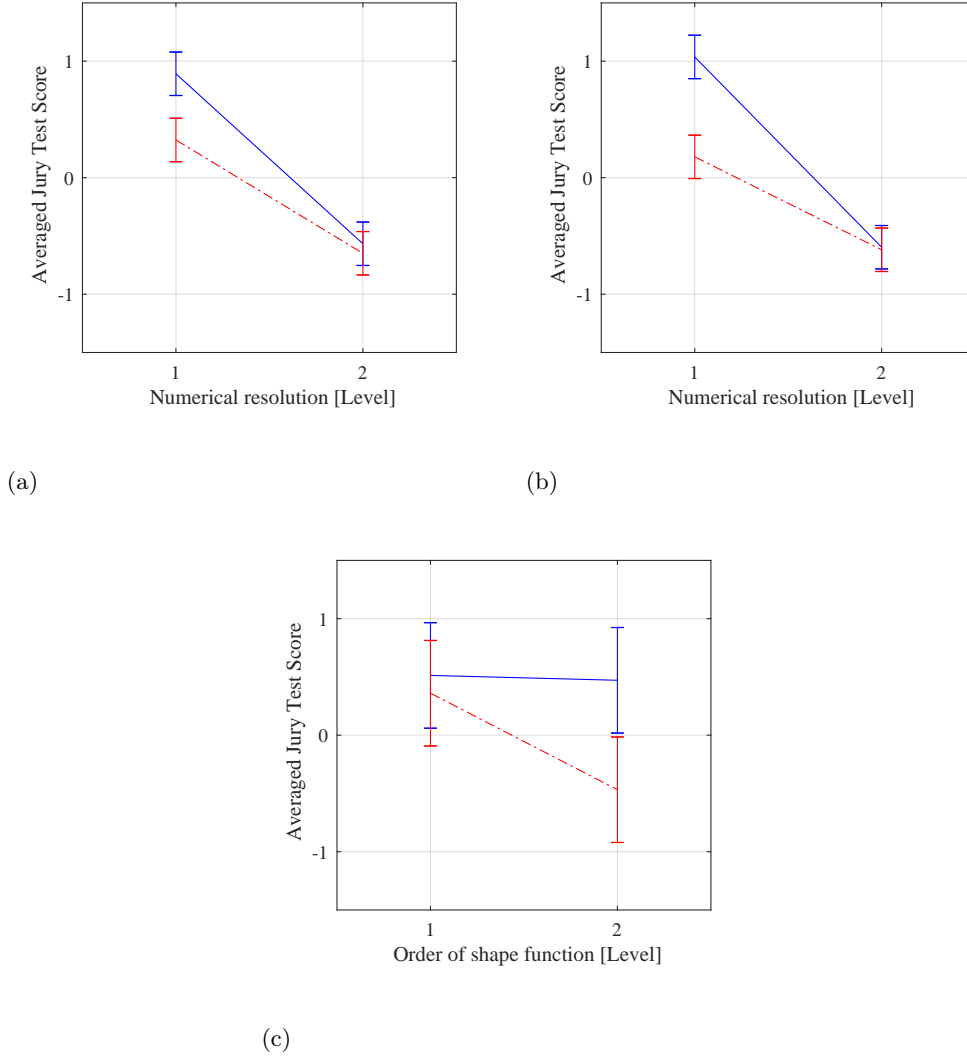


Figure 4.10: Two-factor interactions between numerical resolution \mathfrak{N} and \mathfrak{p}_{FE} (a), \mathfrak{N} and $\frac{t_{PML}}{\lambda}$ (b), and \mathfrak{p}_{FE} and $\frac{t_{PML}}{\lambda}$ (c); blue continuous line: $L[factor] = 1$; red dashed line: $L[factor] = 2$.

Figure 4.10 (b) and (c) show the cross-interactions involving $\frac{t_{PML}}{\lambda}$ with, respectively, \mathfrak{N} and \mathfrak{p}_{FE} ; blue lines are associated to $L\left[\frac{t_{PML}}{\lambda}\right] = 1$, red lines with $L\left[\frac{t_{PML}}{\lambda}\right] = 2$. Figure 4.10 (b) shows that, at high value of \mathfrak{N} , $\frac{t_{PML}}{\lambda}$ does not play any role. In other words, if the error introduced by $\frac{t_{PML}}{\lambda}$ is perceived, it is significant only in case of poor simulations. Figure 4.10 (c) shows that, at high value of \mathfrak{p}_{FE} , $\frac{t_{PML}}{\lambda}$ is important. A deep analysis shows that sounds with $L[\mathfrak{p}_{FE}] = 2$, $L\left[\frac{t_{PML}}{\lambda}\right] = 2$ with worst similarity scores have obtained via models with $L[\mathfrak{N}] = 1$, and are therefore sub-optimal. This cross-interaction has been related to the two groups (1) and (2) individuated in Section 3.4.2, page 90.

^cDue to the nature of the pollution effects, which depends on the dispersive nature of the FEM, at higher frequencies \mathfrak{p}_{FE} is expected to become more important, except for extremely fine meshes that would make the simulation time prohibitively long.

Three-factor interactions: $[\mathfrak{N}] * [\mathfrak{p}_{FE}] * \left[\frac{t_{PML}}{\lambda} \right]$

The interactions involving \mathfrak{N} , \mathfrak{p}_{FE} , and $\frac{t_{PML}}{\lambda}$ are expected, and reflect the results of the numerical experiments in Section 2.5.1. Since these three parameters interact together (see Section 3.4.2, it makes sense to study their three-factor interaction in order to understand if the jury tests provide extra pieces of information^d.

First of all, by referring to Figure 4.11 and Figures 3.21 to 3.23, it is useful to consider four subsets of models separately:

- (1) models with $L[\mathfrak{N}] = 1$ and $L[\mathfrak{p}_{FE}] = 1$ (blue continuous line), with $SPL(A)$, N and S consistently lower than the reference;
- (2) models with $L[\mathfrak{N}] = 2$ and $L[\mathfrak{p}_{FE}] = 1$ (red dash-dot line), with $SPL(A)$, N and S slightly lower than the reference;
- (3) models with $L[\mathfrak{N}] = 1$ and $L[\mathfrak{p}_{FE}] = 2$ (magenta dashed line), with $SPL(A)$, N and S consistently higher than the reference;
- (4) models with $L[\mathfrak{N}] = 2$ and $L[\mathfrak{p}_{FE}] = 2$ (black dotted line), with $SPL(A)$, N and S similar to the reference.

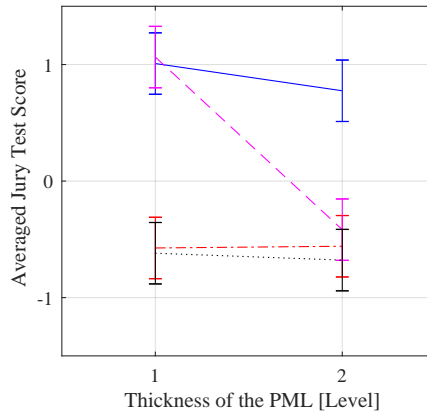


Figure 4.11: Three-factor interactions between \mathfrak{N} , \mathfrak{p}_{FE} and $\frac{t_{PML}}{\lambda}$.

Subset (1), in blue, comprises the least accurate simulations. Recalling Tables E.1 to E.3, in this case, a reduced thickness of the PML resulted in an increased $SPL(A)$ 53% of the times, N 62% of the times, and S 78% of the times. As a result, it is not unsurprising that the factor $\frac{t_{PML}}{\lambda}$ does not played a critical role in the jury tests for this subset.

Subsets (2) and (4), respectively in red and black, comprises the finest simulations in terms of number of nodes per wavelength. In these two cases, a reduced thickness of the PML resulted in an increased $SPL(A)$ 95% of the times, N 97% of the times, and S 70% of the times. However, in both cases the increase (or decrease) of the metrics were negligible (always lower than 0.2db(A) for $SPL(A)$, and lower than 1% for N and S). Again, it comes with no surprise that the factor $\frac{t_{PML}}{\lambda}$ does not played a critical role in the jury tests for these subset.

^dThe three-factor interactions have not been considered for the calculation of the p -values in Table 4.2 and Table 4.3. Indeed, given the relatively high number of factors considered in this analysis, the p -values associated with each factor and interaction would result very close to zero in the case of a three-factors ANOVA, providing no clues.

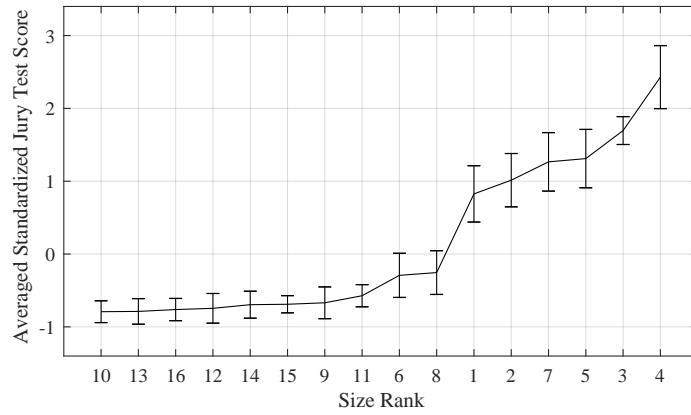
Subset (3), in magenta, comprises the simulations for which the increase of the metrics was the most substantial. First of all, in this case, a reduced thickness of the PML resulted in an increased SPL(A) 100% of the times, N 97% of the times, and S 94% of the times. The more consistent change towards higher energy spectra, and the higher degree of increase, partially explain the influence of factor $\frac{t_{PML}}{\lambda}$ in the jury tests' results for this subset. However, the increased energy alone does not explain the importance of this parameter. It is likely that the change in shape of the spectra, reflected by the low \overline{RVAC} , played a more crucial role. From a numerical perspective, this interaction is likely driven by the different size of the PML elements in the case of quadratic and linear models (see Section 2.5.1)

4.3.2 Post-hoc analysis and grouping

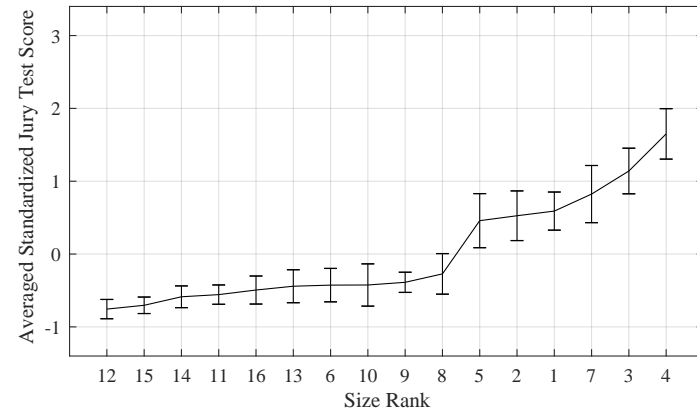
A posthoc analysis based on the Bonferroni test reveals that it is possible to define statistically separate groups in four out of the five tested TPs with a p -value of 1%^e: Figure 4.12 show these four cases, that is, TPs G-11 (a), S-21 (b), G+10 (c), and S+20 (d); the jury test scores are in the ordinate axis, the size ranks (see Table 3.5) in the abscissa. Models are in ascending order based on the jury test score, and the error-bars represent the standard error. Figure 4.13 shows the case of the TP S+11, where it was not possible to isolate statistically different groups.

It is interesting to notice that the worst six models (in terms of similarity perception) are the same across the five TPs. Due to their consistently poor performances, these six acoustic samples are considered to be “different” from the reference in terms of auditory perception. Table 4.4 shows the models that produced such samples and their performances.

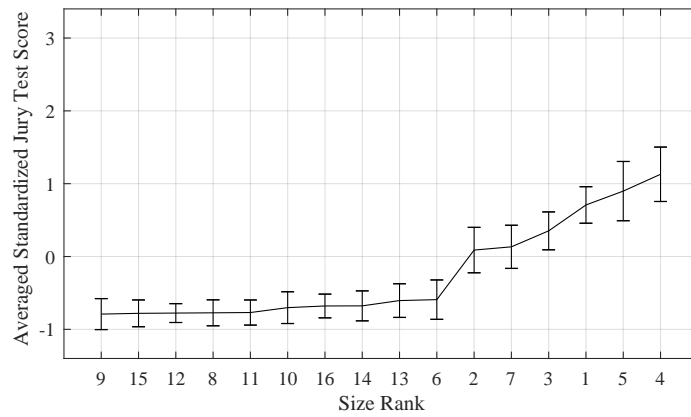
^eA Tukey-Kramer test gave the same results.



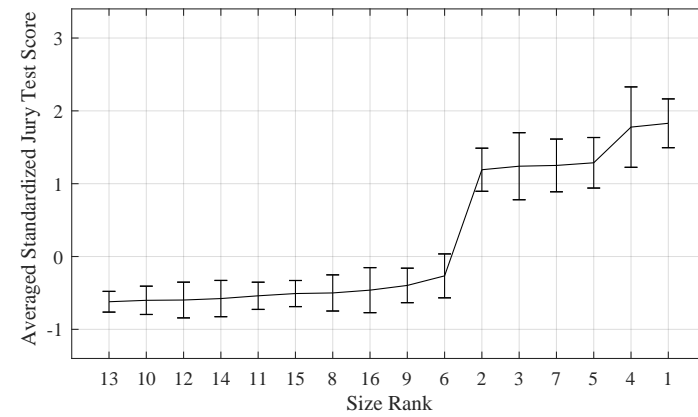
(a)



(b)



(c)



(d)

Figure 4.12: Jury test score with standard errors in the cases of TPs G-11 (a), S-21 (b), G+10 (c), and S+20 (d); size ranks in the abscissa.

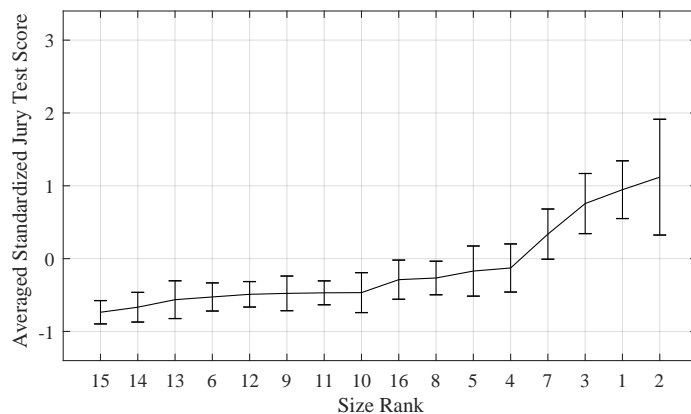


Figure 4.13: Jury test score with standard errors in the case of TP S+11; size ranks in the abscissa.

Size rank	Model				Jury test rank				
	$L[\mathfrak{N}]$	$L[\mathfrak{p}_{FE}]$	$L\left[\frac{t_{FE}}{\lambda}\right]$	$L\left[\frac{t_{PML}}{\lambda}\right]$	G-11	S-21	G+10	S+11	S+02
1	1	1	1	1	11	13	14	15	16
2	1	1	1	2	12	12	11	16	11
3	1	1	2	1	15	15	13	14	12
7	1	1	2	2	13	14	12	13	13
4	1	2	1	1	16	16	16	12	15
5	1	2	2	1	14	11	15	11	14

Table 4.4: Models producing sounds different from the reference ones.

4.4 Linking perception and simulation

4.4.1 Perception vs. numerical errors

At this point, it is critical to understand if there is any relation between numerical errors and perception. Figure 4.14 shows the averaged standardized jury test score in black for the TP S+02 (left y -axis) together with its error (vertical bars) and the averaged quadratic error $\bar{\mathfrak{E}}$ in blue (left y -axis) for each numerical model; the models are identified by their size rank on the x -axis (see Table 3.5) and are ascendingly ordered based on the jury test score. There is not a clear correspondence between the quadratic error $\bar{\mathfrak{E}}$ and the jury test score; however, it is clear that after a specific threshold sounds are perceived differently from the reference: this threshold is indicated with a horizontal black dashed line.

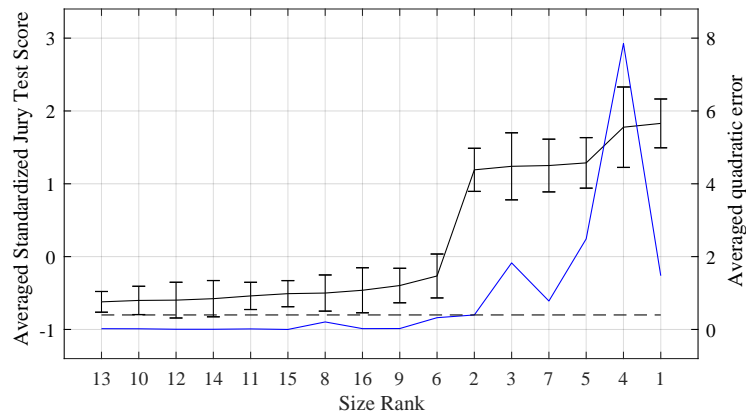


Figure 4.14: Jury test score, in black (left axis), and error $\bar{\mathcal{E}}$, in blue (right axis), in the case of TP S+20; standard errors in the vertical bars, size ranks (see Table 3.5) in the abscissa.

It is useful to compare these results with the ones of another TP. Figure 4.15 show results for the Transfer Path S+11, which is the Transfer Path with fewer sounds statistically different from the reference (it is recalled here the size-rank of the reference model: 15). Some hints can be derived similarly to the above case:

- (1) The same six models occupy the last six positions on the left, but in a different order.
- (2) Again, there is not a clear correspondence between the quadratic error $\bar{\mathcal{E}}$ and the jury test score; a threshold is indicated with a horizontal black dashed line even in this case, but its value is different from the previous case.
- (3) Interestingly, the two sounds obtained with the worst Transfer Functions (in terms of $\bar{\mathcal{E}}$) are not ranked the worst in terms of similarity. Even more interesting, these sounds are not statistically different from the reference one.

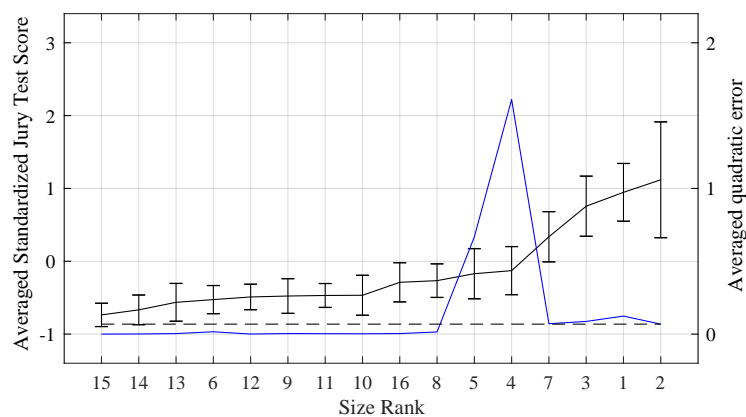


Figure 4.15: Jury test score, in black (left axis), and error $\bar{\mathcal{E}}$, in blue (right axis), in the case of TP S+11 standard errors in the vertical bars, size ranks (see Table 3.5) in the abscissa.

The same plots have been created with the use of other metrics instead of the error $\bar{\mathcal{E}}$:

- (1) a metric obtained by removing the denominator in Equation (3.4) at page 99;

- (2) another one obtained by averaging the absolute value of the differences between two spectra in dB.

Even with these metrics, it was not possible to identify any threshold between the sounds most similar to the reference and the six most difference. On the other hand, the \overline{RVAC} does not change depending on the TPs, and it can be used to identify the worst six sounds with a threshold. Figure 4.16 is a copy of Figure 4.15 showing the \overline{RVAC} (in red) instead of the quadratic error. The worst six models have $\overline{RVAC} \leq 0.94$.

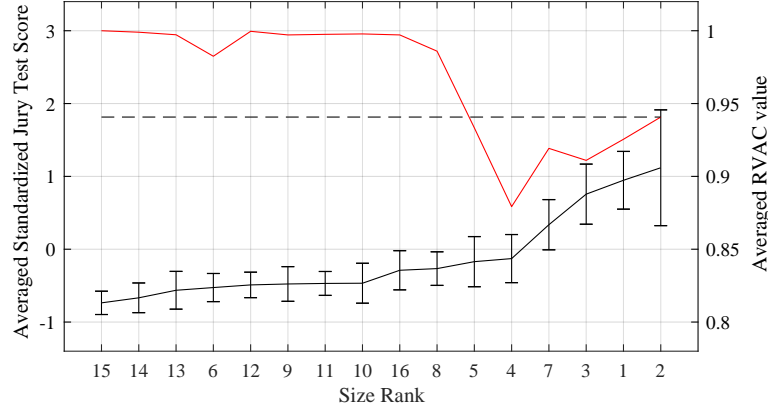


Figure 4.16: Jury test score, in black (left axis), and \overline{RVAC} , in red (right axis), in the case of TP S+11; standard errors in the vertical bars, size ranks (see Table 3.5) in the abscissa.

At this point, there are two contrasting results: on the one hand, six sounds are consistently ranked the worst; on the other hand, they are not statistically different from the reference. However, because of the complexity of the test and the non-normal dataset, statistical results should be taken as hints. By taking into account such context, it can be suggested that models with a low \overline{RVAC} (in this case, lower than 0.94) produce sounds that are perceived differently from the reference since they are consistently ranked the worst, even if in a different order. At the same time, models with high \overline{RVAC} (in this case, higher than 0.98), are perceived very similarly since they are always ranked the best, but in a different order. If a similarity threshold for the \overline{RVAC} exists, it should be between 0.98 and 0.94. Furthermore, the LSD errors and the statistical distance between sounds can be interpreted as a strong signal of the difficulty faced by participants: it can therefore be said that, although people could distinguish sounds auralized from models with low \overline{RVAC} , the differences are not so evident.

A final remark concerns the source: results showed here are valid only in the case of broadband noises. Indeed, as shown in Chapter 3, the most significant differences in terms of TFs are in the high-frequency region; furthermore, participants reported that the most important differences were relative to high frequencies. Therefore, if the band of the source does not adequately cover this area, results would significantly differ: sounds would probably not be distinguishable anymore since the $RVAC$ is considerably good at low frequencies.

4.4.2 Criteria used by participants to distinguish noise samples

At this point, it is clear that participants could distinguish at least some noise samples, although with varying degrees of difficulties. A last critical step is to understand which criteria participants used to distinguish the samples and if these criteria were different among the five

Tps or were always the same. As a first step, the following distances are defined:

$$\begin{aligned}
 d_{\text{SPL(A)}}(s) &= |\text{SPL(A)}_s - \text{SPL(A)}_{ref}|, \\
 d_N(s) &= \frac{\max(N_s, N_{ref})}{\min(N_s, N_{ref})}, \\
 d_S(s) &= \frac{\max(S_s, S_{ref})}{\min(S_s, S_{ref})},
 \end{aligned} \tag{4.3}$$

where s identify the signal and the subscript ref identify the reference. These distances and the perceived score are plotted on a graph to study eventual trends. It turned out that no single acoustic metric can represent the perception behaviour; graphs are not reported to avoid redundancy. Because of that, two methodologies have been tested: a linear regression approach and a dichotomic clustering tree, both providing interesting results.

Linear regression

No single metric proved to correlate well with jury test results. On the other hand, a linear combination of N and S can reproduce the perception quite satisfyingly. Such regression has been calculated separately for each TP, using the entire set of data available, with a least square regression. The lowest value for the correlation was 93%. However, the coefficients for the regression calculated for different TPs were not similar. For this reason, a different approach has been used: a single dataset was built, comprising all the data. A least-square linear regression was then performed. In this case, correlation ρ in the case of each TP was calculated, giving the following values: 0.92 for the TP G-11, 0.98 for the TP S-21, 0.76 for the TP G+10, 0.94 for the TP S+11, and 0.92 for the TP S+02; the correlation calculated over the entire dataset was 0.88. The coefficient of the linear regression were 24,61 (multiplicative factor of the loudness distance), 50,9 (multiplicative factor of the sharpness distance) and -74,52 (intercept term).

Figure 4.17 shows the test results as a function of the predictive model. If the model was perfect, all the points would lie on the bisector (dashed black line in the graph). In the picture, colors and symbols identify the TPs: S+20 in blue diamonds, G-11 in red circles, S-21 in magenta plus signs, G+10 in light blue asterisks, S+11 in green crosses. The figure shows that the points are not uniformly distributed:

- (1) many points appear in the bottom-left corner, at low values of the score;
- (2) a significant amount of points appear in the center of the graph, at medium values of the score;
- (3) only few points appear in other areas.

Figure 4.17 suggests that the three points in the top-right corner (blue diamond, magenta plus and red cross) may impact significantly the correlation of the model with the dataset. The correlation has been recalculated after rejecting these three points, resulting in 0.84. This value for the correlation is a strong index of the model's robustness.

The regressive model has a satisfying capacity to explain the jury test scores and proved to be robust. In other words, people used a combination of N and S to distinguish the noise samples. The combination of these two acoustic metrics appear to retain quite well the differences in terms of amplitude and frequency shift introduced by the numerical errors.

Dichotomic tree

This approach is simpler than the previous one. By comparing the values of the distances (Equation (4.3)), it is shown that all the acoustic signals ranked in the six worst positions during

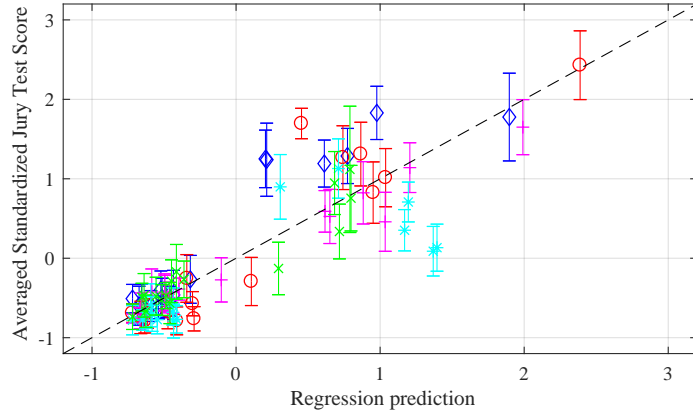


Figure 4.17: Jury test scores vs. predictive model: S+20 in blue diamonds, G-11 in red circles, S-21 in magenta plus signs, G+10 in light blue asterisks, S+11 in green crosses.

jury tests satisfy at least one of the following requirement:

$$\begin{aligned}
 (a) \quad & d_N(s) > 1.07, \\
 (b) \quad & d_S(s) > 1.03, \\
 (c) \quad & d_N(s) > 1.04 \quad \& \quad d_S > 1.02.
 \end{aligned}
 \tag{4.4}$$

No other signals satisfied any of these requirements. This model explicates a dichotomy: if a signal satisfies one of the conditions 4.4 is different from the reference, otherwise its differences are not well perceivable.

4.4.3 Specific loudness and timber features

Up to now, results have proved that the frequency dependency of the numerical error has a crucial role in perception; in fact, sharpness is essential in both the linear regression and the dichotomic tree. Therefore, it is helpful to study the specific loudness as a function of critical bands (see Table 2.1), which reflects the way people perceive energy as a function of frequencies.

Figure 4.18 shows the specific loudness in (a) and (b) of the sounds auralized, respectively, with factor levels $L[\mathfrak{N}] = 1$, $L[\mathfrak{p}_{FE}] = 1$, $L\left[\frac{t_{FE}}{\lambda}\right] = 2$ and $L\left[\frac{t_{pml}}{\lambda}\right] = 2$ and $L[\mathfrak{N}] = 1$, $L[\mathfrak{p}_{FE}] = 1$, $L\left[\frac{t_{FE}}{\lambda}\right] = 1$ and $L\left[\frac{t_{pml}}{\lambda}\right] = 2$ (blue continuous line) vs. the reference (dashed red line), and their spectra in (c) and (d), for the TP G-11. These two sounds belong to the group of sounds very similar to the reference, as the spectra and the specific loudness show.

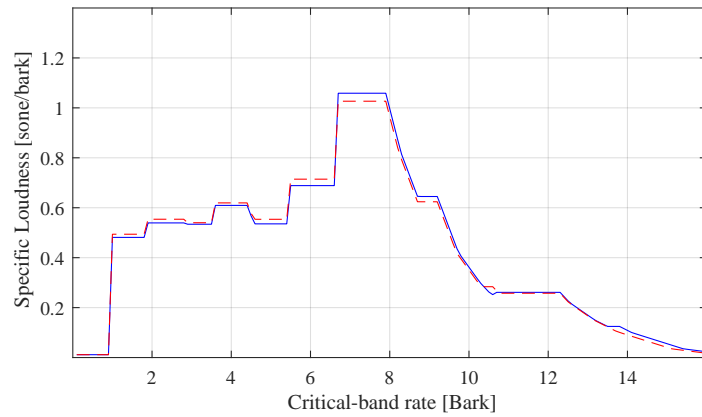
Figure 4.19 shows the specific loudness in (a) and (b) of the sounds auralized, respectively, with factor levels $L[\mathfrak{N}] = 1$, $L[\mathfrak{p}_{FE}] = 1$, $L\left[\frac{t_{FE}}{\lambda}\right] = 2$ and $L\left[\frac{t_{pml}}{\lambda}\right] = 1$ and $L[\mathfrak{N}] = 1$, $L[\mathfrak{p}_{FE}] = 1$, $L\left[\frac{t_{FE}}{\lambda}\right] = 1$ and $L\left[\frac{t_{pml}}{\lambda}\right] = 1$ (blue continuous line) vs. the reference (dashed red line), and their spectra in (c) and (d), for the TP G-11. These two sounds belong to the group of sounds different from the reference. Here, the differences in terms of both specific loudness and spectra are more marked. The specific loudness is constantly greater in the higher part of the spectrum, as reflected by the jury tests. These two models are indeed responsible for the good correlation with sharpness in the linear model of the previous section. Interestingly, from the analysis of the previous four sounds, a lower thickness of the FE volume tends to increase the specific loudness and, therefore, the loudness. However, this relation is found to be true roughly 43% of the

times in the auralized sounds^f. Consequently, the thickness of the FE volume does not affect the properties of the spectrum in a specific way; however, the different meshes lead to different results, especially in coarse discretization.

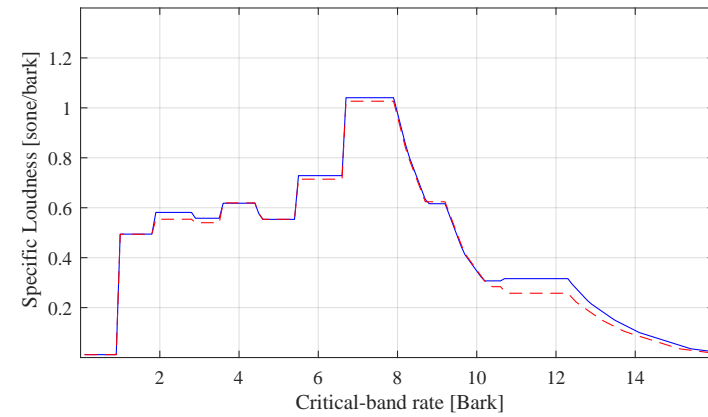
Figure 4.20 shows the specific loudness for the sound auralized with factor levels $L[\mathfrak{N}] = 1$, $L[\mathfrak{p}_{FE}] = 1$, $L\left[\frac{t_{FE}}{\lambda}\right] = 2$, and $L\left[\frac{t_{pml}}{\lambda}\right] = 1$, TP G-11. This sounds belong as well to the group of samples different from the reference. In this case the specific loudness is almost constantly lower than in the reference sound. Similar specific loudness distributions are obtained with $L[\mathfrak{N}] = 1$, $L[\mathfrak{p}_{FE}] = 1$, but different levels for the other two parameters. These four models explain the importance of N highlighted in the previous section.

Similar conclusions come by analyzing the other TPs.

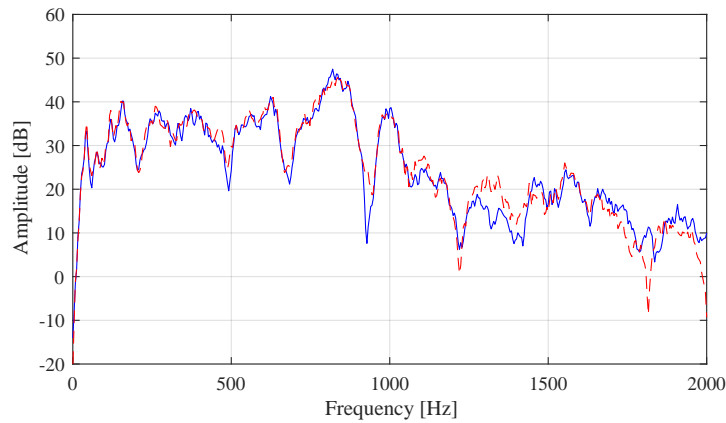
^fThe analysis has been carried out by taking into account all the 256 acoustic samples; if only the acoustic samples used for the jury tests are considered, a lower thickness of the FE volume leads to an increased loudness 45% of the times, a very close result.



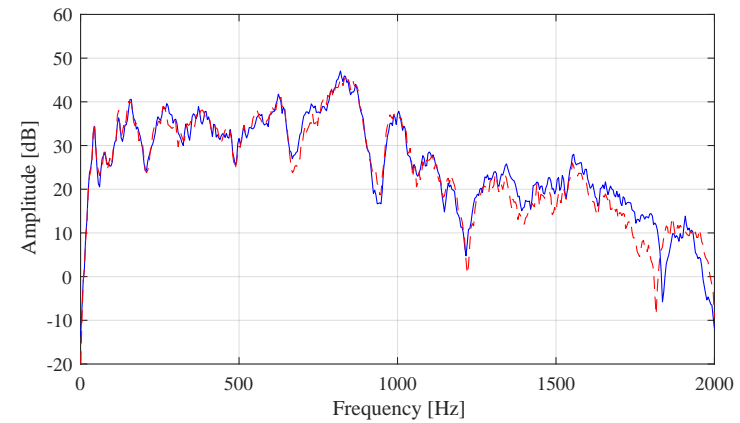
(a)



(b)

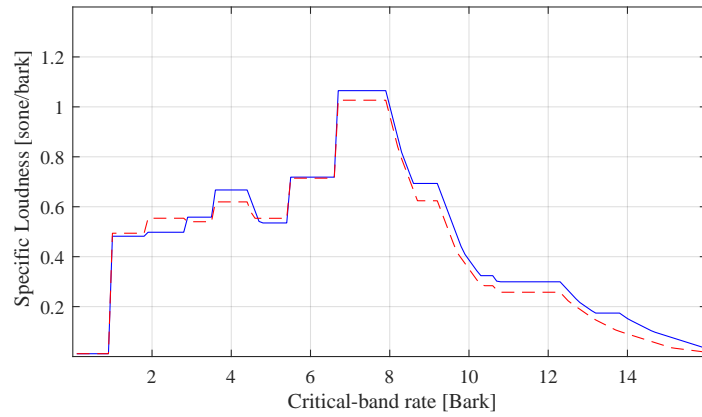


(c)

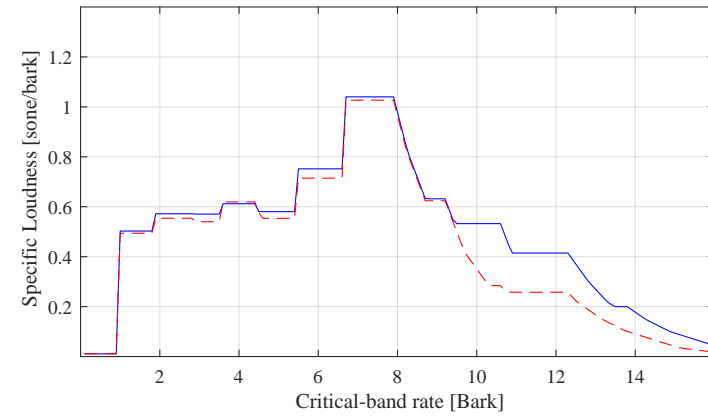


(d)

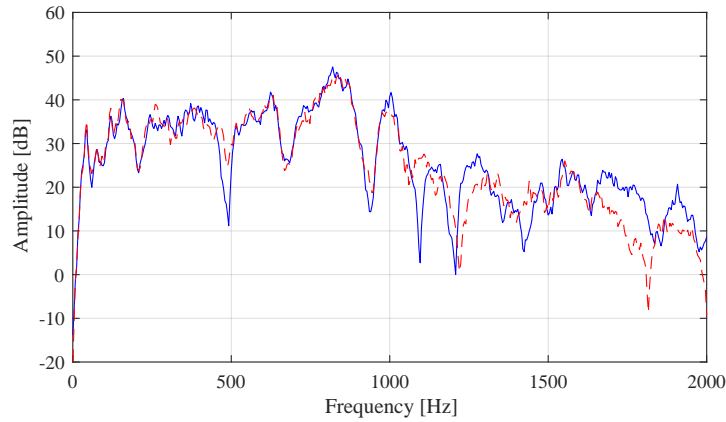
Figure 4.18: Specific loudness (a and b) and spectra (c and d), of the sounds auralized with TP G-11 and factor levels, respectively, $L[\alpha] = 1$, $L[p_{FE}] = 2$, $L\left[\frac{t_{FE}}{\lambda}\right] = 2$ and $L\left[\frac{t_{pml}}{\lambda}\right] = 2$ and $L[\alpha] = 1$, $L[p_{FE}] = 2$, $L\left[\frac{t_{FE}}{\lambda}\right] = 1$ and $L\left[\frac{t_{pml}}{\lambda}\right] = 2$ (blue continuous line) vs. the reference (dashed red line).



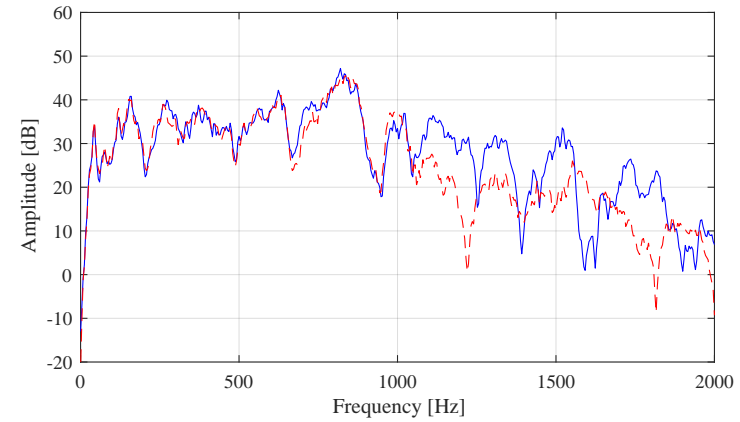
(a)



(b)



(c)



(d)

Figure 4.19: Specific loudness (a and b) and spectra (c and d), of the sounds auralized with TP G-11 and factor levels, respectively, $L[\alpha] = 1$, $L[p_{FE}] = 2$, $L\left[\frac{t_{FE}}{\lambda}\right] = 2$ and $L\left[\frac{t_{pml}}{\lambda}\right] = 1$ and $L[\alpha] = 1$, $L[p_{FE}] = 2$, $L\left[\frac{t_{FE}}{\lambda}\right] = 1$ and $L\left[\frac{t_{pml}}{\lambda}\right] = 1$ (blue continuous line) vs. the reference (dashed red line).

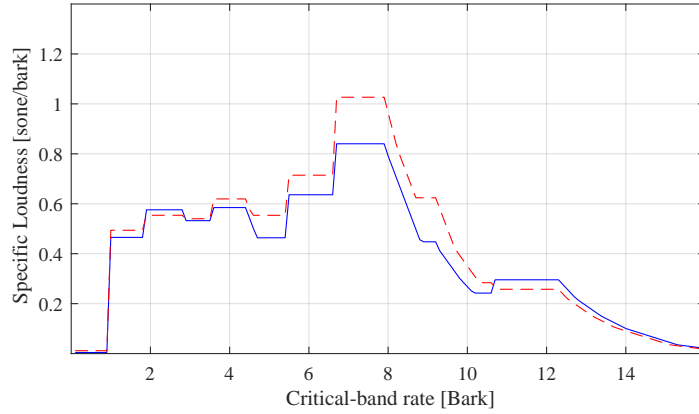


Figure 4.20: Specific loudness and spectrum of the sound auralized with factor levels $L[\mathfrak{N}] = 1$, $L[\mathfrak{p}_{FE}] = 1$, $L\left[\frac{t_{FE}}{\lambda}\right] = 2$, and $L\left[\frac{t_{pml}}{\lambda}\right] = 1$, TP G-11.

4.4.4 From numerical errors to perception: a summary

This chapter showed that humans are sensitive to the numerical error introduced by the FEM. Specifically, the following errors occur and are perceived:

- (1) approximation error, which causes a change of shape in the spectrum of the simulated TF (because it causes an error in the amplitude);
- (2) pollution error, which causes a frequency shift and, possibly, a change in the shape of the simulated spectrum;
- (3) interactions between PML and FE size and order of interpolation, which causes a severe change in the shape of the simulated spectrum.

Error (1) is mainly a consequence of the numerical resolution \mathfrak{N} and, in part, of the order of shape functions \mathfrak{p}_{FE} . Error (2) is mainly a consequence of the order of shape functions \mathfrak{p}_{FE} and, in part, of the numerical resolution \mathfrak{N} . Error (3) depends on the interaction between the two latter parameters and the thickness of the PML t_{PML} . Jury tests result proved that, unsurprisingly, the perception of these errors depends on the TPs. Indeed, the FE error is by nature erratic, especially at low nodal resolution [67]. Furthermore, the theory introduced in this thesis is based on upper limits for the approximation, and pollution error [66, 67, 73], and these limits are based on a global analysis: in other words, the precision of the method can vary locally.

Other errors occur but have not been perceived:

- (1) different thickness and shapes of the FE volume cause changes in the simulated spectrum, but in a random way and only in the case of coarse meshes; furthermore, given the results of the jury tests, these changes are not significant;
- (2) lower thicknesses of the PML tend to increase the energy of the simulated spectrum, as by theory, but in the performed tests, these increases have been lower than the just noticeable differences (for the loudness), except at low nodal resolution.

General Conclusions and Perspectives

5.1 From numerical errors to human perception - overview of the process

At this point, results are sufficient to define the process that goes from setting proper numerical parameters to sound perception. Figure 5.1 schematizes such process, and each step is described in the following paragraphs.

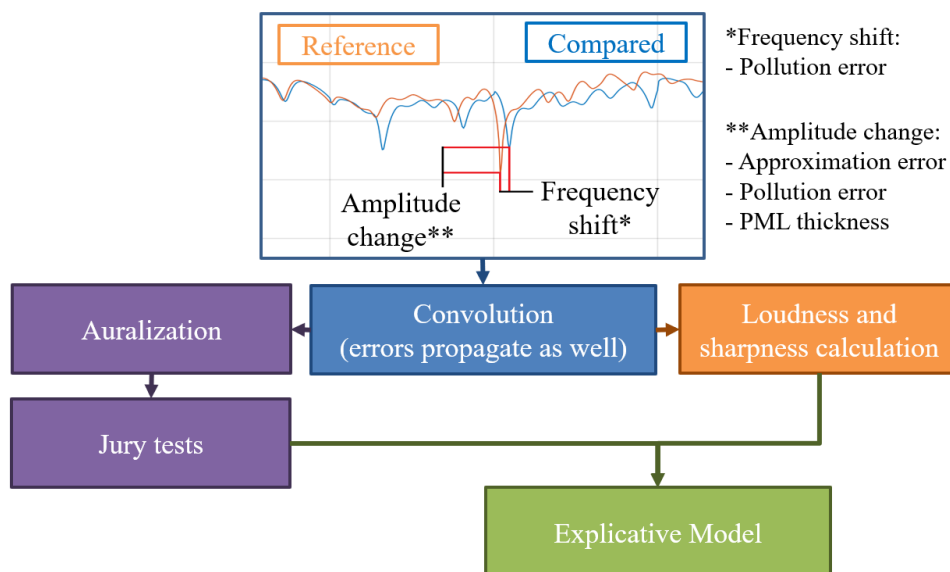


Figure 5.1: The process going from setting proper numerical parameters to sound perception.

Production of the digital acoustic signal (blue boxes)

First of all, engineers or technicians need to appropriately choose the numerical parameters of a simulation. The choices affect the quality of the simulated TFs in two ways:

- (1) by causing a frequency shift;
- (2) by changing the amplitude.

Figure 5.1 indicates these two errors^a.

^aThe points chosen in Figure 5.1 are convenient for visualization, but are not significant from a psycho-acoustic point of view.

The main responsible for the frequency shift is the pollution error. Such error is primarily dependant on numerical resolution \mathfrak{N} and order of polynomial shape functions \mathfrak{p}_{FE} . On the other hand, there are several drivers that play a key role in changing the amplitude: approximation error (caused by low \mathfrak{N}^b), reflection error (caused by thin PML) and pollution error as well. In general, the following considerations have been found or confirmed:

- (1) The PML interacts with the parameters responsible for FEM accuracy (\mathfrak{N} and \mathfrak{p}_{FE}). At high accuracy, a decrease of up to 40% PML thickness was not perceivable, while the same decrease was noticed in coarse models with $\mathfrak{p}_{FE} = 2$.
- (2) Approximation errors is more important at low frequencies, while pollution error become more dominant as far as frequency increases.

The change in amplitude brought by pollution error does not seem to affect massively the overall energy level of the simulated spectrum. Indeed, the pollution error does not modify the amplitude of the acoustic rays reaching a point \tilde{P} in the space, but only their phase (see 2.3.2). Consequently, depending on how many rays hit \tilde{P} , this error can result in:

- (a) a phase delay (only one ray hitting \tilde{P});
- (b) a frequency shift (two rays hitting \tilde{P});
- (c) a dominant frequency shift combined with an amplitude changes (several rays hitting \tilde{P}).

In (a) and (b) there is no change in amplitude and, therefore, in the energy level of the spectrum. In the case of (c), because the amplitude of the hitting rays is not affected by pollution error^c, the total variation of the spectrum energy is, for the practical scenario considered here, limited. It is speculated that such a conclusion holds true for other scenarios of practical interest.

Because of convolution, these two errors propagate to the acoustic signal of interest. The result is a signal with an energetic distribution of the spectra different from the exact solution of the partial differential equation approximated by the simulation.

Human perception (purple)

Jury tests based on the auralized sounds show that people can perceive these errors. In the studied case, the task of perceiving such errors was very hard, even if, at high frequency, the differences were important. Statistical analysis confirmed this trend.

Acoustic metrics (orange box)

Acoustic metrics such as loudness and sharpness reflect the changes caused by numerical errors, because they rely on the energetic distribution of the spectra, which is clearly affected by the errors.

Explicative models (green box)

Explicative models based on jury tests' results and acoustic metrics can identify some trends. Two models are proposed here:

- (1) a linear regression model, able to predict with relative accuracy the jury test score;
- (2) a dichotomic model, that identifies whether or not an acoustic signal should be far from the reference one.

^bIt is reminded that \mathfrak{N} depends on \mathfrak{h} and \mathfrak{p}_{FE} too.

^cAlthough other errors affect it.

5.2 Main results for the tire example

Sixteen different FE models have been used to simulate a set of sixteen TPs. One model has been used as the reference, and validated with by comparing the simulated TFs with those measured on a real mock-up. Then, other fifteen models have been built by degrading the mesh of the reference model. First, the quality of each model with respect to the reference has been assessed with the $RVAC(f)$ and the $\Delta f(f)$. As expected, these vectors have lower values at higher frequencies. The effect of adaptive meshes was clear, since these vectors started degrading at roughly half of the maximum simulated frequency (it is expected that, without adaptivity, the quality of the models would be better until higher frequencies). Despite the strong frequency dependence, the averages \overline{RVAC} and $\overline{\Delta f}$ of these in the whole simulated bandwidth showed to represent well enough the quality of the various numerical models. Furthermore, the \overline{RVAC} and the $\overline{\Delta f}$ showed to behave similarly, that is, a lower \overline{RVAC} generally correspond to a lower $\overline{\Delta f}$, except for minor variations (see Figure 3.15). Because of the above mentioned reasons, only the \overline{RVAC} has been used to consider the quality of the numerical models. Another vector has been used to evaluate the simulated TFs, that is, the quadratic error $\mathfrak{E}(f)$ (see Equation (3.4)). Due to reasons similar to the one mentioned for the \overline{RVAC} , the metric used for this local assessment was the average of the error in the whole simulated bandwidth, that is, $\overline{\mathfrak{E}}$.

The analysis of the simulated acoustic signals has been carried out in two different ways:

- (1) by means of acoustic metrics;
- (2) by means of jury tests.

Acoustic metrics showed that the numerical errors affect the sounds exactly as explained by theory and simple numerical examples. In other words, the complexity of the studied example did not seem to introduce any additional phenomena.

In detail, \mathfrak{N} and \mathfrak{p}_{FE} introduced both approximation and pollution errors. Lower thickness of the PML t_{PML} increased the energy of the spectra, as reflected by $SPL(A)$ and N , but not in very significant way. The interaction between the PML and the FE parameters, especially \mathfrak{p}_{FE} , proved to be more critical. Specifically, at lower \mathfrak{N} , linear FE models tended to have lower energy than the reference, independently of the PML thickness; the contrary happened for quadratic FE models. The shape and volume of the FE mesh, governed by t_{FE} , introduced changes in the simulated TFs, but in an unpredictable way.

Regarding jury tests, participants feedback included the difficulties faced during the tests and the differences detected mainly at high frequencies. Analysis of data reflects the difficulties mentioned by participants; the statistical techniques used included repeatability, cross-correlation, dendrograms and box-plot for evaluating the jury test score ranges. Specifically, it was found that repeatability was higher than what usually found in industrial tests. It was not possible to find subset of participants that acted in a different way from the others with the methodologies used, except for one participants that had a negative correlation with almost all the others: for this reason, this participants has been removed from the dataset.

An univariate ANOVA showed that errors, as introduced in Section 5.1, are perceivable; the ANOVA also highlighted the interaction between \mathfrak{p}_{FE} and $\frac{t_{PML}}{\lambda}$. Results showed that \mathfrak{N} and \mathfrak{p}_{FE} play a critical role, while t_{PML} is especially important due to its interaction with \mathfrak{p}_{FE} and t_{FE} did not play any specific role. These results are in line with the previous ones.

About similarity rankings, interestingly, participants consistently evaluated six models (over sixteen) as the less similar from the reference. This consistence suggests that these acoustic signals are actually different, in perceptual terms, from the reference. It is of special interests that all the models with $\mathfrak{N} = 4$ and $\mathfrak{p}_{FE} = 1$ are part of this set of different sounds; the other two have $\mathfrak{N} = 4$, $\mathfrak{p}_{FE} = 2$ and $\frac{t_{PML}}{\lambda} = 0.6$. These six models are therefore considered different from the reference in perceptual terms.

The most important result is probably about the difficulties that participants faced during jury tests. These difficulties indicate that acoustic signals were not so different. That is, low accuracy in the studied frequency range could be acceptable for sound quality purposes, at least for some tasks. More precisely, a nodal resolution of $\mathfrak{N} = 4$, when combined with thick PML ($\frac{t_{PML}}{\lambda} = 1$) and quadratic elements, produced noise samples very similar to the references. Only more degraded models were perceived as different from the references.

Generalization of this results must be taken with cautions. As Anisworth showed [67], the accuracy of the FEM at low nodal resolution is unpredictable and erratic. In other words, similar experiments could in theory provide different results.

5.3 Future Research

The results discovered in this research are auspicious and wide the door to a series of applications. To fully exploit the potentiality of this work, further research should focus on three areas: generalization of the results, practical applications, and extension of these results to different techniques.

5.3.1 Generalization of the results

The first way to generalize the results proposed here is to continue the same job with other examples and transfer paths. Besides using different TPs, future work could focus on some specific aspects as following.

Source's role

First of all, sources with different spectral characteristics appear in engineering applications. What happens when the convolutions involve a source that introduces more high-frequency energy content? And what happens when there are tonal components in the source spectrum?

Separating internal and external acoustic problems

The FEM has a solid mathematical theory behind itself. The study of internal problems allows removing the reflection errors caused by boundary conditions used to ensure the Sommerfield radiation condition. As such, the effect of pollution and approximation error could be identified. Furthermore, internal acoustic applications are crucial in some engineering fields such as the automotive one (for instance, in the case of the acoustic of the cabin). This thesis already identified the central aspects related to pollution and approximation errors. Still, an ad-hoc study could focus on identifying threshold targets^d and guidelines for sound quality applications (in terms of similarities and preference ratings). Attention could be given to a-posteriori error estimation techniques (for instance, see [124])

Thereafter, the research could focus on techniques such as PML, IEM and others. More mathematical background can be brought to the scientific discussion to identify threshold targets and guidelines, even in these cases.

Higher frequencies and innovative adaptive methodologies

Another step is to extend the proposed results to higher frequencies; this is a crucial aspect because higher frequencies (especially the so-called mid-frequency range [4, 34]) are especially

^dHere, a threshold target is a value for a numerical parameter that allow achieving the desired perceptual properties.

difficult to simulate due to the high computational cost required. However, since this research indicates that lower accuracy might be sufficient for sound quality applications, the computational cost in this range may dramatically decrease.

When moving to higher frequencies, researchers should consider innovative approaches to adaptive meshing techniques. More precisely, instead of focusing on single parameters such as h and p_{FE} , a combination of them should be used, starting from the consideration of Ainsworth [67]

5.3.2 Practical applications

Preference ratings

Previous scientific work [45] shows that sounds auralized with heavily different TFs can preserve preference rankings. A natural extension of the research carried out during this thesis moves in this direction: up to which limit does the numerical errors affect preference ratings? The difficulties that participants found during jury tests are very promising in this sense: a relatively low accuracy would likely prove to be sufficient. A combination of such research with some of the precedent subsection (such as the one on internal acoustic) could quickly and efficiently provide more results to the scientific community.

Predictive models

By making several numerical tests and experiments, it should be possible to create extensive databases. By applying the same principles discussed in Section 4.4.2 it could be possible to develop models able to predict whether a sound is perceived similarly enough to the theoretical solution of the modelled problem. Crossing such results with preference rating may provide even more valuable results. In the long term, it is not unlikely that a comprehensive framework will emerge like the one described by Roy and Oberkampf [125].

5.3.3 Other techniques

The framework proposed in this thesis could be helpful for other techniques. Besides other boundary techniques to ensure the Sommerfeld radiation condition, model order reduction and substructuring techniques are crucial for practical applications. Furthermore, other deterministic methods such as the BEM and statistical techniques like ray tracing and SEA could be studied, together with all the hybrid methodologies based on them.

Bibliography

- [1] Jens Blauert and Ute Jekosch. “Sound-Quality Evaluation – A Multi-Layered Problem”. In: *Acta Acustica united with Acustica* 83.5 (1997). Ed. by Tech Science Press, 747–753(7). URL: <https://www.ingentaconnect.com/content/dav/aaua/1997/00000083/00000005/art00005>.
- [2] Michael Vorländer. *Auralization: Fundamentals of Acoustics, Modelling, Simulation, Algorithms and Acoustic Virtual Reality*. Ed. by Springer. 2008, p. 203. URL: <https://www.springer.com/gp/book/9783540488293>.
- [3] Elke Deckers et al. “Case studies of model order reduction for acoustics and vibrations”. In: *Model Order Reduction - Volume 3, Applications*. Ed. by Peter Benner et al. De Gruyter, 2020. Chap. 3, pp. 75–110. ISBN: 978-3-110-49900-1. DOI: <https://doi.org/10.1515/9783110499001-003>. URL: <https://www.degruyter.com/document/doi/10.1515/9783110499001-003/html>.
- [4] Wim Desmet. “Mid-frequency vibro-acoustic modelling: challenges and potential solutions”. In: *Proceedings of ISMA*. Vol. 2. Leuven, Belgium, 2002, pp. 835–862. URL: <https://citeseerx.ist.psu.edu/viewdoc/summary?doi=10.1.1.389.9515>.
- [5] Lin Fritschi et al. *Burden of disease from environmental noise – quantification of healthy live years lost in Europe*. Report. World Health Organization, 2011, pp. 101–102. URL: http://www.euro.who.int/__data/assets/pdf_file/0008/136466/e94888.pdf.
- [6] ISO 362-1:2015-01. *Measurement of noise emitted by accelerating road vehicles - Engineering method -Part 1: M and N categories*. 2015.
- [7] Lisandra Garay-Vega et al. *Quieter cars and the safety of blind pedestrians: phase I*. Technical Report. National Highway Traffic Safety Administration (NHTSA), 2010. URL: <https://www.nhtsa.gov/DOT/NHTSA/NVS/Crash%20Avoidance/Technical%20Publications/2010/811304rev.pdf>.
- [8] Refaat Hanna. *Incidence of Pedestrian and Bicyclist Crashes by Hybrid Electric Passenger Vehicles*. Technical Report. National Highway Traffic Safety Administration (NHTSA), 2011. URL: <https://crashstats.nhtsa.dot.gov/Api/Public/ViewPublication/811204>.
- [9] Etienne Parizet, Wolfgang Ellermeier, and Ryan Robart. “Auditory warnings for electric vehicles: Detectability in normal-vision and visually-impaired listeners”. In: *Applied Acoustics* 86 (Dec. 2014). Ed. by Elsevier, pp. 50–58. DOI: <https://doi.org/10.1016/j.apacoust.2014.05.006>.

- [10] Gabriella Cerrato. “Automotive Sound Quality – Powertrain, Road and Wind Noise”. In: *Sound and Vibration* 43.4 (Apr. 2009). Ed. by Tech Science Press, pp. 16–24. URL: <http://www.sandv.com/downloads/0904cerr.pdf>.
- [11] Gabriella Cerrato. “Automotive Sound Quality – Accessories, BSR, and Brakes”. In: *Sound and Vibration* 43.9 (Sept. 2009). Ed. by Tech Science Press, pp. 10–15. URL: <http://sandv.com/downloads/0909cerr.pdf>.
- [12] Thomas Beckenbauer. “Road Traffic Noise”. In: *Handbook of Engineering Acoustics*. Ed. by Gerhard Muller and Michael Möser. Springer, 2013. Chap. 15, pp. 367–392. ISBN: 978-3-540-24052-5. DOI: 10.1007/978-3-540-69460-1_15. URL: <https://www.springer.com/gp/book/9783540240525>.
- [13] Wolfgang Kropp Jens Forssén Alice Hoffmann. “Auralization model for the perceptual evaluation of tyre–road noise”. In: *Applied Acoustics* 132 (Mar. 2018). Ed. by Elsevier, pp. 232–240. DOI: <https://doi.org/10.1016/j.apacoust.2017.11.023>.
- [14] Kumbhar Mansinh S et al. “Powertrain Noise & Sound Quality Refinement for New Generation Common Rail Engines”. In: *6th International Styrian Noise, Vibration & Harshness Congress - Sustainable NVH solutions inspired by ecology and economy*. Ed. by SAE. Graz, Austria, June 9, 2010. DOI: <https://doi.org/10.4271/2010-01-1414>.
- [15] Werner Biermayer, Siegmund Thomann, and Franz Brandl. “Brand sound design by using new development tools”. In: *ATZ worldwide* 103 (June 2001). Ed. by Springer, pp. 16–19. DOI: <https://doi.org/10.1007/BF03226789>.
- [16] Etienne Parizet, Erald Guyader, and Valery Nosulenko. “Analysis of car door closing sound quality”. In: *Applied Acoustics* 69.1 (Jan. 2008). Ed. by Elsevier, pp. 12–22. DOI: <https://doi.org/10.1016/j.apacoust.2006.09.004>.
- [17] Brian C. J. Moore. *An introduction to the Psychology of Hearing*. Ed. by Academic Press. fifth edition. 2002.
- [18] Eberhard Zwicker and Hugo Fastl. *Psychoacoustics - Facts and Models*. Ed. by Springer. second updated edition. 1999.
- [19] Arne Nykänen and Örian Johansson. “Design of product sound by blending of sound-sources”. In: *19th International Congress on Acoustics*. Madrid, Sept. 2007. URL: <http://www.diva-portal.org/smash/get/diva2:1002816/FULLTEXT01.pdf>.
- [20] F. Brandl, W. Biermayer, and S. Thoman. “Efficient Passenger Car Sound Engineering using new Development Tools”. In: *Styrian Noise, Vibration & Harshness Congress*. Graz, Austria, Oct. 2001.
- [21] Norm Otto et al. “Guidelines for Jury Evaluations of Automotive Sounds”. In: *Sound and Vibration* (Apr. 2001). Ed. by Tech Science Press, pp. 1–14. URL: <http://www.sandv.com/downloads/0104otto.pdf>.
- [22] Michael Vorlaender and Pascal Dietrich. “TRANSFER PATH ANALYSIS AND SYNTHESIS FOR AURALIZATION”. In: *Techniacústica - 39^o Congreso Espanol de acústica 2008*. Coimbra, Portugal, Oct. 2008. DOI: <https://doi.org/10.4271/2015-01-2360>.
- [23] Maarten V. van der Seijs, Dennise Klerkab, and Daniel J. Rixenc. “General framework for transfer path analysis: History, theory and classification of techniques”. In: *Mechanical Systems and Signal Processing* 68-69 (Feb. 2016). Ed. by Elsevier, pp. 217–244. DOI: <https://doi.org/10.1016/j.ymsp.2015.08.004>.
- [24] Todd Freeman and Gabriella Cerrato. “Source-Path-Contribution Methodologies across a Wide Range of Product Types”. In: *SAE 2015 Noise & Vibration Conference & Exposition*. SAE Technical paper 2015-01-2360. June 15, 2015, pp. 726–766. DOI: <https://doi.org/10.4271/2015-01-2360>.

- [25] Roland Sottek and Bernhard Müller-Held. “Binaural transfer path analysis and synthesis (BTPA/BTPS) using sub-structuring techniques based on finite element analysis (FEA) and measurements”. In: *SAE 2007 Noise and Vibration Conference and Exhibition*. Ed. by SAE. May 15, 2007. DOI: <https://doi.org/10.4271/2007-01-2226>.
- [26] Herman Van der Auweraer et al. “Virtual prototyping for sound quality design of automobiles”. In: *Sound and Vibration* 41.4 (Apr. 2007). Ed. by Tech Science Press, pp. 26–30. URL: http://tsp.techscience.com/uploads/attached/file/20181121/20181121094751_98678.pdf.
- [27] Klaus Genuit and Wade Bray. “A Virtual Car: Prediction of Sound and Vibration in an Interactive Simulation Environment”. In: *SAE 2001 Noise & Vibration Conference & Exposition*. Ed. by SAE. Traverse City, Michigan, USA, Apr. 30, 2001. DOI: <https://doi.org/10.4271/2001-01-1474>.
- [28] Wilhelmus H. Schilders, Henk A. van der Vorst, and Joost Rommes. *Model Order Reduction: Theory, Research Aspects and Applications*. Ed. by Springer. eighth edition. 2008. ISBN: 978-1118-14692-7.
- [29] Shung H. Sung and Donald J. Nefske. “Component mode synthesis of a vehicle structural-acoustic system model”. In: *AIAA Journal* 24.6 (June 1986). Ed. by Aerospace Research Central, pp. 1021–259. DOI: <https://doi.org/10.2514/3.9379>.
- [30] Morvan Ouisse et al. “Patch Transfer Functions as a tool to couple linear acoustic problems”. In: *Journal of Vibration and Acoustics* 127.5 (Dec. 2004). Ed. by ASME, pp. 1372–1399. DOI: 10.1115/1.2013302.
- [31] Murty S. Kompella and Robert J. Bernhard. “Measurement of the statistical variation of structural-acoustic characteristics of automotive vehicles”. In: *Proceedings of the SAE Noise and Vibration conference*. SAE paper 931272. Traverse City, Michigan, USA, 1993, pp. 35–72. DOI: <https://doi.org/10.4271/931272>.
- [32] Antonio Culla and Aldo Sestrieri. “Is it possible to treat confidentially SEA the wolf in sheep’s clothing?” In: *Mechanical System & Signal Processing* 20.6 (Aug. 2006). Ed. by Elsevier, pp. 1372–1399. DOI: <https://doi.org/10.1016/j.ymsp.2005.02.007>.
- [33] Ranier Stelzer et al. “Non resonant contribution and energy distributions using Statistical modal Energy density Analysis”. In: *Proceedings of ISMA*. Leuven, Belgium, 2010, pp. 2039–2054. URL: http://past.isma-isaac.be/downloads/isma2010/papers/isma2010_0346.pdf.
- [34] Wim Desmet, Bert Pluymers, and Onur Atak. “MID-FREQUENCY” *CAE Methodologies for Mid-Frequency Analysis in Vibration and Acoustics*. Ed. by Katholieke Universiteit Leuven - Faculty of Engineering. Final deliverable of the FP7 ITN MID-FREQUENCY project. 2012. ISBN: 978-94-6018-523-6. URL: <https://www.mech.kuleuven.be/en/mod/publications-media/midfrequency2012book>.
- [35] Dries Berckmans et al. “Evaluation of substitution monopole models for tire noise sound synthesis”. In: *Mechanical Systems and Signal Processing* 24.1 (Jan. 2010). Ed. by Elsevier, pp. 240–255. DOI: <https://doi.org/10.1016/j.ymsp.2009.06.005>.
- [36] Marleen Adams and Patrick Van de Ponsele. “Sound Quality Equivalent Modeling for Virtual Car Sound Synthesis”. In: *SAE 2001 Noise & Vibration Conference & Exposition*. SAE Technical paper 2001-01-1540. Traverse City, Michigan, USA, Apr. 30, 2001, pp. 35–72. DOI: <https://doi.org/10.4271/2001-01-1540>.
- [37] Alice Hoffmann and Wolfgang Kropp. “Auralization of simulated tyre noise: Psychoacoustic validation of a combined model”. In: *Applied Acoustics* 145 (Dec. 2019). Ed. by Elsevier, pp. 220–227. DOI: <https://doi.org/10.1016/j.apacoust.2018.08.026>.

- [38] Jie Mao et al. “Experimental validation of sound quality simulation and optimization of a four-cylinder diesel engine”. In: *Journal of Zhejiang University SCIENCE A* 130 (May 2013). Ed. by Elsevier, pp. 341–352. DOI: <https://doi.org/10.1631/jzus.A1300055>.
- [39] Zhongming Xu et al. “Improvement of interior sound quality for passenger car based on optimization of sound pressure distribution in low frequency”. In: *Applied Acoustics* 130 (Jan. 2018). Ed. by Elsevier, pp. 43–51. DOI: <https://doi.org/10.1016/j.apacoust.2017.08.019>.
- [40] Victor Hodor et al. “CFD Prediction with LES for Psycho Acoustic Relevance in Ventilation”. In: *Energy Procedia* 85 (Jan. 2016). Ed. by Elsevier, pp. 252–259. DOI: <https://doi.org/10.1016/j.egypro.2015.12.238>.
- [41] Fabian Duvigneau et al. “Thermo-acoustic performance of full engine encapsulations – A numerical, experimental and psychoacoustic study”. In: *Applied Acoustics* 102 (Jan. 2016). Ed. by Elsevier, pp. 79–87. DOI: <https://doi.org/10.1016/j.apacoust.2015.09.012>.
- [42] Fabian Duvigneau et al. “Analysis of simulated engine sounds using a psychoacoustic model”. In: *Journal of Sound and Vibration* 366 (Mar. 2016). Ed. by Elsevier, pp. 544–555. DOI: <https://doi.org/10.1016/j.jsv.2015.11.034>.
- [43] Arne Nykänen et al. “Assessment of the change in similarity judgements of auralized engine sounds caused by changes in frequency resolution of transfer functions”. In: *Applied Acoustics* 72.2-3 (Feb. 2011). Ed. by Elsevier, pp. 115–123. DOI: <https://doi.org/10.1016/j.apacoust.2010.10.007>.
- [44] Arnaud Trollé, Catherine Marquis-Favre, and Nacer Hamzaoui. “Auditory evaluation of sounds radiated from a vibrating plate inside a damped cavity: adjustment of the frequency resolution of vibro-acoustical computing”. In: *Acta Acustica with Acustica* (Mar. 2012). Ed. by European Acoustics Association (EAA). DOI: <https://doi.org/10.3813/AAA.918528>.
- [45] Arne Nykänen et al. “Assessment of changes in preference ratings of auralized engine sounds caused by changes in frequency resolution of transfer functions”. In: *Applied Acoustics* 74.12 (Dec. 2013). Ed. by Elsevier, pp. 1343–1353. DOI: <https://doi.org/10.1016/j.apacoust.2013.05.005>.
- [46] Nicolas Aujogue and Etienne Parizet. “Influence of the accuracy of Transfer Functions Description on the Perception of Auralised Sounds”. In: *10th International Styrian Noise, Vibration & Harshness Congress: The European Automotive Noise Conference*. Ed. by SAE. Graz, Austria, June 13, 2018. DOI: <https://doi.org/10.4271/2018-01-1490>.
- [47] Douglas C. Montgomery. *Design And Analysis Of Experiments*. Ed. by Inc. John Wiley & Sons. eighth edition. 2012. ISBN: 978-1118-14692-7.
- [48] Sjoerd W. Rienstra and Avraham Hirschberg. *An Introduction to Acoustics*. Eindhoven University of Technology, 2019. URL: <https://www.win.tue.nl/~sjoerdr/papers/boek.pdf>.
- [49] Siegfried Flügge. “ACOUSTICS 1”. In: *ENCYCLOPEDIA OF PHYSICS*. Vol. XI/1. Springer, 1961.
- [50] Steffen Marburg and Bodo Nolte. “A Unified Approach to Finite and Boundary Element Discretization in Linear Time–Harmonic Acoustics”. In: *Computational Acoustics of Noise Propagation in Fluids*. Ed. by Steffen Marburg and Bodo Nolte. Springer, chap. 0. URL: <https://www.springer.com/gp/book/9783540774471>.
- [51] Frank Ihlenburg. *Finite Element Analysis Of Acoustic Scattering*. Ed. by Springer. 1998. ISBN: 978-0-387-22700-9.

- [52] Nouredine Atalla and Franck Sgard. *Finite Element and Boundary Methods in Structural Acoustics and Vibration*. Ed. by CRC Press. 2015. ISBN: 9780429190285.
- [53] Philip McCord Morse and Karl Uno Ingard. *Theoretical Acoustics*. Ed. by MC-Graw Hill. 1968. URL: <https://archive.org/details/TheoreticalAcoustics>.
- [54] Steven H. Schot. “Eighty years of Sommerfeld’s radiation condition”. In: *Historia Mathematica* 19.4 (1992). Ed. by Elsevier, pp. 385–401. DOI: [https://doi.org/10.1016/0315-0860\(92\)90004-U](https://doi.org/10.1016/0315-0860(92)90004-U). URL: <https://www.sciencedirect.com/science/article/pii/S031508609290004U>.
- [55] Dan Givoli. *Numerical Methods for Problems in Infinite Domains*. Ed. by Elsevier. Vol. 33. Studies in Applied Mechanics. first edition. 1992. ISBN: 9781483291086.
- [56] Wolfgang Hackbusch. *Elliptic Differential Equations*. Ed. by Springer. 2017. ISBN: 978-3-662-57217-7. URL: <https://www.springer.com/gp/book/9783662549605>.
- [57] Bruce A. Finlayson. *The Method of Weighted Residuals and Variational Principles*. Ed. by Elsevier. Vol. 87. Mathematics in Science and Engineering. 1972. ISBN: 9780080955964. URL: <http://www.fsiforum.cz/upload/soubory/databaze-predmetu/RME/49280122570502.pdf>.
- [58] Gary Cohen et al. “Different Types of Finite Elements”. In: *Computational Acoustics of Noise Propagation in Fluids*. Ed. by Steffen Marburg and Bodo Nolte. Springer, chap. 0. ISBN: 978-3-540-77448-8. DOI: 10.1007/978-3-540-77448-8_3. URL: https://link.springer.com/chapter/10.1007%5C%2F978-3-540-77448-8_3.
- [59] Hadrien Bériot, Albert Prinn, and Gwénaél Gabard. “Efficient implementation of high-order finite elements for Helmholtz problems”. In: *International Journal for Numerical Methods in Engineering* 106.3 (Apr. 2016). Ed. by John Wiley & Sons, pp. 213–240. URL: <https://doi.org/10.1002/nme.5172>.
- [60] Mats G. Larson and Fredrik Bengzon. *The Finite Element Method: Theory, Implementation, and Applications*. Ed. by Springer. 2013, p. 203. URL: <https://www.springer.com/gp/book/9783642332869>.
- [61] Bruce M. Iron. “A frontal solution program for finite element analysis”. In: *International journal for numerical methods in engineering* 2 (1970). Ed. by John Wiley & Sons, pp. 5–32. DOI: <https://doi.org/10.1002/nme.1620020104>.
- [62] Patrick R. Amestoy, Iain S. Duff, and L’Excellent Jean-Yves. “Multifrontal parallel distributed symmetric and unsymmetric solvers”. In: *Computer Methods in Applied Mechanics and Engineering* 184.2-4 (2000). Ed. by Elsevier, pp. 501–520. URL: [https://doi.org/10.1016/S0045-7825\(99\)00242-X](https://doi.org/10.1016/S0045-7825(99)00242-X).
- [63] Stephen Nettel. *Wave Physics*. Ed. by Springer. fourth edition. 2009. ISBN: 978-3-540-87908-4. DOI: 10.1007/978-3-540-87908-4. URL: http://www.informex.info/html/book__tyre_road_noise_.html.
- [64] Isaac Harari. “Dispersion, Pollution and Resolution”. In: *Computational Acoustics of Noise Propagation in Fluids*. Ed. by Steffen Marburg and Bodo Nolte. Springer, chap. 0. ISBN: 978-3-540-77448-8. DOI: https://doi.org/10.1007/978-3-540-77448-8_2. URL: https://link.springer.com/chapter/10.1007%5C%2F978-3-540-77448-8_2.
- [65] Isaac Harari. “Finite element dispersion of cylindrical and spherical acoustic waves”. In: *Computer Methods in Applied Mechanics and Engineering* 190.20-21 (Feb. 2001). Ed. by Elsevier, pp. 2533–2542. URL: [https://doi.org/10.1016/S0045-7825\(00\)00251-6](https://doi.org/10.1016/S0045-7825(00)00251-6).
- [66] Frank Ihlenburg and Ivo Babuška. “Finite element solution of Helmholtz equation with high wave number - Part I: the h-version of the FEM”. In: *Computers and Mathematics with Applications* 30.9 (Nov. 1995). Ed. by Elsevier, pp. 9–37. URL: [https://doi.org/10.1016/0898-1221\(95\)00144-N](https://doi.org/10.1016/0898-1221(95)00144-N).

- [67] Mark Ainsworth. “Discrete Dispersion Relation for hp-Version Finite Element Approximation at High Wave Number”. In: *SIAM Journal on Numerical Analysis* 42.2 (2004). Ed. by SIAM, pp. 553–575. DOI: <https://doi.org/10.1137/S0036142903423460>. URL: <https://www.newton.ac.uk/files/preprints/ni03005.pdf>.
- [68] Frank Ihlenburg and Ivo Babuška. “Dispersion analysis and error estimation of Galerkin finite element methods for the Helmholtz equation”. In: *International Journal for Numerical Methods in Engineering* 38.22 (Nov. 1995). Ed. by Ltd John Wiley & Sons, pp. 3745–3774. URL: <https://doi.org/10.1002/nme.1620382203>.
- [69] Ivo Babuška et al. “A Generalized Finite Element Method for solving the Helmholtz equation in two dimensions with minimal pollution”. In: *Computer methods in applied mechanics and engineering* 128.3-4 (Dec. 1995). Ed. by Elsevier, pp. 325–359. DOI: [https://doi.org/10.1016/0045-7825\(95\)00890-X](https://doi.org/10.1016/0045-7825(95)00890-X).
- [70] K. Gerdes and Frank Ihlenburg. “On the pollution effect in FE solutions of the 3D-Helmoltz equation”. In: *International Journal for Numerical Methods in Engineering* 170.1-2 (Feb. 1999). Ed. by Ltd John Wiley & Sons, pp. 155–172. URL: [https://doi.org/10.1016/S0045-7825\(98\)00239-4](https://doi.org/10.1016/S0045-7825(98)00239-4).
- [71] Arnaud Deraemaeker, Ivo Babuška, and Philippe Bouillard. “Dispersion and pollution of the FEM solution for the Helmholtz equation in one, two and three dimensions”. In: *Internationa Journal for Numerical Methods in Engineering* 46 (Aug. 1999). Ed. by Ltd John Wiley & Sons, pp. 471–499. DOI: 10.1002/(SICI)1097-0207(19991010)46:4<471::AID-NME684>3.0.CO;2-6.
- [72] Ivo Babuška, Uday Banerjee, and John E. Osborn. “Generalized Finite Element Methods: Main Ideas, Results, and Perspective”. In: *International Journal of Computational Methods* 01.01 (2004). Ed. by World Scientific, pp. 67–103. DOI: <https://doi.org/10.1142/S0219876204000083>.
- [73] Frank Ihlenburg and Ivo Babuška. “Finite element solution of Helmholtz equation with high wave number - Part II: the h-p version of the FEM”. In: *Journal on Numerical Analysis* 34.1 (1997). Ed. by SIAM, pp. 315–358. URL: <https://doi.org/10.1137/S0036142994272337>.
- [74] Isaac Harari and Danny Avraham. “High-order finite elements methods for acoustic problems”. In: *Journal of Computational Acoustics* 5.1 (Mar. 1997). Ed. by World Scientific, pp. 33–51. URL: <https://doi.org/10.1142/S0218396X97000046>.
- [75] Jean François Semblat and J. J. Brioist. “Efficiency of higher order finite elements for the analysis of seismic wave propagation”. In: *Journal of Sound and Vibration* 231.2 (Feb. 2000). Ed. by Elsevier, pp. 460–467. URL: <https://doi.org/10.1006/jsvi.1999.2636>.
- [76] S. C. Keating, C. A. Felippa, and K. C. Park. *ERROR ESTIMATION AND ADAPTIVE MESH REFINEMENT FOR PARALLEL ANALYSIS OF SHELL STRUCTURE*. Technical Report Report No.CU-CAS-94-23. Research supported by NASA Langley Research Center under Grant NAS1-756, monitored by Dr. J. Housner. National Highway Traffic-Safety Administration (NHTSA), 1994. URL: <https://ntrs.nasa.gov/archive/nasa/casi.ntrs.nasa.gov/19950011077.pdf>.
- [77] Ivo Babuška and Benqi Guo. “The h , p and h - p version of the finite element method; basis theory and applications”. In: *Advances in Engineering Software* 15.3-4 (Jan. 1992). Ed. by Elsevier, pp. 159–174. DOI: 10.1016/0965-9978(92)90097-Y.
- [78] Karan S. Surana, Ali R. Ahmadi, and Junuthula N. Reddy. “k-Version of Finite Element Method for Non-Linear Differential Op-erators in BVP”. In: *International Journal of Computational Engineering Science* 5.1 (2004). Ed. by World Scientific, pp. 133–207. DOI: 10.1142/S1465876304002307.

- [79] Karan S. Surana, Ali R. Ahmadi, and Junuthula N. Reddy. “k-Version of Finite Element Method for Non-self-adjoint Operators in BVP”. In: *International Journal of Computational Engineering Science* 4.4 (2003). Ed. by World Scientific, pp. 737–812. DOI: 10.1142/S1465876303002179.
- [80] Karan S. Surana, Ali R. Ahmadi, and Junuthula N. Reddy. “k-Version of Finite Element Method for Self-adjoint Operators in BVP”. In: *International Journal of Computational Engineering Science* 3.2 (2002). Ed. by World Scientific, pp. 155–218. DOI: 10.1142/S1465876302000605.
- [81] Free Field Technologies. *Actran*. Software. Mont-Saint-Guibert Belgium, 2019. URL: <https://www.fft.be/>.
- [82] Lonny L. Thompson. “A review of finite-element methods for time-harmonic acoustics”. In: *Journal of Acoustical Society of America* 119.3 (Mar. 2006). Ed. by Acoustical Society of America, pp. 1315–1330.
- [83] Dan Givoli. “Computational Absorbing Boundaries”. In: *Computational Acoustics of Noise Propagation in Fluids*. Ed. by Steffen Marburg and Bodo Nolte. Springer, chap. 0. ISBN: 978-3-540-77448-8. DOI: 10.1007/978-3-540-77448-8_6. URL: https://link.springer.com/chapter/10.1007%5C%2F978-3-540-77448-8_3.
- [84] F. V. Atkinson. “On Sommerfield’s radiation condition”. In: *The London, Edinburgh, and Dublin Philosophical Magazine and Journal of Science*. 7th ser. 49.305 (1949). Ed. by Taylor & Francis, pp. 645–651. URL: <https://doi.org/10.1080/14786444908561291>.
- [85] C. H. Wilcox. “An expansion theorem for electromagnetic fields”. In: *Communications in Pure and Applied Mathematics* 9.2 (May 1956). Ed. by John Wiley & Sons, pp. 115–134. URL: <https://doi.org/10.1002/cpa.3160090202>.
- [86] Alvin Bayliss, Max Gunzberger, and E. Turkel. “Boundary conditions for the numerical solution of elliptic equations in exterior domains”. In: *SIAM Journal on Applied Mathematics* 42.2 (1982). Ed. by SIAM, pp. 430–451. URL: <https://doi.org/10.1137/0142032>.
- [87] Dan Givoli. “High order local non-reflecting boundary conditions: A review”. In: *Wave Motions* 39.4 (Apr. 2004). Ed. by Elsevier, pp. 319–326. URL: <https://doi.org/10.1016/j.wavemoti.2003.12.004>.
- [88] R. Tezaru et al. “Three dimensional finite element calculations in acoustic scattering using arbitrary shaped convex artificial boundaries”. In: *Communications in Pure and Applied Mathematics* 53.6 (Dec. 2001). Ed. by John Wiley & Sons, pp. 1461–1476. DOI: <https://doi.org/10.1002/nme.346>.
- [89] Joseph B. Keller and Dan Givoli. “Exact non-reflecting boundary conditions”. In: *Journal of Computational Physics* 88.1 (May 1989). Ed. by Elsevier, pp. 172–192. URL: [https://doi.org/10.1016/0021-9991\(89\)90041-7](https://doi.org/10.1016/0021-9991(89)90041-7).
- [90] Cristian Ianculescu and Lonny L. Thompson. “Parallel iterative solution for the Helmholtz equation with exact non-reflecting boundary conditions”. In: *Computer Methods in Applied Mechanics and Engineering* 195.29632 (June 2006). Ed. by Elsevier, pp. 3709–3741. URL: <https://doi.org/10.1016/j.cma.2005.02.030>.
- [91] R. Jeremy Astley. “Infinite elements”. In: *Computational Acoustics of Noise Propagation in Fluids*. Ed. by Steffen Marburg and Bodo Nolte. Springer, chap. 0. ISBN: 978-3-540-77448-8. DOI: https://doi.org/10.1007/978-3-540-77448-8_8. URL: https://link.springer.com/chapter/10.1007%5C%2F978-3-540-77448-8_2.
- [92] Wilcox C.H. “A generalisation of theorems of Rellich and Atkinson.” In: *Proceedings of the American Mathematical Society*. Ed. by American Mathematical Society. 1956, pp. 271–276.

- [93] David S. Burnett. “A three-dimensional acoustic infinite element based on a prolate spheroidal multipole expansion”. In: *Journal of Acoustical Society of America* 96.2798 (1994). Ed. by Acoustical Society of America. DOI: 10.1121/1.411286.
- [94] Alfredo Bermúdez et al. “Perfectly Matched Layers”. In: *Computational Acoustics of Noise Propagation in Fluids*. Ed. by Steffen Marburg and Bodo Nolte. Springer, chap. 0. ISBN: 978-3-540-77448-8. DOI: https://doi.org/10.1007/978-3-540-77448-8_7. URL: https://link.springer.com/chapter/10.1007%5C%2F978-3-540-77448-8_2.
- [95] Manfred Kaltenbacher et al. “Computational Aeroacoustics based on Lighthill’s Acoustic Analogy”. In: *Computational Acoustics of Noise Propagation in Fluids*. Ed. by Steffen Marburg and Bodo Nolte. Springer, chap. 0. ISBN: 978-3-540-77448-8. DOI: 10.1007/978-3-540-77448-8_5. URL: https://link.springer.com/chapter/10.1007%5C%2F978-3-540-77448-8_5.
- [96] Lighthill M.J. “On sound generated aerodynamically. Part I: General theory”. In: *Proceedings of the Royal Society of London*. Ed. by Royal Society of London. 1952, pp. 564–587.
- [97] Curle N. “The influence of solid boundaries upon aerodynamic sound.” In: *Proceedings of the Royal Society of London*. Ed. by Royal Society of London. 1995, pp. 505–514.
- [98] J.E. Ffowcs Williams and D.L. Hawkings. “Sound Generation by Turbulence and Surfaces in Arbitrary Motion”. In: *Proceedings of the Royal Society of London*. Ed. by Royal Society of London. Vol. 264. 1151. 1969, pp. 321–342.
- [99] Farassat F. “Acoustic radiation from rotating blades – the Kirchhoff method in aeroacoustics”. In: *Journal of Sound and Vibration* 239 (2001). Ed. by Elsevier, pp. 785–800.
- [100] Kenneth S. Brentner and F. Farassat. “Analytical Comparison of the Acoustic Analogy and Kirchhoff Formulation for Moving Surfaces”. In: *AIAA Journal* 36.8 (1998). Ed. by ARC. DOI: 10.2514/2.558.
- [101] Jean-Pierre Berenger. “A perfectly matched layer for the absorption of electromagnetic waves”. In: *Journal of Computational Physics* 114.2 (Oct. 1994). Ed. by Elsevier, pp. 185–200. URL: <https://doi.org/10.1006/jcph.1994.1159>.
- [102] Jean-Pierre Berenger. “Three-Dimensional Perfectly Matched Layer for the Absorption of Electromagnetic Waves”. In: *Journal of Computational Physics* 127.2 (Sept. 1996). Ed. by Elsevier, pp. 363–379. DOI: 10.1006/jcph.1996.0181.
- [103] Zhao Li and Cangellaris Andreas C. “A general approach for the development of unsplit-field time-domain implementations of perfectly matched layers for FDTD grid truncation”. In: *IEEE Microwave and Guided Wave Letters* 6 (May 1996). Ed. by IEEE, pp. 209–211. DOI: 10.1109/75.491508.
- [104] S. V. Tsynkov and Turkel E. “A Cartesian perfectly matched layer for the Helmholtz equation”. In: *Absorbing boundaries and layers domain decomposition methods*. Ed. by L. Tournette and L. Halern. 2001, pp. 279–309. ISBN: 1-56072-940-6.
- [105] E. Turkel and A. Yefet. “Absorbing PML boundary layers for wave-like equations”. In: *Applied Numerical Mathematics* 27.4 (Aug. 1998). Ed. by Elsevier, pp. 533–557. URL: [https://doi.org/10.1016/S0168-9274\(98\)00026-9](https://doi.org/10.1016/S0168-9274(98)00026-9).
- [106] Isaac Harari, Michael Slavutin, and Eli Turkel. “Analytical and numerical studies of a finite element pml for the Helmholtz equation”. In: *Journal of Computational Acoustics* 8.1 (2000). Ed. by World Scientific, pp. 121–137. DOI: <https://doi.org/10.1142/S0218396X0000008X>. URL: https://www.cs.tau.ac.il/~turkel/PSmanuscripts/harari_pml.pdf.

- [107] Harvey Fletcher and W. A. Munson. “Loudness, Its Definition, Measurement and Calculation”. In: *Journal of Acoustic Society of America* 5 (1933). Ed. by Wiley, pp. 82–108. DOI: <https://doi.org/10.1002/j.1538-7305.1933.tb00403.x>. URL: http://storeycountywindfarms.org/ref2_fletcher_munson.pdf.
- [108] Harvey Fletcher. “Auditory patterns”. In: *Review of Modern Physics* 12 (Jan. 1940). Ed. by American Physical Society, pp. 47–65. DOI: <https://doi.org/10.1103/RevModPhys.12.47>.
- [109] Hans-Elias de Bree and Tom Basten. “Microflown based monopole sound sources for reciprocal measurements”. In: *SAE Technical Paper 2008-36-0503* (Mar. 30, 2008). Ed. by SAE Brasil Noise and Vibration Conference. URL: <https://doi.org/10.4271/2008-36-0503>.
- [110] Altair Hyperworks. *Hypermesh*. Software. Troy, Michigan, United States, 2019. URL: <https://altairhyperworks.com/product/HyperMesh>.
- [111] N.-S. Lee and K.-J. Bathe. “Effects of Element Distortions on the Performance of Isoparametric Elements”. In: *International Journal for Numerical Methods in Engineering* 36 (Mar. 1993). Ed. by Ltd John Wiley & Sons, pp. 3553–3576.
- [112] Klaus-Jürgen Bathe. *Finite Element Procedures*. 2014, pp. 465–476. ISBN: 978-0-9790049-5-7.
- [113] Bohn D. A. “Environmental Effects on the Speed of Sound”. In: *Journal of Audio Engineering Society* 36.4 (Apr. 1988). Ed. by Audio Engineering Society.
- [114] A. Picard et al. “Revised formula for the density of moist air (CIPM-2007)”. In: *Metrologia* 45.2 (Feb. 18, 2008). Ed. by IOP Publishing Ltd, pp. 149–155. DOI: [doi:10.1088/0026-1394/45/2/004](https://doi.org/10.1088/0026-1394/45/2/004).
- [115] Mathworks. *Matlab*. Software. Natick, Massachusetts, USA, 2017. URL: <https://www.mathworks.com/products/matlab.html>.
- [116] J. F. Mercer, G. S. Aglietti, and A. M. Kiley. “MODAL AND FREQUENCY DOMAIN BASED TECHNIQUES FOR FINITE ELEMENT MODEL CORRELATION”. In: *5th ECCOMAS Thematic Conference on Computational Methods in Structural Dynamics and Earthquake Engineerig*. Crete Island, Greece. 2015, pp. 191–208.
- [117] C. Lein and M. Beitelschmidt. “Comparative study of model correlation methods with application to model order reduction”. In: *Proceedings of ISMA 2014 including USD 2014*. 2014.
- [118] Gabriella Cerrato. “Sound/Vibration Quality Engineering - Part 1”. In: *Sound and Vibration* (Apr. 2007). Ed. by Tech Science Press, pp. 16–23. URL: <http://www.sandv.com/downloads/0704jay.pdf>.
- [119] Joe H. Ward Jr. “Hierarchical Grouping to Optimize an Objective Function”. In: *Journal of the American Statistical Association* 58.301 (1963), pp. 236–244. DOI: [10.1080/01621459.1963.10500845](https://doi.org/10.1080/01621459.1963.10500845). URL: <https://www.tandfonline.com/doi/abs/10.1080/01621459.1963.10500845>.
- [120] Keenan A. Pituch and James P. Stevenson. *Applied Multivariate Statistics for the Social Sciences*. Ed. by Taylor & Francis. sixth edition. 2016.
- [121] Azmeri Khan and Glend D. Rayner. “Robustness to Non-Normality of Common Tests for the Many-Sample Location Problem”. In: *Journal of Applied Mathematics and Decision Sciences* 7.4 (2003). Ed. by Hindawi, pp. 187–206. DOI: <https://doi.org/10.1155/S1173912603000178>. URL: http://www.kurims.kyoto-u.ac.jp/EMIS/journals/HOA/JAMDS/Volume7_4/206.pdf.

- [122] María J. Blanca et al. “Effect of variance ratio on ANOVA robustness: Might 1.5 be the limit?” In: *Behavior Research Methods* 50 (2018), pp. 937–962. DOI: 10.3758/s13428-017-0918-2. URL: https://link-springer-com/article/10.3758/s13428-017-0918-2#auth-Mar_a_J_-Blanca.
- [123] William H. Kruskal and W. Allen Wallis. “Use of Ranks in One-Criterion Variance Analysis”. In: *Journal of the American Statistical Association* 47.260 (1952). Ed. by Taylor & Francis, pp. 583–621. DOI: 10.1080/01621459.1952.10483441. URL: <https://www.tandfonline.com/doi/abs/10.1080/01621459.1952.10483441>.
- [124] Mark Ainsworth and John Tinsley Oden. “A posteriori error estimation in finite element analysis”. In: *Computer Methods in Applied Mechanics and Engineering* 142.1-2 (Mar. 1997). Ed. by Elsevier, pp. 1–88. DOI: [https://doi.org/10.1016/S0045-7825\(96\)01107-3](https://doi.org/10.1016/S0045-7825(96)01107-3). URL: <https://www.sciencedirect.com/science/article/abs/pii/S0045782596011073#!>.
- [125] Christopher J. Roy and William L. Oberkampf. “A comprehensive framework for verification, validation, and uncertainty quantification in scientific computing”. In: *Computer Methods in Applied Mechanics and Engineering* 200.25-28 (June 2011). Ed. by Elsevier, pp. 2131–2144. DOI: <https://doi.org/10.1016/j.cma.2011.03.016>. URL: <https://www.sciencedirect.com/science/article/abs/pii/S0045782511001290>.
- [126] Sandro Salsa. *Partial Differential Equations in Action*. Ed. by Springer. 2009. ISBN: 978-88-470-0752-9. URL: <https://www.springer.com/gp/book/9788847007512#otherversion=9788847007529>.
- [127] Olek Zienkiewicz, Robert Taylor, and Perumal Nithiarasu. *The Finite Element Method for Fluid Dynamics*. Ed. by Elsevier. 7th Edition. 2013. ISBN: 9780080951379.

Basis of Functional Analysis

IN modern mathematics, many tools for solving partial differential equations (PDE) came from the branch of mathematics known as functional analysis. This appendix introduces the most basic concepts of this field necessary to tackle the solution of elliptic PDE, such as the Helmholtz equation. Only the topics necessary to understand the thesis are present. Therefore, things such as Sobolev spaces of real index, trace operators and types of solution (strict, classical, weak and distributional) are omitted, despite their essential role in mathematics. Most elementary concepts coming from the field of real and complex analysis are taken for granted. Some abuse of notation and terminology are present, to make the discussion easier. For strict definitions and a more deep analysis, the reader may refer to [56, 126].

A.1 Norms and semi-norms

Given a vector space X over a field F of \mathbb{R} or \mathbb{C} , a norm is a non-negative valued function $\|\cdot\| \rightarrow \mathbb{R}$ such that:

$$(1) \quad \|\mathbf{a} + \mathbf{b}\| \leq \|\mathbf{a}\| + \|\mathbf{b}\| \quad \forall \mathbf{a}, \mathbf{b} \in X;$$

$$(2) \quad \|b\mathbf{a}\| = |b|\|\mathbf{a}\| \quad \forall \mathbf{a} \in X, \forall b \in F;$$

$$(3) \quad \|\mathbf{a}\| = 0 \quad \forall \mathbf{a} = 0.$$

In case a non-negative valued function $\|\cdot\|^* \rightarrow \mathbb{R}$ satisfies only properties (1) and (2), it is called seminorm.

A.2 Banach and Hilbert spaces

In case a norm $\|\cdot\|$ is introduced in a function space X , a sequence $\{x_n\} \in X$ is said to converge to x if:

$$\lim_{m \rightarrow \infty} \|x_m - x\| = 0. \quad (\text{A.1})$$

A sequence $\{x_n\} \in X$ is called Cauchy sequence if:

$$\lim_{\substack{m \rightarrow \infty \\ k \rightarrow \infty}} \|x_m - x_k\| = 0. \quad (\text{A.2})$$

A normed space in which every Cauchy sequence converges is said to be complete and is called Banach space^a.

In any vector space can be introduced an inner product (\cdot, \cdot) . Such product induces the norm $\|x\| = \sqrt{(x, x)}$. If a linear vector space is complete with respect to this norm, it is called Hilbert space.

A.3 L^p -spaces

Function spaces are vector spaces whose elements are functions. Given a function f_p defined over a domain Ω and a real number $p > 1$, the L^p -norm is introduced for these spaces as^b:

$$\|f_p\|_{L^p(\Omega)} \equiv \left(\int_{\Omega} |f_p|^p d\Omega \right)^{\frac{1}{p}}. \quad (\text{A.3})$$

The L here recall the Lebesgue measure used in the integral. The space $L^p(\Omega)$ is defined as the vector spaces comprising all and only the functions defined over Ω for which $\|f_p\| < \infty$. In the case of $p = 2$, the previous norm is induce by the following inner product:

$$(f, g)_{L^p(\Omega)} = \int_{\Omega} f \bar{g} d\Omega, \quad (\text{A.4})$$

in which the horizontal bar denotes the complex conjugate. Being complete, $L^2(\Omega)$ is a Hilbert space, the only one among L^p -spaces. Functions in $L^2(\Omega)$ are sometimes called square-integrable functions.

A space of fundamental importance is $L^1_{loc}(\Omega)$, of which any space $L^p(\Omega)$ is a subspace. Given any compact subset $K \subset \Omega$, a function f is an element of $L^1_{loc}(\Omega)$ if and only if:

$$\int_K |f| d\Omega < \infty, \quad \forall K \subset \Omega. \quad (\text{A.5})$$

A.4 Functionals and duality

Any linear operator $L : H \rightarrow \mathbb{R}$, with H Hilbert space, is called functional. The space of all functionals $L : H \rightarrow \mathbb{R}$ is called dual of H and is indicated with H^* . The action of a functional on an element $x \in H$ is here indicated with $\langle L, x \rangle_*$ ^c. Riesz's Representation Theorem states that, for each functional L there exists a vector $u_L \in H$ such that $\langle L, f \rangle_* = (u_L, f)_{H(\Omega)}$. Moreover, $\|L\|_{H^*(\Omega)} = \|u_L\|_{H(\Omega)}$.

A.5 Distributions

The space of all functions defined over a domain Ω owning derivatives up to the n -th order is called C^n . An important subspace of the space C^∞ is the one including all its elements whose

^aAn example of a vector space which is not a Banach space is the set of rational number \mathbb{Q} , in which the sequence

$$x_m = \left(1 + \frac{1}{m}\right)^m$$

is defined but does not converge (it does only in \mathbb{R}).

^bEquation A.3 represents L^p -norms in infinite dimensional spaces; in finite dimensional spaces, the L^p -norm is the following more intuitive generalization of the Euclidean norm:

$$\|x\|_{L^p(\Omega)} \equiv \left(\sum |x_i|^p \right)^{\frac{1}{p}},$$

in which x_i are the component of the vector x ; the Euclidean norm itself is the L^2 -norm.

^cThe simpler notation Lx is used as well, but this notation is preferred to emphasize duality.

support is compact. The support of a function “is given by the closure of the set of points where” the function “is different from zero”[126]. The notion of compactness is the generalization of the boundedness in finite-dimension spaces to infinite-dimension spaces. This new subspace, indicated as $C_0^\infty(\Omega)$, can be endowed with a notion of convergence. Given the operator:

$$D^\alpha = \frac{\partial^{\alpha_1}}{\partial \Omega_1^{\alpha_1}} \frac{\partial^{\alpha_2}}{\partial \Omega_2^{\alpha_2}} \cdots \frac{\partial^{\alpha_n}}{\partial \Omega_n^{\alpha_n}}, \quad \alpha = (\alpha_1, \alpha_2, \dots, \alpha_n),$$

a sequence $\{\varphi_k\} \in C_0^\infty(\Omega)$ converge to $\varphi \in C_0^\infty(\Omega)$ as $k \rightarrow \infty$ if:

1. $D^\alpha \varphi_k \rightarrow D^\alpha \varphi$ uniformly in $\Omega \forall \alpha$;
2. there exists a compact set $K \in \Omega$ containing the support of every φ_k .

The space $C_0^\infty(\Omega)$ endowed with such a notion of convergence is indicate as $\mathcal{D}(\Omega)$.

A linear continuous functional $I : \mathcal{D}(\Omega) \rightarrow \mathbb{R}$ is called distributions, and the set of all distributions is indicated with $\mathcal{D}'(\Omega)$. A distribution I_u can be found for each $u_I \in L_{loc}^1(\Omega)$ such that:

$$\langle I_u, \varphi \rangle_* = \int_{\Omega} u_I \varphi d\Omega. \quad (\text{A.6})$$

A.6 Distributional Derivatives and H^1 Sobolev spaces

In case a function is not differentiable, it is possible to build a weaker notion of derivative, called distributional. The trick is to integrate by part and let some ‘test’ functions carry the derivative; the ‘test’ functions used here are chosen to be elements $\varphi \in \mathcal{D}(\Omega)$, since they own derivatives of infinite order. The integration by part starts from the Gauss divergence theorem on a vector field \mathbf{F} defined over a domain Ω :

$$\int_{\Omega} \text{div} \mathbf{F} d\Omega = \int_{\Gamma} \mathbf{F} \cdot \nu d\Gamma, \quad (\text{A.7})$$

in which $d\Omega$ and $d\Gamma$ respectively denote the volume and surface measures on Ω and $\Gamma = \partial\Omega$, and ν denotes the outward unitary vector normal to Γ . Recalling that $\text{div}(v\mathbf{F}) = v \text{div} \mathbf{F} + \nabla v \cdot \mathbf{F}$, the application of Gauss theorem to $(v\mathbf{F})$ gives:

$$\int_{\Omega} v \text{div} \mathbf{F} d\Omega = \int_{\Gamma} v \mathbf{F} \cdot \nu d\Gamma - \int_{\Omega} \nabla v \cdot \mathbf{F} d\Omega. \quad (\text{A.8})$$

Finally, applying formula A.8 to the generic derivative $\frac{\partial u_I}{\partial \Omega_i}$, it comes:

$$\int_{\Omega} \varphi \frac{\partial u_I}{\partial \Omega_i} d\Omega = \int_{\Gamma} \varphi \frac{\partial u_I}{\partial \Omega_i} d\Gamma - \int_{\Omega} u_I \frac{\partial \varphi}{\partial \Omega_i} d\Omega = - \int_{\Omega} u_I \frac{\partial \varphi}{\partial \Omega_i} d\Omega \quad (\text{A.9})$$

since $\varphi = 0$ on $\partial\Omega$. If eq.A.9 is valid for any $\varphi \in \mathcal{D}(\Omega)$, it can be rewritten as:

$$\left\langle \frac{\partial I_u}{\partial \Omega_i}, \varphi \right\rangle_* = - \left\langle I_u, \frac{\partial \varphi}{\partial \Omega_i} \right\rangle_*, \quad \forall \varphi \in \mathcal{D}(\Omega), \quad (\text{A.10})$$

which is the relation defining the distributional derivative. That is, distributional derivative is not defined directly, but through its action on test functions. It is immediate to verify that any distribution possesses derivatives of any order, so that eq.A.10 can be further generalized:

$$\langle D^\alpha I_u, \varphi \rangle_* = (-1)^{|\alpha|} \langle I_u, D^\alpha \varphi \rangle_*, \quad \forall \varphi \in \mathcal{D}(\Omega). \quad (\text{A.11})$$

Distributional derivatives play a key role in the definition of the Sobolev space^d $H^1(\Omega)$. This is the space comprising all and only the functions in $L^2(\Omega)$ whose first partial derivatives in distributional sense are also part of $L^2(\Omega)$. The latter property can be written as:

$$\int_{\Omega} |\nabla f|^2 d\Omega < \infty. \quad (\text{A.12})$$

Since the last integral is often associated with energy, functions in the Sobolev space $H^1(\Omega)$ are associated with finite energy configurations. The inner product is defined as:

$$(f, g)_{H^1(\Omega)} = \int_{\Omega} fg \, d\Omega + \int_{\Omega} \nabla f \cdot \nabla g \, d\Omega, \quad (\text{A.13})$$

and the induced norm is immediately defined as $\|f\|_{H^1(\Omega)} = \sqrt{(f, f)_{H^1(\Omega)}}$.

^dThe general definition of a Sobolev space $W^{k,p}(\Omega)$ is not given here, but can be easily found in literature, including [56, 126]; spaces $W^{k,2}(\Omega)$ are often indicated as $H^k(\Omega)$, as it is done throughout this dissertation.

IN Chapter 2, the FEM has been introduced as a Galerkin method applied on a weak formulation of the Helmholtz problem via weighted residual. However, this way to define the FEM is not an appropriate way from a mathematical perspective. The purpose of this appendix is to introduce a stricter mathematical definition for the FEM and to add some extra insights helpful to better understand the topic.

Formally, a finite element is [60]:

- (1) a polytope Ω_j ;
- (2) a polynomial function space^a P on Ω_j equipped with a basis $\{S_l\}_{l=1}^n$, in which $n = \dim(P)$;
- (3) A set of functionals $L_i(\cdot)$, with $i = 1, 2, \dots, n$, such that $L_i(S_l) = \delta_{il}$.

There exist multiple ways to define the polynomial function space. For self-adjoint forms (as in the case of Helmholtz problems), the Galerkin method gives:

- (1) the minimum error in the energy norm [127];
- (2) systems of symmetric matrices [52].

Thus, such approximations are in a sense optimal, and therefore widely used; in fluid dynamics, the convective term $u \cdot \nabla u$ makes the forms associated to the weak formulation non self-adjoint, but in linear acoustics such term is deleted during the linearization of the Euler's equation. Other methods can be used to derive the FEM (see, for example, [52], chapter 3, and [127], chapter 2); for instance, the least square method always lead to symmetric matrices, even for forms that are not self-adjoint [52].

Not even the weighted residual method is necessary to the FEM; indeed, it can be obtained also from the variational form of a given problem, when available, via the Rayleigh-Ritz method, leading to the same result of the Galerkin method (see [52], appendix 3A.3, and [55], appendix A); a variational form of the Helmholtz equation is available in [52], example 3.3.

^aIf the function space is non-polynomial, the resulting elements are called generalized finite elements [72]

This appendix presents the figures related to the analysis of the numerical models' errors that have not been shown in Section 3.4.2 to avoid redundancy.

C.1 Response vector assurance criterion: matrices

This section shows the **RVAC** matrices for the fourteen models not shown. For obvious reason, the **RVAC** matrix of the reference is not shown: it has unitary values along the diagonal.

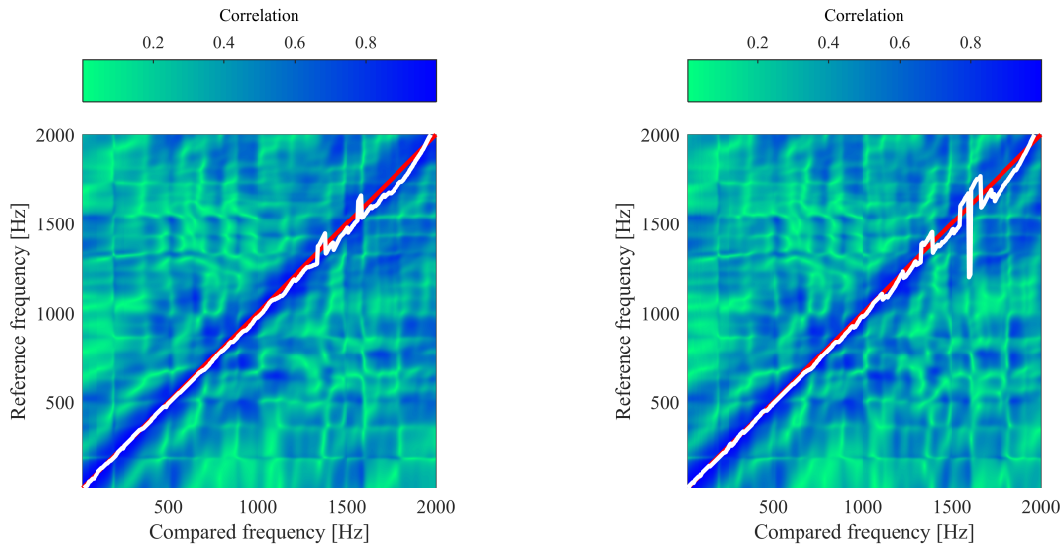


Figure C.1: **RVAC** matrix of the model with levels: $L[\mathfrak{N}] = 1$, $L[\mathfrak{p}_{FE}] = 1$, $L\left[\frac{t_{FE}}{\lambda}\right] = 1$ and $L\left[\frac{t_{pml}}{\lambda}\right] = 2$.

Figure C.2: **RVAC** matrix of the model with levels: $L[\mathfrak{N}] = 1$, $L[\mathfrak{p}_{FE}] = 1$, $L\left[\frac{t_{FE}}{\lambda}\right] = 2$ and $L\left[\frac{t_{pml}}{\lambda}\right] = 1$.

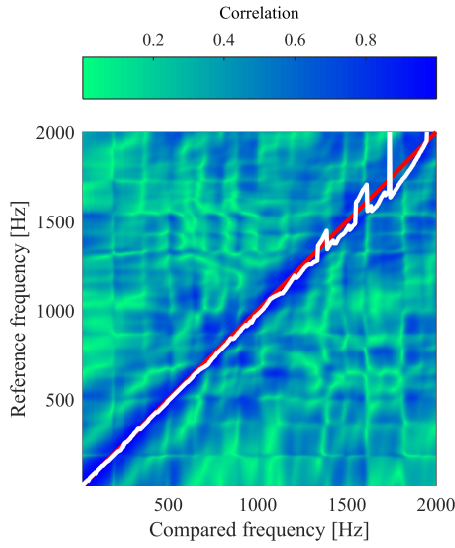


Figure C.3: **RVAC** matrix of the model with levels: $L[\mathfrak{N}] = 1$, $L[\mathfrak{p}_{FE}] = 1$, $L\left[\frac{t_{FE}}{\lambda}\right] = 2$ and $L\left[\frac{t_{pml}}{\lambda}\right] = 2$.

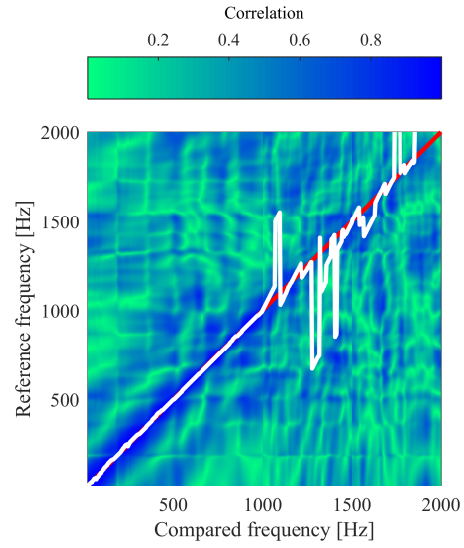


Figure C.4: **RVAC** matrix of the model with levels: $L[\mathfrak{N}] = 1$, $L[\mathfrak{p}_{FE}] = 2$, $L\left[\frac{t_{FE}}{\lambda}\right] = 1$ and $L\left[\frac{t_{pml}}{\lambda}\right] = 1$.

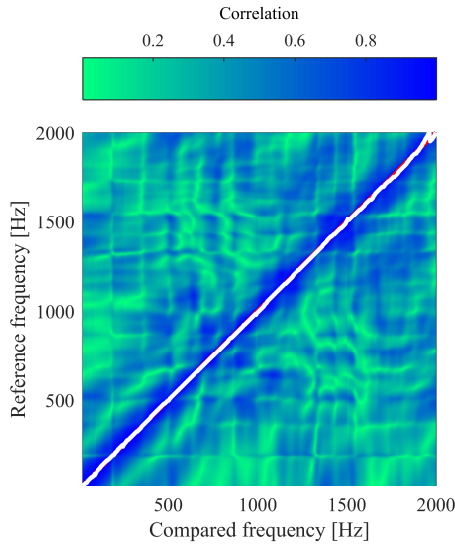


Figure C.5: **RVAC** matrix of the model with levels: $L[\mathfrak{N}] = 1$, $L[\mathfrak{p}_{FE}] = 2$, $L\left[\frac{t_{FE}}{\lambda}\right] = 1$ and $L\left[\frac{t_{pml}}{\lambda}\right] = 2$.

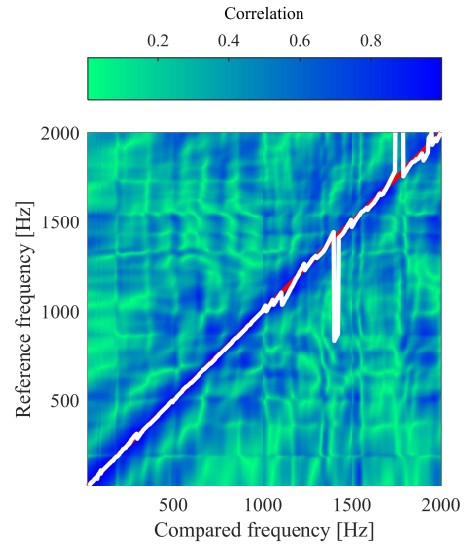


Figure C.6: **RVAC** matrix of the model with levels: $L[\mathfrak{N}] = 1$, $L[\mathfrak{p}_{FE}] = 2$, $L\left[\frac{t_{FE}}{\lambda}\right] = 2$ and $L\left[\frac{t_{pml}}{\lambda}\right] = 1$.

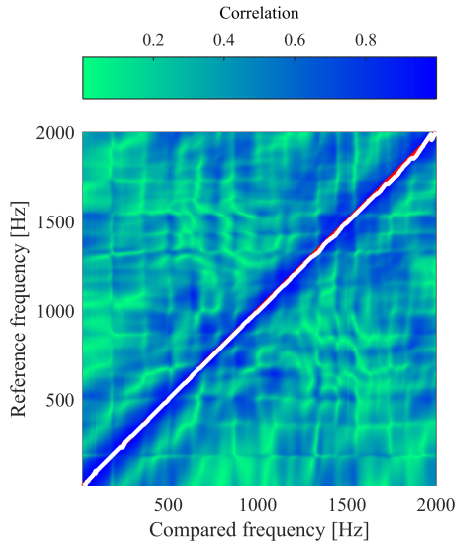


Figure C.7: **RVAC** matrix of the model with levels: $L[\mathfrak{N}] = 1$, $L[\mathfrak{p}_{FE}] = 2$, $L\left[\frac{t_{FE}}{\lambda}\right] = 2$ and $L\left[\frac{t_{pml}}{\lambda}\right] = 2$.

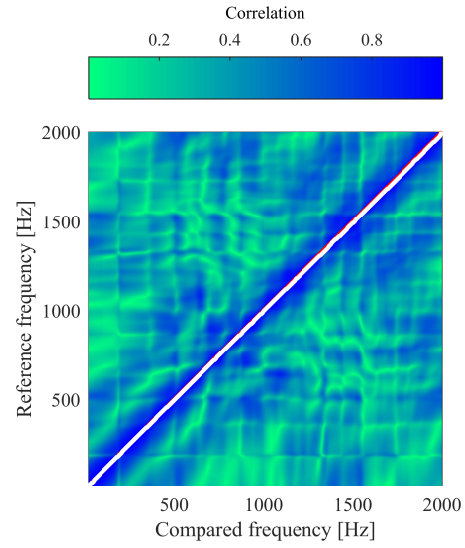


Figure C.8: **RVAC** matrix of the model with levels: $L[\mathfrak{N}] = 2$, $L[\mathfrak{p}_{FE}] = 1$, $L\left[\frac{t_{FE}}{\lambda}\right] = 1$ and $L\left[\frac{t_{pml}}{\lambda}\right] = 1$.

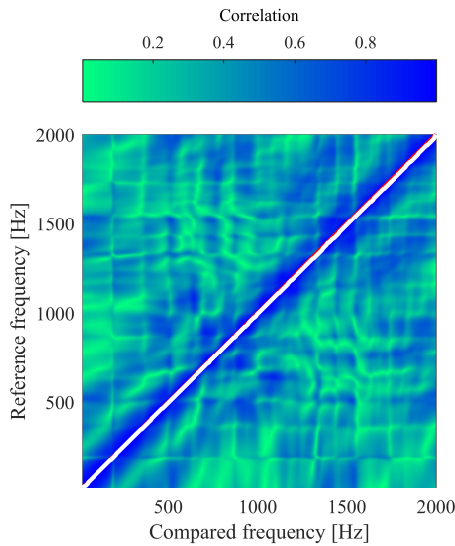


Figure C.9: **RVAC** matrix of the model with levels: $L[\mathfrak{N}] = 2$, $L[\mathfrak{p}_{FE}] = 1$, $L\left[\frac{t_{FE}}{\lambda}\right] = 1$ and $L\left[\frac{t_{pml}}{\lambda}\right] = 2$.

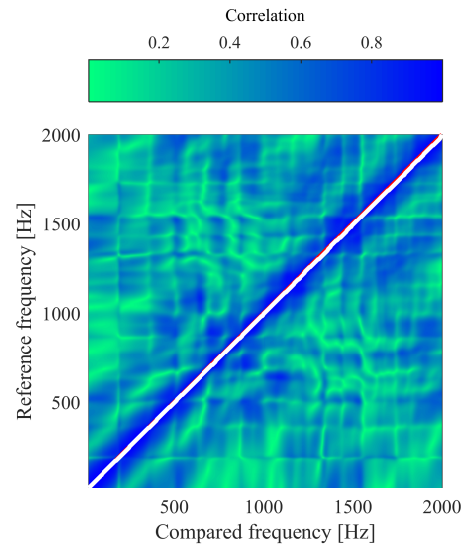


Figure C.10: **RVAC** matrix of the model with levels: $L[\mathfrak{N}] = 2$, $L[\mathfrak{p}_{FE}] = 1$, $L\left[\frac{t_{FE}}{\lambda}\right] = 2$ and $L\left[\frac{t_{pml}}{\lambda}\right] = 1$.

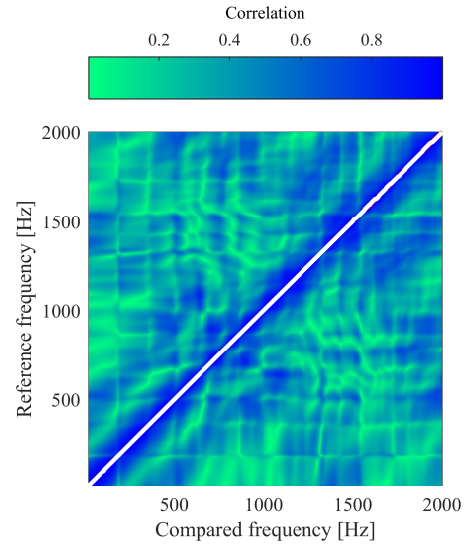
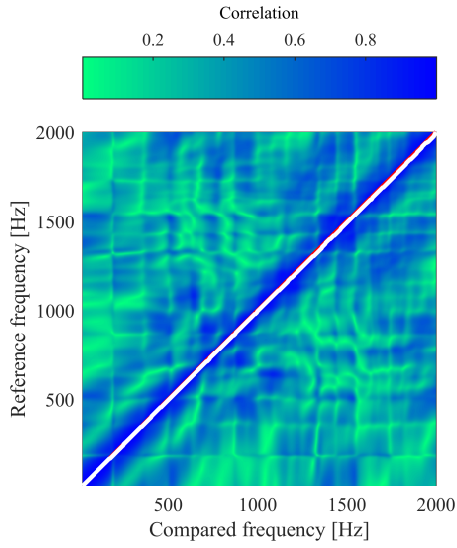


Figure C.11: **RVAC** matrix of the model with levels: $L[\mathfrak{N}] = 2$, $L[\mathfrak{p}_{FE}] = 1$, $L\left[\frac{t_{FE}}{\lambda}\right] = 2$ and $L\left[\frac{t_{pml}}{\lambda}\right] = 2$. Figure C.12: **RVAC** matrix of the model with levels: $L[\mathfrak{N}] = 2$, $L[\mathfrak{p}_{FE}] = 2$, $L\left[\frac{t_{FE}}{\lambda}\right] = 1$ and $L\left[\frac{t_{pml}}{\lambda}\right] = 1$.

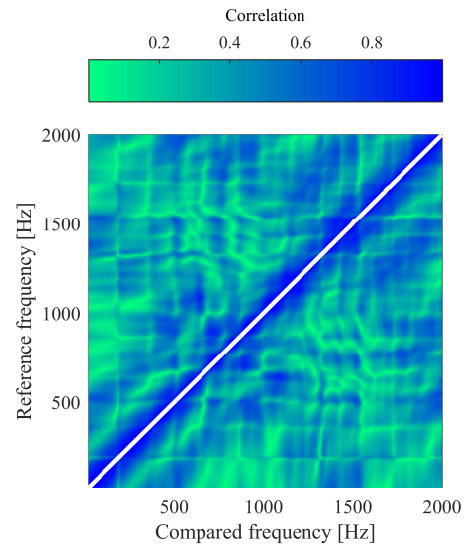
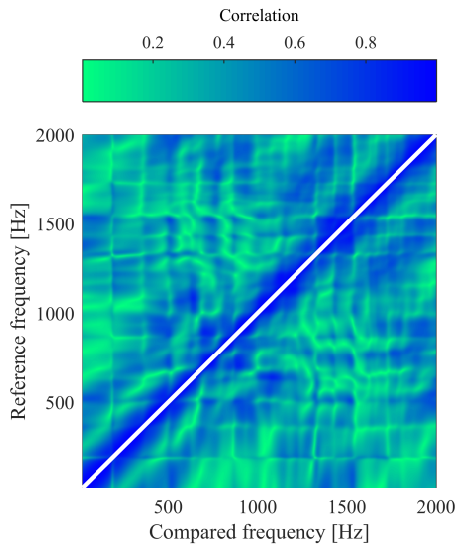


Figure C.13: **RVAC** matrix of the model with levels: $L[\mathfrak{N}] = 2$, $L[\mathfrak{p}_{FE}] = 2$, $L\left[\frac{t_{FE}}{\lambda}\right] = 1$ and $L\left[\frac{t_{pml}}{\lambda}\right] = 2$. Figure C.14: **RVAC** matrix of the model with levels: $L[\mathfrak{N}] = 2$, $L[\mathfrak{p}_{FE}] = 2$, $L\left[\frac{t_{FE}}{\lambda}\right] = 2$ and $L\left[\frac{t_{pml}}{\lambda}\right] = 1$.

C.2 Response vector assurance criterion: vectors

This section shows the $RVAC$ vectors (black continuous line, left y-axis) and $\Delta f(f_{ref})$ (black dashed line, right y-axis) for the other fourteen models. Even in this case, the $RVAC$ vector of the reference is not shown: it is a unitary vector, and the $\Delta f(f_{ref})$ is a null vector.

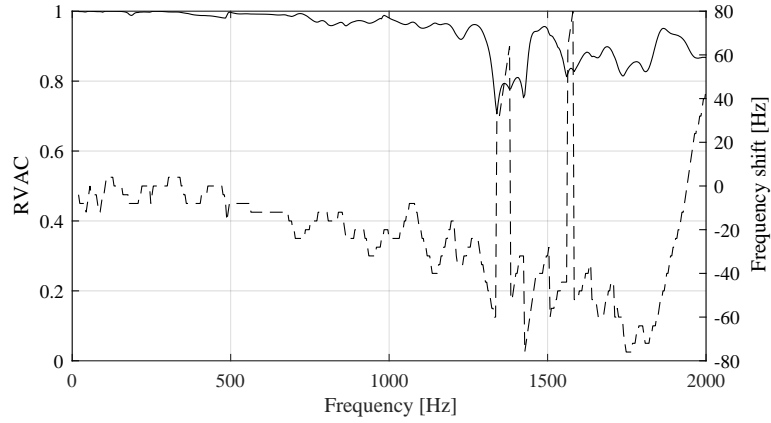


Figure C.15: $RVAC$ and Δf of the model with levels: $L[\mathfrak{N}] = 1$, $L[\mathbf{p}_{FE}] = 1$, $L\left[\frac{t_{FE}}{\lambda}\right] = 1$ and $L\left[\frac{t_{pml}}{\lambda}\right] = 2$.

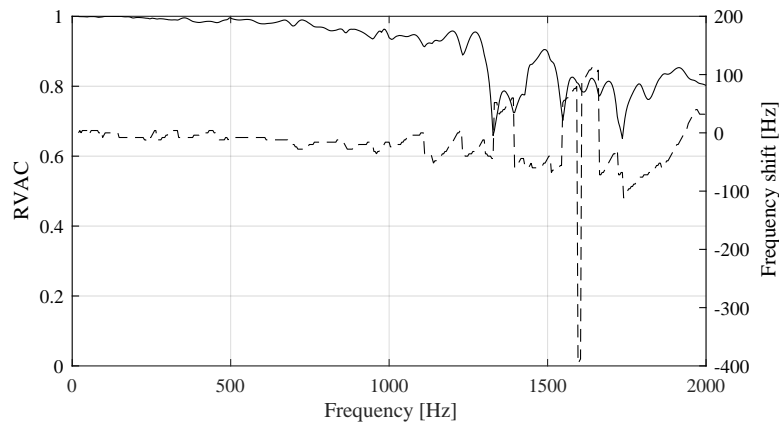


Figure C.16: $RVAC$ and Δf of the model with levels: $L[\mathfrak{N}] = 1$, $L[\mathbf{p}_{FE}] = 1$, $L\left[\frac{t_{FE}}{\lambda}\right] = 2$ and $L\left[\frac{t_{pml}}{\lambda}\right] = 1$.

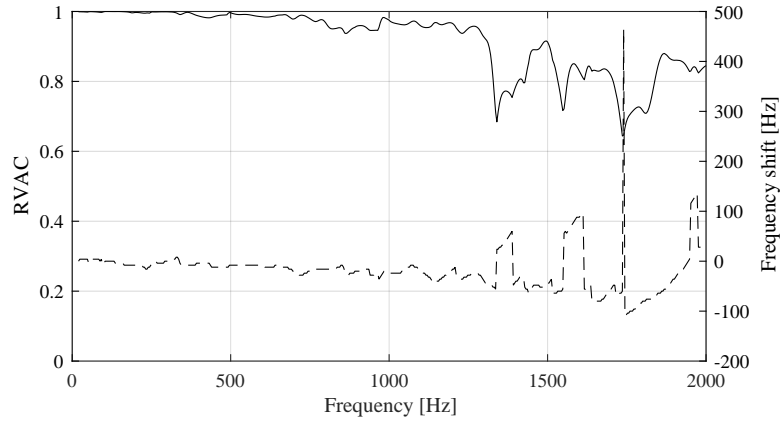


Figure C.17: $RVAC$ and Δf of the model with levels: $L[\mathfrak{N}] = 1$, $L[\mathbf{p}_{FE}] = 1$, $L\left[\frac{t_{FE}}{\lambda}\right] = 2$ and $L\left[\frac{t_{pml}}{\lambda}\right] = 2$.

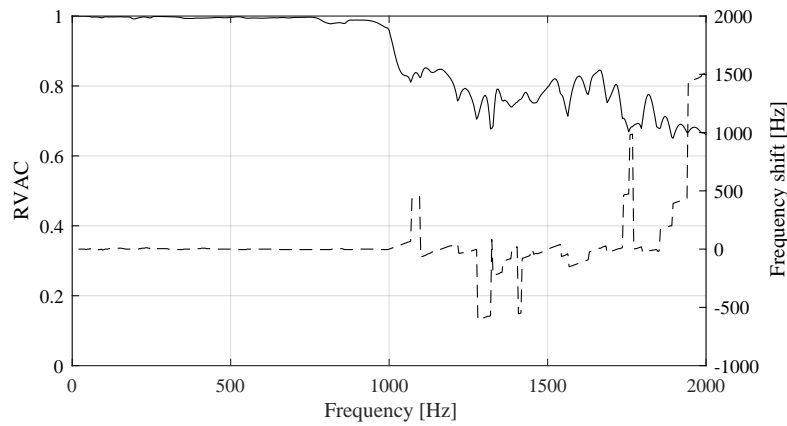


Figure C.18: $RVAC$ and Δf of the model with levels: $L[\mathfrak{N}] = 1$, $L[\mathbf{p}_{FE}] = 2$, $L\left[\frac{t_{FE}}{\lambda}\right] = 1$ and $L\left[\frac{t_{pml}}{\lambda}\right] = 1$.

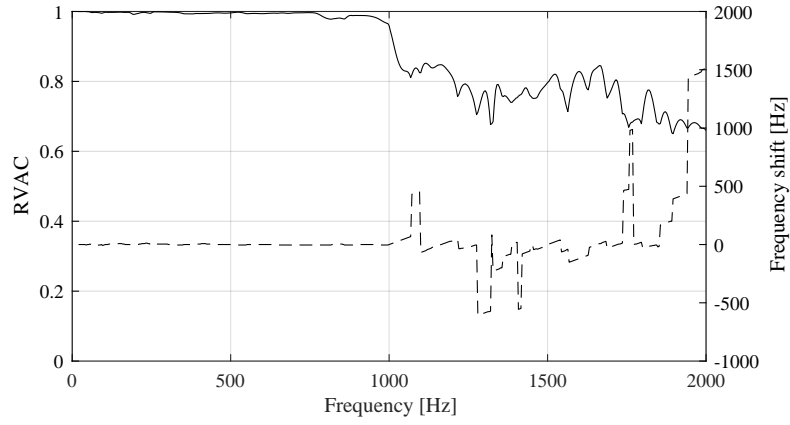


Figure C.19: $RVAC$ and Δf of the model with levels: $L[\mathfrak{N}] = 1$, $L[\mathbf{p}_{FE}] = 2$, $L\left[\frac{t_{FE}}{\lambda}\right] = 1$ and $L\left[\frac{t_{pml}}{\lambda}\right] = 1$.

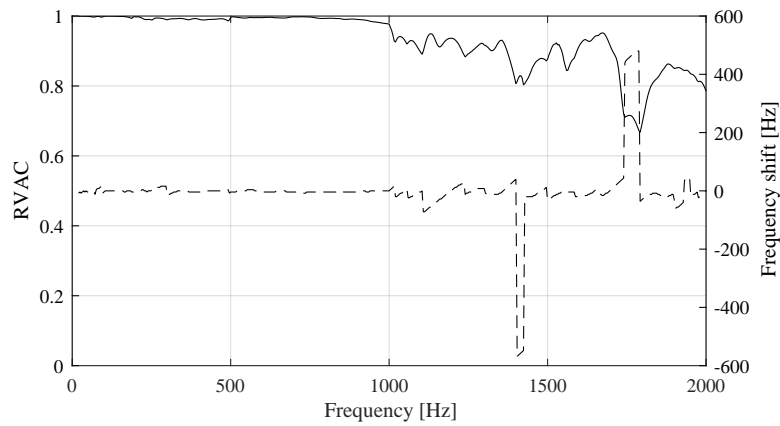


Figure C.20: $RVAC$ and Δf of the model with levels: $L[\mathfrak{N}] = 1$, $L[\mathbf{p}_{FE}] = 2$, $L\left[\frac{t_{FE}}{\lambda}\right] = 2$ and $L\left[\frac{t_{pml}}{\lambda}\right] = 1$.

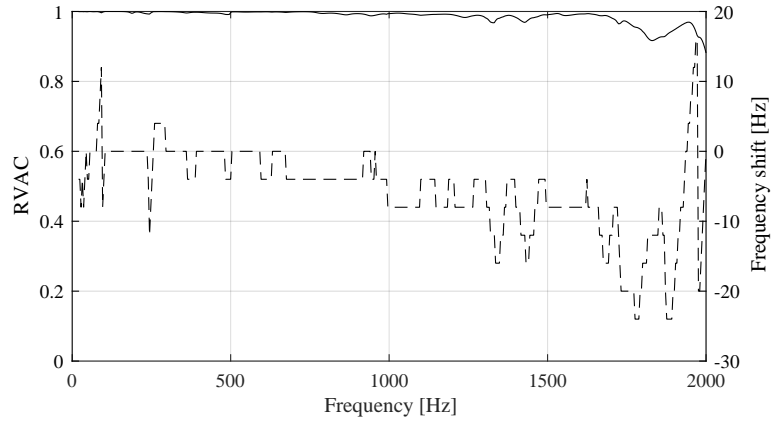


Figure C.21: $RVAC$ and Δf of the model with levels: $L[\mathfrak{N}] = 1$, $L[\mathbf{p}_{FE}] = 2$, $L\left[\frac{t_{FE}}{\lambda}\right] = 2$ and $L\left[\frac{t_{pml}}{\lambda}\right] = 2$.

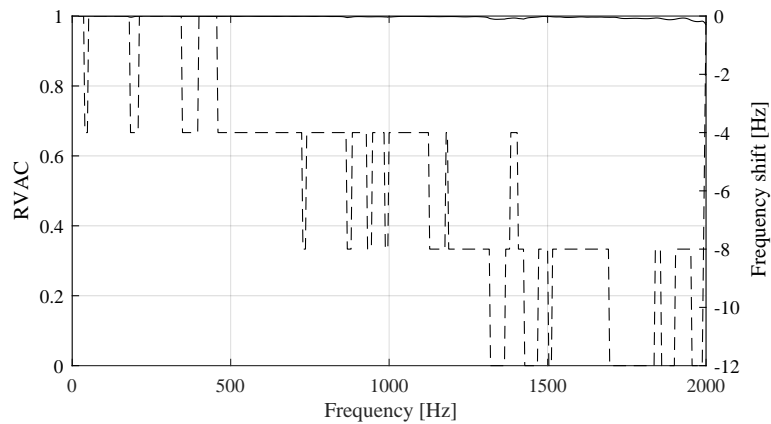


Figure C.22: $RVAC$ and Δf of the model with levels: $L[\mathfrak{N}] = 2$, $L[\mathbf{p}_{FE}] = 1$, $L\left[\frac{t_{FE}}{\lambda}\right] = 1$ and $L\left[\frac{t_{pml}}{\lambda}\right] = 1$.

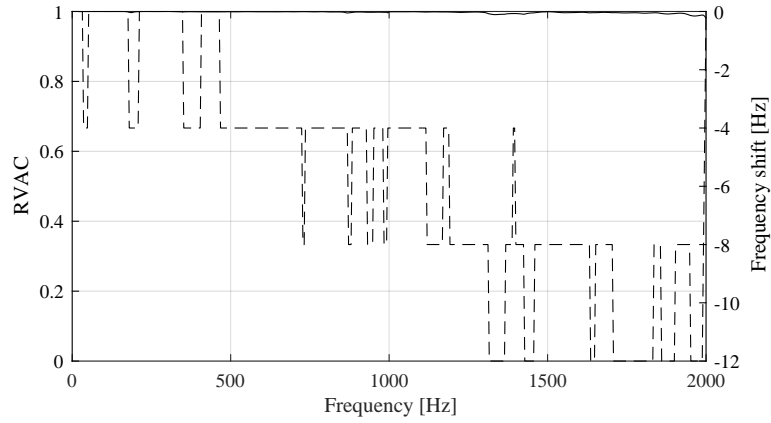


Figure C.23: $RVAC$ and Δf of the model with levels: $L[\mathfrak{N}] = 2$, $L[\mathbf{p}_{FE}] = 1$, $L\left[\frac{t_{FE}}{\lambda}\right] = 1$ and $L\left[\frac{t_{pml}}{\lambda}\right] = 2$.

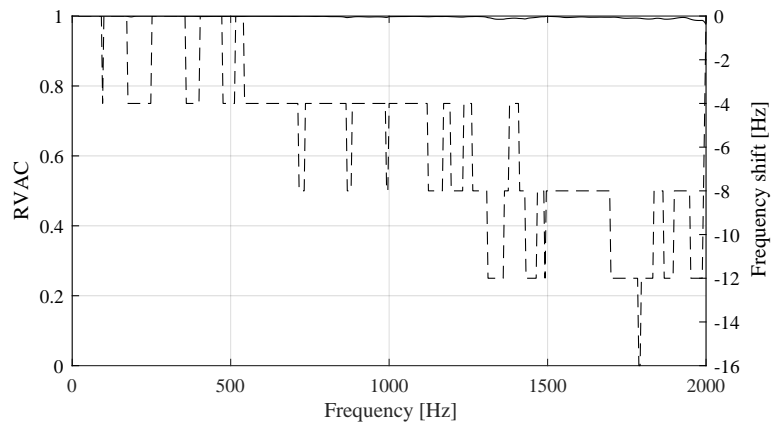


Figure C.24: $RVAC$ and Δf of the model with levels: $L[\mathfrak{N}] = 2$, $L[\mathbf{p}_{FE}] = 1$, $L\left[\frac{t_{FE}}{\lambda}\right] = 2$ and $L\left[\frac{t_{pml}}{\lambda}\right] = 1$.

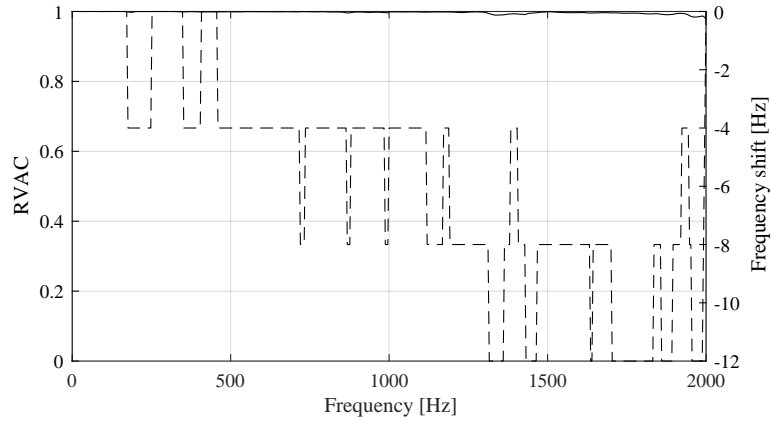


Figure C.25: $RVAC$ and Δf of the model with levels: $L[\mathfrak{N}] = 2$, $L[\mathbf{p}_{FE}] = 1$, $L\left[\frac{t_{FE}}{\lambda}\right] = 2$ and $L\left[\frac{t_{pml}}{\lambda}\right] = 2$.

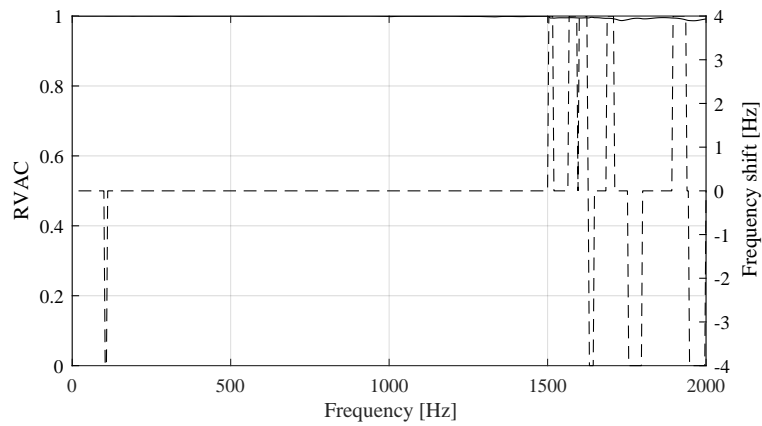


Figure C.26: $RVAC$ and Δf of the model with levels: $L[\mathfrak{N}] = 2$, $L[\mathbf{p}_{FE}] = 2$, $L\left[\frac{t_{FE}}{\lambda}\right] = 1$ and $L\left[\frac{t_{pml}}{\lambda}\right] = 1$.

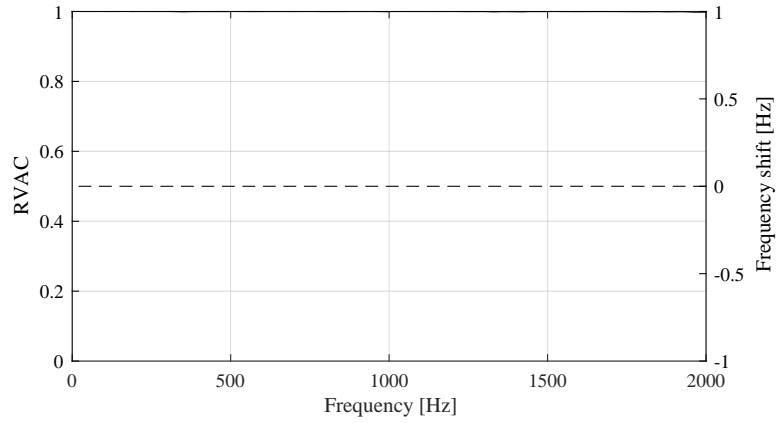


Figure C.27: $RVAC$ and Δf of the model with levels: $L[\mathfrak{N}] = 2$, $L[\mathbf{p}_{FE}] = 2$, $L\left[\frac{t_{FE}}{\lambda}\right] = 1$ and $L\left[\frac{t_{pml}}{\lambda}\right] = 2$.

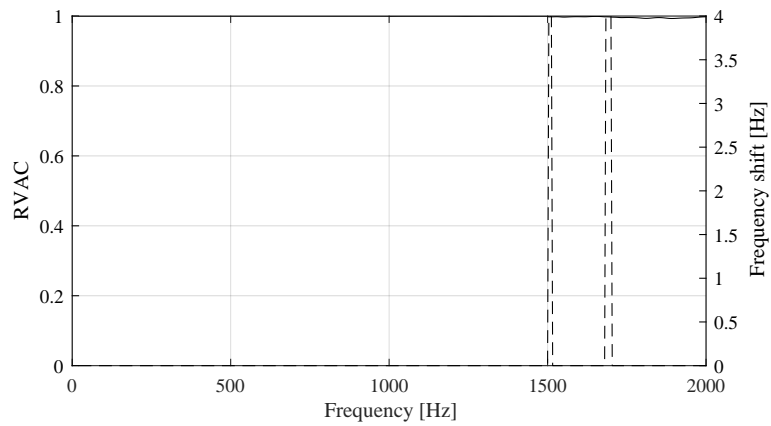


Figure C.28: $RVAC$ and Δf of the model with levels: $L[\mathfrak{N}] = 2$, $L[\mathbf{p}_{FE}] = 2$, $L\left[\frac{t_{FE}}{\lambda}\right] = 2$ and $L\left[\frac{t_{pml}}{\lambda}\right] = 1$.

D.1 The infinite element method

Here, the infinite elements method (IEM) is considered. This methodology rely on an extra layer of discrete elements, the IEs, in charge of the propagation of the acoustic field towards the infinity. From a geometrical perspective, IEs similar to FEs in that they have nodes and shape functions. However, the calculation of IE shape functions is somewhat more complicated than their finite counterpart. Introductions to the IEM are available in literature; the following is a summary of reference [91], with a focus on infinite elements for spherical geometries^a. Extension to meshes for more general geometries are discussed later on.

As a first step, a spherical volume $\Omega_R \supset \Omega_{FE}$ delimited by a surface Γ_R is defined (see fig. D.1). The radius of Γ_R and is indicated here with R . The Sommerfeld radiation condition 2.7 is then approximated by removing the limit and equating the left hand side to zero at large distances from the source, resulting in:

$$\nabla p = -ikp. \quad (D.1)$$

Such a termination, called ρc , is imposed on Γ_R , so that eq. 2.8 is reformulated into the following equation [91]:

$$\int_{\Omega} (\nabla \chi \cdot \nabla p - \chi k^2 p) d\Omega - sk \int_{\Gamma} \chi (Yp + u_s) d\Gamma + ik \int_{\Gamma_R} \chi p d\Gamma_R = 0, \quad \forall \chi \in W(\Omega). \quad (D.2)$$

The computational domain Ω_R is then discretized in FEs (covering Ω_{FE}) and IEs (covering $\Omega_{IE} = \Omega_R - \Omega_{FE}$). This equation is discretized according to the Galerking projection 2.9. Shape functions of FEs do not change with respect to the case of the bounded problem. The contribution of IEs to the matrices of the problem come from the following terms:

$$A = \lim_{R \rightarrow \infty} \int_{\Omega_R - \Omega_{FE}} (\nabla \varrho_i \cdot \nabla \phi^{(IE)} - k^2 \varrho_i \phi^{(IE)}) d\Omega + ik \int_{\Gamma_R} \varrho_i \phi^{(IE)} d\Gamma_R, \quad (D.3)$$

where $\phi^{(IE)}$ are chosen as a product of interpolation functions in radial and transverse direction; by referring to figure D.2, given the nodes $\alpha = i_\mu$ and $\beta = i_\nu$:

$$\phi_\alpha^{(IE)} = g_i(\theta) f_\mu(r, \omega) \quad \text{and} \quad \phi_\beta^{(IE)} = g_j(\theta) f_\nu(r, \omega), \quad \mu, \nu = 1, 2, \dots, q \quad (D.4)$$

^aThe discussion focus on 3-dimensional IEM; mono-dimensional elements are slightly different, but not interesting for the purpose of the present work.

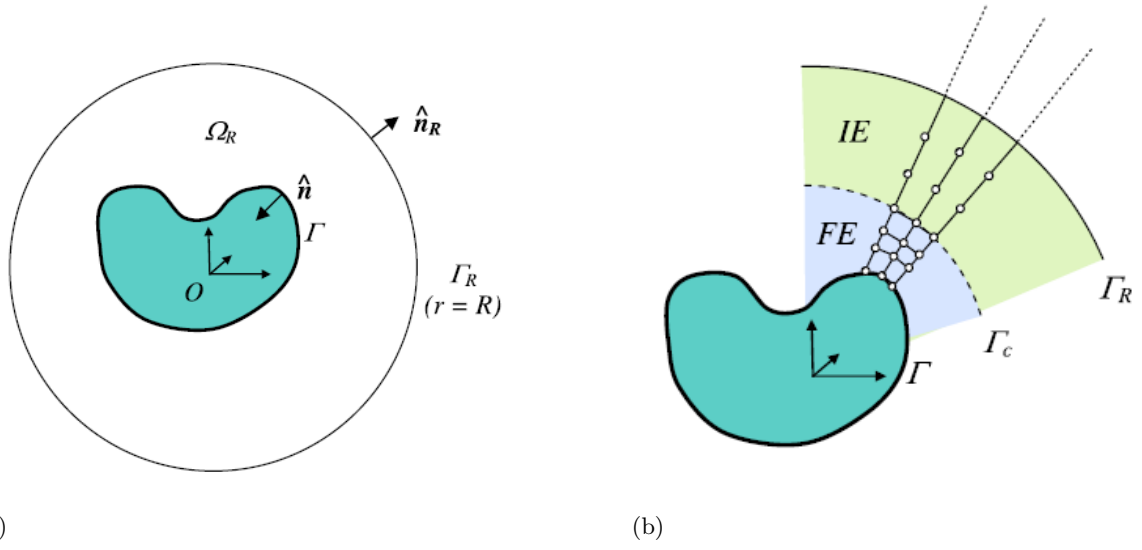


Figure D.1: The FE/IE model:(a) Modified domain with a far field boundary. (b) Finite element (FE) and infinite element (IE) meshes [91]

where q refers to the number of nodes in the radial direction, r is the radial direction and $g_i(\theta)$ is the following interpolation function:

$$g_i(\theta) = \frac{\theta - \theta_j}{\theta_i - \theta_j} \quad \text{and} \quad g_j(\theta) = \frac{\theta - \theta_i}{\theta_j - \theta_i}. \quad (\text{D.5})$$

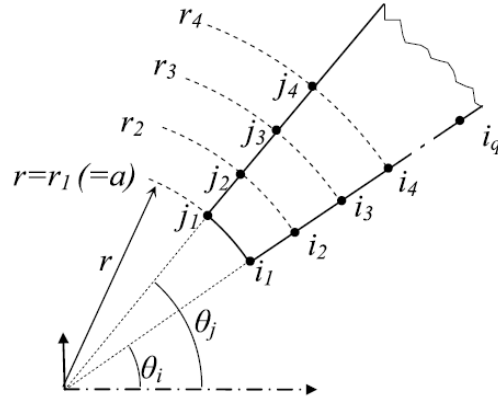


Figure D.2: Geometry of an infinite element [91].

The radial functions $f_\mu(r, \omega)$ and $f_\nu(r, \omega)$ need to ensure an appropriate radiation condition. To do so, first, the following, well-known, multi-pole expansion is considered [91]:

$$p(\mathbf{x}, \omega) = e^{-ikr} \sum_{n=1}^{\infty} \frac{G_n(r, \theta, \varphi)}{r^n}, \quad (\text{D.6})$$

where r , θ and φ are the spherical coordinates and $G_n(r, \theta, \varphi)$ is a directivity function associated with the n^{th} inverse power of the radius^b. The radial functions $f_\mu(r, \omega)$ are chosen to propagate

^bSee [91] for details about the construction of $G_n(r, \theta, \varphi)$.

towards the infinity the first \mathfrak{p}_{IE} terms of the multi-pole D.6, resulting in:

$$f_{\mu}(r, \omega) = \left(\frac{r_{\mu}}{r}\right) \prod_{\nu=1(\neq\mu)}^{\mathfrak{p}_{IE}} \frac{r - r_{\nu}}{r_{\mu} - r_{\nu}} e^{-ik(r-r_{\mu})}. \quad (\text{D.7})$$

The previous concepts can be extended to non spherical FE meshes thanks to mapped elements, which allow IEs to lie on generic surfaces Γ_A (which is the artificial boundary separating the FE mesh from the IE layer). However, the user must always take into account the so called Atkinson-Wilcox theorem [85], that dictates sufficient conditions for the multi-pole expansion D.6 to work. In details, the sound field outside a sphere Γ_A can always be written in form of D.6 if the sphere encloses all radiating and scattering sources. An extension of this theorem to elliptic coordinates exists [93], which implies that Γ_A can be a spheroidal surface. Some software, including Actran [81], use a curvilinear coordinate system, but restriction on the spheroidal surface Γ_A do not change.

From a user perspective, two factors are critical when using the IEM. First, the mesh must satisfy a version of the Atkinson-Wilcox theorem; the requirements to satisfy the theorem may be more complicated of what described here, so it is critical to read and understand the user manual. The second point, which is of critical importance within this work, is an appropriate choice of the order of IE interpolation \mathfrak{p}_{IE} in equation D.7, since it dictates the accuracy of the simulation.

D.2 Infinite element performances

An exhaustive analysis of IE performances is available in [91]. In this section, a simple analysis is shown with the purpose to compare the following results with the ones obtained with PML in Section 2.5. Here, the geometry in Figure 2.7 is discretized with linear FE of size $\mathfrak{h} = 0.009$ m and $\mathfrak{h} = 0.018$ m, thus maintaining the number of nodes per wavelengths \mathfrak{N} constant. These FE meshes are the same used for the numerical experiments in Section 2.5. However, the Sommerfeld radiation condition is now ensured by IE of order $\mathfrak{p}_{IE} = 4$. The choice of the order four is almost arbitrary here; indeed, since this scenario is a monopole in the free space, in theory even the minimum order allowed by the software (namely, $\mathfrak{p}_{IE} = 2$) would be sufficient. The order was slightly increased to avoid minor mistakes due to the discretization. Figure D.3 shows the results: in red (plus signes) one calculated with linear elements of average size $\mathfrak{h} = 0.009$ m, in green (asterisks) another calculated with with linear elements of average size $\mathfrak{h} = 0.037$ m. The spectra are not flat, instead they have a wave-like shape similar to the one obtained with PML. Also, even in this case (as for PML), lower numbers of elements per wavelength lead to a reduce amplitude at high frequencies. Lastly, the wave-like shape is less pronounced than in the PML case.

Figure D.4 shows two spectra obtained with linear FE of size $\mathfrak{h} = 0.009$ m (red plus signs) and with quadratic FE of size $\mathfrak{h} = 0.018$ m (blue asterisks), thus maintaining the number of nodes per wavelengths \mathfrak{N} constant. In this case, the accuracy of the quadratic elements is noticeably better. This fact is in contrast with what obtained with PML (see Section 2.5), and suggests that the higher energy of the spectra calculated with PML and quadratic elements (in comparison with PML and linear elements, see see Figures 2.9 and 2.10) is caused by an interaction between the PML and the FE formulations.

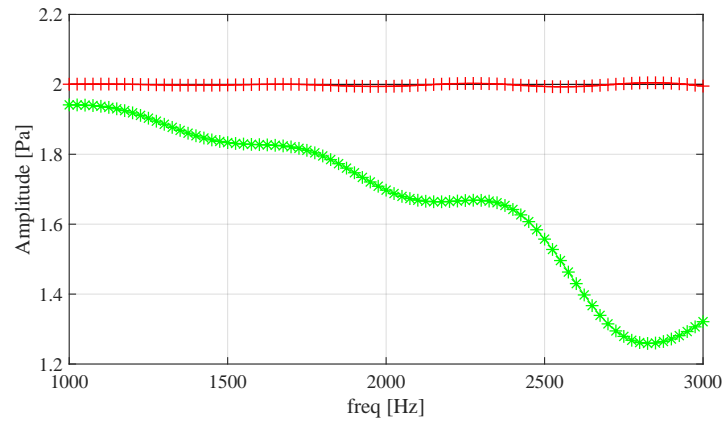


Figure D.3: Spectra of the receiver in Figure 2.7 (a) calculated via linear FE with average size of elements $h = 0.009$ m (red plus signs), and $h = 0.037$ m (green asterisks); the theoretical spectrum is in black.

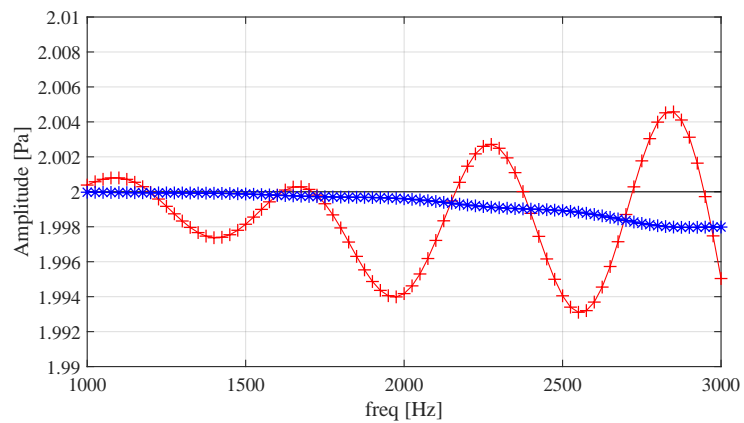


Figure D.4: Spectra of the receiver in Figure 2.7 (a) calculated via linear FE of size $h = 0.009$ m (red plus signs) and via quadratic FE of size $h = 0.018$ m (blue asterisks); the theoretical spectrum is in black.

Detailed effect of PML thickness on the acoustic samples

Figures 3.21 to 3.23 clearly show the effect of parameters \mathfrak{N} and \mathfrak{p}_{FE} on the metrics $SPL(A)$, N and S , but do not say much about the influence of parameters t_{PML} and t_{FE} . To overcome this limitation, some tables have been built.

Table E.1 focuses on $SPL(A)$. The first column on the left indicates the TPs; the last five TPs are the ones used for the jury tests. All the other columns indicate the $SPL(A)$ variation per model due to t_{PML} decreases. For instance, the column associated to $L[\mathfrak{N}]=1$, $L[\mathfrak{p}_{FE}]=1$ and $L\left[\frac{t_{FE}}{\lambda}\right]=1$ indicate, for each TP, the $SPL(A)$ difference between the sounds auralized with the above mentioned parameters and $L\left[\frac{t_{FE}}{\lambda}\right]=1$, and the above mentioned parameters and $L\left[\frac{t_{FE}}{\lambda}\right]=2$. According to the most basic theoretical description, a decrease in the PML thickness should lead to an increase of energy in the simulated TF and, consequently, in the auralized sound. In practice, this energy increase is not always met due to the interaction mentioned in Section 2.5. In the table, the decreases in energy result in a negative variation of $SPL(A)$ and are highlighted in bold. Tables E.2 and E.3 are built following the same principles, but shows the ratios between the loudness N and the sharpness S , respectively.

The general trend is that, at high nodal resolution ($L[\mathfrak{N}]=2$), the change of these metrics are relatively low; furthermore, for $SPL(A)$ and N , most models show an increase of energy for a decrease of PML thickness. At low nodal resolution ($L[\mathfrak{N}]=1$) and quadratic order of polynomial shape functions ($L[\mathfrak{p}_{FE}]=2$), the same trend is present, but the variations are higher, with loudness ratio sometimes approaching or surpassing the just noticeable difference threshold (variation higher than 10%). Lastly, for ($L[\mathfrak{N}]=1$) and linear FEs ($L[\mathfrak{p}_{FE}]=1$), no trend is immediately visible.

Similar tables have been built for the parameter t_{FE} , but no trend appeared, as expected. Indeed, the error introduced by a change of the FE volume (being it in terms of size or shape) change only the discretization patterns. To avoid redundancy, these tables are not shown.

		SPL(A) increase by model [dB(A)]							
TP	$L[\mathfrak{N}]$	1	1	1	1	2	2	2	2
	$L[\mathfrak{p}_{FE}]$	1	1	2	2	1	1	2	2
	$L\left[\frac{t_{FE}}{\lambda}\right]$	1	2	1	2	1	2	1	2
lg01		0.108	0.017	0.256	0.376	0.038	0.023	0.062	0.020
lp01		-0.208	-0.160	0.350	0.111	0.050	-0.003	0.054	0.014
rp01		-0.049	-0.184	0.319	0.028	0.057	-0.001	0.056	0.041
lg02		0.092	-0.136	0.418	0.382	0.073	0.076	0.084	0.044
rg02		0.031	-0.026	0.333	0.384	0.106	0.090	0.083	0.049
lp02		-0.264	-0.057	0.738	0.644	0.140	0.049	0.065	-0.001
lp11		0.027	-0.067	0.082	0.202	0.088	0.031	0.065	0.049
rp11		-0.124	-0.150	0.299	0.411	0.075	0.010	0.070	0.042
lg12		0.147	0.246	1.677	0.678	0.064	0.073	0.036	0.050
rg12		0.216	-0.061	0.323	0.196	0.077	0.060	0.052	0.0615
rp12		0.053	0.018	0.164	0.208	0.089	0.079	0.066	0.053
rg01		0.217	0.061	0.292	0.450	0.036	0.031	0.056	0.0270
rp02		-0.235	-0.167	0.561	0.358	0.128	0.067	0.077	0.027
lg11		0.329	0.071	0.526	0.401	0.119	0.065	0.115	0.072
rg11		-0.032	0.135	0.092	0.014	0.073	0.025	0.086	0.049
lp12		0.144	-0.011	0.475	0.361	0.075	0.078	0.073	0.077

Table E.1: SPL(A) increases due to PML thickness by model.

		N increase by model [sonie]							
TP	$L[\mathfrak{N}]$	1	1	1	1	2	2	2	2
	$L[\mathfrak{p}_{FE}]$	1	1	2	2	1	1	2	2
	$L\left[\frac{t_{FE}}{\lambda}\right]$	1	2	1	2	1	2	1	2
lg01		1.033	1.019	1.045	1.033	1.003	1.001	1.007	1.003
lp01		1.009	1.006	1.042	1.037	1.002	1.002	1.007	0.999
rp01		1.020	0.997	1.023	1.026	1.003	1.001	1.009	1.001
lg02		1.006	0.995	1.096	1.038	1.004	1.004	1.006	1.006
rg02		1.003	0.996	1.067	1.040	1.005	1.005	1.005	1.005
lp02		0.985	1.009	1.083	1.068	1.007	1.005	1.004	1.000
rg11		0.997	1.008	0.994	1.002	1.006	1.002	1.007	1.003
lp11		0.983	1.004	1.016	1.018	1.010	1.005	1.006	1.002
lg12		1.016	1.008	1.168	1.087	1.004	1.007	1.003	0.998
rg12		1.012	1.006	1.053	1.021	1.006	1.004	1.002	1.004
rp12		1.009	1.000	1.054	1.024	1.006	1.005	1.004	1.004
rg01		1.038	1.010	1.056	1.045	1.003	1.000	1.009	1.004
rp02		0.984	0.999	1.083	1.051	1.007	1.005	1.003	1.002
lg11		1.008	1.025	1.092	1.053	1.009	1.004	1.007	1.005
rp11		0.995	0.992	1.029	1.022	1.005	1.001	1.005	1.004
lp12		1.002	0.991	1.100	1.047	1.003	1.006	1.003	1.004

Table E.2: Loudness N increases due to PML thickness by model.

		S increase by model [acuum]							
TP	$L[\mathfrak{N}]$	1	1	1	1	2	2	2	2
	$L[\mathfrak{p}_{FE}]$	1	1	2	2	1	1	2	2
	$L\left[\frac{t_{FE}}{\lambda}\right]$	1	2	1	2	1	2	1	2
lg01		1.033	1.008	1.027	1.014	0.999	1.000	1.004	1.002
lp01		1.020	0.996	1.025	1.021	0.997	1.002	1.004	0.998
rp01		1.020	1.004	1.006	1.025	0.997	1.002	1.006	0.999
lg02		1.011	1.003	1.075	1.022	0.998	1.000	0.999	1.004
rg02		1.007	0.999	1.051	1.022	0.999	1.001	1.000	1.004
lp02		1.003	1.016	1.052	1.044	0.999	1.002	0.999	1.000
rg11		1.005	1.002	0.991	0.996	1.001	1.001	1.003	1.002
lp11		0.979	0.989	1.011	1.004	1.005	1.004	1.004	1.000
lg12		1.014	1.000	1.094	1.053	0.999	1.004	0.998	0.995
rg12		1.006	1.007	1.038	1.008	1.000	1.000	0.998	1.001
rp12		1.011	1.000	1.055	1.010	1.001	1.001	1.000	1.001
rg01		1.030	1.005	1.033	1.028	0.999	1.000	1.005	1.002
rp02		0.992	1.010	1.062	1.035	0.999	1.002	0.998	1.002
lg11		1.000	1.007	1.059	1.030	1.004	1.003	1.002	1.003
rp11		1.008	1.000	1.026	1.007	1.001	1.000	1.002	1.003
lp12		1.005	0.990	1.074	1.030	0.996	1.002	0.998	1.001

Table E.3: Sharpness S increases due to PML thickness by model.

This appendix presents the figures related to the jury tests that have not been shown in Chapter 4 to avoid redundancy.

F.1 Correlation tables

In Section 4.2, Figure 4.7 shows the correlation matrices in the case of TPs G-11 (a) and S+20 (b); participant 18 performed in all the other cases as in S+20. Here the other three cases are shown.

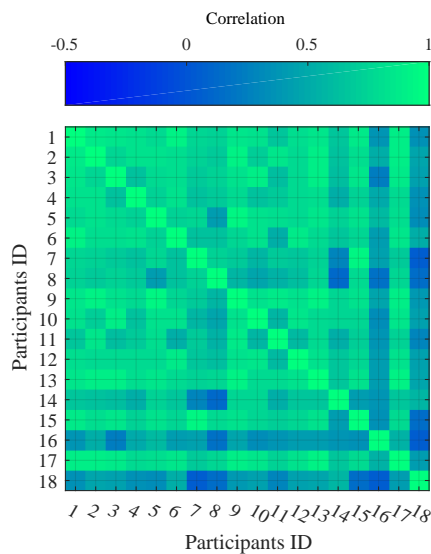


Figure F.1: Correlation matrix in the case of TP S-21.

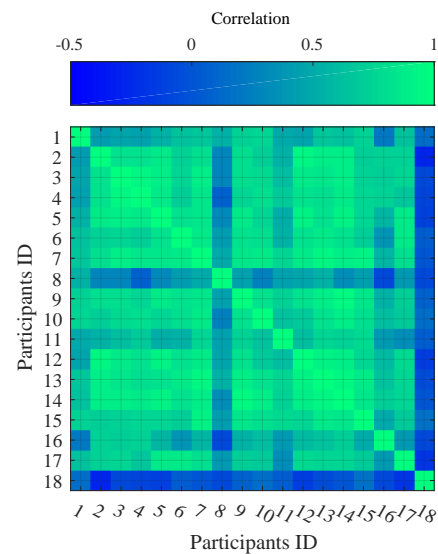


Figure F.2: Correlation matrix in the case of TP G+10.

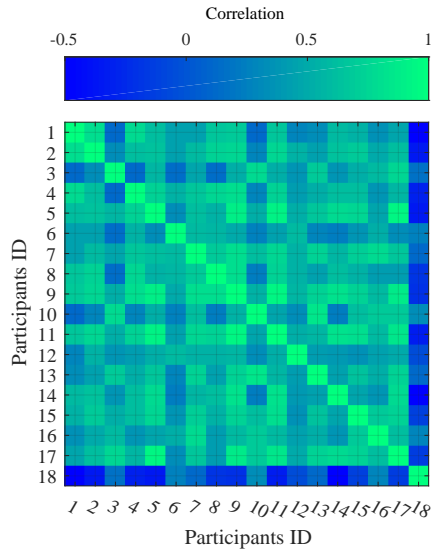


Figure F.3: Correlation matrix in the case of TP S+11.

F.2 Jury test score vs. quadratic error

In Section 4.4.1, Figures 4.14 and 4.15 show the averaged jury test score in black for the TPs S+02 and S+11 together with their standard errors and the averaged quadratic error $\bar{\mathcal{E}}$ in blue for each numerical model. Here the other cases are shown. It is recalled that the averaged jury test scores are in left y -axis, the errors are the vertical bars, and $\bar{\mathcal{E}}$ is in blue on the left y -axis; the models are identified by their size rank on the x -axis (see Table 3.5) and are ascendingly ordered based on the jury test score.

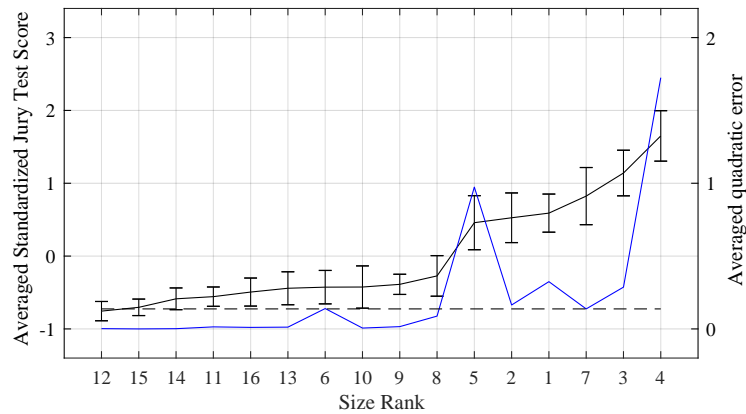


Figure F.4: Jury test score, in black (left axis), and error $\bar{\mathcal{E}}$, in blue (right axis), in the case of TP S-21; standard errors in the vertical bars, size ranks (see Table 3.5) in the abscissa.

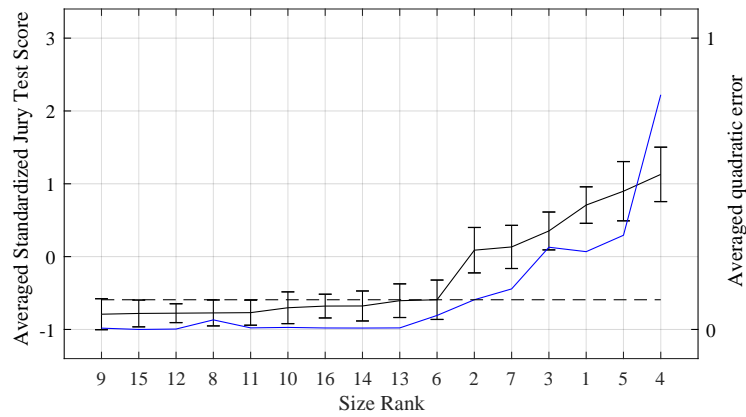


Figure F.5: Jury test score, in black (left axis), and error $\bar{\mathcal{E}}$, in blue (right axis), in the case of TP G+10; standard errors in the vertical bars, size ranks (see Table 3.5) in the abscissa.

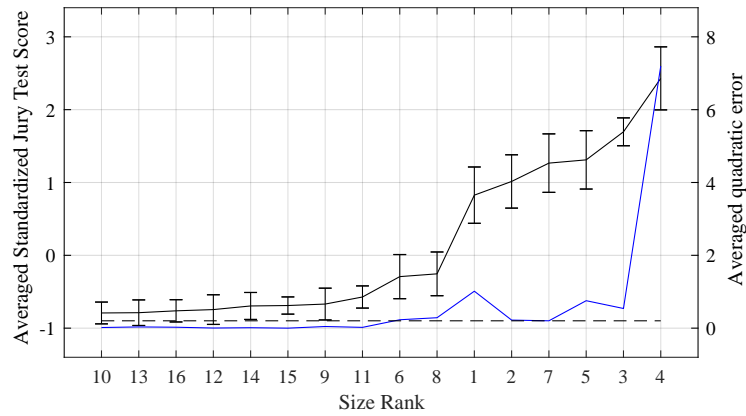


Figure F.6: Jury test score, in black (left axis), and error $\bar{\mathcal{E}}$, in blue (right axis), in the case of TP G-11; standard errors in the vertical bars, size ranks (see Table 3.5) in the abscissa.

F.3 Jury test score vs. \overline{RVAC}

In Section 4.4.1, Figure 4.16 is a copy of Figure 4.15 showing the \overline{RVAC} (in red) instead of the quadratic error. It is recalled here that the worst six models have $\overline{RVAC} \leq 0.94$. Here the other cases are shown.

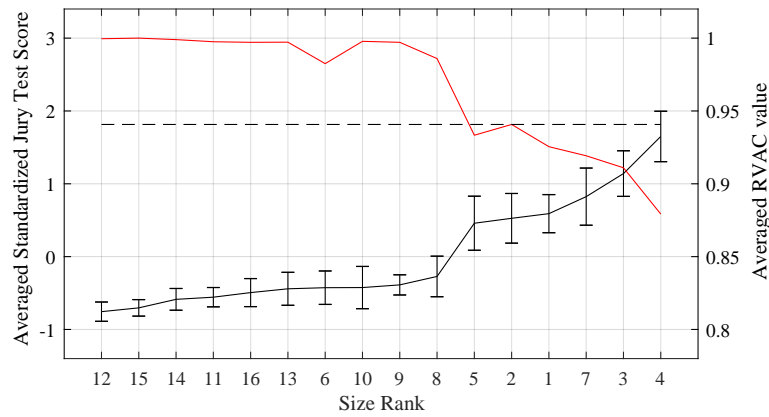


Figure F.7: Jury test score, in black (left axis), and \overline{RVAC} , in red (right axis), in the case of TP S-21; standard errors in the vertical bars, size ranks (see Table 3.5) in the abscissa.

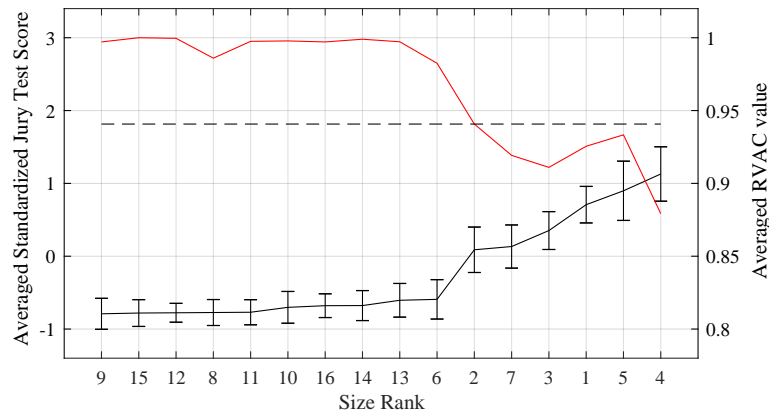


Figure F.8: Jury test score, in black (left axis), and \overline{RVAC} , in red (right axis), in the case of TP G+10; standard errors in the vertical bars, size ranks (see Table 3.5) in the abscissa.

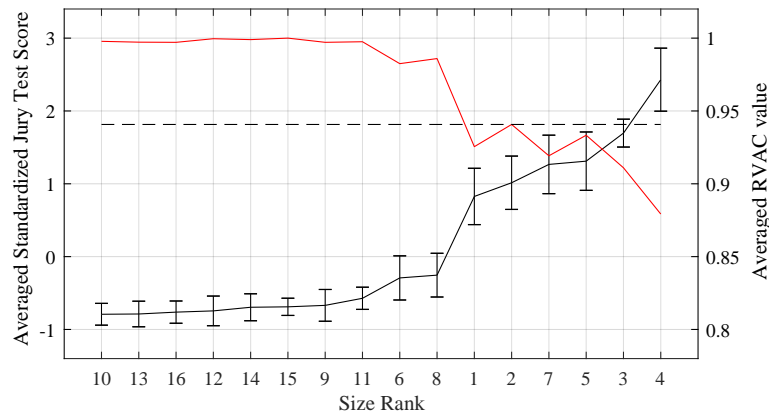


Figure F.9: Jury test score, in black (left axis), and \overline{RVAC} , in red (right axis), in the case of TP G-11; standard errors in the vertical bars, size ranks (see Table 3.5) in the abscissa.

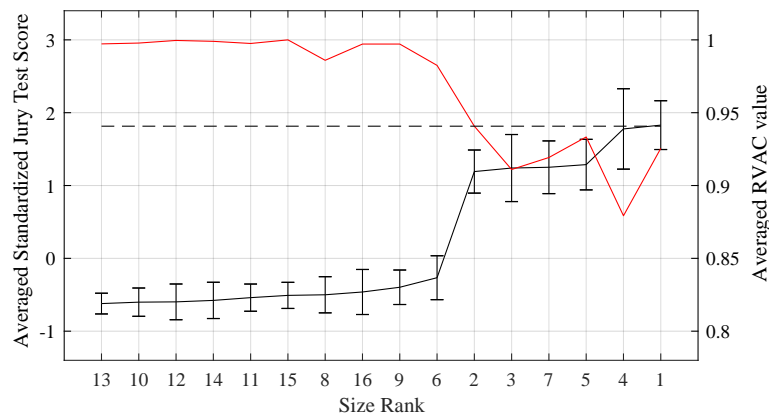


Figure F.10: Jury test score, in black (left axis), and \overline{RVAC} , in red (right axis), in the case of TP S+20; standard errors in the vertical bars, size ranks (see Table 3.5) in the abscissa.



FOLIO ADMINISTRATIF

THESE DE L'UNIVERSITE DE LYON OPEREE AU SEIN DE L'INSA LYON

NOM : PULVIRENTI

DATE de SOUTENANCE : 19/10/2021

Prénoms : Giorgio

TITRE : Finite elements transfer functions accuracy related to human perception

NATURE : Doctorat

Numéro d'ordre : 2021LYSEI059

Ecole doctorale : MEGA (Mécanique, Energétique, Génie Civil, Acoustique)

Spécialité : Acoustique

RESUME : Dans le domaine de la qualité du son, les techniques d'auralisation exploitent les méthodes de simulations numériques pour reproduire les sons même en l'absence de prototype physique, ce qui accélère le processus de conception. Cependant, les simulations nécessitent des temps de calcul importants : comment les réduire ?

Cette thèse évalue l'influence des erreurs des simulations par éléments finis (FEM) sur les sons perçus après synthèse sonore. Si ces erreurs influent peu sur la perception humaine, alors les ingénieurs en acoustique pourraient en tirer parti en utilisant des modèles numériques moins précis mais perçus de manière équivalente à des modèles plus coûteux en ressources numériques. Après un état de l'art, la théorie des éléments finis est ici décrite et les erreurs numériques sont analysées. Des expériences numériques montrent comment cette théorie s'adapte à la réalité des simulations pour cas simples. Ensuite, un prototype de quart de véhicule est construit, simulé et testé ; le cas étudié représente la transmission du son entre le point de contact pneu-chaussée et un piéton à quelques mètres du véhicule. Un modèle de référence est construit et validé à partir des mesures. Quinze autres modèles sont obtenus en dégradant progressivement les paramètres initiaux. Les fonctions de transfert obtenues sont utilisées pour obtenir des signaux acoustiques par convolution avec l'enregistrement temporel d'un pneu. L'analyse de différentes métriques des sons suggère que les différences dues aux erreurs numériques ne sont pas significatives, ce que l'expérience perceptive confirme : les participants ont trouvé les tests difficiles, et seuls certains sons ont été perçus comme "différents" des sons de référence. Toutefois, certains paramètres des éléments finis ont été identifiés comme des paramètres clés de la qualité de la restitution sonore et sont analysés. La thèse se termine par un résumé et des propositions de perspectives pour les recherches futures.

MOTS-CLÉS : Éléments finis, auralisation, fonctions de transfert acoustique, qualité du son.

Laboratoire (s) de recherche : Laboratoire Vibrations Acoustique (LVA) de l'INSA – Lyon

Directeur de thèse : PARIZET Etienne

Présidente de jury : Deckers, Elke

Composition du jury :

Parizet, Etienne, professeur, INSA-LYON

Totaro, Nicolas, professeur, INSA-LYON

Deckers, Elke, professeure, KUL

Kropp, Wolfgang, professeur, Chalmers University

García, Juan J., docteur, Applus+ IDIADA

Directeur de thèse

Co-directeur de thèse

Présidente, rapporteure

Rapporteur

Examineur